VENTRICULAR MECHANICS IN CONGENITAL HEART DISEASES

EDITED BY: Giovanni Biglino and Adelaide de Vecchi
PUBLISHED IN: Frontiers in Pediatrics; Frontiers in Cardiovascular Medicine

frontiers Research Topics

frontiers

ISSN 1664-8714
ISBN 978-2-88945-264-4
DOI 10.3389/978-2-88945-264-4

About Frontiers

Frontiers is more than just an open-access publisher of scholarly articles: it is a pioneering approach to the world of academia, radically improving the way scholarly research is managed. The grand vision of Frontiers is a world where all people have an equal opportunity to seek, share and generate knowledge. Frontiers provides immediate and permanent online open access to all its publications, but this alone is not enough to realize our grand goals.

Frontiers Journal Series

The Frontiers Journal Series is a multi-tier and interdisciplinary set of open-access, online journals, promising a paradigm shift from the current review, selection and dissemination processes in academic publishing. All Frontiers journals are driven by researchers for researchers; therefore, they constitute a service to the scholarly community. At the same time, the Frontiers Journal Series operates on a revolutionary invention, the tiered publishing system, initially addressing specific communities of scholars, and gradually climbing up to broader public understanding, thus serving the interests of the lay society, too.

Dedication to quality

Each Frontiers article is a landmark of the highest quality, thanks to genuinely collaborative interactions between authors and review editors, who include some of the world's best academicians. Research must be certified by peers before entering a stream of knowledge that may eventually reach the public - and shape society; therefore, Frontiers only applies the most rigorous and unbiased reviews.
Frontiers revolutionizes research publishing by freely delivering the most outstanding research, evaluated with no bias from both the academic and social point of view.
By applying the most advanced information technologies, Frontiers is catapulting scholarly publishing into a new generation.

What are Frontiers Research Topics?

Frontiers Research Topics are very popular trademarks of the Frontiers Journals Series: they are collections of at least ten articles, all centered on a particular subject. With their unique mix of varied contributions from Original Research to Review Articles, Frontiers Research Topics unify the most influential researchers, the latest key findings and historical advances in a hot research area! Find out more on how to host your own Frontiers Research Topic or contribute to one as an author by contacting the Frontiers Editorial Office: **researchtopics@frontiersin.org**

VENTRICULAR MECHANICS IN CONGENITAL HEART DISEASES

Topic Editors:
Giovanni Biglino, Bristol Heart Institute, University of Bristol, United Kingdom
Adelaide de Vecchi, St Thomas' Hospital, King's College London, United Kingdom

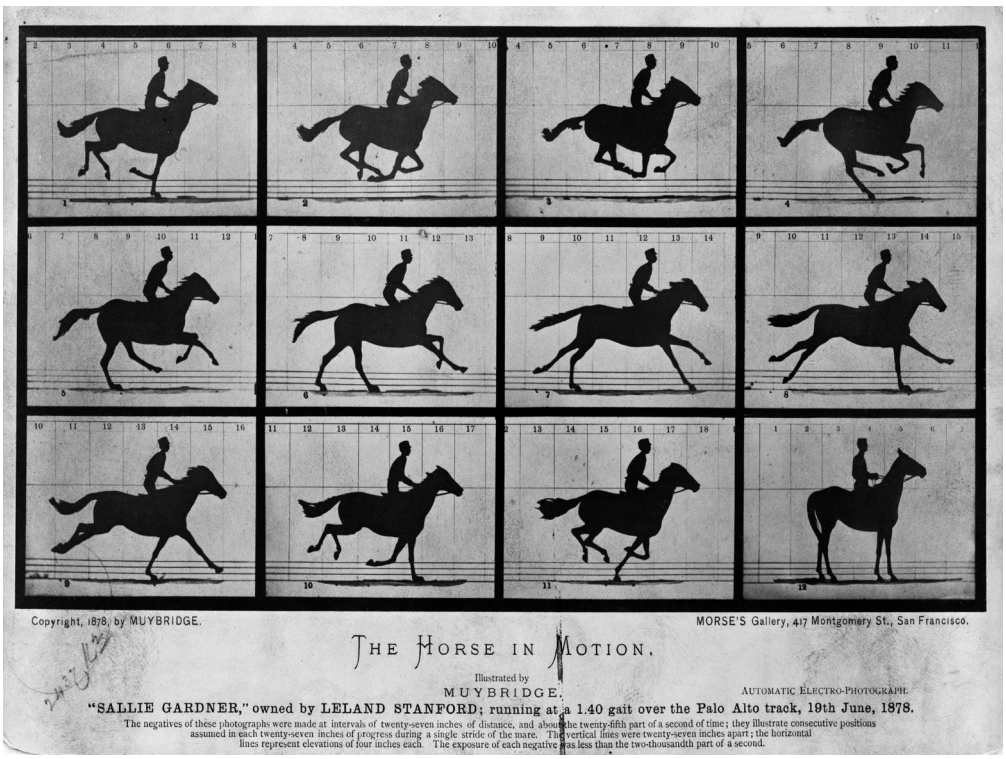

Sallie Gardner at a Gallop, also known as The Horse in Motion, by Eadweard Muybridge, 1878

Looking at "Horse in Motion", the iconic photograph by E. Muybridge, it is almost possible to hear the horse galloping. The pounding sound of the hoofs hitting the ground -like a drum- can also echo the rythmic beating of the human heart. That sound, that visceral rhythm, reminds us of the link between motion and performance: the perfectly executed stride of the horse, the incredible coordination of multiscale phenomena behind a heart beat. Furthermore, the decomposed sequence in Muybridge's photograph has become a well-known example of

breaking motion into its components over time, and as such is reminiscent of those images that are routinely acquired in clinical practice, where the heart appears dilating and shirnking in a sequence of snapshots. The investigation of this motion and its subtleties is essential for refining our understanding of cardiac function, and the appreciation of how and when this motion is no longer perfectly executed can lead us to understand functional impairments and provide insight into the unfolding of pathology.

In the presence of congenital heart disease (CHD), cardiac mechanics is altered: from single ventricle physiology to conduction abnormalities to different cardiomyopathies, it is important to both capture and interpret biomechanical changes that occur in the presence of a congenital defect. This special issue in Frontiers in Pediatrics, now an e-book, focuses on 'Ventricular mechanics in congenital heart disease' and looks at current knowledge of phenomena such as systolic/diastolic dysfuction and current methods (chiefly in cardiovascular magnetic resonance imaging and echocardiography) to evaluate cardiac function in the presence of CHD, and then presents a series of original studies that employ both medical imaging and computational modelling techniques to study specific CHD scenarios.

G.B.
A.d.V.
London, June 2017

Citation: Biglino, G., de Vecchi, A., eds. (2017). Ventricular Mechanics in Congenital Heart Diseases. Lausanne: Frontiers Media. doi: 10.3389/978-2-88945-264-4

Table of Contents

Section 4: Computational Modelling

frontiers in Pediatrics

EDITORIAL
published: 31 May 2017
doi: 10.3389/fped.2017.00129

Editorial: Ventricular Mechanics in Congenital Heart Disease

Giovanni Biglino[1] and Adelaide de Vecchi[2]*

[1] School of Clinical Sciences, Bristol Heart Institute, University of Bristol, Bristol, United Kingdom, [2] Division of Imaging Sciences and Biomedical Engineering, King's College London, London, United Kingdom

Keywords: computational modeling, cardiovascular magnetic resonance imaging, congenital heart disease, ventricular function, patient-specific

The Editorial on the Research Topic

Ventricular Mechanics in Congenital Heart Disease

American dancer and choreographer Martha Graham (1894–1991) famously said: "Nothing is more revealing than movement." Indeed, when thinking about the heart and its incessant dance, a huge amount of information can be derived from analyzing the mechanics of the organ, including mechanical impairments in the presence of disease and particularly in the presence of congenital lesions. This Research Topic aims to present recent research findings on ventricular mechanics in congenital heart disease (CHD) patients, alongside with state-of-the-art reviews that expertly summarize current knowledge in this area.

The reviews cover three crucial components. Panesar and Burch elucidate current knowledge of diastolic dysfunction in CHD, an important yet often overlooked component that can lead to heart failure even in patients with normal systolic function (Panesar and Burch). Ghonim et al. review fibrosis and how cardiovascular magnetic resonance (CMR) imaging can aid in its assessment, discussing techniques such as diffusion tensor imaging, tagging, feature tracking, late gadolinium enhancement imaging, and T1 mapping (Ghonim et al.). Finally, Greil et al. look again at the role of medical imaging in this context, but particularly at 3D whole heart CMR imaging, which they indicate as "a cornerstone" in CHD imaging, in the light of its versatile role that includes volumetric analysis in complex geometries, 3D printing, and computational modeling (Greil et al.).

As emerging from this Research Topic, imaging is undeniably a key component when discussing ventricular mechanics, its assessment, and quantification. Original research articles, in fact, demonstrate how different imaging techniques provide us with new insight in CHD patients. Whether assessing patients with tetralogy of Fallot after pulmonary valve replacement (Burkhardt et al.) or the role of isolated tricuspid valve repair in adults with CHD (Marsico et al.), the insight provided by imaging in looking at both right and left ventricle in patients with CHD is undeniable. Specific imaging modalities also play a crucial role in understanding the mechanics of CHDs, from investigating ventricular function in children with dilated cardiomyopathy using late gadolinium enhancement (Muscogiuri et al.) to identify an element of systolic dysfunction in young people with cardiomyopathies and aortic stenosis by means of CMR-derived wave intensity analysis (Ntsinjana et al.). The Research Topic also discusses more methodological considerations with regards to imaging; in particular, Gomez et al. present observations on landmark-based image registration to align CMR and ultrasound images in patients with hypoplastic left heart syndrome and compare ventricular volume measurements obtained with the two modalities (Gomez et al.).

This topic also offers a flavor of applications of computational modeling for the purpose of simulating and better understanding ventricular mechanics. Computational modeling is an increasingly powerful tool that can facilitate a patient-specific approach in assessing different aspects of CHD, from hemodynamics to devices to morphology (1). In this context, three compelling studies well

OPEN ACCESS

Edited and Reviewed by:
Antonio Francesco Corno, Glenfield Hospital, United Kingdom

****Correspondence:***
Giovanni Biglino
g.biglino@bristol.ac.uk

Specialty section:
This article was submitted to Pediatric Cardiology, a section of the journal Frontiers in Pediatrics

Received: *04 May 2017*
Accepted: *15 May 2017*
Published: *31 May 2017*

Citation:
Biglino G and de Vecchi A (2017) Editorial: Ventricular Mechanics in Congenital Heart Disease. Front. Pediatr. 5:129. doi: 10.3389/fped.2017.00129

exemplify the breath of applications of computational modeling. A finite element model of the fetal heart, accounting for changes in cardiac myocyte growth rates, is proposed, and its application is shown in both a "normal" scenario and in the presence of hypoplastic left heart syndrome (Dewan et al.). From the point of view of patient-specific modeling, a case study of a 4-month-old patient is presented demonstrating how a multi-domain computational model can recapitulate well the hemodynamics in the Blalock–Taussig shunt and in the pulmonary arteries (Arthurs et al.). Finally, a statistical shape analysis approach is presented as a tool allowing insight into ventricular deformations, presenting models of both patients with repaired aortic stenosis and healthy controls, and putting forward intriguing concepts such as "shape biomarkers" and "motion biomarkers" (Biffi et al.).

What emerges from these studies is certainly the multifaceted nature of analyzing ventricular motion and ventricular remodeling in patients which CHD. While this conclusion is not surprising in itself, these studies and reviews provide an opportunity to reflect on two key aspects of ventricular mechanics in the light of the latest cutting-edge technological progress as follows:

1. Population-based vs. patient-specific: depending on the pathophysiology of each CHD, and the consequent morphological and functional changes in the heart, these two competing philosophical approaches have emerged as effective methodologies to assess ventricular mechanics in the context of the individual and the population, respectively;
2. The role of imaging and modeling: different imaging modalities, and in particular CMR, clearly emerge as an essential tool for generating new knowledge and insight (literally as "looking inside") into ventricular mechanics in CHD. Similarly, computational modeling has recently reached a stage, where it can be successfully integrated with imaging techniques to enhance diagnosis and outcome prediction.

The contributions chosen for this special issue are not just a collection of the latest progress on the key aspects mentioned above. The purpose of this volume is to present new research that can shed light on these crucial points with the aim to link methodological approaches to clinical outcomes and, ultimately, patient benefit. Placing these recent advances into the end-user context is a key last step that will enable a true and purposeful translation of science: all these original research contributions strive to achieve this goal by proposing methods to test new biomarkers of disease progression. Movement, or the absence of, can be extremely revealing, but to what extent novel analyses will allow not only quantification of movement but also possible clinically meaningful predictions in the light of movement abnormalities? The simultaneous development of advanced imaging techniques, methodologies for image processing, and computational modeling, as well as the relentless progress made by the research community world-wide to integrate these tools both among each other and within clinical practice, can hold the key to this fundamental question. Ultimately, CHDs encompass a wide range of anatomical and functional maladaptive traits, and as such there is no single recipe for positive outcomes in the clinic. Rather, the ability to understand and interpret the pathological changes from a mechanistic perspective is pivotal to select the most effective approach in the context of each disease.

Future directions include continued efforts for large-scale validation of computational models, as well as the development of user-friendly platforms to render the application of patient-specific simulations not only feasible but also accessible and efficient in the clinical domain. The progress in imaging acquisition techniques and processing presented in this Research Topic also holds significant potential for developing disease classifiers from image feature quantification in conjunction with machine learning algorithms. Another exciting area of future development outside the field of imaging and modeling would in fact be to explore the possibility of developing risk scoring methodologies, such as algorithms trained using electronic health records (2). The latter is beginning to show promise in other medical applications.

While some of the studies presented in this Research Topic are based on too small sample sizes to lead directly to clinical applications, the subtlety of the processes analyzed, together with the knowledge that some of the validated indices routinely used in adults are not necessarily informative in children (3), should at the very least lead to an open-minded approach toward exploring novel indices and measures to unravel this problem and improve the prognosis of these patients.

AUTHOR CONTRIBUTIONS

GB and AdV have contributed equally to this work.

REFERENCES

1. Biglino G, Capelli C, Bruse J, Bosi GM, Taylor AM, Schievano S. Computational modelling for congenital heart disease: how far are we from clinical translation? *Heart* (2017) 103(2):98–103. doi:10.1136/heartjnl-2016-310423
2. Alaa AM, Yoon J, Hu S, van der Schaar M. Personalized risk scoring for critical care prognosis using mixtures of Gaussian processes. *IEEE Trans Biomed Eng* (2017). doi:10.1109/TBME.2017.2698602
3. Dragulescu A, Mertens L, Friedberg MK. Interpretation of left ventricular diastolic dysfunction in children with cardiomyopathy by echocardiography: problems and limitations. *Circ Cardiovasc Imaging* (2013) 6:254–61. doi:10.1161/CIRCIMAGING.112.000175

Conflict of Interest Statement: The authors declare that the research was conducted in the absence of any commercial or financial relationships that could be construed as a potential conflict of interest.

frontiers in Pediatrics

OPINION
published: 14 July 2016
doi: 10.3389/fped.2016.00071

Ventricular Function in Congenital Heart Defects

*Antonio F. Corno**

East Midlands Congenital Heart Centre, Glenfiled Hospital, University Hospital Leicester, Leicester, UK

Keywords: congenital heart disease, ventricular mechanics, ventriculo-arterial coupling, modeling, HFPEF

In order to understand the physiology of the neonatal heart, one must have an understanding of both the fetal circulation and the cardiac function of the adult heart. Transitional changes occur in the neonatal period, where the function of one ventricle has important effects on the function of the contralateral ventricle (1). In the presence of congenital heart defects, the myocardium is exposed to pressure and/or volume overload with the subsequent development of hypertrophy and/or dilatation. This is further complicated by the myocardial exposure to chronic hypoxia (2).

Giovanni Biglino and Adelaide De Vecchi have organized a research topic entitled "Ventricular mechanics in congenital heart disease" in order to increase the current knowledge on the physiology of the neonatal and infant heart, particularly in relationship to the coupling of the ventricular function with the systemic and pulmonary resistance. This research topic will concentrate on myocardial function in complex congenital heart defects, including conditions with a morphologic right ventricle sustaining the systemic circulation and hearts with functionally a single ventricle.

The ventricular interactions in the presence of congenital heart defects have been primarily investigated for the past few decades using ultrasound and radioisotopes (3). This research topic will attract the contribution of researchers using advanced diagnostic techniques to investigate the myocardial function of neonates with normal hearts and with complex congenital heart defects, such as biomedical engineering, non-invasive and invasive diagnostic modalities, cardiovascular magnetic resonance imaging, finite element and statistical shape modeling, and computational fluid dynamics (Biglino et al.). This research topic will be of particular interest to those who involved in the treatment of complex congenital heart defects.

Research articles stimulated by this research topic will improve the understanding of the ventricular function in congenital heart defects and will facilitate the decision-making process related to the timing and type of intervention.

An improved knowledge of the degree of myocardial dysfunction as a result of ventricular pressure and/or volume overload due to the presence of cardiac malformations should result in improved comprehensive management strategies for each type of congenital heart defect.

AUTHOR CONTRIBUTIONS

The author confirms being the sole contributor of this work and approved it for publication.

OPEN ACCESS

Edited and Reviewed by:
Michael L. Moritz, University of Pittsburgh School of Medicine, USA

***Correspondence:**
Antonio F. Corno
tonycorno2@gmail.com

Specialty section:
This article was submitted to Pediatric Cardiology, a section of the journal Frontiers in Pediatrics

Received: *18 May 2016*
Accepted: *29 June 2016*
Published: *14 July 2016*

Citation:
Corno AF (2016) Ventricular Function in Congenital Heart Defects. Front. Pediatr. 4:71. doi: 10.3389/fped.2016.00071

REFERENCES

1. Friedman WF. The intrinsic physiologic properties of the developing heart. *Prog Cardiovasc Dis* (1972) 15:87–111. doi:10.1016/0033-0620(72)90006-0
2. Corno AF, Milano G, Morel S, Tozzi G, Genton CY, Samaja M, et al. Hypoxia: unique myocardial morphology? *J Thorac Cardiovasc Surg* (2004) 127:1301–8. doi:10.1016/j.jtcvs.2003.06.012
3. Friedman WF. Radioisotopes and cross sectional ultrasound in congenital heart disease. *Adv Cardiol* (1976) 17:32–9. doi:10.1159/000398825

Conflict of Interest Statement: The author declares that the research was conducted in the absence of any commercial or financial relationships that could be construed as a potential conflict of interest.

frontiers in Pediatrics

REVIEW
published: 27 February 2017
doi: 10.3389/fped.2017.00036

3D Whole Heart Imaging for Congenital Heart Disease

*Gerald Greil[1,2,3,4,5], Animesh (Aashoo) Tandon[1,2,3,4], Miguel Silva Vieira[5] and Tarique Hussain[1,2,3,4,5]**

[1] Department of Pediatrics, University of Texas Southwestern Medical Center, Dallas, TX, USA, [2] Department of Radiology, University of Texas Southwestern Medical Center, Dallas, TX, USA, [3] Department of Biomedical Engineering, University of Texas Southwestern Medical Center, Dallas, TX, USA, [4] Division of Pediatric Cardiology, Children's Medical Center Dallas, Dallas, TX, USA, [5] Division of Imaging Sciences and Biomedical Engineering, King's College London, London, UK

Three-dimensional (3D) whole heart techniques form a cornerstone in cardiovascular magnetic resonance imaging of congenital heart disease (CHD). It offers significant advantages over other CHD imaging modalities and techniques: no ionizing radiation; ability to be run free-breathing; ECG-gated dual-phase imaging for accurate measurements and tissue properties estimation; and higher signal-to-noise ratio and isotropic voxel resolution for multiplanar reformatting assessment. However, there are limitations, such as potentially long acquisition times with image quality degradation. Recent advances in and current applications of 3D whole heart imaging in CHD are detailed, as well as future directions.

Keywords: three-dimensional whole heart imaging, congenital heart disease, cardiovascular MRI, pediatrics, coronary imaging

OPEN ACCESS

Edited by:
Giovanni Biglino, University of Bristol, UK

Reviewed by:
Jennifer Steeden, University College London, UK
Madhusudan Ganigara, Mt Sinai Medical Centre, USA

***Correspondence:**
Tarique Hussain
mohammad.hussain@utsouthwestern.edu

Specialty section:
This article was submitted to Pediatric Cardiology, a section of the journal Frontiers in Pediatrics

Received: *06 January 2017*
Accepted: *10 February 2017*
Published: *27 February 2017*

Citation:
Greil G, Tandon A(A), Silva Vieira M and Hussain T (2017) 3D Whole Heart Imaging for Congenital Heart Disease. Front. Pediatr. 5:36. doi: 10.3389/fped.2017.00036

INTRODUCTION

The three-dimensional (3D) whole heart approach with respiratory navigator gating and ECG triggering has been developed to enable coronary imaging (1). This free-breathing and radiation-free approach is well established for the detection of coronary artery anomalies in infants and young children with congenital heart disease (CHD) (2) but is less used for assessment of coronary stenoses in adults (3). The comprehensive evaluation of thoracic vasculature it offers is uniquely suited to give detailed morphological information in CHD. There are a number of developments, mostly related to improved motion correction, which have made this approach feasible. Early reports of coronary imaging used multiple breath-holds and set the cardiac motion for diastole by using the estimated percentage of the RR interval (4); however, this approach yielded images of suboptimal quality. Important developments were then made in this regard: first, work by Kim et al. showed that improved image quality was obtained by individually defining the cardiac rest periods (5); second, advances in image contrast improved overall image quality (6); and finally, respiratory motion was addressed through the use of navigators during free-breathing coronary MR (7).

REST PERIODS

Cardiac rest periods for imaging include mid-diastole (between the early and rapid filling periods of the left ventricle) and end-systole (between aortic valve closure and mitral valve opening). In order to "freeze" coronary artery motion and minimize image blurring, the longest rest period with the least cardiac motion is often chosen, which is usually in mid-diastole. The longer rest period allows more

data to be acquired per heartbeat to fill k-space. End-diastole can be reasonably estimated for the majority of patients using a trigger time that starts at approximately 75% of the RR interval (8).

Using a "one-size-fits-all" approach, however, has been shown to result in inferior image quality (5). This is more critical in MRI compared to computer tomography (CT) coronary imaging owing to the greater flexibility in defining the acquisition window and data reconstruction over multiple cardiac cycles, and is particularly true for children, for whom the heart rate and RR interval and respiratory pattern variability is often high. In fact, as the heart rate increases, the mid-diastolic rest period shortens significantly. With this in mind, Tangcharoen et al. showed that prospective selection of end-systole over end-diastole greatly improved the success in implementing the whole heart sequence in children (9). Using this approach, they were able to demonstrate coronary origins (as confirmed by surgery) in greater than 88% of children above 4 months of age. However, success below this age has continued to be elusive and experience limited.

The conundrum regarding the optimal phase for imaging was eventually solved by Uribe et al. by developing a dual-phase sequence that was capable of acquiring both rest periods in a single acquisition with a similar imaging time to a single phase sequence (10). The dual-phase sequence is noteworthy for several reasons. First, it became apparent that although the end-systolic rest period is longer at higher heart rates, some coronary segments, such as the right coronary artery (RCA) within the anterior atrioventricular groove, may still be seen better during mid-diastole. Given this finding, the ability to perform dual-phase imaging with prospective selection of trigger delays for systole and diastole and with retrospective selection of the best phase to depict the coronary segment of interest in all cases appears attractive (10). Using this approach, Hussain et al. noted a number of advantages for CHD imaging, foremost of which was the ability to accurately measure cardiac structures in both phases (11). This is particularly important in gauging tissue properties such as distensibility prior to intervention. Furthermore, as some structures (such as pulmonary veins and atria) are better imaged in systole and others (such as great arteries and post-stenotic areas) in diastole, the dual-phase approach was shown to improve the overall success rate of imaging in CHD (**Figure 1**) (11). The dual-phase acquisition can also be manipulated to measure end-diastole and end-systole, which gives the imaging the ability to define ventricular volumes and ejection fraction. Although no regional wall motion function is provided, this approach allows an isotropic 3D dataset to be acquired without the necessity for breath-holding, potentially allowing for a more accurate approach to ventricular volumetric analysis (12, 13). Radial phase encoding trajectories have been also used for faster data acquisition (14).

Traditionally, the cardiac rest periods are assessed using high temporal resolution 4-chamber cine (e.g., 60–80 cardiac phases per heart beat). The mid-diastolic period is taken from cessation of movement of the RCA (i.e., pause in visible filling of RV) to the beginning of atrial systole. This stringent definition covers both RCA and left anterior descending diastolic rest periods (5). The end-systolic period is taken from cessation of movement of the RCA (corresponding to lowest RV volume) to just before the beginning of opening of the tricuspid valve. However, this method can be time-consuming and prone to interobserver error, and it has been shown that an automated program is capable of more accurate definitions of cardiac rest periods than visual inspection (15).

IMAGE CONTRAST

The importance of considering tissue boundaries for the whole heart approach was noted early on (7). Botnar et al. showed that the addition of a T2-preparation pulse resulted in relative suppression of myocardial signal and an improvement in image quality. They noted a 33% improvement in vessel sharpness and 123% improvement in contrast-to-noise ratio (CNR).

Another important aspect of image contrast is to suppress the signal from epicardial fat (16). Fat suppression techniques that have been proposed for whole heart angiography include short tau inversion recovery and spectral presaturation with inversion recovery (SPIR). SPIR has a slight advantage in terms of tissue specificity for this purpose and results in a higher signal-to-noise ratio. Therefore, it is currently the preferred choice for fat suppression in whole heart imaging. Both methods suffer

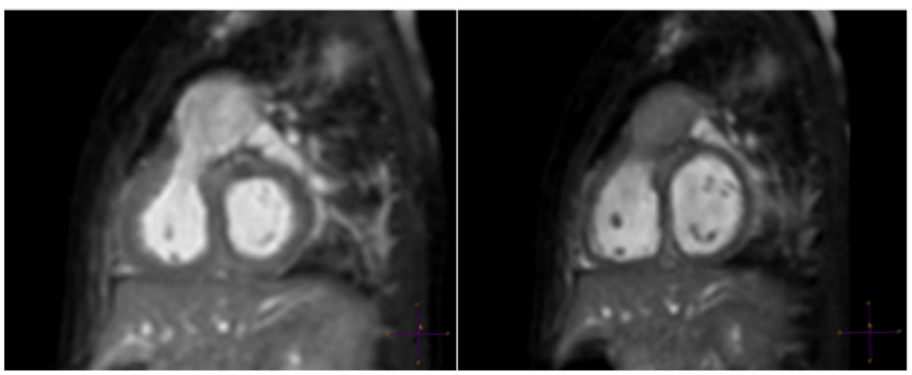

FIGURE 1 | A 6-month-old patient with right ventricular outflow tract (RVOT) aneurysm. "Windowing" levels and geometry are linked in this multiplanar reformat of a RVOT aneurysm showing clear superiority of the systolic image (left).

from potentially introducing misregistration artifacts or field inhomogeneity. An increasingly used method for fat suppression, the Dixon technique, relies on the phase shifts that occur due to resonance frequency differences between water and fat by acquiring images at carefully chosen echo times. This technique has been shown to give improved imaging at 1.5-T field strength (17, 18). Field homogeneity is difficult to achieve for whole heart coronary imaging at higher field strengths. This has a major impact on image quality. Therefore, the Dixon technique may offer even greater superiority over the traditional fat suppression techniques at 3.0 T (**Figure 2**) (17, 18).

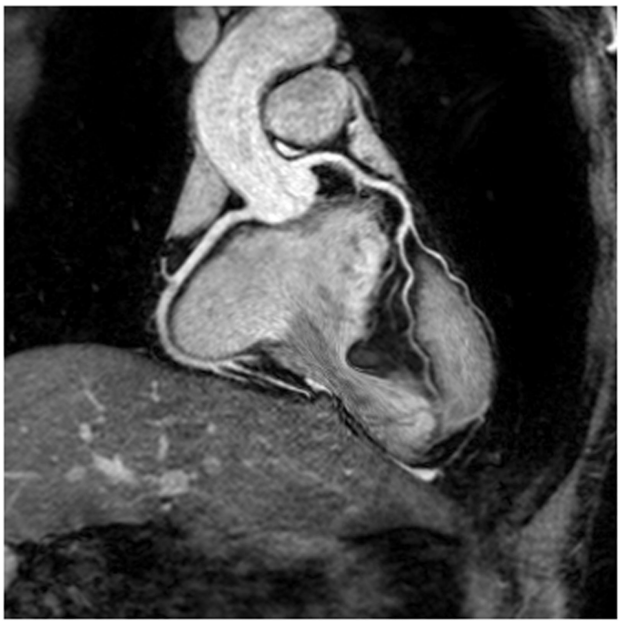

FIGURE 2 | Example of Dixon water–fat separation technique. Reformatted coronary images demonstrating quality and superior fat suppression achieved using Dixon technique at 3 T. Courtesy of Rene Botnar and Markus Henningsson, King's College London, London, UK.

For CHD imaging, fluid in the pericardial recesses can also cause interference with the diagnostic quality. One approach to overcome this is the use of an inversion pulse to reduce the signal from long T1 species. In addition, the null point can be set at or around the myocardium to reduce myocardial signal and obviate the need for a T2-preparation pulse. This requires shortening of the T1 time of blood by injection of a gadolinium-based contrast agent. Given the risk of contrast washout with a long acquisition time for the whole heart sequence, blood pool contrast agents have been used. Makowski et al. showed that the use of gadofosveset trisodium in combination with an inversion recovery steady-state-free-precession (SSFP) whole heart sequence was able to improve diagnostic quality and accuracy on CHD cases compared with standard extracellular contrast agents (19).

From a clinical standpoint, 3D inversion recovery SSFP imaging approach has produced the most reliable image quality, improving the ease of generating 3D models for computational simulation or 3D printing (**Figure 3**; Video S1 in Supplementary Material). There has been some debate as to whether this 3D whole heart inversion recovery is better with SSFP, which may give more signal, or with a spoiled gradient echo sequence, which may give greater T1-weighting allowing for more effective contrast in the presence of a blood pool gadolinium chelate. This was evaluated by Febbo et al. who concluded that SSFP was a superior approach at 1.5 T (20). However, there may be certain advantages of using a spoiled gradient echo approach, namely in terms of reduced susceptibility artifacts with metallic implants (21). Furthermore, at 3 T, SSFP sequences suffer from artifacts due to the greater field inhomogeneity at this field strength. Not surprisingly, spoiled gradient echo 3D whole heart has been shown to be superior at 3 T (Video S2 in Supplementary Material) (22).

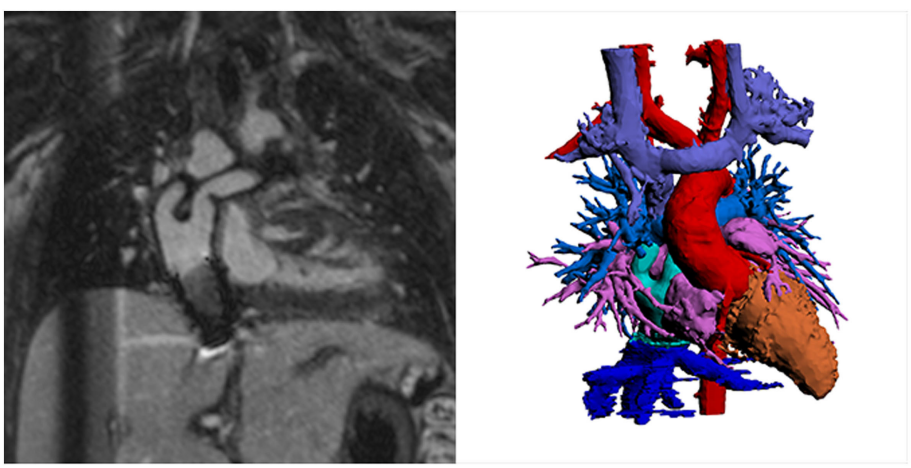

FIGURE 3 | Example inversion recovery three-dimensional spoiled gradient echo using gadofosveset trisodium image showing novel Y-graft cavopulmonary connection and inferior vena cava stent. Spoiled gradient echo techniques show less susceptibility artifact and may be preferable for this reason. The left hand image shows source images, and the volume-rendered segmentation is shown on the right. Courtesy Tim Slesnick, MD, Children's Healthcare of Atlanta/Emory University.

Although providing excellent image quality, there are two problems with the inversion recovery whole heart and blood pool agent approach. First, myocardial late enhancement imaging is not possible, and second, there are currently no intravascular blood pool agents being manufactured. One possible strategy is to use gadobenate dimeglumine, which has been shown to produce similar images as gadofosveset (23) given its partial albumin-binding characteristics. However, given its linear nature, there are theoretical concerns regarding a higher risk of central nervous system deposition (24) and nephrogenic systemic fibrosis than with macrocyclic gadolinium compounds (25). For this reason, Tandon et al. recently described a practical approach to routinely using a gadobutrol slow infusion for implementation of the whole heart inversion recovery sequence. Gadobutrol is a widely used extracellular contrast agent that is macrocyclic. By administering it by slow infusion, Tandon et al. showed the ability to use this agent for inversion recovery whole heart imaging (**Figure 4**). Moreover, they demonstrated that it can be simultaneously used for myocardial late enhancement (26).

RESPIRATORY MOTION

If the move from multiple breath-holds to free-breathing techniques has opened the way for higher spatial resolution coronary magnetic resonance angiography, "freezing" cardiac and coronary motion has resulted in relatively long 3D whole heart MRI acquisition times while providing sharp images (6). Besides the motion artifacts induced by cardiac pump activity and pulsatile arterial flow patterns, respiratory motion is also inevitable in free-breathing imaging techniques.

The first step toward correcting motion is to be able to measure it. This is commonly achieved by means of a respiratory navigator. This is a real-time image acquisition, which is interleaved with the high-resolution whole heart sequence, providing snapshots of the respiratory position before or after each segmented whole heart k-space acquisition. The vast majority of motion occurs in a foot–head direction, but important motion can occur in the anteroposterior and left–right directions (27). The most widely used approach for whole heart imaging is a one-dimensional diaphragmatic (1D) navigator (28). This consists of a narrow excitation pulse, typically placed at the dome of the right hemi-diaphragm, measuring the foot–head motion using a 1D representation of the lung–liver interface. However, this approach does not estimate true heart displacement, as the foot–head motion of the diaphragm is greater than the heart foot–head motion. Therefore, a correction factor of 0.6 is used to account for this. There are two problems with this estimation. First, the amount of heart motion compared to the diaphragm varies from individual to individual. Second, the heart is not "rigid," and so respiratory motion has a more complex effect on the heart causing some shear and rotation as well. In fact, such complex motion models relating diaphragmatic to heart motion exist and are known as affine motion models, but implementation on patient-specific basis is cumbersome (29). Commercially available whole heart imaging sequences use a 1D diaphragmatic navigator, which requires a separate excitation pulse, coupled to the whole heart pulse sequence. It also requires dedicated planning alongside the imaging volume.

More recently, novel approaches have been described using simply the whole heart data itself to correct for motion. This method is known as "self-gating" (30). It has the advantage of being able to correct motion in not only the foot–head dimension, but also in all three dimensions (31). Typically, self-navigation uses a 1D projection of the FOV and so static tissue such as the chest wall is also included in the navigator image, which may interfere with the motion estimation. One method to avoid this is to confine the projection to the area of interest (e.g., the heart), using "image-based" navigation. This type of motion compensation has been applied to CHD imaging with favorable results. Henningsson et al. demonstrated that such an approach reduced scan time and improved image quality in patients with CHD compared to the convention 1D diaphragmatic navigator (32). The approach used by Henningsson et al. was further novel in that the image navigator was generated by using a low resolution 2D projection image of the heart obtained from the start-up pulses in the SSFP sequence. Hence, no further image

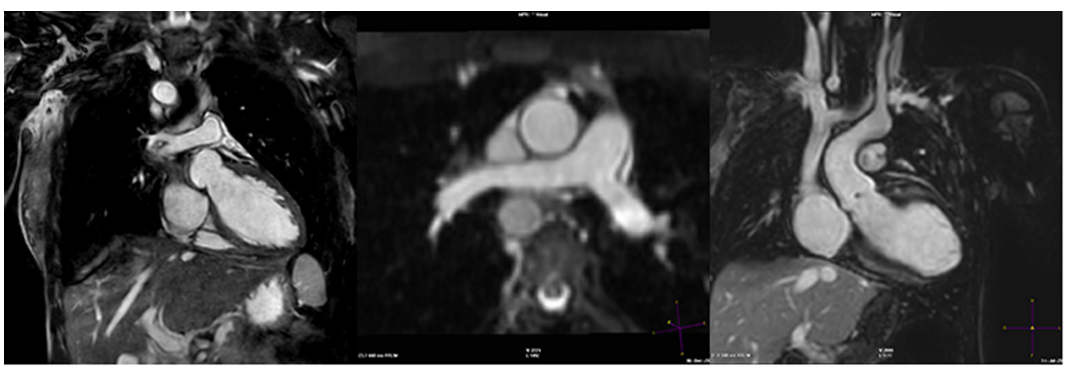

FIGURE 4 | Example images produced with gadobutrol slow infusion technique. Image quality for slow infusion protocol with inversion recovery steady-state-free-precession three-dimensional whole heart imaging can be excellent. The inversion pulse removes signal from fluid in the pericardial recesses resulting in superior vessel sharpness.

planning or acquisition was required. Furthermore, there was no need to extend the pulse sequence design. The implementation obviated the need for dedicated navigator planning and reduced significantly the acquisition time while improving image quality. **Figure 5** shows representative images showing how image-based navigation was able to depict the distal RCA. This type of image navigation is capable of correcting rigid motion in the foot–head and the left–right directions. More recently, image-based self-navigation has been implemented, which corrects for rigid and non-rigid motion in all three-dimensions (33). This type of 3D affine motion correction is currently computationally demanding, and hence difficult to implement widely.

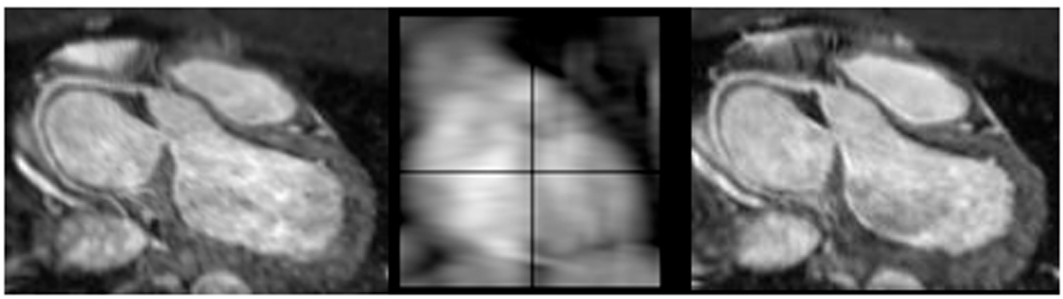

FIGURE 5 | Example images using self-navigation technique. iNAV self-navigation using an image navigator approach depicting right coronary artery (left); sample navigator image (center); one-dimensional diaphragmatic navigator approach for comparison (right).

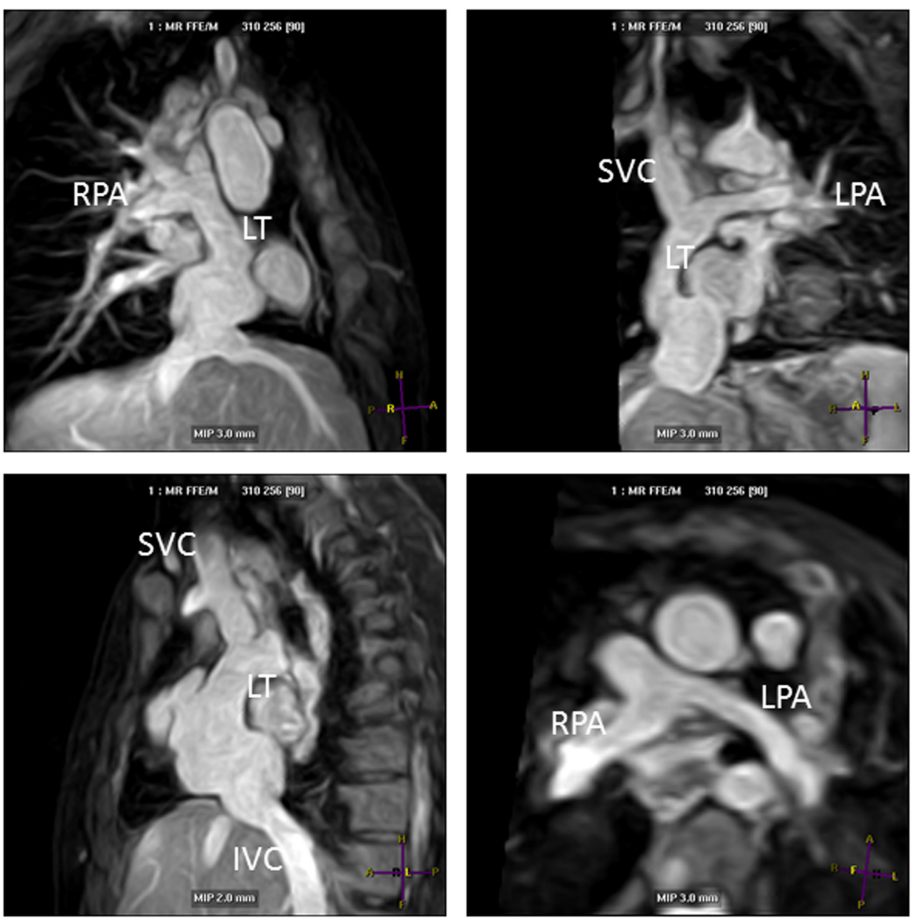

FIGURE 6 | Lateral tunnel Fontan pathways imaged using non-contrast three-dimensional (3D) balanced steady-state-free-precession (SSFP) technique. 3D SSFP reformatted views. Abbreviations: LT, lateral tunnel; RPA, right pulmonary artery; LPA, left pulmonary artery; SVC, superior vena cava; IVC, inferior vena cava.

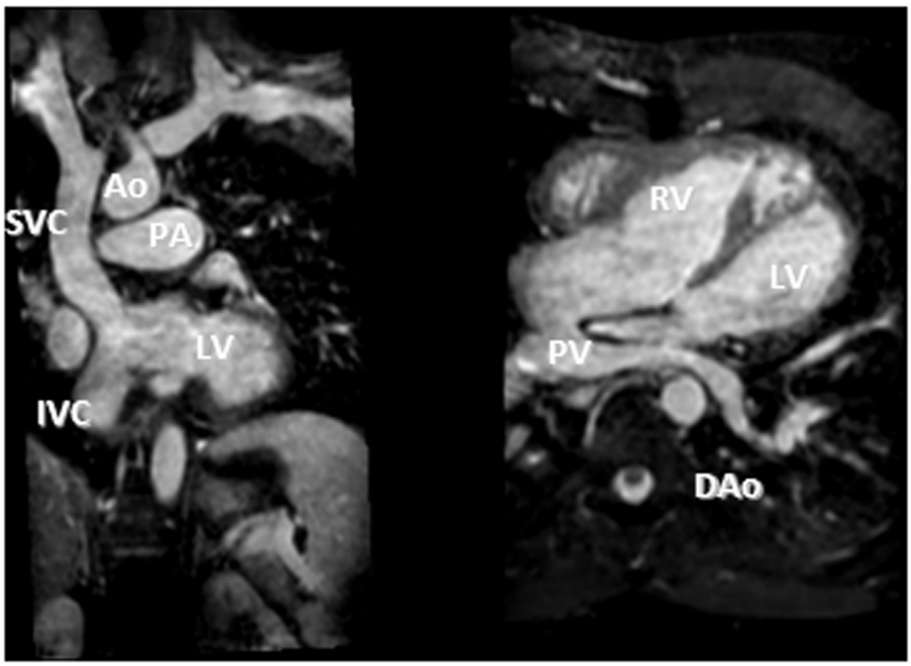

FIGURE 7 | **D-TGA after atrial redirection surgery (Senning)**. Systemic venous return redirected to the left ventricle (LV), i.e., the atrial switch redirection of the inferior vena cava (IVC) and superior vena cava (SVC) flow to the LV (left). Atrial baffle redirecting pulmonary venous return to the right atrium, i.e., unobstructed pulmonary venous return, draining *via* an intracardiac tunnel at the back of the heart to the right atrium, and directed to the anatomic right ventricle (right). Also shown is how the intraatrial systemic venous Senning pathway returning to the LV is compressed in the anterior–posterior dimension.

CHD APPLICATIONS

Another major improvement in CHD MRI was the implementation of time-efficient data acquisition methods (34). These acceleration methods have allowed data acquisition of a complete 3D dataset in currently less than 5 min (26). Currently, parallel imaging is the most commonly used acceleration technique with an acceleration factor of 2 (34). This means that the sequence can be routinely clinically applied in a CHD MRI study. The acquisition of a complete 3D dataset of the cardiovascular structures of the chest and upper abdomen during systole and/or diastole allows assessment of all cardiac segments within one dataset (35). Accordingly, the segmental approach used to diagnose CHD can be easily applied retrospectively (35, 36). Moreover, the detailed 3D dataset can be used to plan further sequences (e.g., flows) to clarify specific questions as appropriate, during the scanning session. This makes this method user-independent to diagnose structural heart disease (35). Initially, the successful use has been demonstrated in adolescents and young adults (35), but with improved data acquisition techniques, infants of 4 months and older were successfully imaged using 3D whole heart imaging, both with the single phase (37) and the dual-phase approach (11). Importantly, magnetization preparation schemes have allowed arterial and venous structures to be assessed simultaneously in the majority of cases, regardless of the use of a contrast agent (**Figure 6** shows Fontan pathways imaged without contrast agent use). This is a great advantage compared to CT, where high-quality coronary and vascular imaging is limited to the first pass of iodinated contrast and timed for a specific region of interest. Currently, CT studies are therefore targeted to a specific vascular structure such as the coronaries, the aorta, the pulmonary arteries, etc., and good venous and arterial signal acquisition requires additional expertise. Furthermore, despite dramatic reduction in ionizing radiation with current technologies, imaging tends to be limited to one phase if heart rate enables prospective gating. **Figures 6–8** show the advantage of cardiac MRI, which is able to image both arterial and venous phases with high image signal and CNRs, while avoiding administration of contrast agents.

High quality 3D whole heart MRI datasets can display the entire lumen of the coronary arteries including their relation to neighboring structures. Accordingly, this technique has become an important and critical part of the MRI protocol for exclusion of abnormal coronary artery origins (**Figure 9**) (38). This is particularly important in the setting of aborted sudden cardiac death, in pediatric patients with chest pain, and in the setting of planning interventions in CHD. As described above, the advance of technology allows successful imaging of the origin and proximal course of coronary arteries in the majority of infants and young children (9). Another relevant application of this technology is the assessment of the morphology of coronary arteries in patients post-Kawasaki disease, including the location, morphology, and maximal dimensions of coronary artery aneurysms (**Figure 10**) (39–42). However, accurate coronary wall assessment requires specialized techniques, and unlike CT, cannot

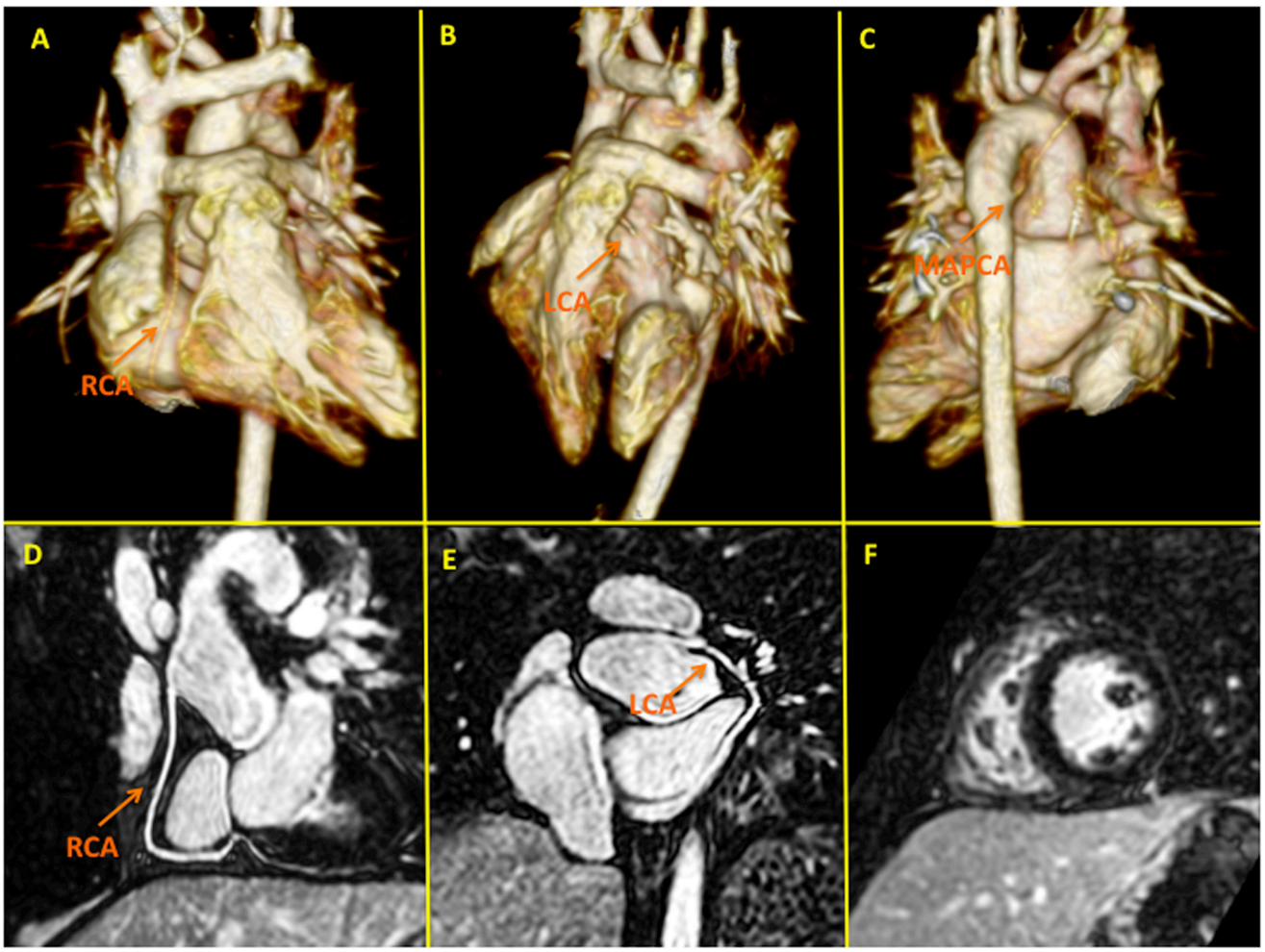

FIGURE 8 | High-spatial resolution coronary MR angiography using gadobenate dimeglumine and a novel self-navigated inversion recovery sequence in a 7-year-old patient with transposition of the great arteries. This sequence design takes advantage of the prolonged intravascular half-life of Gd-BOPTA allowing in a single examination detailed functional **(F)**, myocardial late gadolinium enhancement, and anatomical (pulmonary, aortic, and coronary) assessment **(D,E)**. Panels **(A–C)** depict three-dimensional volume-rendered images of the pulmonary arteries following LeCompte procedure and the relation with the unobstructed coronary arteries. LCA, left coronary artery; RCA, right coronary artery; MAPCA, major aortopulmonary collateral artery.

depict calcified lesions. Furthermore, other MRI techniques have shown superiority over the 3D approach described here for the assessment of coronary artery stenoses (42).

Finally, isotropic 3D whole heart datasets are particularly useful in CHD for interventional planning. MR angiography has already been shown to be accurate for planning cardiac catheterization procedures, with the 3D nature of the dataset being critical (43). 3D whole heart datasets, with the added advantage of gating, are well-suited to the production of 3D printed models to aid surgical planning (44, 45). More recently, clinicians have been fusing 3D whole heart datasets with conventional fluoroscopy angiography to augment procedural guidance. This approach can be used to minimize radiation, preplan angulations for fluoroscopic imaging, and reduce the required dose of iodinated contrast agent (**Figure 11**).

SUMMARY

ECG-gated respiratory-navigated 3D whole heart MRI has opened the door for isotropic submillimeter coronary imaging. Improved rest period delineation, image contrast agent use, and motion compensation, along with sequence acceleration and appropriate use of magnetization pre-pulses, have resulted in iterative improvements in image quality. The detail offered allows accurate segmental morphological analysis and has opened new avenues in research, teaching, and clinical diagnostics. A myriad of imaging applications, ranging from improved sequence planning during the course of the study, to volumetric analysis in complex ventricular geometries, and from 3D printing for surgical planning to computational modeling, have placed this sequence at the cornerstone of congenital cardiac MRI. The technique still

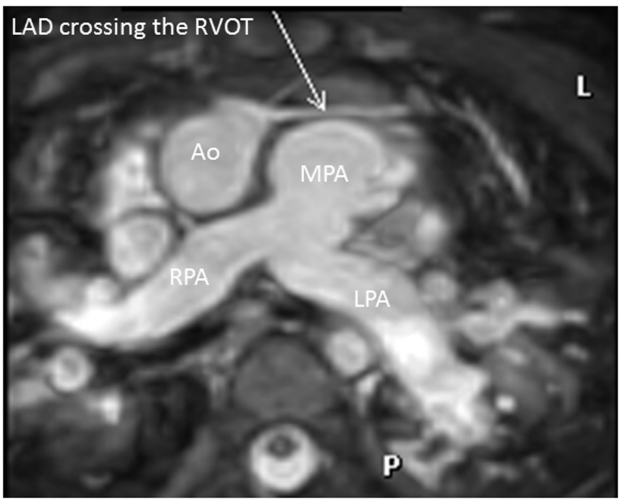

FIGURE 9 | **Coronary in double outlet right ventricle**. Three-dimensional balanced steady-state-free-precession sequence demonstrating left anterior descending (LAD) artery crossing the right ventricular outflow tract (RVOT). This is an important finding to plan accurately the appropriate intervention. Abbreviations: MPA, main pulmonary artery; RPA, right pulmonary artery; LPA, left pulmonary artery.

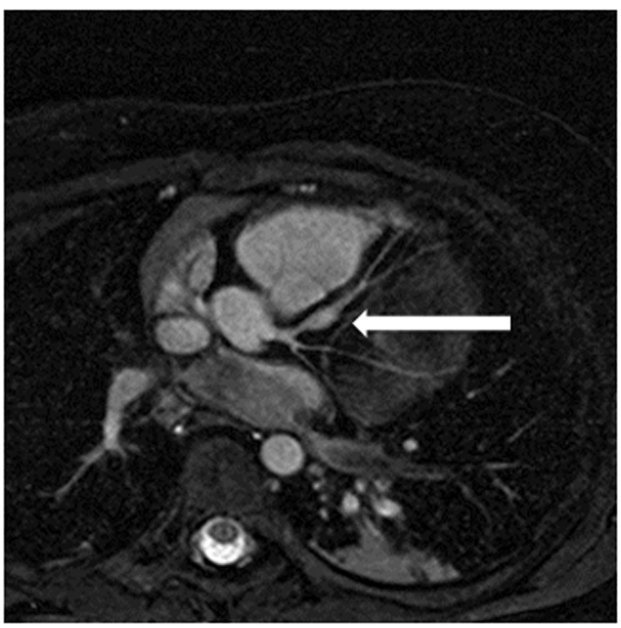

FIGURE 10 | **Coronary aneurysm**. Reformatted image of a 4-year-old patient with Kawasaki disease showing aneurysm in left anterior descending coronary artery (arrow).

requires diligence in planning, but current 3D whole heart images provide excellent quality overall and are often used to showcase image quality in clinical and commercial practice.

AUTHOR CONTRIBUTIONS

All the authors (GG, AT, MV, and TH) made substantial contributions to this review, worked on drafting and revising the work; approved the final version; and agreed to be held responsible for all aspects of the work.

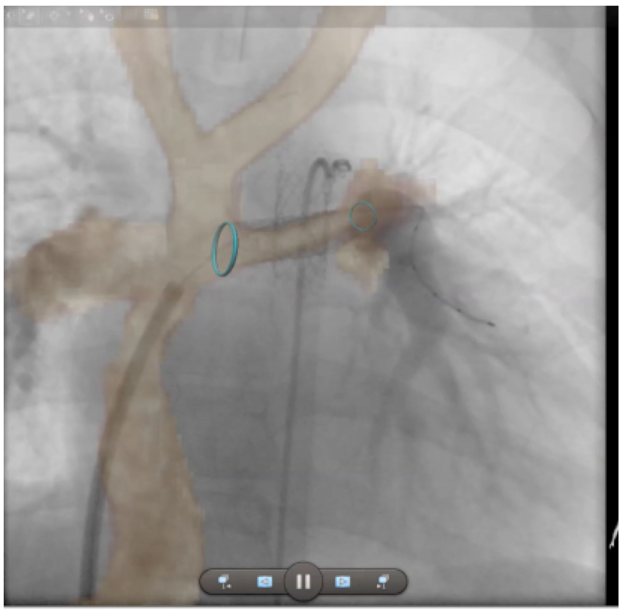

FIGURE 11 | **Augmented fluoroscopy**. Three-dimensional whole heart MR images are fused with angiographic images to augment procedural guidance. In this case, the left pulmonary artery in a child with a Fontan circuit has been stented. The optimal angulation for imaging is predetermined using the MR dataset. Blue ring markers on the MRI dataset are used to guide the positioning of the stent. The images show good registration on the angiogram after stenting has taken place.

ACKNOWLEDGMENTS

The authors would like to thank Tim Slesnick, MD, Children's Healthcare of Atlanta/Emory University, for help with images.

FUNDING

MV acknowledges support from the European Research Council under the European Union's Seventh Framework Programme (FP/2007-2013)/ERC grant agreement no. 307532.

SUPPLEMENTARY MATERIAL

The Supplementary Material for this article can be found online at http://journal.frontiersin.org/article/10.3389/fped.2017.00036/full#supplementary-material.

VIDEO S1 | A patient with functional single ventricle, who has undergone a Damus–Kaye–Stansel anastomosis and most recently a Fontan procedure. This image was acquired using 3D whole heart techniques with gadofosveset trisodium as described in the text.

VIDEO S2 | A patient with Scimitar syndrome. This image was acquired using gadofosveset trisodium contrast and a 3D spoiled gradient echo 3D whole heart sequence.

REFERENCES

1. Li D, Kaushikkar S, Haacke EM, Woodard PK, Dhawale PJ, Kroeker RM, et al. Coronary arteries: three-dimensional MR imaging with retrospective respiratory gating. *Radiology* (1996) 201(3):857–63. doi:10.1148/radiology.201.3.8939242
2. Valsangiacomo Buechel ER, Grosse-Wortmann L, Fratz S, Eichhorn J, Sarikouch S, Greil GF, et al. Indications for cardiovascular magnetic resonance in children with congenital and acquired heart disease: an expert consensus paper of the Imaging Working Group of the AEPC and the Cardiovascular Magnetic Resonance Section of the EACVI. *Eur Heart J Cardiovasc Imaging* (2015) 16(3):281–97. doi:10.1093/ehjci/jeu129
3. Kim WY, Danias PG, Stuber M, Flamm SD, Plein S, Nagel E, et al. Coronary magnetic resonance angiography for the detection of coronary stenoses. *N Engl J Med* (2001) 345(26):1863–9. doi:10.1056/NEJMoa010866
4. Edelman RR, Manning WJ, Burstein D, Paulin S. Coronary arteries: breath-hold MR angiography. *Radiology* (1991) 181(3):641–3. doi:10.1148/radiology.181.3.1947074
5. Kim WY, Stuber M, Kissinger KV, Andersen NT, Manning WJ, Botnar RM. Impact of bulk cardiac motion on right coronary MR angiography and vessel wall imaging. *J Magn Reson Imaging* (2001) 14(4):383–90. doi:10.1002/jmri.1198
6. Stuber M, Botnar RM, Danias PG, Kissinger KV, Manning WJ. Breathhold three-dimensional coronary magnetic resonance angiography using real-time navigator technology. *J Cardiovasc Magn Reson* (1999) 1(3):233–8. doi:10.3109/10976649909088335
7. Botnar RM, Stuber M, Danias PG, Kissinger KV, Manning WJ. Improved coronary artery definition with T2-weighted, free-breathing, three-dimensional coronary MRA. *Circulation* (1999) 99(24):3139–48. doi:10.1161/01.CIR.99.24.3139
8. Isma'eel H, Hamirani YS, Mehrinfar R, Mao S, Ahmadi N, Larijani V, et al. Optimal phase for coronary interpretations and correlation of ejection fraction using late-diastole and end-diastole imaging in cardiac computed tomography angiography: implications for prospective triggering. *Int J Cardiovasc Imaging* (2009) 25(7):739–49. doi:10.1007/s10554-009-9481-y
9. Tangcharoen T, Bell A, Hegde S, Hussain T, Beerbaum P, Schaeffter T, et al. Detection of coronary artery anomalies in infants and young children with congenital heart disease by using MR imaging. *Radiology* (2011) 259(1):240–7. doi:10.1148/radiol.10100828
10. Uribe S, Hussain T, Valverde I, Tejos C, Irarrazaval P, Fava M, et al. Congenital heart disease in children: coronary MR angiography during systole and diastole with dual cardiac phase whole-heart imaging. *Radiology* (2011) 260(1):232–40. doi:10.1148/radiol.11101659
11. Hussain T, Lossnitzer D, Bellsham-Revell H, Valverde I, Beerbaum P, Razavi R, et al. Three-dimensional dual-phase whole-heart MR imaging: clinical implications for congenital heart disease. *Radiology* (2012) 263(2):547–54. doi:10.1148/radiol.12111700
12. Delgado JA, Abad P, Rascovsky S, Calvo V, Castrillon G, Greil G, et al. Assessment of cardiac volumes using an isotropic whole-heart dual cardiac phase sequence in pediatric patients. *J Magn Reson Imaging* (2014) 39(3):708–16. doi:10.1002/jmri.24203
13. Uribe S, Tangchaoren T, Parish V, Wolf I, Razavi R, Greil G, et al. Volumetric cardiac quantification by using 3D dual-phase whole-heart MR imaging. *Radiology* (2008) 248(2):606–14. doi:10.1148/radiol.2482071568
14. Letelier K, Urbina J, Andia M, Tejos C, Irarrazaval P, Prieto C, et al. Accelerating dual cardiac phase images using undersampled radial phase encoding trajectories. *Magn Reson Imaging* (2016) 34(7):1017–25. doi:10.1016/j.mri.2016.03.017
15. Ustun A, Desai M, Abd-Elmoniem KZ, Schar M, Stuber M. Automated identification of minimal myocardial motion for improved image quality on MR angiography at 3 T. *AJR Am J Roentgenol* (2007) 188(3):W283–90. doi:10.2214/AJR.06.0334
16. Bornert P, Stuber M, Botnar RM, Kissinger KV, Manning WJ. Comparison of fat suppression strategies in 3D spiral coronary magnetic resonance angiography. *J Magn Reson Imaging* (2002) 15(4):462–6. doi:10.1002/jmri.10078
17. Bornert P, Koken P, Nehrke K, Eggers H, Ostendorf P. Water/fat-resolved whole-heart Dixon coronary MRA: an initial comparison. *Magn Reson Med* (2014) 71(1):156–63. doi:10.1002/mrm.24648
18. Nezafat M, Henningsson M, Ripley DP, Dedieu N, Greil G, Greenwood JP, et al. Coronary MR angiography at 3T: fat suppression versus water-fat separation. *MAGMA* (2016) 29(5):733–8. doi:10.1007/s10334-016-0550-7
19. Makowski MR, Wiethoff AJ, Uribe S, Parish V, Botnar RM, Bell A, et al. Congenital heart disease: cardiovascular MR imaging by using an intravascular blood pool contrast agent. *Radiology* (2011) 260(3):680–8. doi:10.1148/radiol.11102327
20. Febbo JA, Galizia MS, Murphy IG, Popescu A, Bi X, Turin A, et al. Congenital heart disease in adults: quantitative and qualitative evaluation of IR FLASH and IR SSFP MRA techniques using a blood pool contrast agent in the steady state and comparison to first pass MRA. *Eur J Radiol* (2015) 84(10):1921–9. doi:10.1016/j.ejrad.2015.06.030
21. Tandon A, Hashemi S, Parks WJ, Kelleman MS, Sallee D, Slesnick TC. Improved high-resolution pediatric vascular cardiovascular magnetic resonance with gadofosveset-enhanced 3D respiratory navigated, inversion recovery prepared gradient echo readout imaging compared to 3D balanced steady-state free precession readout imaging. *J Cardiovasc Magn Reson* (2016) 18(1):74. doi:10.1186/s12968-016-0296-4
22. Kaul MG, Stork A, Bansmann PM, Nolte-Ernsting C, Lund GK, Weber C, et al. Evaluation of balanced steady-state free precession (TrueFISP) and K-space segmented gradient echo sequences for 3D coronary MR angiography with navigator gating at 3 Tesla. *Rofo* (2004) 176(11):1560–5. doi:10.1055/s-2004-813629
23. Camren GP, Wilson GJ, Bamra VR, Nguyen KQ, Hippe DS, Maki JH. A comparison between gadofosveset trisodium and gadobenate dimeglumine for steady state MRA of the thoracic vasculature. *Biomed Res Int* (2014) 2014:625614. doi:10.1155/2014/625614
24. Robert P, Violas X, Grand S, Lehericy S, Idee JM, Ballet S, et al. Linear gadolinium-based contrast agents are associated with brain gadolinium retention in healthy rats. *Invest Radiol* (2016) 51(2):73–82. doi:10.1097/RLI.0000000000000241
25. Reiter T, Ritter O, Prince MR, Nordbeck P, Wanner C, Nagel E, et al. Minimizing risk of nephrogenic systemic fibrosis in cardiovascular magnetic resonance. *J Cardiovasc Magn Reson* (2012) 14:31. doi:10.1186/1532-429X-14-31
26. Tandon A, James L, Henningsson M, Botnar RM, Potersnak A, Greil GF, et al. A clinical combined gadobutrol bolus and slow infusion protocol enabling angiography, inversion recovery whole heart, and late gadolinium enhancement imaging in a single study. *J Cardiovasc Magn Reson* (2016) 18(1):66. doi:10.1186/s12968-016-0285-7
27. Henningsson M, Botnar RM. Advanced respiratory motion compensation for coronary MR angiography. *Sensors* (2013) 13(6):6882–99. doi:10.3390/s130606882
28. Ehman RL, Felmlee JP. Adaptive technique for high-definition MR imaging of moving structures. *Radiology* (1989) 173(1):255–63. doi:10.1148/radiology.173.1.2781017
29. Nehrke K, Bornert P. Prospective correction of affine motion for arbitrary MR sequences on a clinical scanner. *Magn Reson Med* (2005) 54(5):1130–8. doi:10.1002/mrm.20686
30. Piccini D, Littmann A, Nielles-Vallespin S, Zenge MO. Respiratory self-navigation for whole-heart bright-blood coronary MRI: methods for robust isolation and automatic segmentation of the blood pool. *Magn Reson Med* (2012) 68(2):571–9. doi:10.1002/mrm.23247
31. Lai P, Bi X, Jerecic R, Li D. A respiratory self-gating technique with 3D-translation compensation for free-breathing whole-heart coronary MRA. *Magn Reson Med* (2009) 62(3):731–8. doi:10.1002/mrm.22058
32. Henningsson M, Hussain T, Vieira MS, Greil GF, Smink J, Ensbergen GV, et al. Whole-heart coronary MR angiography using image-based navigation for the detection of coronary anomalies in adult patients with congenital heart disease. *J Magn Reson Imaging* (2016) 43(4):947–55. doi:10.1002/jmri.25058
33. Henningsson M, Prieto C, Chiribiri A, Vaillant G, Razavi R, Botnar RM. Whole-heart coronary MRA with 3D affine motion correction using 3D image-based navigation. *Magn Reson Med* (2014) 71(1):173–81. doi:10.1002/mrm.24652
34. Kozerke S, Tsao J. Reduced data acquisition methods in cardiac imaging. *Top Magn Reson Imaging* (2004) 15(3):161–8. doi:10.1097/01.rmr.0000132789.84706.9d
35. Sorensen TS, Korperich H, Greil GF, Eichhorn J, Barth P, Meyer H, et al. Operator-independent isotropic three-dimensional magnetic resonance

imaging for morphology in congenital heart disease: a validation study. *Circulation* (2004) 110(2):163–9. doi:10.1161/01.CIR.0000134282.35183.AD

36. van Praagh R, van Praagh S. Morphologic anatomy. In: Fyler DC, editor. *Nadas' Pediatric Cardiology*. Philadelphia: Hanley & Belfus Inc. (1992). p. 17–26.
37. Monney P, Piccini D, Rutz T, Vincenti G, Coppo S, Koestner SC, et al. Single centre experience of the application of self navigated 3D whole heart cardiovascular magnetic resonance for the assessment of cardiac anatomy in congenital heart disease. *J Cardiovasc Magn Reson* (2015) 17:55. doi:10.1186/s12968-015-0156-7
38. Beerbaum P, Sarikouch S, Laser KT, Greil G, Burchert W, Korperich H. Coronary anomalies assessed by whole-heart isotropic 3D magnetic resonance imaging for cardiac morphology in congenital heart disease. *J Magn Reson Imaging* (2009) 29(2):320–7. doi:10.1002/jmri.21655
39. Greil GF, Stuber M, Botnar RM, Kissinger KV, Geva T, Newburger JW, et al. Coronary magnetic resonance angiography in adolescents and young adults with Kawasaki disease. *Circulation* (2002) 105(8):908–11. doi:10.1161/hc0802.105563
40. Mavrogeni S, Papadopoulos G, Douskou M, Kaklis S, Seimenis I, Baras P, et al. Magnetic resonance angiography is equivalent to X-ray coronary angiography for the evaluation of coronary arteries in Kawasaki disease. *J Am Coll Cardiol* (2004) 43(4):649–52. doi:10.1016/j.jacc.2003.08.052
41. Mavrogeni S, Bratis K, Karanasios E, Georgakopoulos D, Kaklis S, Varlamis G, et al. CMR evaluation of cardiac involvement during the convalescence of Kawasaki disease. *JACC Cardiovasc Imaging* (2011) 4(10):1140–1. doi:10.1016/j.jcmg.2011.04.021
42. Mavrogeni S, Papadopoulos G, Hussain T, Chiribiri A, Botnar R, Greil GF. The emerging role of cardiovascular magnetic resonance in the evaluation of Kawasaki disease. *Int J Cardiovasc Imaging* (2013) 29(8):1787–98. doi:10.1007/s10554-013-0276-9
43. Valverde I, Parish V, Hussain T, Rosenthal E, Beerbaum P, Krasemann T. Planning of catheter interventions for pulmonary artery stenosis: improved measurement agreement with magnetic resonance angiography using identical angulations. *Catheter Cardiovasc Interv* (2011) 77(3):400–8. doi:10.1002/ccd.22695
44. Byrne N, Velasco Forte M, Tandon A, Valverde I, Hussain T. A systematic review of image segmentation methodology, used in the additive manufacture of patient-specific 3D printed models of the cardiovascular system. *JRSM Cardiovasc Dis* (2016) 5:2048004016645467. doi:10.1177/2048004016645467
45. Valverde I, Gomez G, Gonzalez A, Suarez-Mejias C, Adsuar A, Coserria JF, et al. Three-dimensional patient-specific cardiac model for surgical planning in Nikaidoh procedure. *Cardiol Young* (2015) 25(4):698–704. doi:10.1017/S1047951114000742

Conflict of Interest Statement: The authors declare that the research was conducted in the absence of any commercial or financial relationships that could be construed as a potential conflict of interest.

frontiers in Cardiovascular Medicine

REVIEW
published: 15 February 2017
doi: 10.3389/fcvm.2017.00005

Assessment of Diastolic Function in Congenital Heart Disease

Dilveer Kaur Panesar[1,2] and Michael Burch[1]*

[1] Cardiothoracic Unit, Great Ormond Street Hospital for Children NHS Foundation Trust, London, UK, [2]Centre for Cardiovascular Imaging, Institute of Cardiovascular Science, University College London, London, UK

Diastolic function is an important component of left ventricular (LV) function which is often overlooked. It can cause symptoms of heart failure in patients even in the presence of normal systolic function. The parameters used to assess diastolic function often measure flow and are affected by the loading conditions of the heart. The interpretation of diastolic function in the context of congenital heart disease requires some understanding of the effects of the lesions themselves on these parameters. Individual congenital lesions will be discussed in this paper. Recently, load-independent techniques have led to more accurate measurements of ventricular compliance and remodeling in heart disease. The combination of inflow velocities and tissue Doppler measurements can be used to estimate diastolic function and LV filling pressures. This review focuses on diastolic function and assessment in congenital heart disease.

Keywords: diastolic function, congenital heart disease, echocardiography, CMR, diastolic heart failure

OPEN ACCESS

Edited by:
Giovanni Biglino,
University of Bristol, UK

Reviewed by:
Yasuhiro Fujii,
Okayama University, Japan
Meena Nathan,
Boston Children's Hospital, USA

****Correspondence:***
Dilveer Kaur Panesar
dilveer.panesar@ucl.ac.uk

Specialty section:
This article was submitted to Pediatric Cardiology, a section of the journal Frontiers in Cardiovascular Medicine

Received: *28 October 2016*
Accepted: *23 January 2017*
Published: *15 February 2017*

Citation:
Panesar D and Burch M (2017) Assessment of Diastolic Function in Congenital Heart Disease. Front. Cardiovasc. Med. 4:5. doi: 10.3389/fcvm.2017.00005

INTRODUCTION

Myocardial function has been extensively studied in the context of congenital heart disease. The focus to date has been on systolic function due to its importance and ease of measurement. However, the heart also needs to be adequately filled in order to function optimally, and this aspect of cardiac function is relatively under-investigated. The difficulties (as with systolic function) come when attempting to measure the relaxation of the myocardium while negating any effect of pre- or after-load. This is a difficult task and has led to the development of several tools which track myocardial movement independently of the usual flow-based parameters; the latter are heavily influenced by loading conditions. This article will summarize the current assessment of diastolic function using echocardiography and cardiac magnetic resonance (CMR) imaging in the normal heart and in patients with congenital heart disease.

DIASTOLIC DYSFUNCTION (DD)

Diastole denotes the filling phase of the cardiac cycle. Filling is determined by myocardial relaxation as well as atrial contraction and atrial and ventricular compliance. Myocardial relaxation begins when the myofibrils return to an unstressed state and this precedes mitral valve (MV) opening (isovolumic relaxation). ATP is used to actively uncouple calcium from the contractile apparatus and return it to the sarcoplasmic reticulum. Active relaxation is only responsible for early diastolic filling, whereas compliance is important throughout filling and especially during atrial contraction.

The early part of diastole is active relaxation, which is an energy-consuming process. The latter part is due to compliance or stiffness of the ventricle. Isovolumic relaxation time (IVRT) can be measured by invasive catheterization measurements. The index used in its measurement is the time constant

of isovolumic pressure decline (τ). In non-invasive measurement, IVRT is the closest measurement to assess this value. However, as with all indices of diastolic function, the loading conditions must be taken into account.

The stiffness of the myocardium also plays an important role in diastolic function. The mass of the left ventricular (LV) affects the stiffness as do the viscoelastic properties of the myocardium (cellular and extracellular components). Attempts are made to measure this increase in myocardial stiffness. However, the difficulty arises in the mechanism of measurement as well as the timing and nature of diastole. Flow-based measurements rely on a change in volume to occur, and so they are unable to quantify isovolumic relaxation as they assess only the last stage of diastole. There is also no universal measurement of diastole [equivalent to ejection fraction (EF) in systole] and torsion and dyssynchrony are difficult to quantify.

NON-INVASIVE ASSESSMENT METHODS

Echocardiography

As the ventricle stiffens, the velocity of blood flowing into the ventricle decreases. This downward trend would continue if not for compensation which takes the form of increased heart rate or increased diastolic filling pressure to maintain stroke volume (SV). The latter causes an increase toward normal filling velocities (pseudonormalization) and a prolongation of rapid filling. Ventricular elastance is an important marker for ventricular stiffness and is correlated with increased cardiac morbidity (1). Increased strength of atrial contraction is a related compensatory mechanism to cope with increased diastolic filling pressures.

Left Atrium (LA) Volume

The LA is exposed to the LV loading pressure during MV opening and gradually remodels and increases in size. As LA remodeling takes place over time, it is a marker of the duration of DD as well as severity. The amount of dilatation also correlates with cardiovascular risk burden (2). There is a correlation between LA size and the risk of developing congestive cardiac failure (3, 4), atrial fibrillation (5), and ischemic heart disease (6). LA size is also a predictor of adverse outcome in patients with hypertrophic cardiomyopathy (7). LA size is measured from the apical four-chamber view at end-systole. It is also possible to calculate LA area from 2D four-chamber and two-chamber views.

Transmitral Doppler Inflow

The mitral inflow velocity profile helps characterize LV inflow dynamics. It is best measured from the apical four-chamber view (in both children and adults) with the cursor placed across the MV just inside the LV. The E wave is the early diastolic filling wave seen on Doppler interrogation of the MV. It is caused by the drop of LV pressure below LA pressure during the cardiac cycle and is therefore influenced by LA pressure, LV compliance, and the rate of LV relaxation. The A wave, or atrial contraction wave, is immediately after the E wave on Doppler flow analysis. This is influenced by LV compliance and LA pressure and LA contractility rate. All MV inflow velocities are affected by preload and afterload. Under normal conditions, the E velocity is greater than A velocity (**Figure 1**). As the ventricle becomes less compliant, the E velocity decreases and the ratio lowers. When the A velocity surpasses the E velocity, true DD is present. The mitral inflow is affected by preload, heart rate (including arrhythmias) and age (8).

E wave deceleration time is the rate at which the atrial and ventricular pressures equilibrate after onset of the E wave and is shorter in compliant ventricles (160–240 ms in adults). The IVRT is the period between closure of the aortic valve and opening of the MV. This is normally 70–90 ms long in adults and is prolonged in the case of decreased LV compliance. It is also affected by heart rate and ventricular function. It is best recorded from the apical five-chamber view with the cursor placed to record LV outflow tract velocities and LV inflow simultaneously.

Pulmonary Venous (PV) Inflow

Pulmonary venous flow can enhance the information provided by MV inflow velocities. The pulsed-waved Doppler cursor should be placed in the right or left upper pulmonary vein from the apical four-chamber view, as distally into the vein as possible. The variables which are measured include peak systolic flow velocity (S), the peak diastolic flow velocity (D), peak atrial reversal flow velocity (AR), and AR duration (ARdur). The normal PV flow profile shows an initial, large S wave followed by a small D wave and then some retrograde flow during atrial contraction. As LA pressures increase, flow becomes predominantly diastolic and the S/D ratio reverses. A decreased systolic fraction of 40% is associated with elevated mean LA pressure of >15 mmHg (9). AR and ARdur also help, as an increase in AR velocity and duration indicates increased LA pressure.

Color M-Mode Doppler

An intraventricular pressure gradient exists between the base and apex of the ventricle, which acts to cause a suction effect on blood during diastole (10, 11). This can be measured using color M-mode across the MV (from the apical four-chamber view) and measuring the slope of the first aliasing velocity (red–blue) from the MV plane to 4 cm distal in the LV (Vp in centimeters per second) (12). This is known as the color M-mode velocity propagation index (Vp). Vp is not subject to pseudonormalization, which suggests that it is preload independent (13). It does not change with alteration of preload in dogs (14, 15) and humans (14, 16). There is an inverse correlation between the isovolumetric time constant of relaxation (τ) and Vp in humans (13, 14, 17) and dogs (14). Vp is associated with ventricular wall relaxation, becoming less steep as diastolic function worsens (17). The ratio of early LV filling (E) to Vp is a commonly used parameter, which corresponds to pulmonary capillary wedge pressure (PCWP), brain natriuretic peptide, and NYHA class (16).

ASSESSMENT OF SEVERITY

There are different grades of DD. Early (grade I/impaired relaxation) dysfunction is caused by a decrease in LV compliance,

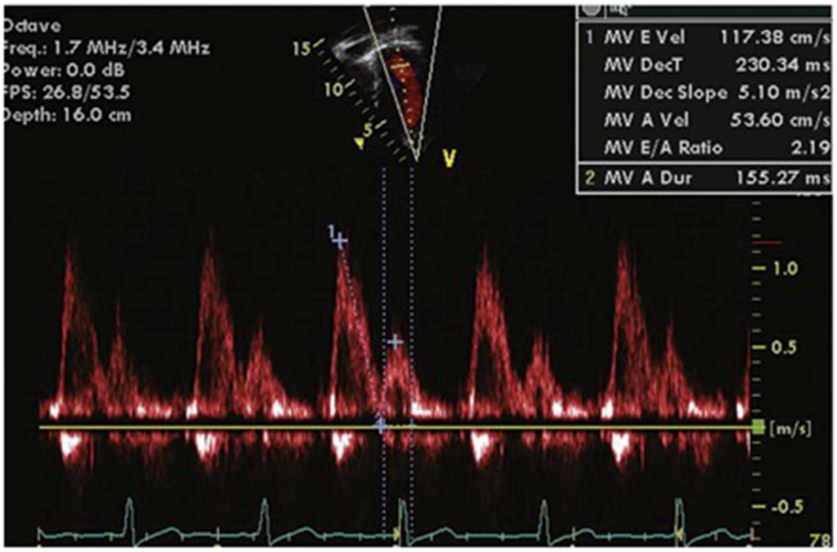

FIGURE 1 | **Normal mitral inflow velocity profile.** Maximum E Velocity (cm/s) = early diastolic mitral inflow velocity. MV Deceleration Time (ms) = duration of deceleration of E wave. MV Dec Slope (m/s^2) = rate of decrease of E wave. Maximum A Velocity (cm/s) = atrial component of mitral filling. A wave duration (ms) = duration of A wave. MV E/A ratio = ratio of E velocity to A velocity (normal value <8).

thereby leading to increased LV filling pressure. This delays atrial emptying and prolongs the E wave deceleration time (DT > 240 ms). Atrial contraction becomes more vigorous, reducing the E/A ratio to <0.9. Worsening LV DD leads to increased atrial pressure and a decrease in the pressure gradient between the LA and LV, thereby leading to a shortened DT. The E/A ratio increases (0.9–1.5), but the E/A profile may appear normal (grade II or pseudonormalization). However, the e′ velocity on tissue Doppler imaging (TDI) (see below) remains low, giving a clue to the underlying abnormality (18). In grade III dysfunction (restrictive), the E/A ratio is >2, DT <160 ms, and the inflow profile can be altered by the Valsalva maneuver. This works because LA pressure is reduced during the strain phase of the Valsalva maneuver, and this unmasks the underlying DD. In grade IV dysfunction, the abnormalities are fixed in the face of the Valsalva maneuver, as LA pressure is too elevated to respond to decreased preload (see **Figure 2**). The timing of onset of E and e′ waves is important. Normally, the e′ occurs at the onset of or before the E wave. If the LA pressure is elevated, the E wave may precede e′ (19, 20).

Tissue Doppler Imaging

Tissue Doppler imaging directly measures myocardial wall velocities by focusing on the high-amplitude, low-frequency signals reflected by the myocardium rather than the blood pool. The areas sampled include the lateral aspect of the mitral annulus in the apical four-chamber view, the basal septal region in the same view, and the lateral tricuspid valve annulus. This serves to minimize translational artifact and to align the probe with the direction of movement. Three waves are usually seen—the systolic (s′) wave, the early diastolic (e′) wave, and the late diastolic wave caused by atrial contraction (a′). Normal values and *Z*-scores are available for each age group in pediatrics (21).

Nagueh et al. were the first to show that E/e′ ratio (ratio of transmitral E velocity and TDI mitral annular e′ velocity) corresponded to PCWP (18). In 125 patients classified by systolic and diastolic function and symptoms, PCWP correlated strongly with E/e′ ratio $r = 0.87$. PCWP correlated only weakly with E velocity but not e′ velocity. Patients with abnormal relaxation and pseudonormalization of the mitral inflow E/A ratio had a decreased e′ velocity ($P < 0.001$). In patients with DD, a saline bolus affects the E/A wave as measured by transmitral Doppler measurement but did not affect the e′ or e′/a′ ratios (22). These studies show that e′ acts as a preload-independent marker of LV relaxation. E wave velocity on mitral inflow Doppler, corrected for e′, correlates strongly with PCWP, and can be used to estimate LA pressure non-invasively.

Tissue Doppler imaging can also differentiate between restrictive cardiomyopathy and constrictive pericarditis (23). As e′ is a property of the myocardium, theoretically, it should remain unchanged in the presence of extrinsic constriction and should only be reduced in true restrictive cardiomyopathy. This is indeed the case, with a significantly lower e′ in restrictive cardiomyopathy than constrictive pericarditis ($P < 0.001$) (23). This has been corroborated by other groups (24, 25).

E/e′ ratio is an independent predictor of outcome in patients assessed 1–6 days after acute myocardial infarction (26). In a population study of 2,042 patients in the community, any degree of DD was predictive of all-cause mortality, whether the patient had clinical symptoms or not (27). In the ADEPT trial, of 225 patients with symptomatic heart failure (HF), diastolic parameters including shorter deceleration time, lower S/D pulmonary vein flow ratio, and increasing E/e′ and E/Vp ratios were all independent predictors of the primary end-points of death, hospitalization, or transplantation (28).

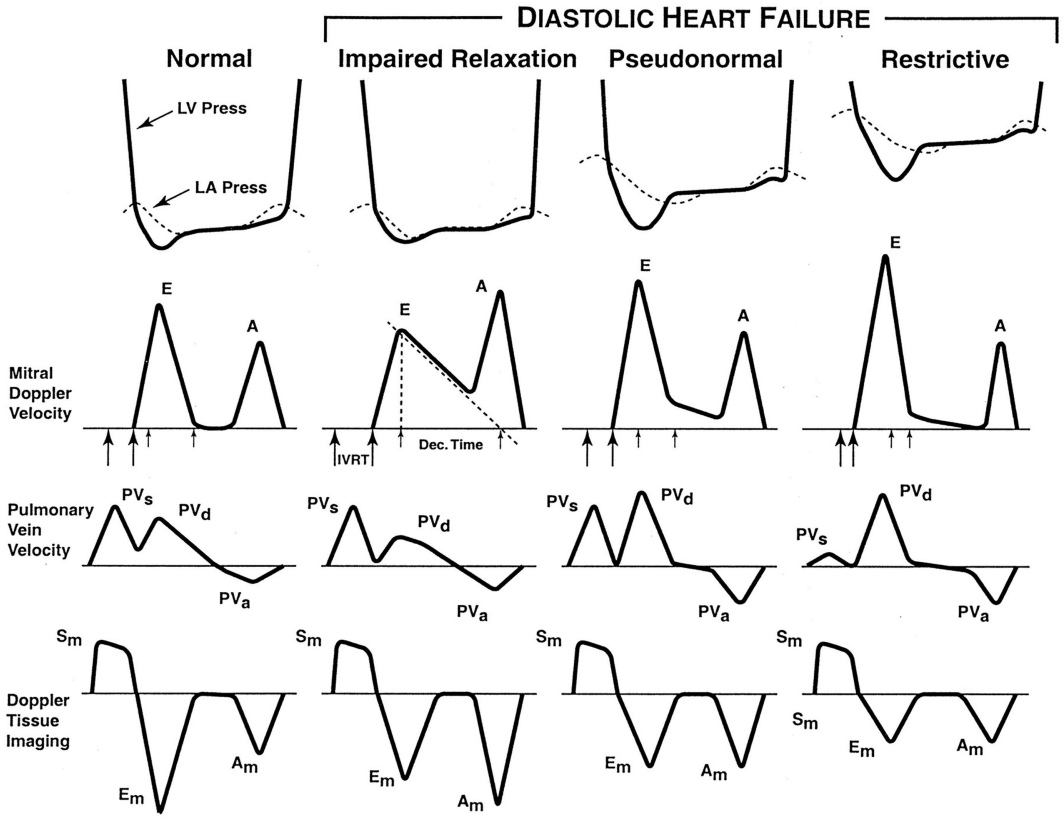

FIGURE 2 | The stages of diastolic heart failure. LV and left atrial (LA) pressures during diastole, transmitral Doppler LV inflow velocity, pulmonary vein Doppler velocity, and Doppler tissue velocity. IVRT indicates isovolumic relaxation time; Dec. Time, e-wave deceleration time; E, early LV filling velocity; A, velocity of LV filling contributed by atrial contraction; PVs, systolic pulmonary vein velocity; PVd, diastolic pulmonary vein velocity; PVa, pulmonary vein velocity resulting from atrial contraction; Sm, myocardial velocity during systole; Em, myocardial velocity during early filling; and Am, myocardial velocity during filling produced by atrial contraction.

EMERGING TECHNIQUES FOR ASSESSMENT OF DIASTOLIC FUNCTION

Torsion

Measurement of LV torsion provides insight into an important mechanism of LV filling and ejection. LV rotation is sensitive to changes in regional and global LV function (29–31). MRI tagging can be used for this purpose but can be difficult and costly to obtain (31–34). Speckle tracking may be used to measure torsion, using the largely experimental practice of "torsion echocardiography" (35–37).

Strain

Strain is a dimensionless index of change in myocardial length in response to applied force and is expressed as a fraction or percentage change. Strain rate is the change in length over time (per second). By convention, myocardial lengthening or thinning is given a positive value. The techniques used to measure strain include echocardiography M-mode (38) or TDI (39, 40) as well as MRI tagging (41, 42). The limitations of echocardiographic measurement include beam direction, which will allow measurement of longitudinal, radial, and circumferential directions depending on the view and angle of interrogation.

Strain imaging aims to provide a high-resolution, real-time measure of myocardial deformation which is independent of loading conditions. A normal pattern of diastolic relaxation has been studied and described (43). Strain imaging can be used to distinguish between restrictive cardiomyopathy and constrictive pericarditis (44) as well as physiological hypertrophy and hypertrophic cardiomyopathy (45).

In a study of 194 patients with chronic systolic HF, global longitudinal strain (GLS) correlated with worse NYHA class and higher NT-proBNP. It also correlated with LV structure and LVEF, as well as LV and RV DD. GLS also predicted long-term adverse events after adjustment for age, ischemic etiology, E/e′ septal, and NT-proBNP with HR 2.04 ($P = 0.024$).

CMR IMAGING

Magnetic resonance imaging can be used to assess diastolic function by the inflow of blood or the movement of myocardium in much the same way as echocardiography. A number of

techniques exist which can help to evaluate diastolic function: gradient echo assesses functional dimensions; phase-contrast measures flow, and myocardial tagging measures regional dynamics (46). Flow measurements are more complete as they include the entire annulus, rather than a point as in echocardiography. Tissue phase mapping (TPM) can be used to measure myocardial velocities and obtain similar information to TDI. This process allows calculation of E/Ea ratio (E = MV inflow E wave and Ea = early myocardial relaxation on TPM).

It is also possible to evaluate tissue characteristics (47), including interstitial and replacement fibrosis using CMR. In a study of 50 patients, with reduced EF, late gadolinium enhancement (a technique which identifies replacement fibrosis) was correlated with a lower septal E/e′ ratio than patients without a scar ($P = 0.05$).

Measurement of dimensions and flow are evaluated similarly to echocardiographic measures, although volumes are more accurate. In tagging, the myocardium is labeled using selective saturation prepulses in specific myocardial regions perpendicular to the imaging plane. This allows strain and 3-D motion analysis (48).

CELLULAR CHANGES WITH AGING

Increased ventricular stiffness and a change in the microscopic structure of the myocardium are inevitable parts of aging. This, coupled with changes in vascular stiffness, may lead to increased vulnerability in certain groups to developing symptomatic HF (1). Traditional assessment of systolic heart function will not identify these patients. The increased stiffness of the myocardium is thought to be due to changes in the collagen content of the extracellular matrix and increased fibrosis (49). There are other changes including reduced phosphorylation of sarcomeric proteins (50) and changes in Titin (51), which may be of importance at a cellular level.

CONGENITAL HEART DISEASE

Overview

There are five main classes of CHD, which affect diastolic function. Pressure–overload lesions such as aortic stenosis and systemic hypertension cause a decrease in compliance due to hypertrophy. Volume overload leads to increased compliance up until a point, when hypertrophy or fibrosis occurs. Mixed pressure and volume overload can combine to affect compliance, such as in repaired Tetralogy of Fallot with some pulmonary valve stenosis and incompetence. Primary or secondary myocardial diseases can decrease compliance directly, such as in amyloidosis or restrictive cardiomyopathy. Transposition of the great arteries leads to a special situation in which the RV is faced with increased afterload and the LV with a much lower pressure than normal, both of which may cause decreased compliance (52). A summary of lesions and the changes in various parameters used to quantify DD is provided in **Table 1**.

TABLE 1 | Findings in various congenital cardiac lesions with the onset of diastolic dysfunction.

Lesion	LA size	Mitral inflow	TDI
HcM	Increased	Increased E/A ratio, DT reduced	E/e′ increased
Aortic stenosis	Increased/ normal	DT reduced, shortened A wave duration	E′, A′ reduced, E′ increased
Aortic regurgitation	Enlarged	Increased E/A	MV e′ decreased, E/e′ increased
Mitral stenosis	Enlarged	Low transmitral gradient, short DT	IVRT–$T_{E\text{-}e'}$ decreased, E/e′ increased
Mitral regurgitation	Enlarged	Increased A wave reversal velocity	Decreased IVRT–$T_{E\text{-}e'}$
Tetralogy of Fallot[a]	Normal	Reduced E/A ratio, shorter IVRT	Reduced MV e′ and a′, reduced TV s′ and e′, increased TV a′
Single ventricle	Normal/ enlarged (dependent on anatomy)	MV E decreased	E/e′ increased

IVRT, isovolumic relaxation time; DT, e-wave deceleration time; E, early left ventricular (LV) filling velocity; A, velocity of LV filling contributed by atrial contraction; s′, myocardial velocity during systole; e′, myocardial velocity during early filling; a′, myocardial velocity during filling produced by atrial contraction; $T_{E\text{-}e'}$, time interval from onset of E wave to e′; LA, left atrium; MV, mitral valve; TDI, tissue Doppler imaging.
[a]End-diastolic forward flow in PA and reduced pulmonary regurgitation.

TETRALOGY OF FALLOT

As with the left ventricle, the right ventricle can become stiff and restrictive due to hypertrophy. In Tetralogy of Fallot, the RV becomes a stiff conduit due to RV outflow tract obstruction, with poor diastolic function. This is evidenced by anterograde pulmonary flow with atrial contraction (end-diastolic forward flow in the PA). The presence of DD is a marker of poor short-term surgical outcome. In a study of 50 children with TOF (mean age 5.0 years), 24 had restrictive RV physiology as described. This correlated with lower E/A ratio and IVRT duration. DD also correlated with prolonged intensive care unit stay, longer duration of ionotropic support, and higher doses of diuretics. It was more commonly seen in patients after transannular patch repair (53). In a study of 112 patients, 50 were found to have a restrictive RV. This was associated with larger RV dimensions and RA dimensions, and increased LA length and LA indexed volume on echocardiography (54). There appeared to be a bigger effect on late filling than early filling of the LV and RV restriction appeared to affect LV filling and diastole (decreasing filling and increasing diastolic pressures). This may be due to mechanical effects of the RV on LV filling or increased fibrosis of the LV. Interestingly, children with restrictive RV have an increased RV volume, whereas adults have a reduced volume (55–57). After the initial period, restrictive RV physiology appears to be protective, with decreased duration of pulmonary regurgitation and better maximum oxygen uptake seen in patients with restriction (58).

SINGLE VENTRICLE

The Fontan procedure suddenly offloads a previously volume-overloaded ventricle. There is evidence that even in patients with normal systolic function, diastolic function is impaired (59). This is correlated with the length of time since the Fontan operation and decreases over time. Both left and right systemic single ventricles appear to experience systolic and DD, although systemic right ventricular function is more depressed (60). This may be due to adverse remodeling of the right ventricle, which is being exposed to an abnormally high afterload. A study of 28 patients showed a significant correlation between LV filling pressures (measured by E/e′ ratio) and ventilatory efficiency (VE/VO_2 slope) ($r = 0.93$; $P < 0.01$) (61). This is interesting as parameters of CPET are correlated with hospitalization in Fontan patients (62).

ATRIAL SEPTAL DEFECT (ASD)

In the presence of an ASD with normal pulmonary pressures, the left–right shunt results in reduced LV filling and SV, reduced tissue perfusion, fluid accumulation, increased RV volume, greater RV SV, and finally normalization of LV filling and SV (63). In a small study of patients ($n = 18$) undergoing percutaneous device closure of their ASD, there were no significant changes in TDI and Doppler M-mode indices of diastolic function after closure. However, E wave velocity and E/e′ ratio at the MV annulus did increase significantly, thereby suggesting they are more load-dependent parameters (64). In children with ASD, TDI velocities do not change immediately after device closure. There is also no indication of elevation of left heart filling pressures after device closure in children, suggesting that children are able to accept increased preload and preserve diastolic function (65). This has implications on timing of closure, suggesting that earlier closure is beneficial.

AORTIC STENOSIS

In a study of patients with aortic valve disease (8–39 years), those with aortic stenosis or mixed disease were found to have DD, which was related to the degree of left ventricular hypertrophy (LVH). E/e′ correlated with LV end-diastolic pressure on catheterization. DD was found in 37% of all patients in the study, consisting of 37% of those with AS and 47% of those with mixed valve disease (66). Increased chamber stiffness is related to an increased LV mass/EDV ratio. Patients with aortic stenosis have increased interstitial fibrosis, which is related to a worse prognosis (67) and is known to be related to increased chamber stiffness. Secondary pulmonary hypertension may occur due to DD (68).

Cardiac magnetic resonance has a role in functional assessment of the LV in patients with AS. It is also used in tissue characterization and can quantify the degree of interstitial fibrosis and replacement fibrosis (69). There is some evidence that the degree of fibrosis can predict surgical outcome (67).

AORTIC REGURGITATION

An incompetent aortic valve increases the end-diastolic volume of the left ventricle. The LV remodels to cope with this extra volume and becomes more compliant, so that diastolic pressures remain normal. Over time, decompensation may occur, in which case diastolic pressures increase as the LV loses the ability to compensate further (70). This is due to increased myocyte cellular diameter and fibrous content of the myocardium (71).

In aortic regurgitation with normal diastolic function, MV inflow consists of predominant E wave filling and annular e′ is increased or normal due to increased LV SV. However, E/e′ is not increased and PA pressures are normal. With the onset of DD (DD), LV filling pressures are elevated on exercise initially and then at rest.

MITRAL STENOSIS

Mitral stenosis results in increased LV filling pressure and reduced LV filling due to the restriction of blood flow through the MV. Most patients have normal intrinsic systolic and diastolic myocardial function. Some studies have found DD using conductance catheters, which are independent of loading conditions and acutely reversed after balloon valvuloplasty (72). The mechanism for this is not clear and may be due to restriction of LV relaxation by an immobile and thickened MV.

MITRAL REGURGITATION

In isolated MR, LV compliance usually decreases as it dilates to accommodate an increased volume (73). In acute MR, increased LV diastolic pressure is due to increased LV dilatation and a shift upward on the pressure–volume relationship. Chronic MR often leads to remodeling and LV dilatation, thereby retaining LV SV (74).

MR, in the absence of LV DD, will cause an increase in E/A ratio (>1) and increase in transmitral E velocity (75). The e′ velocity is also increased, and E/e′ is not indicative of filling pressures (76). However, A reversal wave velocity does relate to LV diastolic pressures independently of MR (77). The ratio of IVRT to $T_{E\text{-}e'}$ can also be used to assess diastolic function irrespective of MR (77).

CARDIOMYOPATHIES

HF with Preserved Ejection Fraction (HFpEF)

One theory of the mechanism of HFpEF is that it is caused by DD. Increased LV filling pressures cause back pressure on the pulmonary circulation, leading to symptoms of HF, including breathlessness. This is assumed to be the case as EF remains in the normal range, which is thought to denote normal systolic function (78). However, there have been studies which show that symptoms of HF in these patients correlate with left ventricular end-diastolic volume and that the SV is only maintained due to LV dilatation. The mechanism postulated is that of excessive LV diastolic dilatation by fiber slippage and creep (79).

The process of LV remodeling to compensate for decreased systolic function in these patients occurs due to feedback from the periphery, causing the heart to adapt with an increase in volume to maintain SV (80). Therefore, an EF of 20% in a dilated ventricle may produce the same SV of a normally sized ventricle with a normal EF (81). Patients with LVH manage to avoid this excessive distension and may be more prone to HF with reduced EF (76). Symptoms of HF, such as breathlessness on exertion, are not related to PCWP (82) or systolic function (83). Instead, the determinants appear to be musculoskeletal status, body composition, motivation, and tolerance of discomfort (82). Therefore, using symptoms alone to determine whether a patient has HF may not be valid.

A number of problems with the definition of HFpEF have been highlighted above; HF may not be reliably diagnosed using symptoms alone, and a preserved EF does not always correlate with normal systolic function. The notion of this type of disease being the definitive model for DD is flawed.

Hypertrophic Cardiomyopathy

Diastolic dysfunction is well recognized in hypertrophic cardiomyopathy, due to the active component of actin–myosin dissociation in the early filling phase and the passive compliance of the left ventricle (84–87). DD causes a reduced rate and magnitude of LV filling and reduced SV. This results in elevation of LV end-diastolic pressures leading to symptoms of HF. Evaluation of diastolic function is similar to other conditions, with values and ratios changing with severity as expected. In some patients, a restrictive phenotype is present, characterized by increased mitral inflow E/A ratio, reduced DT, and increased pulmonary vein A reversal wave velocity (88). TDI may help to distinguish mild disease in the seemingly normal hearts of disease-causing gene carriers (89, 90).

CONCLUSION

Diastolic dysfunction is a characteristic of many types of congenital heart disease as well as of infancy and the aging heart. Thorough and thoughtful evaluation of diastolic function can help to explain symptoms and affect the treatment of patients with seemingly normal ventricular function. Ventricular function should be thought of as a combination of ventricular filling as well as systolic ejection so that the contribution of ventricular compliance to overall heart function is taken into account. Finally, loading conditions and effects of exertion should be taken into account during evaluation.

AUTHOR CONTRIBUTIONS

Literature search and writing initial draft: DP. Critical revision and editing: MB. Final draft: DP.

FUNDING

This study was funded by Information Communication Technologies Programme (contract number 600932), part of the MD-Paedigree project.

REFERENCES

1. Redfield M, Jacobsen SJ, Borlaug BA, Rodeheffer RJ, Kass DA. Age- and gender-related ventricular-vascular stiffening: a community-based study. *Circulation* (2005) 112(15):2254–62. doi:10.1161/CIRCULATIONAHA.105.541078
2. Tsang TS, Barnes ME, Gersh BJ, Bailey KR, Seward JB. Left atrial volume as a morphophysiologic expression of left ventricular diastolic dysfunction and relation to cardiovascular risk burden. *Am J Cardiol* (2002) 90(12):1284–9. doi:10.1016/S0002-9149(02)02864-3
3. Takemoto Y. Usefulness of left atrial volume in predicting first congestive heart failure in patients > or = 65 years of age with well-preserved left ventricular systolic function. *Am J Cardiol* (2005) 96(6):832–6. doi:10.1016/j.amjcard.2005.05.031
4. Douglas P. The left atrium: a biomarker of chronic diastolic dysfunction and cardiovascular disease risk. *J Am Coll Cardiol* (2003) 42(7):1206–7. doi:10.1016/S0735-1097(03)00956-2
5. Tsang T, Gersh BJ, Appleton CP, Tajik AJ, Barnes ME, Bailey KR, et al. Left ventricular diastolic dysfunction: an important predictor of first diagnosed nonvalvular atrial fibrillation in 840 elderly men and women. *J Am Coll Cardiol* (2002) 39:460–460. doi:10.1016/S0735-1097(02)82067-8
6. Tsang TS, Barnes ME, Gersh BJ, Takemoto Y, Rosales AG, Bailey KR, et al. Prediction of risk for first age-related cardiovascular events in an elderly population: the incremental value of echocardiography. *J Am Coll Cardiol* (2003) 42(7):1199–205. doi:10.1016/S0735-1097(03)00943-4
7. Nistri S, Olivotto I, Betocchi S, Losi MA, Valsecchi G, Pinamonti B, et al. Prognostic significance of left atrial size in patients with hypertrophic cardiomyopathy (from the Italian registry for hypertrophic cardiomyopathy). *Am J Cardiol* (2006) 98(7):960–5. doi:10.1016/j.amjcard.2006.05.013
8. Lester S, Tajik AJ, Nishimura RA, Oh JK, Khandheria BK, Seward JB, et al. Unlocking the mysteries of diastolic function. *J Am Coll Cardiol* (2008) 51(7):679–89. doi:10.1016/j.jacc.2007.09.061
9. Kuecherer HF, Kuecherer HF, Muhiudeen IA, Kusumoto FM, Lee E, Moulinier LE, et al. Estimation of mean left atrial pressure from transesophageal pulsed Doppler echocardiography of pulmonary venous flow. *Circulation* (1990) 82(4):1127–39. doi:10.1161/01.CIR.82.4.1127
10. Ling D, Rankin JS, Edwards CH II, McHale PA, Anderson RW. Regional diastolic mechanics of the left ventricle in the conscious dog. *Am J Physiol* (1979) 5(2):H323–30.
11. Courtois M. Transmitral pressure-flow velocity relation. Importance of regional pressure gradients in the left ventricle during diastole. *Circulation* (1988) 78(3):661–71.
12. Garcia MJ, Ares MA, Asher C, Rodriguez L, Vandervoort P, Thomas JD. An index of early left ventricular filling that combined with pulsed Doppler peak e velocity may estimate capillary wedge pressure. *J Am Coll Cardiol* (1997) 29(2):448–54. doi:10.1016/S0735-1097(96)00496-2
13. Takatsuji H, Mikami T, Urasawa K, Teranishi J, Onozuka H, Takagi C, et al. A new approach for evaluation of left ventricular diastolic function: spatial and temporal analysis of left ventricular filling flow propagation by color M-mode Doppler echocardiography. *J Am Coll Cardiol* (1996) 27(2):365–71. doi:10.1016/0735-1097(96)81240-X
14. Garcia MJ, Smedira NG, Greenberg NL, Main M, Firstenberg MS, Odabashian J, et al. Color M-mode Doppler flow propagation velocity is a preload insensitive index of left ventricular relaxation: animal and human validation. *J Am Coll Cardiol* (2000) 35(1):201–8. doi:10.1016/S0735-1097(99)00503-3
15. Stugaard M. Intraventricular early diastolic filling during acute myocardial ischemia, assessment by multigated color m-mode Doppler echocardiography. *Circulation* (1993) 88(6):2705–13. doi:10.1161/01.CIR.88.6.2705

16. Firstenberg MS, Levine BD, Garcia MJ, Greenberg NL, Cardon L, Morehead AJ, et al. Relationship of echocardiographic indices to pulmonary capillary wedge pressures in healthy volunteers. *J Am Coll Cardiol* (2000) 36(5):1664–9. doi:10.1016/S0735-1097(00)00909-8
17. Brun P, Tribouilloy C, Duval AM, Iserin L, Meguira A, Pelle G, et al. Left ventricular flow propagation during early filling is related to wall relaxation: a color M-mode Doppler analysis. *J Am Coll Cardiol* (1992) 20(2):420–32. doi:10.1016/0735-1097(92)90112-Z
18. Nagueh SF, Middleton KJ, Kopelen HA, Zoghbi WA, Quiñones MA. Doppler tissue imaging: a noninvasive technique for evaluation of left ventricular relaxation and estimation of filling pressures. *J Am Coll Cardiol* (1997) 30(6):1527–33. doi:10.1016/S0735-1097(97)00344-6
19. Oh J, Tajik J. The return of cardiac time intervals. *J Am Coll Cardiol* (2003) 42(8):1471–4. doi:10.1016/S0735-1097(03)01036-2
20. Rivas Gotz C, Khoury DS, Manolios M, Rao L, Kopelen HA, Nagueh SF, et al. Time interval between onset of mitral inflow and onset of early diastolic velocity by tissue Doppler: a novel index of left ventricular relaxation. *J Am Coll Cardiol* (2003) 42(8):1463–70. doi:10.1016/S0735-1097(03)01034-9
21. Mori K, Hayabuchi Y, Kuroda Y, Nii M, Manabe T. Left ventricular wall motion velocities in healthy children measured by pulsed wave Doppler tissue echocardiography: normal values and relation to age and heart rate. *J Am Soc Echocardiogr* (2000) 13(11):1002–11. doi:10.1067/mje.2000.108131
22. Sohn DW, Chai IH, Lee DJ, Kim HC, Kim HS, Oh BH, et al. Assessment of mitral annulus velocity by Doppler tissue imaging in the evaluation of left ventricular diastolic function. *J Am Coll Cardiol* (1997) 30(2):474–80. doi:10.1016/S0735-1097(97)88335-0
23. Garcia MJ, Rodriguez L, Ares M, Griffin BP, Thomas JD, Klein AL. Differentiation of constrictive pericarditis from restrictive cardiomyopathy: assessment of left ventricular diastolic velocities in longitudinal axis by Doppler tissue imaging. *J Am Coll Cardiol* (1996) 27(1):108–14. doi:10.1016/0735-1097(95)00434-3
24. Oki T, Tabata T, Yamada H, Abe M, Onose Y, Wakatsuki T, et al. Right and left ventricular wall motion velocities as diagnostic indicators of constrictive pericarditis. *Am J Cardiol* (1998) 81(4):465–70. doi:10.1016/S0002-9149(97)00939-9
25. Rajagopalan N, Garcia MJ, Rodriguez L, Murray RD, Apperson-Hansen C, Stugaard M, et al. Comparison of new Doppler echocardiographic methods to differentiate constrictive pericardial heart disease and restrictive cardiomyopathy. *Am J Cardiol* (2001) 87(1):86–94. doi:10.1016/S0002-9149(00)01278-9
26. Hillis G, Møller JE, Pellikka PA, Gersh BJ, Wright RS, Ommen SR, et al. Noninvasive estimation of left ventricular filling pressure by E/e': a powerful predictor of survival following acute myocardial infarction. *J Am Coll Cardiol* (2003) 41(6):452–452. doi:10.1016/S0735-1097(03)82510-X
27. Redfield M, Jacobsen SJ, Burnett JC Jr, Mahoney DW, Bailey KR, Rodeheffer RJ. Burden of systolic and diastolic ventricular dysfunction in the community: appreciating the scope of the heart failure epidemic. *JAMA* (2003) 289(2):194–202. doi:10.1001/jama.289.2.194
28. Troughton RW, Prior DL, Frampton CM, Nash PJ, Pereira JJ, Martin M, et al. Usefulness of tissue Doppler and color M-mode indexes of left ventricular diastolic function in predicting outcomes in systolic left ventricular heart failure (from the ADEPT study). *Am J Cardiol* (2005) 96(2):257–62. doi:10.1016/j.amjcard.2005.03.055
29. Gibbons Kroeker CA, Tyberg JV, Beyar R. Effects of load manipulations, heart rate, and contractility on left ventricular apical rotation. An experimental study in anesthetized dogs. *Circulation* (1995) 92(1):130–41. doi:10.1161/01.CIR.92.1.130
30. Hansen DE, Daughters GT II, Alderman EL, Ingels NB, Stinson EB, Miller DC. Effect of volume loading, pressure loading, and inotropic stimulation on left ventricular torsion in humans. *Circulation* (1991) 83(4):1315–26. doi:10.1161/01.CIR.83.4.1315
31. Maier SE, Fischer SE, McKinnon GC, Hess OM, Krayenbuehl HP, Boesiger P. Evaluation of left ventricular segmental wall motion in hypertrophic cardiomyopathy with myocardial tagging. *Circulation* (1992) 86(6):1919–28. doi:10.1161/01.CIR.86.6.1919
32. Stuber M, Scheidegger MB, Fischer SE, Nagel E, Steinemann F, Hess OM, et al. Alterations in the local myocardial motion pattern in patients suffering from pressure overload due to aortic stenosis. *Circulation* (1999) 100(4):361–8. doi:10.1161/01.CIR.100.4.361
33. Nagel E, Stuber M, Burkhard B, Fischer SE, Scheidegger MB, Boesiger P, et al. Cardiac rotation and relaxation in patients with aortic valve stenosis. *Eur Heart J* (2000) 21(7):582–9. doi:10.1053/euhj.1999.1736
34. Buchalter MB, Weiss JL, Rogers WJ, Zerhouni EA, Weisfeldt ML, Beyar R, et al. Noninvasive quantification of left ventricular rotational deformation in normal humans using magnetic resonance imaging myocardial tagging. *Circulation* (1990) 81(4):1236–44. doi:10.1161/01.CIR.81.4.1236
35. Behar V, Adam D, Lysyansky P, Friedman Z. The combined effect of nonlinear filtration and window size on the accuracy of tissue displacement estimation using detected echo signals. *Ultrasonics* (2004) 41(9):743–53. doi:10.1016/j.ultras.2003.09.003
36. Reisner SA. "Global longitudinal strain" – a novel index of left ventricular function. *Circulation* (2003) 108(17):659–659.
37. Leitman M, Lysyansky P, Sidenko S, Shir V, Peleg E, Binenbaum M, et al. Two-dimensional strain – a novel software for real-time quantitative echocardiographic assessment of myocardial function. *J Am Soc Echocardiogr* (2004) 17(10):1021–9. doi:10.1016/j.echo.2004.06.019
38. Weidemann F, Jamal F, Sutherland GR, Claus P, Kowalski M, Hatle L, et al. Myocardial function defined by strain rate and strain during alterations in inotropic states and heart rate. *Am J Physiol Heart Circ Physiol* (2002) 283(2):H792–9. doi:10.1152/ajpheart.00025.2002
39. Derumeaux G, Ovize M, Loufoua J, Pontier G, André-Fouet X, Cribier A. Assessment of nonuniformity of transmural myocardial velocities by color-coded tissue Doppler imaging: characterization of normal, ischemic, and stunned myocardium. *Circulation* (2000) 101(12):1390–5. doi:10.1161/01.CIR.101.12.1390
40. Firstenberg MS, Greenberg NL, Smedira NG, Castro P, Thomas JD, Garcia MJ. The effects of acute coronary occlusion on noninvasive echocardiographically derived systolic and diastolic myocardial strain rates. *Curr Surg* (2000) 57(5):466–72. doi:10.1016/S0149-7944(00)00296-8
41. Voigt J-U, Arnold MF, Karlsson M, Hübbert L, Kukulski T, Hatle L, et al. Assessment of regional longitudinal myocardial strain rate derived from Doppler myocardial imaging indexes in normal and infarcted myocardium. *J Am Soc Echocardiogr* (2000) 13(6):588–98. doi:10.1067/mje.2000.105631
42. Jamal F, Kukulski T, Strotmann J, Sutherland GR. Quantification of the spectrum of changes in regional myocardial function during acute ischemia in closed chest pigs: an ultrasonic strain rate and strain study. *J Am Soc Echocardiogr* (2001) 14(9):874–84. doi:10.1067/mje.2001.112037
43. Støylen A, Slørdahl S, Skjelvan GK, Heimdal A, Skjaerpe T. Strain rate imaging in normal and reduced diastolic function: comparison with pulsed Doppler tissue imaging of the mitral annulus. *J Am Soc Echocardiogr* (2001) 14(4):264–74. doi:10.1067/mje.2001.110375
44. Palka P, Lange A, Donnelly JE, Nihoyannopoulos P. Differentiation between restrictive cardiomyopathy and constrictive pericarditis by early diastolic Doppler myocardial velocity gradient at the posterior wall. *Circulation* (2000) 102(6):655–62. doi:10.1161/01.CIR.102.6.655
45. Afonso L, Kondur A, Simegn M, Niraj A, Hari P, Kaur R, et al. Two-dimensional strain profiles in patients with physiological and pathological hypertrophy and preserved left ventricular systolic function: a comparative analyses. *BMJ Open* (2012) 2(4):e001390. doi:10.1136/bmjopen-2012-001390
46. Paelinck BP, Lamb HJ, Bax JJ, Van der Wall EE, de Roos A. Assessment of diastolic function by cardiovascular magnetic resonance. *Am Heart J* (2002) 144(2):198–205. doi:10.1067/mhj.2002.123316
47. Moreo A, Ambrosio G, De Chiara B, Pu M, Tran T, Mauri F, et al. Influence of myocardial fibrosis on left ventricular diastolic function: noninvasive assessment by cardiac magnetic resonance and echo. *Circ Cardiovasc Imaging* (2009) 2(6):437–43. doi:10.1161/CIRCIMAGING.108.838367
48. Fischer SE, McKinnon GC, Scheidegger MB, Prins W, Meier D, Boesiger P. True myocardial motion tracking. *Magn Reson Med* (1994) 31(4):401–13. doi:10.1002/mrm.1910310409
49. van Heerebeek L, Borbély A, Niessen HW, Bronzwaer JG, van der Velden J, Stienen GJ, et al. Myocardial structure and function differ in systolic and diastolic heart failure. *Circulation* (2006) 113(16):1966–73. doi:10.1161/CIRCULATIONAHA.105.587519
50. Borbély A, Velden JVD, Papp Z, Bronzwaer JGF, Edes I, Stienen GJM, et al. Cardiomyocyte stiffness in diastolic heart failure. *Circulation* (2005) 111(6):774–81. doi:10.1161/01.CIR.0000155257.33485.6D

51. Katz A. New molecular mechanism in diastolic heart failure. *Circulation* (2006) 113(16):1922–5. doi:10.1161/CIRCULATIONAHA.106.620765
52. Danford DA, Huhta JC, Murphy DJ. Doppler echocardiographic approaches to ventricular diastolic function. *Echocardiography* (1986) 3(1):33–40. doi:10.1111/j.1540-8175.1986.tb00182.x
53. Sachdev MS, Bhagyavathy A, Varghese R, Coelho R, Kumar RS. Right ventricular diastolic function after repair of Tetralogy of Fallot. *Pediatr Cardiol* (2006) 27(2):250–5. doi:10.1007/s00246-005-1186-y
54. Ahmad N, Kantor PF, Grosse-Wortmann L, Seller N, Jaeggi ET, Friedberg MK, et al. Influence of RV restrictive physiology on LV diastolic function in children after Tetralogy of Fallot repair. *J Am Soc Echocardiogr* (2012) 25(8):866–73. doi:10.1016/j.echo.2012.05.011
55. Berg JVD, Wielopolski PA, Meijboom FJ, Witsenburg M, Bogers AJJC, Pattynama PMT, et al. Diastolic function in repaired Tetralogy of Fallot at rest and during stress: assessment with MR imaging. *Radiology* (2007) 243(1):212–9. doi:10.1148/radiol.2431060213
56. Helbing WA, Niezen RA, Le Cessie S, van der Geest RJ, Ottenkamp J, de Roos A. Right ventricular diastolic function in children with pulmonary regurgitation after repair of Tetralogy of Fallot: volumetric evaluation by magnetic resonance velocity mapping. *J Am Coll Cardiol* (1996) 28(7):1827–35. doi:10.1016/S0735-1097(96)00387-7
57. Lu JC, Cotts TB, Agarwal PP, Attili AK, Dorfman AL. Relation of right ventricular dilation, age of repair, and restrictive right ventricular physiology with patient-reported quality of life in adolescents and adults with repaired Tetralogy of Fallot. *Am J Cardiol* (2010) 106(12):1798–802. doi:10.1016/j.amjcard.2010.08.021
58. Gatzoulis MA, Clark AL, Cullen S, Newman CG, Redington AN, et al. Right ventricular diastolic function 15 to 35 years after repair of Tetralogy of Fallot. Restrictive physiology predicts superior exercise performance. *Circulation* (1995) 91(6):1775–81.
59. Vitarelli A, Conde Y, Cimino E, D'Angeli I, D'Orazio S, Ventriglia F, et al. Quantitative assessment of systolic and diastolic ventricular function with tissue Doppler imaging after Fontan type of operation. *Int J Cardiol* (2005) 102(1):61–9. doi:10.1016/j.ijcard.2004.04.008
60. Hershenson JA, Zaidi AN, Texter KM, Moiduddin N, Stefaniak CA, Hayes J, et al. Differences in tissue Doppler imaging between single ventricles after the Fontan operation and normal controls. *Am J Cardiol* (2010) 106(1):99–103. doi:10.1016/j.amjcard.2010.02.020
61. Tomkiewicz Pajak L. Single ventricle diastolic function and exercise capacity in patients after Fontan operation. *Eur Heart J* (2010) 31:121–2.
62. Diller GP, Giardini A, Dimopoulos K, Gargiulo G, Müller J, Derrick G, et al. Predictors of morbidity and mortality in contemporary Fontan patients: results from a multicenter study including cardiopulmonary exercise testing in 321 patients. *Eur Heart J* (2010) 31(24):3073–83. doi:10.1093/eurheartj/ehq356
63. Flamm MD, Cohn KE, Hancock EW. Ventricular function in atrial septal defect. *Am J Med* (1970) 48(3):286–94. doi:10.1016/0002-9343(70)90058-6
64. Vanoverschelde JJ, Essamri B, Vanbutsele R, d'Hondt A, Cosyns JR, Detry JR, et al. Contribution of left ventricular diastolic function to exercise capacity in normal subjects. *J Appl Physiol* (1993) 74(5):2225–33.
65. Giardini A, Moore P, Brook M, Stratton V, Tacy T. Effect of transcatheter atrial septal defect closure in children on left ventricular diastolic function. *Am J Cardiol* (2005) 95(10):1255–7. doi:10.1016/j.amjcard.2005.01.062
66. Friedman KG, McElhinney DB, Rhodes J, Powell AJ, Colan SD, Lock JE, et al. Left ventricular diastolic function in children and young adults with congenital aortic valve disease. *Am J Cardiol* (2013) 111(2):243–9. doi:10.1016/j.amjcard.2012.09.026
67. Milano AD, Faggian G, Dodonov M, Golia G, Tomezzoli A, Bortolotti U, et al. Prognostic value of myocardial fibrosis in patients with severe aortic valve stenosis. *J Thorac Cardiovasc Surg* (2012) 144(4):830–7. doi:10.1016/j.jtcvs.2011.11.024
68. Lancellotti P, Magne J, Donal E, O'Connor K, Dulgheru R, Rosca M, et al. Determinants and prognostic significance of exercise pulmonary hypertension in asymptomatic severe aortic stenosis. *Circulation* (2012) 126(7):851–9. doi:10.1161/CIRCULATIONAHA.111.088427
69. Weidemann F, Herrmann S, Störk S, Niemann M, Frantz S, Lange V, et al. Impact of myocardial fibrosis in patients with symptomatic severe aortic stenosis. *Circulation* (2009) 120(7):577–84. doi:10.1161/CIRCULATIONAHA.108.847772
70. Villari B, Hess OM, Kaufmann P, Krogmann ON, Grimm J, Krayenbuehl HP. Effect of aortic valve stenosis (pressure overload) and regurgitation (volume overload) on left ventricular systolic and diastolic function. *Am J Cardiol* (1992) 69(9):927–34. doi:10.1016/0002-9149(92)90795-Z
71. Villari B, Campbell SE, Hess OM, Mall G, Vassalli G, Weber KT, et al. Influence of collagen network on left ventricular systolic and diastolic function in aortic valve disease. *J Am Coll Cardiol* (1993) 22(5):1477–84. doi:10.1016/0735-1097(93)90560-N
72. Liu CP, Ting CT, Yang TM, Chen JW, Chang MS, Maughan WL, et al. Reduced left ventricular compliance in human mitral stenosis. Role of reversible internal constraint. *Circulation* (1992) 85(4):1447–56. doi:10.1161/01.CIR.85.4.1447
73. Corin W, Murakami T, Monrad ES, Hess OM, Krayenbuehl HP. Left ventricular passive diastolic properties in chronic mitral regurgitation. *Circulation* (1991) 83(3):797–807. doi:10.1161/01.CIR.83.3.797
74. Zile MR, Tomita M, Nakano K, Mirsky I, Usher B, Lindroth J, et al. Effects of left ventricular volume overload produced by mitral regurgitation on diastolic function. *Am J Physiol* (1991) 261(5):H1471–80.
75. Nagueh SF, Smiseth OA, Appleton CP, Byrd BF III, Dokainish H, Edvardsen T, et al. Recommendations for the evaluation of left ventricular diastolic function by echocardiography: an update from the American society of echocardiography and the European Association of Cardiovascular Imaging. *J Am Soc Echocardiogr* (2016) 29(4):277–314. doi:10.1016/j.echo.2016.01.011
76. Maciver DH, Townsend M. A novel mechanism of heart failure with normal ejection fraction. *Heart* (2007) 94(4):446–9. doi:10.1136/hrt.2006.114082
77. Diwan A, McCulloch M, Lawrie GM, Reardon MJ, Nagueh SF. Doppler estimation of left ventricular filling pressures in patients with mitral valve disease. *Circulation* (2005) 111(24):3281–9. doi:10.1161/CIRCULATIONAHA.104.508812
78. Lekavich CL, Barksdale DJ, Neelon V, Wu JR. Heart failure preserved ejection fraction (HFpEF): an integrated and strategic review. *Heart Fail Rev* (2015) 20(6):643–53. doi:10.1007/s10741-015-9506-7
79. Weber KT. Cardiac interstitium in health and disease: the fibrillar collagen network. *J Am Coll Cardiol* (1989) 13(7):1637–52. doi:10.1016/0735-1097(89)90360-4
80. Hill J, Olson EN. Cardiac plasticity. *N Engl J Med* (2008) 358(13):1370–80. doi:10.1056/NEJMra072139
81. Maciver DH, Dayer MJ. An alternative approach to understanding the pathophysiological mechanisms of chronic heart failure. *Int J Cardiol* (2012) 154(2):102–10. doi:10.1016/j.ijcard.2011.05.075
82. Wilson JR, Rayos G, Yeoh TK, Gothard P, Bak K. Dissociation between exertional symptoms and circulatory function in patients with heart failure. *Circulation* (1995) 92(1):47–53. doi:10.1161/01.CIR.92.1.47
83. Franciosa JA, Ziesche S, Mary Wilen RN. Functional capacity of patients with chronic left ventricular failure. *Am J Med* (1979) 67(3):460–6. doi:10.1016/0002-9343(79)90794-0
84. Elliott P, McKenna WJ. Hypertrophic cardiomyopathy. *Lancet* (2004) 363(9424):1881–91. doi:10.1016/S0140-6736(04)16358-7
85. Bonow RO, Dilsizian V, Rosing DR, Maron BJ, Bacharach SL, Green MV. Verapamil-induced improvement in left ventricular diastolic filling and increased exercise tolerance in patients with hypertrophic cardiomyopathy: short- and long-term effects. *Circulation* (1985) 72(4):853–64. doi:10.1161/01.CIR.72.4.853
86. Chikamori T, Dickie S, Poloniecki JD, Myers MJ, Lavender JP, McKenna WJ. Prognostic significance of radionuclide-assessed diastolic function in hypertrophic cardiomyopathy. *Am J Cardiol* (1990) 65(7):478–82. doi:10.1016/0002-9149(90)90814-H
87. Pak PH, Maughan L, Baughman KL, Kass DA. Marked discordance between dynamic and passive diastolic pressure-volume relations in idiopathic hypertrophic cardiomyopathy. *Circulation* (1996) 94(1):52–60. doi:10.1161/01.CIR.94.1.52

88. Kubo T, Gimeno JR, Bahl A, Steffensen U, Steffensen M, Osman E, et al. Prevalence, clinical significance, and genetic basis of hypertrophic cardiomyopathy with restrictive phenotype. *J Am Coll Cardiol* (2007) 49(25):2419–26. doi:10.1016/j.jacc.2007.02.061
89. Nagueh SF, Bachinski LL, Meyer D, Hill R, Zoghbi WA, Tam JW, et al. Tissue Doppler imaging consistently detects myocardial abnormalities in patients with hypertrophic cardiomyopathy and provides a novel means for an early diagnosis before and independently of hypertrophy. *Circulation* (2001) 104(2):128–30. doi:10.1161/01.CIR.104.2.128
90. Poutanen T, Tikanoja T, Jääskeläinen P, Jokinen E, Silvast A, Laakso M, et al. Diastolic dysfunction without left ventricular hypertrophy is an early finding in children with hypertrophic cardiomyopathy-causing mutations in the beta-myosin heavy chain, alpha-tropomyosin, and myosin-binding protein C genes. *Am Heart J* (2006) 151(3):725.e1–725.e9. doi:10.1016/j.ahj.2005.12.005

Conflict of Interest Statement: The authors declare that the research was conducted in the absence of any commercial or financial relationships that could be construed as a potential conflict of interest.

frontiers in Cardiovascular Medicine

REVIEW
published: 23 May 2017
doi: 10.3389/fcvm.2017.00030

Myocardial Architecture, Mechanics, and Fibrosis in Congenital Heart Disease

*Sarah Ghonim[1,2,3], Inga Voges[1,2], Peter D. Gatehouse[2], Jennifer Keegan[2], Michael A. Gatzoulis[1,3], Philip J. Kilner[2] and Sonya V. Babu-Narayan[1,2,3]**

[1] Adult Congenital Heart Unit, Royal Brompton Hospital, London, UK, [2] Cardiovascular Magnetic Resonance Unit, Royal Brompton Hospital, London, UK, [3] National Heart and Lung Institute, Imperial College, London, UK

Congenital heart disease (CHD) is the most common category of birth defect, affecting 1% of the population and requiring cardiovascular surgery in the first months of life in many patients. Due to advances in congenital cardiovascular surgery and patient management, most children with CHD now survive into adulthood. However, residual and postoperative defects are common resulting in abnormal hemodynamics, which may interact further with scar formation related to surgical procedures. Cardiovascular magnetic resonance (CMR) has become an important diagnostic imaging modality in the long-term management of CHD patients. It is the gold standard technique to assess ventricular volumes and systolic function. Besides this, advanced CMR techniques allow the acquisition of more detailed information about myocardial architecture, ventricular mechanics, and fibrosis. The left ventricle (LV) and right ventricle have unique myocardial architecture that underpins their mechanics; however, this becomes disorganized under conditions of volume and pressure overload. CMR diffusion tensor imaging is able to interrogate non-invasively the principal alignments of microstructures in the left ventricular wall. Myocardial tissue tagging (displacement encoding using stimulated echoes) and feature tracking are CMR techniques that can be used to examine the deformation and strain of the myocardium in CHD, whereas 3D feature tracking can assess the twisting motion of the LV chamber. Late gadolinium enhancement imaging and more recently T1 mapping can help in detecting fibrotic myocardial changes and evolve our understanding of the pathophysiology of CHD patients. This review not only gives an overview about available or emerging CMR techniques for assessing myocardial mechanics and fibrosis but it also describes their clinical value and how they can be used to detect abnormalities in myocardial architecture and mechanics in CHD patients.

Keywords: cardiology, congenital heart disease, cardiovascular magnetic resonance imaging, late gadolinium enhancement cardiovascular magnetic resonance, myocardial strain, fibrosis, diffusion tensor imaging

OPEN ACCESS

Edited by:
Giovanni Biglino, University of Bristol, UK

Reviewed by:
Giulia Pontecorboli, NIHR Bristol Cardiovascular Biomedical Research Unit, UK
Marina Hughes, Great Ormond St Hospital, UK

***Correspondence:**
Sonya V. Babu-Narayan
s.babu-narayan@imperial.ac.uk

Specialty section:
This article was submitted to Pediatric Cardiology, a section of the journal Frontiers in Cardiovascular Medicine

Received: *03 February 2017*
Accepted: *28 April 2017*
Published: *23 May 2017*

Citation:
Ghonim S, Voges I, Gatehouse PD, Keegan J, Gatzoulis MA, Kilner PJ and Babu-Narayan SV (2017) Myocardial Architecture, Mechanics, and Fibrosis in Congenital Heart Disease. Front. Cardiovasc. Med. 4:30. doi: 10.3389/fcvm.2017.00030

VENTRICULAR ARCHITECTURE AND MECHANICS

Architecture of the Left Ventricle (LV)

The normal myo-architecture of the heart differs between the LV and the right ventricle (RV). The LV has a thicker compact layer with its myocytes arrayed in varying orientations through its depth, while the more apical parts of the human RV are predominantly trabeculated, with only a thin outermost compact layer.

The LV subepicardial layer contains fibers orientated in a left-handed helical arrangement, which is largely responsible for torsion of the apex relative to the base. The mid-wall layer contains circumferential fibers that generate radial contraction. The subendocardial layer has right-handed helical as well as longitudinal fibers that function in conjunction with the helical subepicardial layer and papillary muscles to generate longitudinal strain (1, 2). The ventricular myocardial fibers are connected and are generally aligned with their neighbors, with only gradual change in the direction of the fibers from layer to layer (3, 4). Because of their opposing helical orientation, myocytes of the subepicardial and subendocardial layers of a given wall region contract almost orthogonally to one another during systole. They and those of the circumferential mid-layer also counter thicken, as they maintain their cell volume. In the compact myocardium, myocytes are also aggregated in micro-laminar arrays known as sheetlets, with intervening cracks or shear layers. These laminar arrays of sheetlets all slope obliquely relative to the local wall tangent plane and change orientation through the cycle, tilting to be more wall perpendicular in systole and more wall parallel in diastole. This reorientation of micro-laminar structures not only accommodates the counter thickening of myocytes in the circumferential layer while those of the endocardial and epicardial layers are contracting but also translates this forced cross-myocyte shortening into enhanced wall thickening (5–7). In the normal myocardium, the LV wall thickens radially by 30–50%, resulting in a normal ejection fraction. Yet, on a cellular level, myocytes shorten only by about 15% thus increasing their mean diameter by about 8% (8, 9). The change in sheetlet orientation in systole is thought to account for most of the wall thickening seen (5, 6, 10). The overall result of the combined twisting, laminar reorientation, and compressive forces is the ejection of the stroke volume from the LV cavity.

It may also be the case that diastolic relaxation of the laminar structures facilitates perfusion, in diastole, of blood through microvessels passing between the sheetlets; however, the papillary muscles and the trabeculars that are particularly prevalent in the RV lack laminar microstructures (11). Their less complex but nevertheless dense local myocardial structure, combined with their relative remoteness from epicardial coronary arteries, may predispose them to ischemia if abnormally loaded, for example, by ventricular volume and/or pressure loading. Regrettably, current methods of myocardial perfusion imaging lack the spatial resolution to confirm this, but it may be surmised that trabecular ischemia is a contributor to the gradual dysfunction of RVs that are hypertrophied due to chronic pressure and volume overload. In a study by Babu-Narayan et al., focal fibrosis as represented by late gadolinium enhancement (LGE) was found in trabeculation remote from surgical sites in patients with repaired tetralogy of Fallot (rToF) (12).

In conditions with pressure or volume overloading, changes in LV myo-architecture have been reported. An increase in the amount of longitudinal fibers was found in the subendocardial layer, and a decreased number of circumferential fibers in the mid-layer were found. Furthermore, a change in orientation of the subendocardial fibers was noted (13, 14).

Architecture of the RV

The myo-architecture of a normal RV wall is not considered to contain a middle layer of circumferential fibers apart from the right ventricular outflow tract (RVOT) (15). However, in a diseased RV [tetralogy of Fallot (ToF)], a middle circumferential layer was identified (13).

Histological studies have demonstrated disorganization in the RV myocardial architecture in patients with ToF. They have been found to have a more substantial proportion of circumferential fibers in the hypertrophied sub-pulmonary infundibulum (15). A key difference in myo-architecture in ToF is the presence of circumferential fibers in the mid-wall, which is particularly abundant in hypertrophied RV cavities and may be responsible for the reduced compliance (13). These changes in myo-architecture were not only found in adult ToF patients' post-repair but also in infants before surgery (13).

The RV has a complex geometrical shape. The RV is wrapped around the LV, which allows it to shorten in systole as well as to benefit from ventricle–ventricle interdependence from the LV contraction due to its sharing of common fibers, septum, and pericardial space. The RV subendocardial fibers are shared with the LV subendocardial layer *via* the interventricular septum. Likewise, the RV subepicardial fibers are shared with the LV subepicardial layer (16). Chronic RV pressure or volume overload in congenital heart disease (CHD) such as ToF, conditions with a systemic RV, Ebstein's anomaly, and atrial septal defects alter the mechanical properties of the interventricular septum whereby it becomes strained and deformed. Consequently, LV function can be affected (17). It has also been reported that on a cellular level abnormal septal mechanics induce a process of apoptosis and dysregulation of the angiogenic factors in the LV wall that can further impair LV function (17).

The Myocardial Extracellular Space

The myocardial extracellular space is the interstitial tissue that contains the fibro-collagenous material, endomysium. The endomysium acts like a mesh that coordinates the conduction of impulses and transmission of forces and provides a supportive framework. In immediate proximity to cardiac myocytes is the perimysium, which is the thicker connective tissue that transmits shearing forces. Abnormal accumulation and/or change in the quality of the connective tissue increases myocardial stiffness and reduces the compliance of the ventricle (5–7).

Relatively few studies have investigated the significance of collagenous matrix with relation to CHD (18, 19), the most relevant of which was a study that quantified the collagen matrix in 23 heart specimens with univentricular repair of hypoplastic left heart syndrome (HLHS) compared to a control group. Hearts with HLHS had significantly less collagen fibrous matrix in the RV (the systemic ventricle) and LV compared to normal hearts. In addition intrinsic myocardial abnormality could also be found in the hypoplastic LV. Myocardial fibrosis, therefore, could potentially affect long-term function and outcomes of the systemic RV (20).

Cardiac Diffusion Tensor Imaging (cDTI)

Cardiac diffusion tensor imaging has long been utilized in the imaging of the central nervous system. However, more recent

developments in cDTI sequences have enabled its use in the non-invasive interrogation of the myo-architecture and fiber orientation. Until recently, cDTI was mainly used to investigate myofiber orientation in *ex vivo* heart tissues due to the problems of imaging beating hearts because of motion artifact. Results of cDTI have been verified with histological findings in a number of studies (21, 22). More recently, sequence developments have enabled *in vivo* use for cDTI and there is increasing evidence that cardiovascular disease processes can be associated with abnormal cDTI parameters (10). Water has the ability to diffuse in all directions; however, microstructural boundaries may limit molecular displacement in certain directions more than others (anisotropic diffusion). In the myocardium, water diffusion is thought to be limited by cell boundaries and their aggregates in sheetlets. Diffusion of water appears to be greatest in directions parallel to myocytes. In cDTI, the direction and the magnitude of diffusion of water molecules are measured for each voxel, which will contain numerous myocytes and sheetlets. After a diffusion gradient is applied, the greatest signal attenuation, i.e., the darkest signal, is obtained when the diffusion gradients are parallel to the length of the myofibers. A diffusion tensor is calculated from measurements of diffusion in six or more directions. A diffusion tensor represents the anisotropic diffusion of water in three dimensions. The principle eigenvector (E1) is therefore the value that represents the direction of water diffusion along the length of the myofiber from which the direction of the myofiber can be inferred. The greatest vector (E2) represents the largest magnitude of diffusion when the myofibers are en face. E3 is the smallest eigenvector. Diffusion tensor imaging (DTI) measures the average of the eigenvectors for each voxel. An *in vivo* sequence has been developed for cDTI using imaging at 3 T. A diffusion weighted stimulated echo acquisition mode (STEAM) sequence is used in conjunction with echo planer imaging, a hybrid single-shot spin echo and gradient echo sequence. This sequence works over two cardiac cycles and assumes that myocardial tissue returns to the same position, at both diffusion encoding times at end systole. Parallel imaging is applied to reduce the length of single-shot imaging in each cardiac cycle. Each 2D slice can be acquired in breath-holds of 18 heart beats duration. Typically eight breath-hold acquisitions are performed per 2D slice and the data averaged to improve signal-to-noise ratio (SNR) (10). Complex postprocessing techniques allow for E1 mapping giving a 3D visual display of the orientation of myofibers in the wall of the LV (**Figure 1**). Limitations of the cDTI STEAM sequence to date are low SNR, low spatial resolution, and susceptibility to strain artifact (23), and it is dependent on a regular R–R interval.

Cardiac DTI has been applied in some studies to interrogate myocardial fiber orientation in certain disease processes; however, to date, very little has been trialed with respect to CHD. Investigators have studied hypertrophic cardiomyopathy and have identified abnormal orientation of myocardial fibers in diastole that remains in a relatively systolic conformation (10). This was thought to be responsible for the abnormal wall thickness seen in hypertrophic cardiomyopathy rather than replacement fibrosis seen by LGE. cDTI has also been used to study ventricular remodeling postinfarction (25, 26). There are few data for the use of DTI in CHD.

Ventricular Function Analysis

Cardiovascular magnetic resonance (CMR) has the capability of providing important data on global and regional ventricular function. It is the gold standard in the estimation of ventricular volumes and ejection fraction using a disk-area summation method and in comparison to other modalities as it does not rely on assuming ventricular geometry (27, 28). For global and regional assessment of ventricular function, cine imaging with a balanced steady-state free precession (bSSFP) sequence can provide useful functional information. These ideally are acquired in breath-hold in order to achieve the sharpest delineation between the myocardium and blood pool. Furthermore, bSSFP imaging uses a high flip angle as well as short-echo time and short-repeat time in order to produce images with a high SNR and therefore better contrast between blood and myocardium. Typically, data acquisition is segmented over 10–12 cardiac cycles. The data segment for a given cardiac cycle being acquired is then repeated at multiple time points in the cardiac cycle to create cine phases. The acquired images are repeated on a loop to form cine. Normal flow in the ventricle is represented on these "white-blood" images as high signal whereas turbulence, stenosis, regurgitation, or shunt is represented as low signal. For further assessment of function, using bSSFP images, RV and LV end-diastolic and end-systolic volumes, RV and LV mass, stroke volume, and ejection fraction can be derived.

While acquiring SSFP images in breath-hold, misregistration artifact may arise. This is due the natural variability in the size and depth of breath a patient may take that can cause small changes in the location of the heart each time between acquisitions. Secondly, there are the physiological effects of respiration (e.g., increased venous return) that may affect reproducibility. Four-dimensional, multiphase, steady-state imaging with contrast enhancement is a respiratory gated technique that may overcome breath-holding problems that was developed by Han and colleagues in 2014 to study pediatric patients with complex CHD. The results of this small study showed good correlation of cardiac volumes with conventional 2D cines (29).

MYOCARDIAL STRAIN

Markers of intrinsic myocardial contractility are investigated with the aim of identifying early myocardial abnormalities that are subclinical and precede ventricular systolic dysfunction. Myocardial strain is a measure of how much myocardial tissue gets larger and thickens (positive strain) or how much it gets smaller or thins (negative strain) in relation to its state in end diastole. It occurs in three different planes in accordance with the orientation of myofibers in the LV subepicardial (helical), middle (circumferential), and subendocardial (longitudinal) layers as described above. Several CMR methods have been developed to interrogate myocardial strain in these planes. Myocardial tagging has been long established as a gold standard technique (30). In this technique, images are acquired in systole and diastole following the disruption of the magnetic field with multiple radio-frequency saturation pulses using sequences such as harmonic phase analysis or spatial modulation of magnetization. Parallel saturation lines (or tags) are superimposed on the

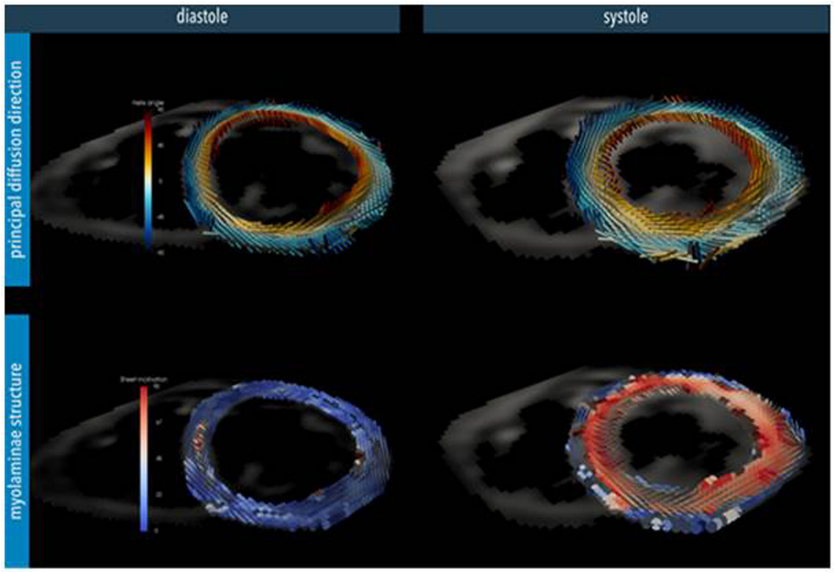

FIGURE 1 | **Myocardial microstructure probed with diffusion tensor imaging in a short-axis slice at peak systole and diastole in a healthy heart**. Top: the principal diffusion direction of water molecules is along the local myocyte long-axis orientation, depicting its helical arrangement. Bottom: additional diffusion directions also hint at the myocardial laminar organization where sheets of myocytes are surrounded by collagen-lined shear layers. These myo-laminae moderate cellular reorganization during cardiac contraction. In the normal heart, myocyte orientation remains similar between systole and diastole, but there is a tilting of the sheets toward a more wall-perpendicular conformation during systole (24). (Image reconstruction below is courtesy of Pedro Ferreira, Senior Physicist, Royal Brompton Hospital.)

myocardium and their deformation with cardiac motion imaged in a cine acquisition. However, while the technique is visually appealing the spatial resolution is limited to the tag spacing and processing time is very long as automatic detection of the tags and their displacement through the cardiac cycle is difficult. This is particularly so in the late phase of the cardiac cycle when the tags have faded. Displacement encoding using stimulated echoes (DENSE) (31) and tissue tracking (two and three dimensional) (32) are newer techniques which in some studies have shown equivalent accuracy (33). These techniques are discussed in depth by Simpson and colleagues in 2012 (34).

Displacement Encoding Using Stimulated Echoes

Displacement encoding using stimulated echoes is a newer MRI technique that was developed after myocardial tagging. It has a relatively high spatial resolution that can be used to quantify the displacement and strain of the myocardium on a pixel by pixel basis. With this technique, displacement information is directly encoded in to the phase of the sequence for each voxel 2D or 3D image, and a displacement map can be produced. This is used to calculate strains in longitudinal, circumferential, and radial directions in tissue.

The original DENSE sequence produced a displacement-encoded image at a single-time point in the cardiac cycle. Subsequently, cineDENSE incorporated highly efficient data acquisition to produce images throughout the cardiac cycle (33, 35), while fast cine DENSE incorporated parallel imaging and other advanced image processing techniques to improve SNR and spatial and temporal resolution in a reduced acquisition time (36). To date, however, DENSE is still a research tool and has not been used for strain analysis in clinical management of CHD.

Feature Tracking-CMR (FT-CMR)

Feature tracking-CMR is a technique that is comparable to speckle tracking in echocardiography. Although it is not a direct measure of "true" strain in the myocardium, it is an estimate of endocardial contractility and relaxation properties. The postprocessing technique identifies patterns of features or irregularities in a small window and searches for the same pattern of features in the following images. The measured displacements between the two patterns enable a feature-tracked strain-related index (FTSI) to be calculated. The tissue represented by each voxel in the cine images has their FTSI measured in the longitudinal, radial, and circumferential directions (37).

Longitudinal and circumferential FTSI are derived by tracking tissue components along the length of the myocardium in the long axis. Radial FTSI is estimated from tracking tissue components in the perpendicular direction to the myocardium in the short axis. In a normal heart, there is predominantly a positive radial strain that thickens the LV wall and negative longitudinal and circumferential strains that reduce LV cavity size in systole. Tissue components of interest are preferably selected along the endocardial border rather than the epicardial border as the reduction of the endocardial surface is a better representation of the efficiency of the LV cavity emptying its stroke volume (38).

Rapid acquisition of images is performed using a bSSFP sequence. Current bSSFP images are good at distinguishing blood

pool from myocardium with a spatial resolution of 1–2 mm (in-plane). However, with CMR, it is difficult to distinguish features within the compact myocardium due to its homogeneity and large size voxels. Therefore, instead of tracking features within the myocardium, FT-CMR utilizes the endocardial border features that become easily distinguishable by CMR. One limitation of CMR is its limited spatial resolution through-plane (6–10 mm), which means that FT-CMR is unable to track features that move out of plane in subsequent frames in the through-plane direction (38).

3D-FT-CMR is an area of growing interest where all three strain parameters can be measured from a single-3D acquisition. An assumption of shear motion between the layers (circumferential–longitudinal, longitudinal–radial, and circumferential–radial) may be made. The shear motion between the circumferential–longitudinal layers in particular is responsible for LV torsional motion. 3D-FT-CMR is again limited by lower through-plane spatial resolution, and therefore it is not ideal in measuring longitudinal strain in the short-axis LV stacks; however, it has shown comparable results for radial and circumferential strains. 3D-FT-CMR involves longer acquisitions and so a navigator is required for avoiding respiratory motion artifact.

Several studies have compared FT-CMR with myocardial tagging techniques and have demonstrated good agreement in circumferential strain measurements recorded between both techniques in healthy subjects, aortic stenosis, and non-ischemic cardiomyopathy (39–41). FT-CMR has the advantage of not requiring any additional imaging to cine images acquired and has a shorter postprocessing time (42). Interobserver variability has been reported to be at least equivocal to myocardial tagging for circumferential strain measurements. However, FT-CMR-derived longitudinal and radial strain, however, is not as reliably correlated with myocardial tagging (39).

Clinical Applications of Feature Tracking

Patients with *ToF* commonly have RV dysfunction that can progress through their adult life and several mechanisms for this have been described (please see above). RV dysfunction is in keeping with impaired myocardial strain and intraventricular RV dyssynchrony and interventricular dyssynchrony. Several studies have used FT-CMR to examine strain and its prognostic significance.

It has been reported ToF patients who experience adverse outcomes (death or sustained ventricular tachycardia), all have globally lower RV FTSI indices compared to patients with no adverse outcome. Impaired longitudinal "strain" of both ventricles was strongly associated with adverse clinical outcomes (43). Orwat et al. also recently studied the correlation between FT-CMR derived indices with adverse outcomes. They reported that RV-longitudinal FTSI and LV-circumferential FTSI were predictors of adverse outcomes independent of other known risk factors and suggested that these parameters should be included in the risk assessment process (44). Jing and colleagues did not find a correlation between FT-CMR parameters and RV dilation and RVEF, reporting that they were not independent predictors of developing RV dysfunction and subsequent adverse outcomes (45).

Feature tracking-CMR has been used to investigate RV function following different types of RVOT obstruction (RVOTO) repair. The current move in surgical approach to relieve RV infundibular obstruction is to do perform minimum resection and preserve the pulmonary valve in order to prevent pulmonary valve incompetence (46). The effect of this approach is to leave residual RVOTO. It is thought that the increased RV pressure overload causes hypertrophy and increased contractile function. Several investigators have reported this to be protective on RV remodeling in comparison to a volume overloaded RV from pulmonary regurgitation. Latus et al. used FT-CMR to investigate the underlying mechanism for this and found that residual RVOTO following a more conservative surgical approach, RV circumferential and radial strain were higher than in the control group though RV longitudinal strain did not change (47). Stronger RV–LV interaction and reduced ventricular dyssynchrony were reported (47). LV longitudinal strain, which was reduced in the RVOTO group, an area that still needs further investigation, given LV dysfunction is an adverse prognostic marker for mortality in ToF.

In atrial redirection surgery for *the great arteries (TGA)*, Tutarel et al. also found that circumferential FTSI correlated moderately with RV (systemic) ejection fraction and that there was a negative correlation with QRS duration; weak correlations between FTSI and LVEF were found (48). Velocity vector imaging as part of FT-CMR was used in another study to compare "strain" parameters in patients after atrial redirection surgery for TGA with patients who underwent arterial switch operation (49). Patients after atrial switch operation showed reduced RV ejection fraction (RVEF) and decreased longitudinal and circumferential strain parameters compared to patients with arterial switch operation (49).

The prognostic significance of FT-CMR derived indices were assessed in a small group of adults with *single-ventricle* post-Fontan surgery. Systemic ventricle longitudinal, radial, and circumferential FTSI correlated with NYHA class, peak oxygen uptake on cardiopulmonary exercise testing, and age of complete Fontan surgery (50).

Ventricular Regional and Global Function for Predicting Outcomes

More sensitive parameters for both regional ventricular function and intrinsic myocardial contractility are sought after in order to identify abnormalities early when patients are asymptomatic prior to the establishment of systolic dysfunction. Often when systolic dysfunction sets in, it is indicative of an advanced stage of the myocardial disease process. In patients with repaired ToF, several CMR parameters of ventricular function have been assessed with their prognostic significance determined. RVOT regional wall motion abnormalities were found to have important prognostic implications. RVOT aneurysms or akinetic RVOT portions are common features related to scar tissue due to transannular patching or previous generous infundibular stenosis resection (12, 51). These akinetic RVOT areas contribute to a larger RV end-diastolic and end-systolic volume (RVEDV and RVESV) hence having a negative impact on the RVEF

(12, 52). Delay of conduction is also found within this region leading to prolongation of QRS elongation, representing intraventricular (RV) dyssynchrony (53). Bonello et al. have reported a correlation between the length of the akinetic RVOT wall and the first onset of ventricular arrhythmias (54). Another marker of function is RV volumes. Studies have focused on these to determine preoperative thresholds that predict timing for pulmonary valve replacement surgery that results in normalization of RV volumes in rToF patients (55). As an overall consensus from several studies, indexed RVEDV between 150 and 170 ml (and 158 ml/m^2 from our center) or indexed RVESV between 80 and 90 ml (and 82 ml/m^2 from our center) are when pulmonary valve replacement for pulmonary regurgitation should be considered for asymptomatic patients (56). Past this point, it is thought that a degree of permanent RV damage has occurred. Following an optimally timed pulmonary valve replacement, RV volumes improve at CMR (57).

Left ventricle longitudinal impairment was reported to be a predictor of sudden cardiac death (SCD) in patients with repaired ToF (58). The INDICATOR multicentre trial in 2014 investigated 873 adult Fallot patients found that RV hypertrophy that was out of proportion to volume dilation (quantified on CMR by RV mass/RV volume ratio of >0.3 g/ml) was further found to be a risk factor for SCD. Other risk factors assessed by this trial found to have an association with SCD were reduced LV and RVEF and a history of sustained atrial arrhythmia (59).

Cardiovascular magnetic resonance ventricular function parameters are a useful risk stratification tool for patients with Eisenmenger's syndrome. A study by Jensen et al. found that CMR derived RVEF less than 40% and LVEF less than 50% was associated with increased risk of death in Eisenmenger's patients with post-tricuspid shunts (60).

MYOCARDIAL FIBROSIS

Myocardial fibrosis may be a final common pathophysiological pathway that links a wide spectrum of congenital heart conditions. There is great importance in detecting its various forms and understanding its prognostic significance for a more targeted treatment approach. Broadly, there are two forms of fibrotic processes that can occur: replacement fibrosis and interstitial fibrosis.

Replacement fibrosis is irreversible and occurs following an insult to myocytes, commonly ischemia. This focal type of fibrosis can be detected usually by LGE imaging, assuming there is a neighboring normal myocardium.

Interstitial fibrosis is secondary to increased collagen deposition within the extracellular matrix (ECM) as a response to abnormal loading conditions on the myocardium such as typically occurs in CHD patients. It can be detected with T1 mapping and extracellular (ECV) measurements and remains undetected by LGE imaging because it is more diffuse and widespread throughout the myocardium preventing identification by comparison to neighboring "normal" myocardium.

Technical developments in LGE imaging, T1 mapping, and ECV measurements have enabled the non-invasive quantification of myocardial fibrosis that was previously only possible on a biopsy or during postmortem. A recent study has demonstrated that the incremental value of detecting focal fibrosis using LGE alongside conventional parameter (LVEF), in predicting 5-year mortality in patients with aortic stenosis (61). Furthermore, Halliday et al. have reported recently the value of mid-wall focal fibrosis as detected by LGE in predicting SCD in patients with dilated cardiomyopathy and LVEF >40% (62).

Diffuse myocardial fibrosis or interstitial disease is increasingly of interest. Its presence leads to abnormal T1 (pre- and postcontrast agent) and abnormal ECV measurements, which is speculated to predate cardiac dysfunction. Previous studies of cardiomyopathy have demonstrated correlation between increased ECV with diastolic dysfunction (63) and reduced myocardial blood flow (64). Correlation was found between ECV and reduced ventricular EF in a study of 50 patients with adult CHD (65).

FOCAL FIBROSIS AND SCARRING

Late Gadolinium Enhancement

The differences between normal and abnormal myocardial tissue may be subtle on CMR; however, differences between these tissues are emphasized after the administration of intravenous gadolinium-based contrast agent (GBCA). Gadolinium, in its chelated form, is rendered non-toxic, and its distribution is confined to the extracellular compartment due to its large molecular weight. The proportion of extracellular space in a healthy myocardium is ~15% and increases in with heart disease due to increased collagen deposition and fibrosis. This results in an increased volume of distribution of gadolinium that further is compounded in conditions where the myocardial function is depressed; slowing down the gadolinium washout kinetics. Gadolinium has paramagnetic properties that allow it to interact with spins promoting more rapid exchange of energy thus T1 is shorter and results in a high signal (bright).

In practice, 0.5 μg to 0.1 μg/kg bolus GBCA is injected, and after 10–30 min, images are acquired. An inversion recovery fast gradient echo sequence is used in breath-hold. LGE imaging is performed using a non-selective 180° inversion preparation pulse. Following the inversion pulse, the longitudinal magnetization returns to its original value exponentially with a time constant T1. Due to the difference in GBCA concentrations between normal and abnormal myocardium, there is a difference in T1 values and hence different magnetization recovery curves. The inversion time (Ti) of normal myocardium is the time after the inversion pulse when the magnetization of normal myocardium is passing through 0 (the null point). At this Ti, normal myocardium is black in the resulting images. This Ti varies with GBCA dose, time after administration, and with patient-specific factors such as kidney function and disease state. In order to maximize the contrast between abnormal and normal myocardium, normal myocardium should be nulled. The Ti can be determined empirically or by performing a breath-hold Ti scout acquisition (using a Look–Locker sequence). This is either calculated manually or by performing a Ti scout (Look–Locker sequence). The Ti scout sequence acquires images at multiple time points following a

single-inversion recovery pulse. Each image is therefore effectively acquired with a different Ti, and visual inspection allows the Ti to null the signal from normal myocardium to be determined. The optimal Ti needs to be increased as the study proceeds as the GBCA washes out of the myocardium. The inversion pulse and data acquisition are repeated on every second R–R interval to allow full T1 relaxation between pulses, which improves the SNR and makes the sequence less sensitive to variability in the R–R interval. In cases of tachycardia, images can be acquired on every third R–R interval at the expense of increasing the imaging time. With conventional LGE imaging, incorrect setting of the Ti adversely affects the contrast between normal and abnormal myocardium.

Common challenges in patients with CHD are difficulties of ECG gating due to arrhythmia, wide and abnormally shaped QRS complexes, breath-holding difficulties as well as metallic artifacts from sternal wires and transcatheter devices. LGE false positive scans occur more commonly when imaging the thin-walled RV due to partial volume effects. Partial volume effects are seen when one pixel contains both normal tissue and abnormal myocardium (e.g., fat and RV wall). Partial volume effects can be reduced by acquiring images with higher spatial resolution and in a shorter acquisition window (to reduce motion blurring) but both of these will increase breath-hold duration. Acquiring images in systole (when the RV wall is thickest) can be beneficial. In patients who have intracardiac shunts, the washout kinetics of gadolinium are different and hard to predict as GBCA clearance can be rapid (66).

To reduce false positive diagnosis of LGE phase swapping, cross cutting and comparing the LGE images with cine images are helpful. Imaging the RV for small areas of fibrosis requires meticulous choices in Ti.

While conventional LGE images are magnitude reconstructions that take no account of the polarity of the magnetization following the inversion pulse, phase sensitive inversion recovery (PSIR) LGE image reconstructions take into account both the magnitude and the polarity. With this type of reconstruction, the sequence is more tolerant to incorrect setting of the Ti to null normal myocardium, and the contrast between normal and abnormal myocardium is maintained over a range of values (67). While the inversion pulses are output and the data segments acquired on alternate cardiac cycles, with the PSIR sequence, additional low flip angle data are acquired in the redundant cardiac cycles and used to correct for other sources of phase variation in the reconstruction.

In cases where patients may find breath-holding difficult, motion corrected, free breathing, PSIR LGE imaging helps (68). In this technique, complete images are acquired using an inversion prepared bSSFP in each of a number of cardiac cycles. Non-rigid motion correction of these low SNR images is then performed (to correct for respiration) prior to averaging to generate a single high-SNR image. This technique has been shown to produce high quality images in patients with poor breath-hold capability and with arrhythmia (68). We have found this to be an excellent approach in CHD including for the RV.

For 3D coverage of the heart with high spatial resolution, respiratory-gated free breathing acquisitions can be performed. These navigated sequences may enable the assessment of thin walled structures such as atria and RV free wall although acquisition durations are long (typically 5–10 min) and unpredictable (69).

Clinical Applications of LGE Imaging

Repaired Tetralogy of Fallot

Patients with *repaired ToF* encounter problems in adulthood relating to RV dysfunction, pulmonary regurgitation, and clinical arrhythmia and are at greater risk of SCD. Detection of myocardial scarring has contributed to the understanding of RV dysfunction late after repair. We systematically investigated LGE and clinical status in a cohort of adult ToF patients and found focal areas of fibrosis not only at the ventriculotomy, VSD repair, and apical vent sites but also in remote locations in the LV and RV wall and trabeculations (12) The RVOT was an important area of CMR defined focal fibrosis and dyskinesia (see **Figure 2**). Though by definition of the surgical intervention required to repair the heart the RV always has LGE in this region, the extent is highly variable.

There are several postulated mechanisms that explain the distribution of focal fibrosis seen in repaired ToF. Fibrosis in remote areas of the LV and RV could be as a result of ischemic insult in the pre-, peri-, or postoperative phase or related to RV hypertrophy and dilation secondary to pulmonary stenosis or regurgitation. Older patients with repaired ToF were reported to have greater LGE in the RVOT and dyskinesia probably relating to previous surgical methods of reconstructing the RVOT such as transannular patch repair that involved extensive resection (12). The amount of LGE found in the RV was associated with RV dysfunction, exercise intolerance, and previous presentation with clinical arrhythmia (12). In a separate study including heterogenous operated and unoperated CHD patients, the absence of LGE together with good peak oxygen consumption on exercise testing was found to correlate with lack of inducible ventricular tachycardia (70). Other groups revealed that RV fibrosis is associated with diastolic dysfunction and surface ECG abnormalities associated with arrhythmia in ToF patients (71, 72).

Systemic RV after Atrial Redirection Surgery for TGA

In patients with *transposition of TGA* who underwent *surgical palliation by atrial redirection surgery*, the RV needs to sustain the systemic circulation for the long term. The hemodynamic burden on the maladapted systemic RV can lead to RV dysfunction, reduced exercise capacity, arrhythmia, and SCD. A likely mechanism of dysfunction of the systemic RV is a myocardial perfusion mismatch leading to myocardial ischemia and fibrosis (12).

The first prospective study to investigate myocardial fibrosis by LGE imaging in individuals with systemic RV following atrial redirection surgery found that RV LGE was present in 56% of studied patients. Among other variables in the study, the mere presence of RV LGE independently and strongly predicted adverse clinical outcomes (atrial/ventricular arrhythmia and death) with a hazard ration of 4.95 (73) (see **Figures 3** and **4**). The extent of LGE correlated with age, RV dysfunction, and dyssynchrony as well as clinical arrhythmia (73, 74). Focal fibrosis has also been demonstrated also by others in the systemic RV (congenitally corrected TGA and Mustard/Senning) correlating

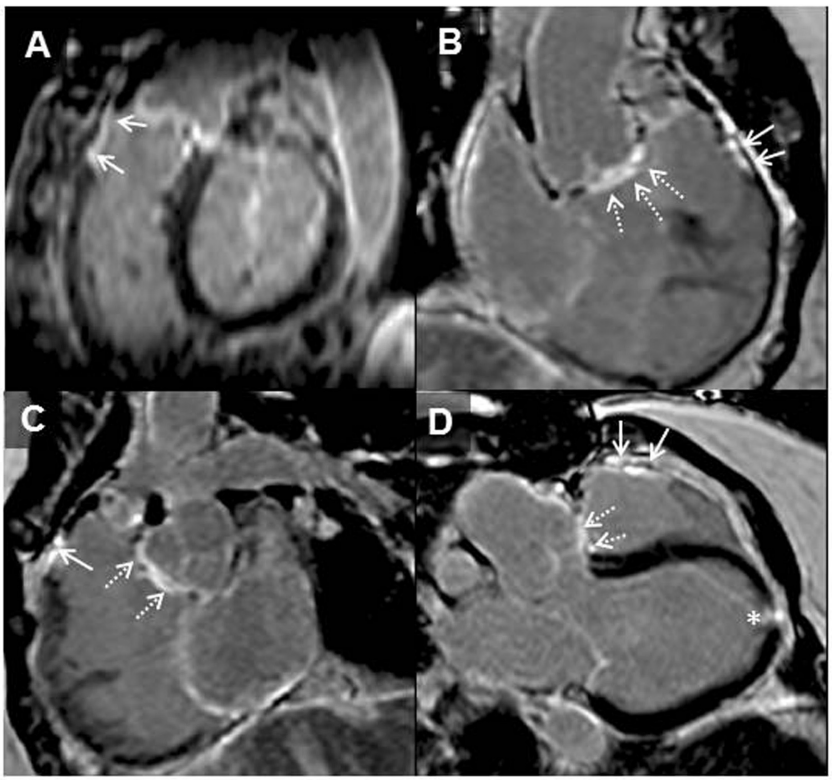

FIGURE 2 | **Adult patient after repair of tetralogy of Fallot and later surgery for pulmonary valve implantation**. Solid arrows demonstrating late gadolinium enhancement (LGE) in the right ventricle (RV) outflow tract **(A–D)**. Broken arrows showing LGE in the ventricular septal defect region **(B–D)**. LGE of the apical vent site following surgery* **(D)** is also present. Where present, these may be useful when acquiring LGE images to guide optimal nulling of the normal myocardium; RV–left ventricle inferior insertion point faint LGE is ubiquitous **(A)** and similarly useful (66).

with RV dysfunction, arrhythmia presentation, and exercise intolerance (75).

Late gadolinium enhancement was also studied in patients who underwent the *arterial switch operation for TGA*, a population at risk for coronary stenosis, occlusions, and late death. Despite the reported prevalence of 3–7% for coronary problems, LGE was only found in 1.8% of 220 patients. Approximately 20% of patients had (mostly mild) LV dysfunction post-arterial switch surgery (77, 78).

Single Ventricle

While undergoing several surgical procedures in the first years of life, *single-ventricle* patients are affected by significant morbidity and mortality (79, 80). Ventricular dimensions and dysfunction played a major role in the long-term outcome in a cohort of 215 patients after the Fontan palliation (81). In particular, the end-diastolic volume of the primary ventricle was the strongest volumetric parameter associated with adverse clinical outcomes (81). Myocardial fibrosis as imaged by LGE was detected in 28% of patients studied. Although LGE was found at the surgical sites as expected, this was only in 8% of cases. The large majority of the LGE distribution was found in the free wall of the primary ventricle (64%) with lesser degrees in the secondary ventricle (36%), septal insertion points (16%), papillary muscles (12%), and ventricular apex (8%) (82). LGE lesions were categorized as transmural (40%), subendocardial (36%), and diffuse LGE (12%) (see **Figure 5**). The presence and extent of ventricular LGE closely correlated with adverse ventricular size and function as well as non-sustained ventricular tachycardia, all risk factors for poor clinical outcomes (82).

Eisenmenger Syndrome

A small study in *Eisenmenger* syndrome involving 30 patients showed that a large majority had LGE (73%), of which 70% was found in the RV myocardium but LV LGE was also found. No correlation with ventricular size and function, exercise capacity, or survival was found. Fast gadolinium washout kinetics was also found (66). Therefore, to date, the routine use of LGE for this condition was not considered justified (83).

DIFFUSE AND INTERSTITIAL FIBROSIS

T1 Mapping

Diffuse myocardial fibrosis has been shown to be an important predictor for SCD, ventricular tachycardia, and heart failure. Rapid advances in CMR have enabled the non-invasive detection and quantification of diffuse myocardial fibrosis and interstitial disease in the myocardium using T1 mapping (84, 85).

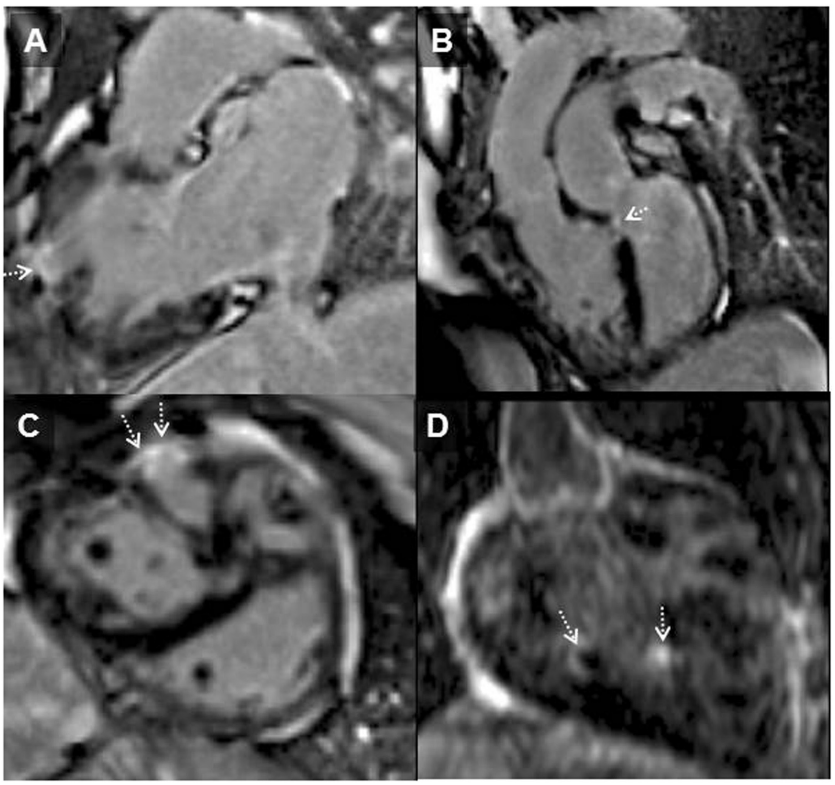

FIGURE 3 | **Systemic right ventricle (RV) following atrial redirection surgery (Mustard operation)**. RV in-out view **(A)** showing free wall localized transmural RV late gadolinium enhancement (arrowhead); LGE in the ventricular septum consistent with previous VSD repair [**(B)**; dotted arrow], in the free wall of the RV [**(C)**; dotted arrows] and of trabeculations within the body of the RV [**(D)**; dotted arrows]. This is the typical pattern of fibrosis seen in systemic RV following atrial redirection surgery (76).

After the magnetization has been excited with a radio-frequency pulse, it relaxes back to its equilibrium state in the longitudinal direction aligned with the main magnetic field. T1 is a property constant characterizing how long the magnetization takes to recover to 63% of its original longitudinal equilibrium value in the main field. The rate of T1 relaxation is dependent on each proton's ability to exchange energy with its surroundings. The T1 constant differs between tissues depending largely but not solely on the concentration of water. The paramagnetic properties of (ionic) iron and (complex chelated ionic) gadolinium shorten T1. With T1 mapping, an estimate is calculated from a series of different T1-weighted images during the magnetization recovery process and is written as a "T1 map" where the T1 value of each pixel is encoded in to the intensity of the T1-map pixels. This involves a series of assumptions about alignment of the pixels in all images of the supporting series (typically subject to errors such as inter-cycle differences, breath-hold imperfection, and corruption by blood signal artifacts) (86, 87).

T1-Mapping Imaging Sequences: Modified Look–Locker Imaging (MOLLI)

Following a 180° inversion pulse, single-shot images are acquired in typically diastole, typically over three to five heart beats at different inversion recovery times (Ti). After a recovery period to allow for complete T1 recovery another, inversion pulse is applied followed by a similar series of images but slightly different Ti values thereby sampling more points along the T1 recovery curve. Images are then organized in order of increasing Ti (88). When this process is performed for all pixels in the image, a T1 map is created. MOLLI acquisition duration is heart rate dependent; the greater the number of beats involved in the acquisition, the longer the breath-hold. Therefore, a shortened MOLLI sequence is often used acquiring single shots during five heart beats, followed by three beats recovery, and then a second "set" of single shots acquired over three beats following a second inversion pulse, written as 5(3)3 (89). This allows for a breath-hold T1 map taking only over 11 beats rather than the 17 beats in the original innovative sequences used. A modified arrangement 4(1)3(1)2 is applied postcontrast because its arrangement of TI values is more suitable to the shorter T1 values post-gadolinium (89).

Shortened Modified Look–Locker Imaging (shMOLLI)

An "shMOLLI" is a shorter sequence that involves image acquisition during fewer heart beats thereby shortening breath-hold time (90). An example is acquiring single-shot images over the first five beats followed by one recovery beat and cycles thereafter that are only single beat in duration 5 (1)1(1)1. This reduces the

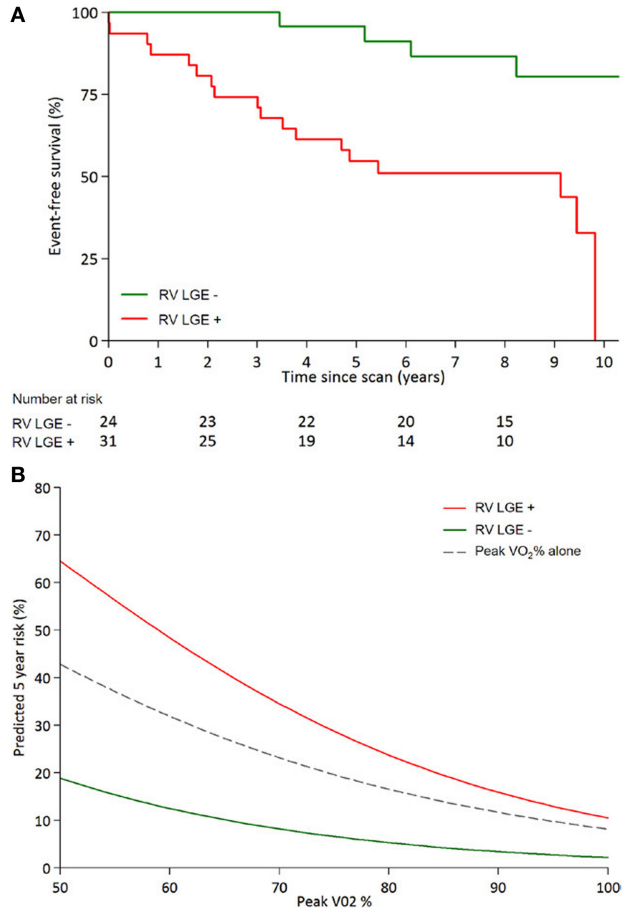

FIGURE 4 | Kaplan–Meier curves adapted from Rydman et al. (A) Event free survival from combined clinical composite end points (arrhythmia, congestive heart failure, transplant, and death) for systemic ventricles post-atrial redirection surgery showing a significant difference between patients with fibrosis [late gadolinium enhancement (LGE)] and without fibrosis (Log-rank $P = 0.001$). **(B)** Fibrosis (LGE) contributes significantly to prediction of 5-year survival when used in conjunction with predicted peak VO_2 (peak VO_2%), compared to peak VO_2 alone (73).

breath-hold time to nine beats; however, this approach is suited best to long-native T1 values rather than the short-post-Gad values.

Saturation Recovery Single-Shot Acquisition (SASHA)

Following an initial acquisition of an image taken with the magnetization vector being in the equilibrium state, a saturation recovery pulse is used multiple times instead of an inversion pulse. At varies times from the application of the saturation pulse (Ts), images are acquired. The signal intensity of the pixels is fitted as a function of the Ts values acquired to calculate the pixel-wise T1 map. The SASHA technique is more accurate at estimating T1 whereas MOLLI and shMOLLI may underestimate T1 with various reasons for their bias; however, SASHA is less precise mainly because it uses of a saturation pulse compared to an inversion pulse leading to reduced "contrast-to-noise" in the fitting process and therefore more random noise in the T1 maps. An advantage is that it is less susceptible to changes in R–R intervals and therefore may perform better in arrhythmias. Some debate continues over the optimum T1-mapping approach for maximum sensitivity to disease (while accuracy of T1 itself is possibly less important except that leads to difficulties in widespread clinical inter-vendor multicentre use), while also having minimal scatter (imprecision) for technical factors: these aspects are to a large extent contradictory in the physics requiring further development for early detection of diffuse fibrosis as no adequate solution seems evident.

There are two main techniques involving T1 mapping: native T1 is a non-contrast technique that detects pathological changes in the myocardium that occur associated with a relative increase in the concentration of water (edema) or increased interstitial space caused by protein deposition (from increased collagen causing fibrosis) or other proteins such as amyloid. The increase in native T1 is not specific to diffuse fibrosis because it occurs also (and somewhat more strongly) in other disease processes such as myocarditis and infarction. The advantage is that it can be used in patients with severe renal failure as it does not involve contrast agent. Crucially, it avoids contrast agent in CHD patients who are likely to require multiple follow-up scans from a young age (91).

ECV Measurements

This requires the application of extracellular GBCA. The volume of the myocardium that is not taken up by cardiomyocytes is the extracellular compartment, which contains the ECM. ECV is not identical to the ECM, which cannot be measured. However, ECV is a surrogate marker that is to some unclear extent sensitive to an abnormal amount of ECM.

ECV is derived by measuring the change in tissue T1-relaxation rate (R1 = 1/T1) and comparing this to the change in blood T1-relaxation rate pre- and postcontrast application, built on several assumptions, also requiring knowledge of the hematocrit (88). The more fibrosis in the extracellular space, the longer the native T1 because from a physics perspective, the average water content of the myocardium is slightly higher with more interstitial fluid (intracellular cytoplasm containing a high concentration of macromolecules). However, on the images postcontrast, there will be more GBCA accumulation in the increased interstitial space of abnormal myocardium, therefore shortening post-gadolinium T1 relative to normal myocardium. The changes in 1/T1 for tissue, when used in the formula to calculate ECV, result in a larger ECV value. In normal subjects, gender-related associations of ECV with age have been demonstrated, with some contradictions (92).

In the absence of edema, the pathological expansion of the ECM is primarily due to the increased proportion of myocardial collagen within the matrix. This fibrotic process leads to mechanical, electrical, and vasomotor dysfunction. Investigators have reported the interstitial disease association with SCD (84, 85, 93). This ECM expansion may have important implications for identifying distinct therapeutic targets.

Clinical Applications of T1 Mapping

Clinical studies reported to date mostly include the systemic LV. The RV is much thinner. For the RV myocardium, unless it is systemic or for some other reason abnormally thickened

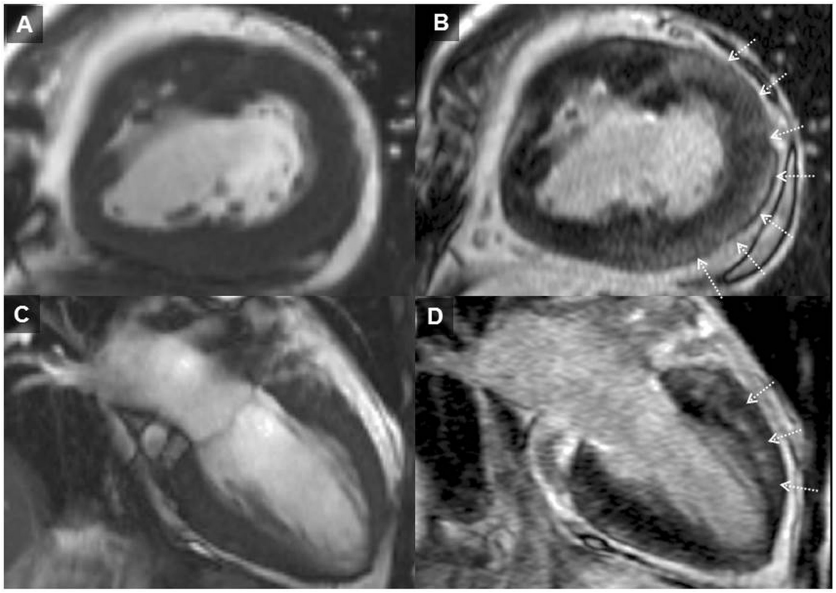

FIGURE 5 | **Cardiovascular magnetic resonance images status post-lateral tunnel total cavopulmonary connection surgery for single-left ventricle (LV) physiology**. **(A)** and **(C)** (2D cine images) compared to **(B)** and **(D)** (LGE images). Arrows represent diffuse appearance late gadolinium enhancement in the free wall of the LV, which is the primary ventricle. This kind of fibrosis pattern in Fontan is one of the several previously described patterns (82).

or immobile, the T1-mapping methods face major technical limitations affecting reliability, such as adjoining fat and blood signals next to the thin trabeculated highly mobile RV wall. Suppression of these corrupting signals is usually associated with some additional unreliability or loss of myocardial data, further complicated by the proximity of sternal wires, and new MRI methods are needed to make RV T1 or ECV clinically reliable (94). The difficulties that are encountered with T1 mapping and ECV become less important in the diagnosis of conditions such as cardiac amyloid and Anderson Fabry's disease where there large abnormalities in the T1 and ECV indices; however, they are affected when this technique is used to detect and monitor subtle changes in diffuse fibrosis.

The presence of interstitial fibrosis has been shown to be of prognostic significance in the general adult cardiology population. In the CHD population, we can speculate that non-invasive detection of interstitial fibrosis may offer better tracking of RV disease than currently utilized volumes and ejection fraction. However, even in those patients with CHD and relatively thicker RV such as systemic RV after atrial redirection surgery, HLHS, ToF, and CHD patients with pulmonary hypertension but extrapolation of current techniques for the LV cannot be assumed.

The only prospective study of T1 mapping and outcomes in tetralogy of Fallot relates to LV ECV in the study by Broberg and colleagues. Approximately 25% of subjects with rToF had elevated LV ECV compared to the control group, of which subjects with LV ECV >30% had significant clinical events (sustained clinically relevant arrhythmia and death) during their follow-up (65). More patients with myocardial fibrosis were identified by LV ECV than with LGE, consistent with other studies (95). LV ECV was abnormal in patients with normal LV ejection fraction suggesting that interstitial fibrosis could precede systolic dysfunction and therefore have a potential role as an early biomarker for myocardial disease (65).

In a different study, 11 patients with a systemic RV had higher ECV, which correlated with elevated end-diastolic volumes and impaired ejection fraction (95). A further study in patients with systemic RV found high ECV measurements in the interventricular septum (the free RV wall could not be reliably studied), which correlated with higher B type natriuretic peptide levels (96).

Several studies have investigated biventricular diffuse fibrosis in ToF subjects using T1 mapping and ECV. However, these were cross-sectional studies with limitations in their methodology, namely, using postcontrast T1 times only due to unavailable hematocrit values (technique not validated to measure diffuse fibrosis in the RV) (97) and limited methods for optimizing MRI sequences or acquisition planes to mitigate challenges of RV imaging (97, 98). High RV ECV was associated with lower RVOT pressure gradient and lower RV mass-to-volume-ratio. LV ECV was found to correlate with arrhythmia, but this category included frequent ventricular systoles (>100 beats or more in 24 h), and the relevance to clinically significant arrhythmia in ToF needs further study (98).

Native T1 times and ECV in LV myocardium were measured in 31 rToF patients and compared to controls. Prolonged cardiopulmonary bypass and aortic cross-clamp time during their previous surgery, biventricular enlargement, and reduced exercise tolerance correlated with higher native T1 times and ECV in the LV (99).

FURTHER CHALLENGES

From the interrogation of the intricate myocardial architecture and its properties, to assessment of regional and global myocardial function, cardiac MRI has proven invaluable in providing data that have several important clinical implications for CHD patients.

The functional assessment of the RV is very important for CHD patients as it is the chamber that is most often affected, yet it is also the chamber that is most challenging to image due to its thin, highly mobile wall, and more complex geometry. The RV wall location may change between cardiac cycles due to intercycle variations in returning venous flow. Imaging of the RV can be further complicated by the proximity of postsurgical sternal wires. These factors make RV imaging an extreme technical challenge for the reliability of conventional cardiac MRI. On the other hand, as the RV is adjacent to the anterior surface coil in cardiac MRI, it can be imaged with high SNR.

A technique that shows potential in the study of the RV is black-blood LGE imaging. LGE imaging with the addition of PSIR is excellent in differentiating myocardial scar from normal myocardium; however, the contrast between subendocardial scar and blood pool on the white-blood images may be reduced and therefore scar may be difficult to identify. Furthermore, differentiation of fibrosis from fat and metallic artifact can be difficult. Black-blood LGE images using an inversion recovery T2 weighted SSFP have been proposed as one possible solution to this (100). Recently, Kellman and colleagues showed good results using this sequence in patients with subendocardial myocardial infarction. They speculated that black-blood LGE sequences may help imaging thin walled fibrous structures (100).

Quantification of diffuse fibrosis with T1 mapping until now has largely been for research interest rather than clinical application. Its clinical value in CHD patients still requires clarification. Technical challenges that lie ahead include the difficulty of mapping the relatively thin-structured RV walls. Furthermore, the potential role for T1 mapping and ECV to help identify and target treatment for "reversible" interstitial disease remains unclear. A study investigated diffuse fibrosis post-aortic valve replacement for aortic stenosis with T1 mapping and found that diffuse fibrosis persistent at 6 months following aortic valve replacements despite normalization of LV-loading conditions and regression of LVH (101), suggesting that interstitial fibrosis may not be a reversible process after all. Second, in the presence of late gadolinium representing scar, the additional prognostic value of diffuse fibrosis measurement remains unclear. If T1 mapping and ECV prognostic capability becomes well established as new biomarkers for CHD, this can open new investigational avenues to develop targeted therapeutic interventions that can retard the fibrotic process.

Cardiac DTI may have potential future use in identifying intrinsic differences in myo-architecture that predates fibrosis associated with remodeling. With further development, cDTI may provide non-invasive means of identifying areas of myocardial disarray as potential substrates (anatomical isthmuses) for arrhythmia propagation, which can help guide electrophysiological therapeutic intervention. Further development, however, is required to improve the spatial resolution of cDTI including to enable it to differentiate myocardial fiber orientation in the relatively thinned walled RV (a chamber commonly of clinical interest in CHD), and therefore its use today is limited to that of a research tool.

AUTHOR CONTRIBUTIONS

SB-N and SG were responsible for the conception and design of the work. SB-N and IV substantially contributed to CMR and CHD content. MG substantially contributed toward CHD content. PG and JK substantially contributed to MRI physics content. PK substantially contributed to the myocardial mechanics and myocardial architecture section. SB-N and SG contributed to the first draft and revisions. All authors contributed to revising the work critically for important intellectual content prior to final approval. The final approval of the manuscript was done by SB-N.

FUNDING

SB-N was supported by an Intermediate Clinical Research Fellowship from the British Heart Foundation (FS/11/38/28864).

REFERENCES

1. Streeter DD, Spotnitz HM, Patel DP, Ross J, Sonnenblick EH. Fiber orientation in the canine left ventricle during diastole and systole. *Circ Res* (1969) 24(3):339–47. doi:10.1161/01.RES.24.3.339
2. Greenbaum RA, Ho SY, Gibson DG, Becker AE, Anderson RH. Left ventricular fibre architecture in man. *Br Heart J* (1981) 45(3):248–63. doi:10.1136/hrt.45.3.248
3. Streeter DD, Bassett DL. An engineering analysis of myocardial fiber orientation in pig's left ventricle in systole. *Anat Rec* (1966) 155(4):503–11. doi:10.1002/ar.1091550403
4. Lev M, Simkins CS. Architecture of the human ventricular myocardium; technic for study using a modification of the Mall-MacCallum method. *Lab Invest* (1956) 5(5):396.
5. LeGrice IJ, Smaill BH, Chai LZ, Edgar SG, Gavin JB, Hunter PJ. Laminar structure of the heart: ventricular myocyte arrangement and connective tissue architecture in the dog. *Am J Physiol* (1995) 269(2): H571–82.
6. LeGrice IJ, Takayama Y, Covell JW. Transverse shear along myocardial cleavage planes provides a mechanism for normal systolic wall thickening. *Circ Res* (1995) 77(1):182–93. doi:10.1161/01.RES.77.1.182
7. Anderson RH, Ho SY, Redmann K, Sanchez-Quintana D, Lunkenheimer PP. The anatomical arrangement of the myocardial cells making up the ventricular mass. *Eur J Cardiothorac Surg* (2005) 28(4):517–25. doi:10.1016/j.ejcts.2005.06.043
8. Sonnenblick EH, Ross J, Covell JW, Spotnitz HM, Spiro D. The ultrastructure of the heart in systole and diastole. *Circ Res* (1967) 21(4):423–31. doi:10.1161/01.RES.21.4.423
9. Costa KD, Takayama Y, McCulloch AD, Covell JW. Laminar fiber architecture and three-dimensional systolic mechanics in canine ventricular myocardium. *Am J Physiol* (1999) 276(2):H595–607.
10. Ferreira PF, Kilner PJ, McGill LA, Nielles-Vallespin S, Scott AD, Ho SY, et al. In vivo cardiovascular magnetic resonance diffusion tensor imaging shows evidence of abnormal myocardial laminar orientations and mobility in hypertrophic cardiomyopathy. *J Cardiovasc Magn Reson* (2014) 16(1):87. doi:10.1186/s12968-014-0087-8

11. Hanley PJ, Young AA, LeGrice IJ, Edgar SG, Loiselle DS. 3-Dimensional configuration of perimysial collagen fibres in rat cardiac muscle at resting and extended sarcomere lengths. *J Physiol* (1999) 517(3):831–7. doi:10.1111/j.1469-7793.1999.0831s.x
12. Babu-Narayan SV, Kilner PJ, Li W, Moon JC, Goktekin O, Davlouros PA, et al. Ventricular fibrosis suggested by cardiovascular magnetic resonance in adults with repaired tetralogy of Fallot and its relationship to adverse markers of clinical outcome. *Circulation* (2006) 113(3):405–13. doi:10.1161/CIRCULATIONAHA.105.548727
13. Sanchez-Quintana D, Anderson RH, Ho SY. Ventricular myoarchitecture in tetralogy of Fallot. *Heart* (1996) 76(3):280–6. doi:10.1136/hrt.76.3.280
14. Carew TE, Covell JW. Fiber orientation in hypertrophied canine left ventricle. *Am J Physiol* (1979) 236(3):H487–93.
15. Redington A, Anderson R, Van Arsdell G. *Congenital Diseases in the Right Heart*. London: Springer (2009).
16. Dell'Italia LJ. The right ventricle: anatomy, physiology, and clinical importance. *Curr Probl Cardiol* (1991) 16(10):658–720. doi:10.1016/0146-2806(91)90009-Y
17. Kitahori K, He H, Kawata M, Cowan DB, Friehs I, Del Nido PJ, et al. Development of left ventricular diastolic dysfunction with preservation of ejection fraction during progression of infant right ventricular hypertrophy. *Circ Heart Fail* (2009) 2:599–607. doi:10.1161/CIRCHEARTFAILURE.109.862664
18. Jones M, Ferrans VJ, Morrow AG, Roberts WC. Ultrastructure of crista supraventricularis muscle in patients with congenital heart diseases associated with right ventricular outflow tract obstruction. *Circulation* (1975) 51(1):39–67. doi:10.1161/01.CIR.51.1.39
19. Hess OM, Schneider J, Koch R, Bamert C, Grimm J, Krayenbuehl HP. Diastolic function and myocardial structure in patients with myocardial hypertrophy. *Circulation* (1981) 63(2):360–71. doi:10.1161/01.CIR.63.2.360
20. Salih C, McCarthy KP, Ho SY. The fibrous matrix of ventricular myocardium in hypoplastic left heart syndrome: a quantitative and qualitative analysis. *Ann Thorac Surg* (2004) 77(1):36–40. doi:10.1016/S0003-4975(03)01472-3
21. Scollan DF, Holmes A, Winslow R, Forder J. Histological validation of myocardial microstructure obtained from diffusion tensor magnetic resonance imaging. *Am J Physiol* (1998) 275(6 Pt 2):H2308–18.
22. Hsu EW, Muzikant AL, Matulevicius SA, Penland RC, Henriquez CS. Magnetic resonance myocardial fiber-orientation mapping with direct histological correlation. *Am J Physiol* (1998) 274(5):H1627–34.
23. McGill LA, Ferreira PF, Scott AD, Nielles-Vallespin S, Giannakidis A, Kilner PJ, et al. Relationship between cardiac diffusion tensor imaging parameters and anthropometrics in healthy volunteers. *J Cardiovasc Magn Reson* (2016) 18(1):2. doi:10.1186/s12968-015-0215-0
24. Nielles-Vallespin S, Khalique Z, Ferreira PF, de Silva R, Scott AD, Kilner P, et al. Assessment of myocardial microstructural dynamics by in vivo diffusion tensor cardiac magnetic resonance. *J Am Coll Cardiol* (2017) 69(6):661–76. doi:10.1016/j.jacc.2016.11.051
25. Tseng WY, Dou J, Reese TG, Wedeen VJ. Imaging myocardial fiber disarray and intramural strain hypokinesis in hypertrophic cardiomyopathy with MRI. *J Magn Reson Imaging* (2006) 23(1):1–8. doi:10.1002/jmri.20473
26. Wu MT, Tseng WY, Su MY, Liu CP, Chiou KR, Wedeen VJ, et al. Diffusion tensor magnetic resonance imaging mapping the fiber architecture remodeling in human myocardium after infarction. *Circulation* (2006) 114(10):1036–45. doi:10.1161/CIRCULATIONAHA.105.545863
27. Grothues F, Smith GC, Moon JC, Bellenger NG, Collins P, Klein HU, et al. Comparison of interstudy reproducibility of cardiovascular magnetic resonance with two-dimensional echocardiography in normal subjects and in patients with heart failure or left ventricular hypertrophy. *Am J Cardiol* (2002) 90(1):29–34. doi:10.1016/S0002-9149(02)02381-0
28. Grothues F, Moon JC, Bellenger NG, Smith GS, Klein HU, Pennell DJ. Interstudy reproducibility of right ventricular volumes, function, and mass with cardiovascular magnetic resonance. *Am Heart J* (2004) 147(2):218–23. doi:10.1016/j.ahj.2003.10.005
29. Han F, Rapacchi S, Khan S, Ayad I, Salusky I, Gabriel S, et al. Four-dimensional, multiphase, steady-state imaging with contrast enhancement (MUSIC) in the heart: a feasibility study in children. *Magn Reson Med* (2015) 74(4):1042–9. doi:10.1002/mrm.25491
30. Shehata ML, Cheng S, Osman NF, Bluemke DA, Lima JA. Myocardial tissue tagging with cardiovascular magnetic resonance. *J Cardiovasc Magn Reson* (2009) 11(1):55. doi:10.1186/1532-429X-11-55
31. Aletras AH, Ding S, Balaban RS, Wen H. DENSE: displacement encoding with stimulated echoes in cardiac functional MRI. *J Magn Reson* (1999) 137(1):247–52. doi:10.1006/jmre.1998.1676
32. Maret E, Todt T, Brudin L, Nylander E, Swahn E, Ohlsson JL, et al. Functional measurements based on feature tracking of cine magnetic resonance images identify left ventricular segments with myocardial scar. *Cardiovasc Ultrasound* (2009) 7(1):53. doi:10.1186/1476-7120-7-53
33. Kim D, Gilson WD, Kramer CM, Epstein FH. Myocardial tissue tracking with two-dimensional cine displacement-encoded MR imaging: development and initial evaluation 1. *Radiology* (2004) 230(3):862–71. doi:10.1148/radiol.2303021213
34. Simpson RM, Keegan J, Firmin DN. MR assessment of regional myocardial mechanics. *J Magn Reson Imaging* (2013) 37(3):576–99. doi:10.1002/jmri.23756
35. Zhong X, Spottiswoode BS, Meyer CH, Kramer CM, Epstein FH. Imaging three-dimensional myocardial mechanics using navigator-gated volumetric spiral cine DENSE MRI. *Magn Reson Med* (2010) 64(4):1089–97. doi:10.1002/mrm.22503
36. Chen X, Yang Y, Cai X, Auger DA, Meyer CH, Salerno M, et al. Accelerated two-dimensional cine DENSE cardiovascular magnetic resonance using compressed sensing and parallel imaging. *J Cardiovasc Magn Reson* (2016) 18(1):38. doi:10.1186/s12968-016-0253-2
37. Schuster A, Kutty S, Padiyath A, Parish V, Gribben P, Danford DA, et al. Cardiovascular magnetic resonance myocardial feature tracking detects quantitative wall motion during dobutamine stress. *J Cardiovasc Magn Reson* (2011) 13(1):58. doi:10.1186/1532-429X-13-58
38. Pedrizzetti G, Claus P, Kilner PJ, Nagel E. Principles of cardiovascular magnetic resonance feature tracking and echocardiographic speckle tracking for informed clinical use. *J Cardiovasc Magn Reson* (2016) 18(1):51. doi:10.1186/s12968-016-0269-7
39. Augustine D, Lewandowski AJ, Lazdam M, Rai A, Francis J, Myerson S, et al. Global and regional left ventricular myocardial deformation measures by magnetic resonance feature tracking in healthy volunteers: comparison with tagging and relevance of gender. *J Cardiovasc Magn Reson* (2013) 15(1):8. doi:10.1186/1532-429X-15-8
40. Schneeweis C, Lapinskas T, Schnackenburg B, Berger A, Hucko T, Kelle S, et al. Comparison of myocardial tagging and feature tracking in patients with severe aortic stenosis. *J Cardiovasc Magn Reson* (2013) 15(S1):100. doi:10.1186/1532-429X-15-S1-P100
41. Hor KN, Gottliebson WM, Carson C, Wash E, Cnota J, Fleck R, et al. Comparison of magnetic resonance feature tracking for strain calculation with harmonic phase imaging analysis. *JACC Cardiovasc Imaging* (2010) 3(2):144–51. doi:10.1016/j.jcmg.2009.11.006
42. Khan JN, Singh A, Nazir SA, Kanagala P, Gershlick AH, McCann GP. Comparison of cardiovascular magnetic resonance feature tracking and tagging for the assessment of left ventricular systolic strain in acute myocardial infarction. *Eur J Radiol* (2015) 84(5):840–8. doi:10.1016/j.ejrad.2015.02.002
43. Moon TJ, Choueiter N, Geva T, Valente AM, Gauvreau K, Harrild DM. Relation of biventricular strain and dyssynchrony in repaired tetralogy of Fallot measured by cardiac magnetic resonance to death and sustained ventricular tachycardia. *Am J Cardiol* (2015) 115(5):676–80. doi:10.1016/j.amjcard.2014.12.024
44. Orwat S, Diller GP, Kempny A, Radke R, Peters B, Kühne T, et al. Myocardial deformation parameters predict outcome in patients with repaired tetralogy of Fallot. *Heart* (2016) 102(3):209–15. doi:10.1136/heartjnl-2015-308569
45. Jing L, Wehner GJ, Suever JD, Charnigo RJ, Alhadad S, Stearns E, et al. Left and right ventricular dyssynchrony and strains from cardiovascular magnetic resonance feature tracking do not predict deterioration of ventricular function in patients with repaired tetralogy of Fallot. *J Cardiovasc Magn Reson* (2016) 18(1):49. doi:10.1186/s12968-016-0268-8
46. Voges I, Fischer G, Scheewe J, Schumacher M, Babu-Narayan SV, Jung O, et al. Restrictive enlargement of the pulmonary annulus at surgical repair of tetralogy of Fallot: 10-year experience with a uniform surgical strategy. *Eur J Cardiothorac Surg* (2008) 34(5):1041–5. doi:10.1016/j.ejcts.2008.07.048

47. Latus H, Hachmann P, Gummel K, Khalil M, Yerebakan C, Bauer J, et al. Impact of residual right ventricular outflow tract obstruction on biventricular strain and synchrony in patients after repair of tetralogy of Fallot: a cardiac magnetic resonance feature tracking study. *Eur J Cardiothorac Surg* (2015) 48:83–90. doi:10.1093/ejcts/ezu396
48. Tutarel O, Orwat S, Radke RM, Westhoff-Bleck M, Vossler C, Schülke C, et al. Assessment of myocardial function using MRI-based feature tracking in adults after atrial repair of transposition of the great arteries: reference values and clinical utility. *Int J Cardiol* (2016) 220:246–50. doi:10.1016/j.ijcard.2016.06.108
49. Thattaliyath BD, Forsha DE, Stewart C, Barker PC, Campbell MJ. Evaluation of right ventricular myocardial mechanics using velocity vector imaging of cardiac MRI cine images in transposition of the great arteries following atrial and arterial switch operations. *Congenit Heart Dis* (2015) 10(4):371–9. doi:10.1111/chd.12250
50. Schmidt R, Orwat S, Kempny A, Schuler P, Radke R, Kahr PC, et al. Value of speckle-tracking echocardiography and MRI-based feature tracking analysis in adult patients after Fontan-type palliation. *Congenit Heart Dis* (2014) 9(5):397–406. doi:10.1111/chd.12156
51. Davlouros PA, Kilner PJ, Hornung TS, Li W, Francis JM, Moon JC, et al. Right ventricular function in adults with repaired tetralogy of Fallot assessed with cardiovascular magnetic resonance imaging: detrimental role of right ventricular outflow aneurysms or akinesia and adverse right-to-left ventricular interaction. *J Am Coll Cardiol* (2002) 40(11):2044–52. doi:10.1016/S0735-1097(02)02566-4
52. Wald RM, Haber I, Wald R, Valente AM, Powell AJ, Geva T. Effects of regional dysfunction and late gadolinium enhancement on global right ventricular function and exercise capacity in patients with repaired tetralogy of Fallot. *Circulation* (2009) 119(10):1370–7. doi:10.1161/CIRCULATIONAHA.108.816546
53. Uebing A, Gibson DG, Babu-Narayan SV, Diller GP, Dimopoulos K, Goktekin O, et al. Right ventricular mechanics and QRS duration in patients with repaired tetralogy of Fallot. *Circulation* (2007) 116(14):1532–9. doi:10.1161/CIRCULATIONAHA.107.688770
54. Bonello B, Kempny A, Uebing A, Li W, Kilner PJ, Diller GP, et al. Right atrial area and right ventricular outflow tract akinetic length predict sustained tachyarrhythmia in repaired tetralogy of Fallot. *Int J Cardiol* (2013) 168(4):3280–6. doi:10.1016/j.ijcard.2013.04.048
55. Geva T. Repaired tetralogy of Fallot: the roles of cardiovascular magnetic resonance in evaluating pathophysiology and for pulmonary valve replacement decision support. *J Cardiovasc Magn Reson* (2011) 13(1):9. doi:10.1186/1532-429X-13-9
56. Heng EL, Gatzoulis MA, Smith GC, Shore DF, Sethia B, Uemura H, et al. *Early Cardiac Remodelling Post-Pulmonary Valve Replacement in Patients with Repaired Tetralogy of Fallot*. London: Congress of the European-Society-of-Cardiology (ESC) (2015). p. 357–8.
57. Cavalcanti PE, Sá MP, Santos CA, Esmeraldo IM, de Escobar RR, de Menezes AM, et al. Pulmonary valve replacement after operative repair of tetralogy of Fallot: meta-analysis and meta-regression of 3,118 patients from 48 studies. *J Am Coll Cardiol* (2013) 62(23):2227–43. doi:10.1016/j.jacc.2013.04.107
58. Diller GP, Kempny A, Liodakis E, Alonso-Gonzalez R, Inuzuka R, Uebing A, et al. Left ventricular longitudinal function predicts life-threatening ventricular arrhythmia and death in adults with repaired tetralogy of Fallot. *Circulation* (2012) 125(20):2440–6. doi:10.1161/CIRCULATIONAHA.111.086983
59. Valente AM, Gauvreau K, Assenza GE, Babu-Narayan SV, Schreier J, Gatzoulis MA, et al. Contemporary predictors of death and sustained ventricular tachycardia in patients with repaired tetralogy of Fallot enrolled in the INDICATOR cohort. *Heart* (2013) 100(3):247–53. doi:10.1136/heartjnl-2013-304958
60. Jensen AS, Broberg CS, Rydman R, Diller GP, Li W, Dimopoulos K, et al. Impaired right, left, or biventricular function and resting oxygen saturation are associated with mortality in Eisenmenger syndrome: a clinical and cardiovascular magnetic resonance study. *Circ Cardiovasc Imaging* (2015) 8(12):e003596. doi:10.1161/CIRCIMAGING.115.003596
61. Vassiliou VS, Perperoglou A, Raphael CE, Joshi S, Malley T, Everett R, et al. Midwall fibrosis and 5-year outcome in moderate and severe aortic stenosis. *J Am Coll Cardiol* (2017) 69(13):1755–6. doi:10.1016/j.jacc.2017.01.034
62. Halliday B, Gulati A, Ali A, Guha K, Newsome SJ, Arzanauskaite M, et al. Association between mid-wall late gadolinium enhancement and sudden cardiac death in patients with dilated cardiomyopathy and mild and moderate left ventricular systolic dysfunction. *Circulation* (2017) 116: I-157–64. doi:10.1161/CIRCULATIONAHA.116.026910
63. Collins J, Sommerville C, Magrath P, Spottiswoode B, Freed BH, Benzuly KH, et al. Extracellular volume fraction is more closely associated with altered regional left ventricular velocities than left ventricular ejection fraction in nonischemic cardiomyopathy. *Circ Cardiovasc Imaging* (2015) 8(1):e001998. doi:10.1161/CIRCIMAGING.114.001998
64. Jerosch-Herold M, Sheridan DC, Kushner JD, Nauman D, Burgess D, Dutton D, et al. Cardiac magnetic resonance imaging of myocardial contrast uptake and blood flow in patients affected with idiopathic or familial dilated cardiomyopathy. *Am J Physiol Heart Circ Physiol* (2008) 295(3):H1234–42. doi:10.1152/ajpheart.00429.2008
65. Broberg CS, Chugh SS, Conklin C, Sahn DJ, Jerosch-Herold M. Quantification of diffuse myocardial fibrosis and its association with myocardial dysfunction in congenital heart disease. *Circ Cardiovasc Imaging* (2010) 3(6):727–34. doi:10.1161/CIRCIMAGING.108.842096
66. Babu-Narayan SV. The role of late gadolinium enhancement cardiovascular magnetic resonance in the assessment of congenital and acquired heart disease. *Prog Pediatr Cardiol* (2010) 28(1):11–9. doi:10.1016/j.ppedcard.2009.10.006
67. Kellman P, Arai AE. Cardiac imaging techniques for physicians: late enhancement. *J Magn Reson Imaging* (2012) 36(3):529–42. doi:10.1002/jmri.23605
68. Xue H, Greiser A, Zuehlsdorff S, Jolly MP, Guehring J, Arai AE, et al. Phase-sensitive inversion recovery for myocardial T1 mapping with motion correction and parametric fitting. *Magn Reson Med* (2013) 69(5):1408–20. doi:10.1002/mrm.24385
69. Bratis K, Henningsson M, Grigoratos C, Omodarme MD, Chasapides K, Botnar R, et al. Clinical evaluation of three-dimensional late enhancement MRI. *J Magn Reson Imaging* (2016). doi:10.1002/jmri.25512
70. Tsai SF, Chan DP, Ro PS, Boettner B, Daniels CJ. Rate of inducible ventricular arrhythmia in adults with congenital heart disease. *Am J Cardiol* (2010) 106(5):730–6. doi:10.1016/j.amjcard.2010.04.036
71. Park SJ, On YK, Kim JS, Park SW, Yang JH, Jun TG, et al. Relation of fragmented QRS complex to right ventricular fibrosis detected by late gadolinium enhancement cardiac magnetic resonance in adults with repaired tetralogy of Fallot. *Am J Cardiol* (2012) 109(1):110–5. doi:10.1016/j.amjcard.2011.07.070
72. Munkhammar P, Carlsson M, Arheden H, Pesonen E. Restrictive right ventricular physiology after tetralogy of Fallot repair is associated with fibrosis of the right ventricular outflow tract visualized on cardiac magnetic resonance imaging. *Eur Heart J Cardiovasc Imaging* (2013) 14(10):978–85. doi:10.1093/ehjci/jet009
73. Rydman R, Gatzoulis MA, Ho SY, Ernst S, Swan L, Li W, et al. Systemic right ventricular fibrosis detected by cardiovascular magnetic resonance is associated with clinical outcome, mainly new-onset atrial arrhythmia, in patients after atrial redirection surgery for transposition of the great arteries. *Circ Cardiovasc Imaging* (2015) 8(5):e002628. doi:10.1161/CIRCIMAGING.114.002628
74. Babu-Narayan SV, Prati D, Rydman R, Dimopoulos K, Diller GP, Uebing A, et al. Dyssynchrony and electromechanical delay are associated with focal fibrosis in the systemic right ventricle – insights from echocardiography. *Int J Cardiol* (2016) 220:382–8. doi:10.1016/j.ijcard.2016.06.090
75. Giardini A, Lovato L, Donti A, Formigari R, Oppido G, Gargiulo G, et al. Relation between right ventricular structural alterations and markers of adverse clinical outcome in adults with systemic right ventricle and either congenital complete (after Senning operation) or congenitally corrected transposition of the great arteries. *Am J Cardiol* (2006) 98(9):1277–82. doi:10.1016/j.amjcard.2006.05.062
76. Babu-Narayan SV, Goktekin O, Moon JC, Broberg CS, Pantely GA, Pennell DJ, et al. Late gadolinium enhancement cardiovascular magnetic 24 resonance of the systemic right ventricle in adults with previous atrial redirection 25 surgery for transposition of the great arteries. *Circulation* (2005) 111(16):2091–8. doi:10.1161/01.CIR.0000162463.61626.3B
77. Shepard CW, Germanakis I, White MT, Powell AJ, Co-Vu J, Geva T. Cardiovascular magnetic resonance findings late after the arterial switch operation. *Circ Cardiovasc Imaging* (2016) 9(9):e004618. doi:10.1161/CIRCIMAGING.116.004618
78. Tobler D, Motwani M, Wald RM, Roche SL, Verocai F, Iwanochko RM, et al. Evaluation of a comprehensive cardiovascular magnetic resonance protocol in young adults late after the arterial switch operation for d-transposition

of the great arteries. *J Cardiovasc Magn Reson* (2014) 16(1):98. doi:10.1186/s12968-014-0098-5
79. d'Udekem Y, Iyengar AJ, Cochrane AD, Grigg LE, Ramsay JM, Wheaton GR, et al. The Fontan procedure: contemporary techniques have improved long-term outcomes. *Circulation* (2007) 116(11 Suppl):I157–64. doi:10.1161/CIRCULATIONAHA.106.676445
80. Newburger JW, Sleeper LA, Frommelt PC, Pearson GD, Mahle WT, Chen S, et al. Transplant-free survival and interventions at 3 years in the single ventricle reconstruction trial. *Circulation* (2014) 129(20):2013–20. doi:10.1161/CIRCULATIONAHA.113.006191
81. Rathod RH, Prakash A, Kim YY, Germanakis IE, Powell AJ, Gauvreau K, et al. Cardiac magnetic resonance parameters predict transplant-free survival in Fontan patients. *Circ Cardiovasc Imaging* (2014) 7(3):502–9. doi:10.1161/CIRCIMAGING.113.001473
82. Rathod RH, Prakash A, Powell AJ, Geva T. Myocardial fibrosis identified by cardiac magnetic resonance late gadolinium enhancement is associated with adverse ventricular mechanics and ventricular tachycardia late after Fontan operation. *J Am Coll Cardiol* (2010) 55(16):1721–8. doi:10.1016/j.jacc.2009.12.036
83. Broberg CS, Prasad SK, Carr C, Babu-Narayan SV, Dimopoulos K, Gatzoulis MA. Myocardial fibrosis in Eisenmenger syndrome: a descriptive cohort study exploring associations of late gadolinium enhancement with clinical status and survival. *J Cardiovasc Magn Reson* (2014) 16(1):32. doi:10.1186/1532-429X-16-32
84. Puntmann VO, Voigt T, Chen Z, Mayr M, Karim R, Rhode K, et al. Native T1 mapping in differentiation of normal myocardium from diffuse disease in hypertrophic and dilated cardiomyopathy. *JACC Cardiovasc Imaging* (2013) 6(4):475–84. doi:10.1016/j.jcmg.2012.08.019
85. Puntmann VO, Carr-White G, Jabbour A, Yu CY, Gebker R, Kelle S, et al. T1-mapping and outcome in nonischemic cardiomyopathy: all-cause mortality and heart failure. *JACC Cardiovasc Imaging* (2016) 9(1):40–50. doi:10.1016/j.jcmg.2015.12.001
86. Taylor AJ, Salerno M, Dharmakumar R, Jerosch-Herold M. T1 mapping: basic techniques and clinical applications. *JACC Cardiovasc Imaging* (2016) 9(1):67–81. doi:10.1016/j.jcmg.2015.11.005
87. Haaf P, Garg P, Messroghli DR, Broadbent DA, Greenwood JP, Plein S. Cardiac T1 mapping and extracellular volume (ECV) in clinical practice: a comprehensive review. *J Cardiovasc Magn Reson* (2016) 18(1):89. doi:10.1186/s12968-016-0308-4
88. Messroghli DR, Radjenovic A, Kozerke S, Higgins DM, Sivananthan MU, Ridgway JP. Modified look-locker inversion recovery (MOLLI) for high-resolution T1 mapping of the heart. *Magn Reson Med* (2004) 52(1):141–6. doi:10.1002/mrm.20110
89. Kellman P, Hansen MS. T1-mapping in the heart: accuracy and precision. *J Cardiovasc Magn Reson* (2014) 16(1):2. doi:10.1186/1532-429X-16-2
90. Piechnik SK, Ferreira VM, Dall'Armellina E, Cochlin LE, Greiser A, Neubauer S, et al. Shortened modified look-locker inversion recovery (ShMOLLI) for clinical myocardial T1-mapping at 1.5 and 3 T within a 9 heartbeat breathhold. *J Cardiovasc Magn Reson* (2010) 12(1):69. doi:10.1186/1532-429X-12-69
91. McDonald RJ, McDonald JS, Kallmes DF, Jentoft ME, Murray DL, Thielen KR, et al. Intracranial gadolinium deposition after contrast-enhanced MR imaging. *Radiology* (2015) 275(3):772–82. doi:10.1148/radiol.15150025
92. Moon JC, Messroghli DR, Kellman P, Piechnik SK, Robson MD, Ugander M, et al. Myocardial T1 mapping and extracellular volume quantification: a Society for Cardiovascular Magnetic Resonance (SCMR) and CMR Working Group of the European Society of Cardiology consensus statement. *J Cardiovasc Magn Reson* (2013) 15(1):92. doi:10.1186/1532-429X-15-92
93. Schelbert EB, Piehler KM, Zareba KM, Moon JC, Ugander M, Messroghli DR, et al. Myocardial fibrosis quantified by extracellular volume is associated with subsequent hospitalization for heart failure, death, or both across the spectrum of ejection fraction and heart failure stage. *J Am Heart Assoc* (2015) 4(12):e002613. doi:10.1161/JAHA.115.002613
94. Mehta BB, Auger DA, Gonzalez JA, Workman V, Chen X, Chow K, et al. Detection of elevated right ventricular extracellular volume in pulmonary hypertension using accelerated and navigator-gated look-locker imaging for cardiac T1 estimation (ANGIE) cardiovascular magnetic resonance. *J Cardiovas Magn Reson* (2015) 17(1):110. doi:10.1186/s12968-015-0209-y
95. Broberg CS, Aboulhosn J, Mongeon FP, Kay J, Valente AM, Khairy P, et al. Prevalence of left ventricular systolic dysfunction in adults with repaired tetralogy of Fallot. *Am J Cardiol* (2011) 107(8):1215–20. doi:10.1016/j.amjcard.2010.12.026
96. Plymen CM, Sado DM, Taylor AM, Bolger AP, Lambiase PD, Hughes M, et al. Diffuse myocardial fibrosis in the systemic right ventricle of patients late after Mustard or Senning surgery: an equilibrium contrast cardiovascular magnetic resonance study. *Eur Heart J Cardiovasc Imaging* (2013) 14(10):963–8. doi:10.1093/ehjci/jet014
97. Kozak MF, Redington A, Yoo SJ, Seed M, Greiser A, Grosse-Wortmann L. Diffuse myocardial fibrosis following tetralogy of Fallot repair: a T1 mapping cardiac magnetic resonance study. *Pediatr Radiol* (2014) 44(4):403–9. doi:10.1007/s00247-013-2840-9
98. Chen CA, Dusenbery SM, Valente AM, Powell AJ, Geva T. Myocardial ECV fraction assessed by CMR is associated with type of hemodynamic load and arrhythmia in repaired tetralogy of Fallot. *JACC Cardiovasc Imaging* (2016) 9(1):1–0. doi:10.1016/j.jacc.2016.03.009
99. Riesenkampff E, Luining W, Seed M, Chungsomprasong P, Manlhiot C, Elders B, et al. Increased left ventricular myocardial extracellular volume is associated with longer cardiopulmonary bypass times, biventricular enlargement and reduced exercise tolerance in children after repair of tetralogy of Fallot. *J Cardiovasc Magn Reson* (2016) 18(1):75. doi:10.1186/1532-429X-18-S1-Q25
100. Kellman P, Xue H, Olivieri LJ, Cross RR, Grant EK, Fontana M, et al. Dark blood late enhancement imaging. *J Cardiovasc Magn Reson* (2016) 18(1):77. doi:10.1186/1532-429X-18-S1-P211
101. Flett AS, Sado DM, Quarta G, Mirabel M, Pellerin D, Herrey AS, et al. Diffuse myocardial fibrosis in severe aortic stenosis: an equilibrium contrast cardiovascular magnetic resonance study. *Eur Heart J Cardiovasc Imaging* (2012) 13:819–26. doi:10.1093/ehjci/jes102

Conflict of Interest Statement: The authors declare that the research was conducted in the absence of any commercial or financial relationships that could be construed as a potential conflict of interest.

frontiers in Cardiovascular Medicine

ORIGINAL RESEARCH
published: 28 April 2017
doi: 10.3389/fcvm.2017.00021

Impact of Isolated Tricuspid Valve Repair on Right Ventricular Remodelling in an Adult Congenital Heart Disease Population

Roberto Marsico[1], Vito Domenico Bruno[1], Pierpaolo Chivasso[1], Anna Baritussio[2], Filippo Rapetto[1], Gustavo A. Guida[1], Umberto Benedetto[1] and Massimo Caputo[1]*

[1] School of Clinical Sciences, Bristol Heart Institute, University of Bristol, Bristol, UK, [2] Cardiovascular Magnetic Resonance Unit, NIHR Bristol Cardiovascular Biomedical Research Unit, Bristol Heart Institute, University of Bristol, Bristol, UK

Background: Surgical repair of isolated congenital tricuspid valve (TV) disease is rare with no well-defined indication and outcomes. Moreover, the role of right ventricle (RV) in this context has not yet been investigated.

Objectives: We sought to assess the impact of congenital TV repair on cardiac remodelling and clinical–functional status and the importance of the RV function in an adult congenital heart disease (ACHD) population.

Methods and results: From January 2005 to December 2015, 304 patients underwent TV surgery in our centre. Of these, 27 (ACHD) patients had isolated TV repair. Patients were evaluated with preoperative and postoperative transthoracic echocardiogram. Survival rate has been investigated with a mean clinical follow-up (FU) of 3.7 ± 2.3 years, whereas the mean echocardiographic FU was 2.9 ± 1.8 years. The clinical and functional status of patients showed a statistically significant improvement after the surgical repair in terms of New York Heart Association class (66.7 vs 7.4%; $p < 0.01$), clinical signs of heart failure (29.6 vs 7.4%; $p < 0.01$), and left ventricular function (14.8 vs 7.4%; $p < 0.01$). The RV and right atrium diameter were significantly reduced after surgery (5.15 ± 1.21 vs 4.32 ± 1.16; $p < 0.01$) and (44.7 ± 16.7 vs 26.7 ± 9.2; $p < 0.01$), respectively. The degree of postoperative pulmonary hypertension was also significantly reduced (40.7 vs 7.4%; $p < 0.01$). The survival rate was 96.3% at 1 year and 93.7% at 5 years. One patient (3.7%) had early failure of the tricuspid repair requiring a reoperation.

Conclusion: Isolated TV repair for adult congenital disease significantly improved patients' clinical and functional status and allowed right ventricular remodelling and functional improvement.

Keywords: tricuspid valve repair, adult congenital heart disease, echocardiography, right ventricular dysfunction, ventricular reverse remodelling

OPEN ACCESS

Edited by:
Adelaide De Vecchi, King's College London, UK

Reviewed by:
Yasuhiro Fujii, Okayama University, Japan
Vladimiro Vida, University of Padua, Italy

****Correspondence:***
Roberto Marsico
Roberto.Marsico@UHBristol.nhs.uk

Specialty section:
This article was submitted to Pediatric Cardiology, a section of the journal Frontiers in Cardiovascular Medicine

Received: *30 November 2016*
Accepted: *27 March 2017*
Published: *28 April 2017*

Citation:
Marsico R, Bruno VD, Chivasso P, Baritussio A, Rapetto F, Guida GA, Benedetto U and Caputo M (2017) Impact of Isolated Tricuspid Valve Repair on Right Ventricular Remodelling in an Adult Congenital Heart Disease Population. Front. Cardiovasc. Med. 4:21. doi: 10.3389/fcvm.2017.00021

INTRODUCTION

Isolated severe congenital tricuspid regurgitation (TR) is an uncommon condition, most frequently associated with a variety of concomitant heart diseases. Regardless of the presentation, the surgical management is similar (1, 2). To date, a limited body of evidence is available on the outcomes of this subset of patients, and the published surgical guidelines are not clear in terms of surgical procedure and timing for surgery (3, 4). Furthermore, the negative impact of TR on long-term prognosis has

been largely demonstrated (5), and it has been advocated that surgery should be considered before the development of right ventricle (RV) systolic dysfunction (6); in fact, these patients frequently have evidence of right heart failure and its concomitant complications (7). Patients are rarely referred for isolated surgical tricuspid valve (TV) repair, and most repairs are done in the context of other planned cardiac operations (4). In this study, we sought to assess the impact of isolated TV repair on cardiac remodelling and clinical–functional status, and specifically its effect on the RV function in an adult congenital heart disease (ACHD) population.

MATERIALS AND METHODS

The study was conducted in accordance with the principles of the Declaration of Helsinki. The local audit committee approved the study, and the requirement for individual patient consent was waived.

From January 2005 to December 2015, a total of 304 adult patients underwent TV repair or replacement at Bristol Heart Institute. Patients with concomitant left heart valve diseases and/or other cardiac congenital diseases, those who underwent TV replacement and those with endocarditis were excluded (**Figure 1**) from our analysis. Of these, 179 (58.8%) had a functional TR secondary to left heart valve failure (mitral regurgitation and/or aortic valve disease); 29 (9.5%) patients had TR associated with pulmonary valve dysfunction; 28 patients (9.2%) had isolated TV regurgitation secondary to endocarditis. Forty-one patients (13.5%) had TV replacement with prosthesis.

The remaining 27 (8.8%) were defined as ACHD patients undergoing surgical TV repair for isolated TR.

Clinical and Functional Assessment

The clinical conditions were assessed following the classification proposed by the New York Heart Association (NYHA) and Canadian Cardiovascular Society (CCS). Both preoperatively and at the end of follow-up (FU), patients were assigned to a correlated class. Clinical signs and symptoms of RV failure and onset of newly discovered cardiac arrhythmias were regularly assessed during FU outpatient clinics. Short-term outcomes were derived from clinical notes: acute kidney injury was defined as an increase, during admission, of over 50% in serum creatinine compared to preoperative values, as previously recommended (8); acute renal failure was defined as the need for perioperative kidney replacement therapy. Cerebrovascular accident (CVA) was defined on the basis of a focal or global neurological impairment at physical examination or at CT scan/magnetic resonance imaging. Deep wound infection was defined as a surgical site-related infection affecting the median sternotomy wound and requiring antibiotics and/or surgical re-exploration. Short- and long-term survival data

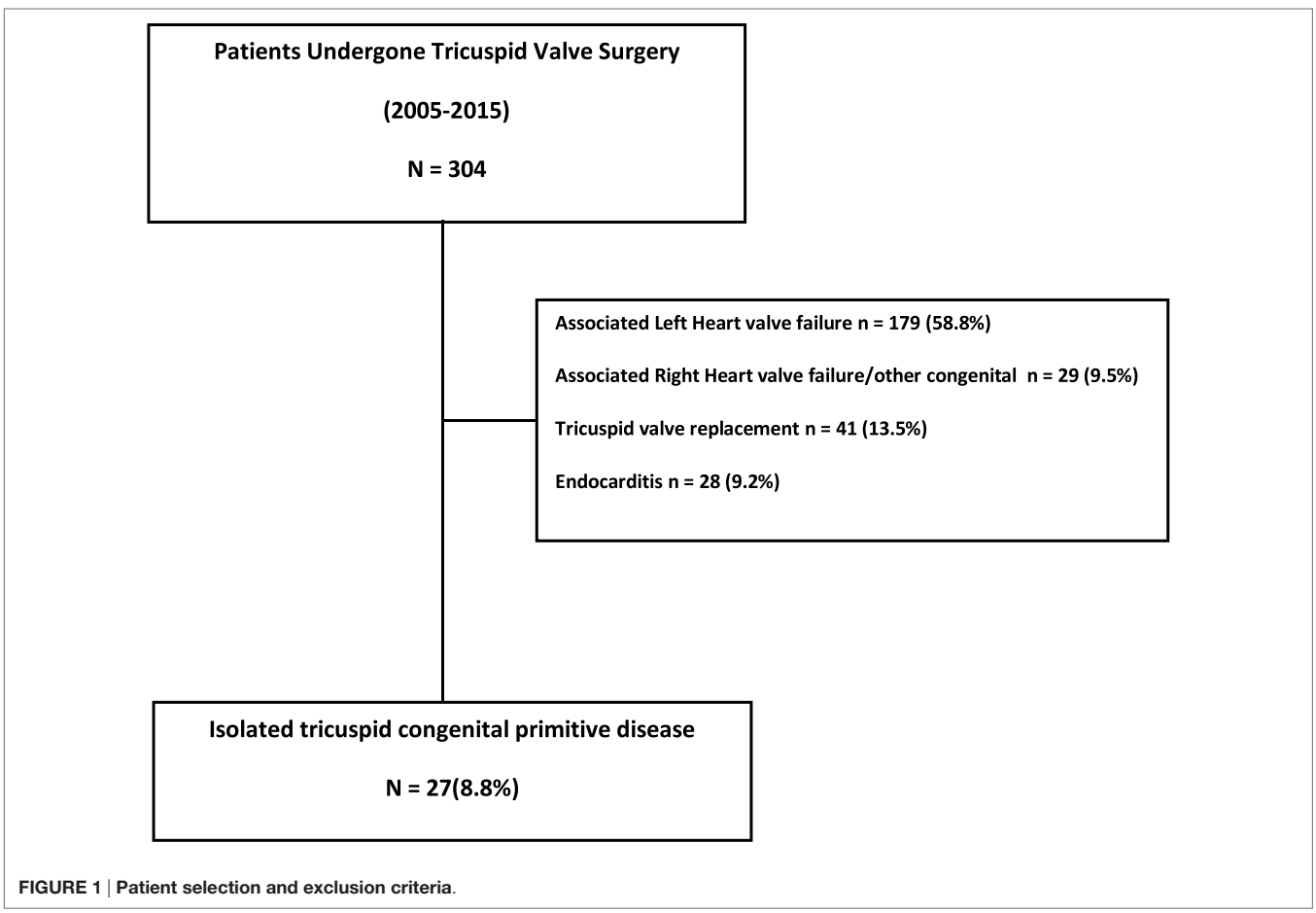

FIGURE 1 | **Patient selection and exclusion criteria**.

have been collected from the National Institute for Cardiovascular Outcome Research. The 30-day mortality was defined as death from any cause during the first 30 days following surgery.

Echocardiographic Evaluation

All patients underwent transthoracic echocardiography preoperatively, within 2 weeks after the operation and at FU. The following parameters were assessed: left ventricular ejection fraction (LVEF), left ventricular internal diastolic diameter, left ventricular internal systolic diameter, thickness of the interventricular septum in diastole, diameter of the posterior wall, RV functional assessment (RV failure), right ventricular internal diastolic diameter, right ventricle dilatation (RV dilatation), area of left atrium (LA area), area of right atrium (RA area), pulmonary artery pressure (PAP), grade of pulmonary hypertension, grade of TV regurgitation, tricuspid annular plane systolic excursion (tapse), and presence of haepatic veins backflow.

Statistical Analysis

Data are presented as mean ± 1 SD for continuous variables or as number and percentages for dichotomous variables. Continuous variables were tested for normality using the Kolmogorov–Smirnov test and then compared between groups with unpaired Student's *t*-test if normally distributed or Mann–Whitney *U* test if not normally distributed. In the case of dichotomous or categorical variables, Pearson chi-square or Fisher exact tests were used as appropriate. Overall long-term survival was estimated by Kaplan–Meier curve. All tests were two-sided with the alpha level set at 0.05 for statistical significance. The statistical analysis was computed using R version 3.0.2 for Windows (R Foundation for Statistical Computing, Vienna, Austria).

RESULTS

Patient characteristics and preoperative variables are summarised in **Table 1**. Mean age was 51.62 ± 14.4 years (range 17–73 years) and 18 patients (66.7%) were female. The mean clinical FU was 3.7 ± 2.3 years, while the mean echocardiographic FU time was 2.9 ± 1.8 years. **Table 2** shows the AHDC population including the TV aetiopathology for each patient. Ebstein anomaly was diagnosed in 14 (51.8%) patients, whereas the remaining 13 patients (48.1%) were affected by non-Ebstein tricuspid dysplasia. Thirteen patients (48.1%) had right ventricular failure at the time of surgery and 22 (81.4%) had dilated RV. Four patients were found to have reduced left ventricular function (14.7%). Of our cohort of patients, 33.3% were diagnosed with preoperative atrial fibrillation, and one patient (3.7%) had a permanent pace maker for atrioventricular block. Ascites was present in almost one-third of the patients, while two-thirds of the patients were in NYHA class III or IV (**Table 1**). Mean logistic Euroscore was 5.39 ± 8.3 and three (11.1%) patients had a previous cardiac surgery operation.

Intraoperative and postoperative findings are shown in **Table 3**. Nine patients (33.3%) underwent Cone procedure (http://www.ctsnet.org/article/cone-reconstruction-tricuspid-valve-repair-ebstein-anomaly), seven patients (25.9%) had annuloplasty ring and the remaining patients (40.7%) had other types of repair (De Vega procedure, Alfieri Stitch procedure and/or commissuroplasty/plication). Most patients had isolated TV surgery; concomitant ASD closure was performed in four

TABLE 1 | Preoperative characteristics of patients with isolated tricuspid repair (*n* = 27).

Characteristic	Patients
Age: years	51.62 ± 14.39
Female gender	18 (66.7%)
Reduced LVEF (moderate to severe)	4 (14.7%)
RV failure (moderate to severe)	13 (48.1%)
RV dilatation	22 (81.4%)
Renal impairment	0
COPD	5 (18.5%)
Diabetes	2 (7.4%)
Hypertension	8 (29.6%)
Previous CVA	3 (11.1%)
TIA	1 (3.7%)
Smoking history	
Current	0
Ex-smoker	8 (29.6%)
PVD	0
Reoperation	3 (11.1%)
Number of previous heart operations	
2	1 (3.7%)
1	2 (7.4%)
Ebstein disease	14 (51.8%)
Tricuspid dysplasia	13 (48.1%)
Euro score: %	5.39 ± 8.30
Min: %	1.52
Max: %	44.82
Heart rhythm	
Sinus rhythm	17 (62.9%)
AF	9 (33.3%)
AV block (paced)	1 (3.7%)
Ascites	8 (29.6%)
NYHA class 3 or 4	18 (66.7%)
CCS class 3 or 4	6 (22.2%)

Data are presented as mean ± SD, median (range), or n (%).
LVEF, left ventricular ejection fraction; RV, right ventricle; COPD, chronic obstructive pulmonary disease; CVA, cardiovascular accidents; TIA, transient ischaemic attack; PVD, peripheral vascular disease; NYHA, New York Heart Association; CCS, Canadian Cardiovascular Society.
Data are expressed as number of events and percentages or otherwise expressed.

TABLE 2 | Preoperative classification of congenital heart disease in patients with isolated tricuspid repair (*n* = 27).

Characteristic	Patients
Ebstein disease	14 (51.8%)
Non-Ebstein TR	13 (48.1%)
– Previous congenital heart surgery in childhood	3 (11.1%)
ASD	1 (3.7%)
TOF	1 (3.7%)
VSD	1 (3.7%)
– Tricuspid dysplasia associated PFO-small ASD	4 (14.8%)
– TV delamination defect/Ebsteinoid anomaly	6 (22.2%)

Data are presented as mean ± SD, median (range), or n (%).
ASD, atrial septal defect; TOF, tetralogy of fallot; VSD, ventricular septal defect; TR, tricuspid regurgitation; PFO, patent foramen ovale; TV, tricuspid valve.
Ebsteinoid anomaly (9): variable field of disease associated with TV leaflets' failure of delamination.
Data are expressed as number of events and percentages or otherwise expressed.

TABLE 3 | Operative and postoperative characteristics of patients with isolated tricuspid repair ($n = 27$).

Characteristic	Patients
Tricuspid valve procedure	
Cone	9 (33.3%)
Annuloplasty ring	7 (25.9%)
Alfieri–plication–commissuroplasty	3 (11.1%)
Others	8 (29.6%)
PFO-small ASD closure	4 (14.8%)
MAZE	4 (14.8%)
CPB time (min)	104.96 ± 44.72
Cross-clamp time (min)	66.29 ± 32.41
Return to theatre	1 (3.7%)
Repair failure	1 (3.7%)
Deep wound infection	1 (3.7%)
New CVA	0
Post op dialysis	0
Length of hospital stay (days)	14.59 ± 11.30
Min (days)	5
Max (days)	53

Data are presented as mean ± SD, median (range), or n (%).
PFO, patent foramen ovale; ASD, atrial septal defect; CPB, cardio pulmonary bypass; CVA, cardiovascular accidents.
Data are expressed as number of events and percentages or otherwise expressed.

(14.8%) patients; antiarrhythmic surgery such as MAZE procedure was also performed in four (14.8%) patients. Mean cardiopulmonary bypass time was 104.9 ± 44.7 min, and mean cross-clamp time was 66.3 ± 32.4 min. In one case (3.7%), with Ebstein disorder, it was necessary to re-operate during the postoperative course for failure of TV repair; this patient eventually underwent TV replacement. One patient (3.7%) suffered a postoperative deep wound infection (mediastinitis), which required surgical re-exploration: this condition deteriorated to postoperative sepsis and subsequent death. No patient experienced episodes of cerebral ischaemia (CVA) or renal impairment in the perioperative period.

Follow-up

Clinical and Functional Results

The clinical and functional status of patients assessed according to the NYHA and CCS classification shows a statistically significant improvement: 66.7% patients in NYHA class III-IV preoperatively vs 7.4% at FU ($p < 0.01$) and 22.2% in CCS class III–IV preoperatively vs 3.7% at FU ($p < 0.01$). Also, our study demonstrated a significant reduction of clinical signs of heart failure such as ascites and peripheral oedema (29.6 vs 7.4%; $p < 0.01$). These data are shown in **Table 4**.

Echocardiographic Evaluations

Table 5 shows the preoperative and postoperative echocardiographic evaluation, with a mean FU echocardiographic time of 2.9 ± 1.8 years. There was a marked improvement in left ventricular function (14.8 vs 7.4%; $p < 0.01$), while no significant differences were found regard to the left ventricular diameters and wall thickness. Similarly, no significant differences were found concerning the left atrial volumes. At FU, all patients showed a significant reduction in right ventricular diameters (5.15 ± 1.21 vs 4.32 ± 1.16 cm; $p < 0.01$). We also observed a

TABLE 4 | Clinical and functional assessment of patients with isolated tricuspid repair ($n = 27$).

Characteristic	Preoperative	Follow-up	*p*-Value
NYHA 3–4	18 (66.7%)	2 (7.4%)	<0.01
CCS high class	6 (22.2%)	1 (3.7%)	<0.01
Heart rhythm			
NSR	17 (62.9%)	18 (74%)	0.1
AF	9 (33.3%)	8 (29.6%)	0.1
Paced	1 (3.7%)	1 (3.7%)	0.1
Ascites p. oedema	8 (29.6%)	2 (7.4%)	<0.01

Data are presented as mean ± SD, median (range), or n (%).
NYHA, New York Heart Association; CCS, Canadian Cardiovascular Society; NSR, normal sinus rhythm; AF, atrial fibrillation.
Data are expressed as number of events and percentages or otherwise expressed.

TABLE 5 | Echocardiographic evaluations of patients with isolated tricuspid repair ($n = 27$).

Characteristic	Preoperative	Follow-up	*p*-Value
Reduced left ventricular ejection fraction (mod-severe)	4 (14.8%)	2 (7.4%)	<0.01
LVIDD (cm)	4.18 ± 0.79	4.34 ± 0.70	0.1
LVISD (cm)	2.76 ± 0.71	2.87 ± 0.58	0.22
IVSD (cm)	0.93 ± 0.17	0.98 ± 0.16	0.1
PWD (cm)	0.89 ± 0.13	0.94 ± 0.14	0.1
RV failure (mod-severe)	13 (48.1%)	8 (29.6%)	0.1
RV dilatation	22 (81.4%)	11 (40.7%)	<0.01
Right ventricular internal diastolic diameter (cm)	5.15 ± 1.21	4.32 ± 1.16	<0.01
LA area (cm^2)	21.3 ± 7.6	22.4 ± 8.39	0.57
RA area (cm^2)	44.7 ± 16.7	26.7 ± 9.2	<0.01
Tricuspid regurgitation			
Moderate	6 (22.2%)	2 (7.4%)	0.04
Severe	21(77.7%)	1 (3.7%)	<0.01
Haepatic veins backflow	11(40.7%)	2 (7.4%)	<0.01
PAP (mmHg)	38.91 ± 7.88	33.37 ± 5.5	0.03
TAPSE (mm)	1.91 ± 0.85	1.26 ± 0.36	<0.01
P.Hypertension (mod-severe)	11(40.7%)	2 (7.4%)	<0.01

Data are presented as mean ± SD, median (range), or n (%).
LV, left ventricle; RV, right ventricle; LVIDD, left ventricular internal dimension in diastole; LVISD, left ventricular internal end-systolic dimension; IVSD, interventricular septum in diastole; PWD, posterior wall dimensions; RV, right ventricle; LA, left atrium; RA, right atrium; PAP, pulmonary arterial pressure; TAPSE, tricuspid annular plane systolic excursion; P.Hypertension, pulmonary hypertension.
Data are expressed as number of events and percentages or otherwise expressed.

different remodelling in right atrial geometry (44.7 ± 16.7 vs 26.7 ± 9.2 cm^2; $p < 0.01$). Regarding the functionality of TV, a clear reduction of valvular regurgitation has been observed at FU. Furthermore, TR significantly improved both in patients with moderate (22.2 vs 7.4%; $p = 0.04$) and severe baseline TR (77.7 vs 3.7%; $p < 0.01$). In addition, the pulmonary pressure (38.9 ± 7.8 vs 33.3 ± 5.5 mmHg; $p = 0.03$) and the degree of pulmonary hypertension (40.7 vs 7.4%; $p < 0.01$) were significantly reduced. A net reduction was also noticed in the number of patients with haepatic veins backflow (40.7 vs 7.4%; $p < 0.01$). On the other hand, TAPSE values dropped significantly in this period of evaluation (1.9 ± 0.85 vs 1.2 ± 0.36 mm; $p < 0.01$).

In **Table 6**, we reported the results of a sub-analysis that was conducted on the preoperative and postoperative echocardiographic evaluation in the Ebstein population. A significant

TABLE 6 | Echocardiographic evaluations of patients with isolated tricuspid repair, subset analysis in Ebstein population (n = 14).

Characteristic	Preoperative	Follow-up	p-Value
Reduced left ventricular ejection fraction (mod-severe)	2 (14.3%)	0	NA
LVIDD (cm)	3.64 ± 0.4	4.0 ± 0.50	0.01
LVISD (cm)	2.41 ± 0.49	2.59 ± 0.43	0.09
IVSD (cm)	0.87 ± 0.18	0.92 ± 0.11	0.28
PWD (cm)	0.88 ± 0.13	0.91 ± 0.11	0.53
RV failure (mod-severe)	7 (50%)	2 (14.3%)	0.47
RV dilatation	14 (100%)	6 (42.8%)	<0.01
Right ventricular internal diastolic diameter (cm)	5.54 ± 1.17	4.28 ± 1.08	*0.03*
LA area (cm^2)	17.3 ± 1.9	19.6 ± 6.5	0.29
RA area (cm^2)	48.3 ± 11.2	26.0 ± 10.5	<0.01
Tricuspid regurgitation			
Severe	14 (100%)	0	NA
Haepatic veins backflow	6(42.8%)	2 (14.3%)	0.47
PAP (mmHg)	37.8 ± 5.05	33.3 ± 3.9	0.06
TAPSE (mm)	2.2 ± 1.04	1.35 ± 0.39	<0.01
P.Hypertension (mod-severe)	7(50%)	2 (14.3%)	<0.48

Data are presented as mean ± SD, median (range), or n (%).
LV, left ventricle; RV, right ventricle; LVIDD, left ventricular internal dimension in diastole; LVISD, left ventricular internal end-systolic dimension; IVSD, interventricular septum in diastole; PWD, posterior wall dimensions; RV, right ventricle; LA, left atrium; RA, right atrium; PAP, pulmonary arterial pressure; TAPSE, tricuspid annular plane systolic excursion; P.Hypertension, pulmonary hypertension.
Data are expressed as number of events and percentages or otherwise expressed.

improvement was found in left ventricular function and on the left ventricular diameters (3.64 ± 0.4 vs 4.0 ± 0.5 cm; $p = 0.01$) without supplementary modification of wall thickness.

Similar to the main analysis, this sub group showed a substantial reduction in right ventricular diameters (5.54 ± 1.17 vs 4.28 ± 1.08 cm; $p = 0.03$) and RV dilatation (100 vs 42.8%; $p < 0.01$).

An interesting reduction has been observed on right atrial area (48.3 ± 11.2 vs 26 ± 10.5 cm^2; $p < 0.01$). Furthermore, the Ebstein population also showed a visible reduction of valvular regurgitation between the preoperative and the FU (100 vs 0%; p: NA). In addition, TAPSE values were considerably reduced (2.2 ± 1.04 vs 1.35 ± 0.39 mm; $p < 0.01$).

Survival

Figure 2 reports the survival after surgery. Early mortality shows that one patient (3.7%) died during the admission due to infection of the surgical site (mediastinitis). One patient died, during the FU, from non-cardiac related disease (neoplastic disease). The long-term survival was 96.3% at 1 year and 93.7% at 5 years.

All but one patient remained free from reoperation during the FU.

DISCUSSION

The incidence of isolated TR among congenital heart disease patients is quite rare, being reported approximately around 1–2% in the Dutch nationwide Congenital Corvitia registry (10). Although previously long underappreciated, TV disease is nowadays receiving increasing attention. However, guidelines for surgical management of tricuspid disease are less aggressive and more subjective than those related to left-sided cardiac valves (3, 11), thus implying that the indications to surgical intervention and methods of approach and repair are not uniform across institutions (7, 12, 13). Interestingly, some studies report no significant differences in outcome among the different surgical strategies (2), whereas other series showed better outcomes of repair vs replacement (1).

Congenital TV disease requiring surgical correction remains a rare entity: we found that, of the TV operations performed over 10 years at our institute, primary isolated tricuspid disease in ACHD patients represented only 8.8% of cases. Previous clinical reports suggest that surgery is beneficial in terms of improvements of symptoms and functional status (6). As reported by Nath et al. (5), improvement in TR severity, regardless of LVEF or PAP, is associated with better survival, while the presence of a severe TR is associated with a poor prognosis (6). Our results showed a significant reduction of TV regurgitation at FU with consequent reduction in haepatic veins flow and mean PAP. Furthermore, patients had a significant improvement in clinical status and reduction of clinical signs of heart failure, thus leading to a significant improvement in quality of life. These findings are in keeping with previous reports showing clinical improvements after TV repair as described by Kim et al. (6).

The 30-day mortality rate also appears to be low in our series (2): one patient died of a surgery-related cause while another patient had a non-cardiac-related death: similar results were demonstrated by previous studies where the operative mortality rate was calculated at 4% (14). The mid-term and long-term survival rates are also reassuring.

The optimal timing for surgical intervention is still debated (10, 15), but in daily practice patients are referred to surgery mainly because of symptoms secondary to RV impairment (1, 10, 15). Our findings were consistent with these data, as patients were referred to surgery at a late stage in the disease course, when highly symptomatic: more than two thirds (67%) were in NYHA class III or IV and clinical signs of right heart failure were reported in 30% of patients. RV failure was reported in 48% of patients and RV dilatation in 81%. Surgical intervention had a significant impact on the remodelling of the RV as shown in our 3-year FU. Echocardiography showed a reduction in RV dimensions (5.15 ± 1.2 vs 4.32 ± 1.16 cm; $p < 0.01$), and RA area (44.7 ± 16.7 vs 26.7 ± 9.2 cm^2; $p < 0.01$); this is most likely due to the effect of reduced RV pre-load. On the other hand, there was no significant change in RV function ($p = 0.1$); this is probably due to advanced structural modification of the RV which may have occurred before the time of the surgery (16). Therefore, the timing of surgery may be crucial to prevent damage to the RV and to achieve better results in the long term.

Annular repair also leads to increased stability of the cardiac skeleton, which might partially explain the reduction of the TAPSE at FU (1.91 ± 0.85 vs 1.26 ± 0.36 cm; $p < 0.01$).

There was a marked improvement in left ventricular function (14.8 vs 7.4%; $p < 0.01$) despite there being no changes in the left ventricular diameters and wall thickness; possibly due to a reduction of volume of the RV which decreases the compression on the left ventricle.

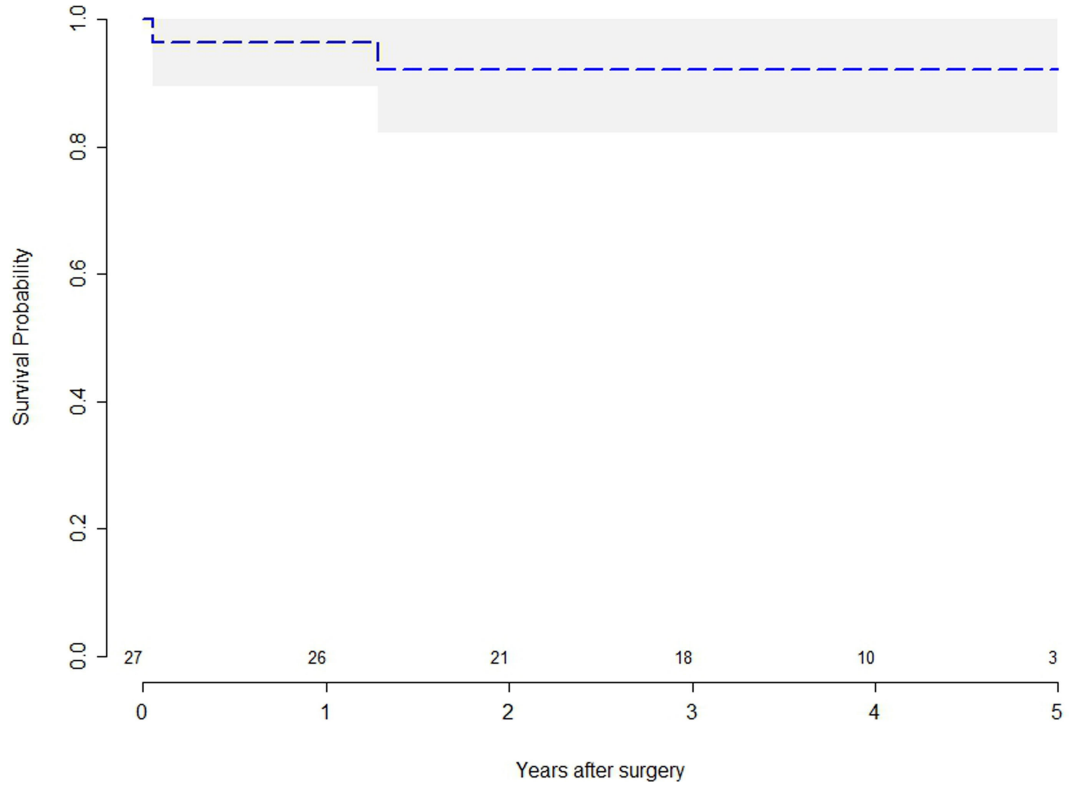

FIGURE 2 | **Kaplan–Meier survival curves for patients with tricuspid regurgitation after tricuspid valve repair**.

After performing a sub-analysis of the echocardiographic findings in the Ebstein disease group, we have interestingly noted that the FU findings were in keeping with the results of the whole population analysed.

The incidence of arrhythmia did not change at FU ($p < 0.1$), strengthening the idea that structural damage is a non-reversible phenomenon. As reported in the literature, AF has been recognised as an objective predictor of survival, rising mortality and morbidity due to thromboembolism risk and heart failure (17), making the argument that indication for surgery should be based on RV volumes and function, and leading to surgical intervention before RV failure (6, 12). The right cavities overload reduction leads to a significant clinical benefit, freedom from symptoms and signs of heart failure, and an improvement in quality of life.

For these reasons, we believe that surgical treatment of TR in congenital heart disease should be performed before the onset of heart failure. This concept has already been supported by other studies (1, 2, 6, 12).

Among the cohort of ACHD patients, the RV has also been defined as "forgotten" (12), even though, in the last decade, increasing attention has been focussed on it, in an effort to avoid the adverse outcomes associated with its dysfunction and fibrosis (16). These include not only exercise limitation but also malignant ventricular arrhythmias (17). In various clinical scenarios, TV surgery, as well as pulmonary surgery, is performed earlier in an attempt to "save" the RV, and the surgical mortality in experienced centres is acceptably low (12, 18).

As reported by Warnes (12), the conventional echocardiographic evaluations focussed on the functional assessment of the RV are very challenging because of its complex structure. In contrast, Cardiac Magnetic Resonance and the improved 3D echocardiographic imaging offer better evaluation of the right chambers of the heart (19–21). For these reasons, ACHD should be referred to specific centres in which adequate imaging and better understanding of the pathology can improve assessment and optimise surgical timing when appropriate.

Our study is a retrospective analysis of a relatively small cohort of patients, due to the rarity of isolated TR in ACHD, further multi-centric studies on a larger population should be performed to confirm and expand our findings. The cohort of analysis of this study is also too small to draw a conclusion on long-term re-TV rate.

CONCLUSION

Tricuspid valve repair is efficient and durable for the majority of patients with isolated TV regurgitation.

The medium and long-term evaluation show good results on durability and functionality.

When operated at optimal timing, TV repair allows a volume reduction of right cavities associated with both atrial and ventricular reverse remodelling at long-term FU. This condition leads to an improvement in quality of life due to the freedom from symptoms of heart failure.

However, in ACHD populations, these benefits are mostly represented when TV repair intervenes once RV structural damage has not already occurred.

INFORMED CONSENT

The data were derived from previous audits conducted on AHCD patients. The study was conducted in accordance with the principles of the Declaration of Helsinki. The local audit committee approved the study, and the requirement for individual patient consent was waived.

AUTHOR CONTRIBUTIONS

Substantial contributions to the conception or design of the work; or the acquisition, analysis, or interpretation of data for the work; drafting the work or revising it critically for important intellectual content; final approval of the version to be published; and agreement to be accountable for all aspects of the work in ensuring that questions related to the accuracy or integrity of any part of the work are appropriately investigated and resolved: RM, VB, PC, GG, FR, AB, UB, and MC.

FUNDING

This research was supported by the National Institute for Health Research Biomedical Research Unit in Cardiovascular Disease at the University Hospitals Bristol NHS Foundation Trust and the University of Bristol, the British Heart Foundation (RJ5862).

REFERENCES

1. Said SM, Dearani JA, Burkhart HM, Connolly HM, Eidem B, Stensrud PE, et al. Management of tricuspid regurgitation in congenital heart disease: is survival better with valve repair? *J Thorac Cardiovasc Surg* (2014) 147(1):412–7. doi:10.1016/j.jtcvs.2013.08.034
2. Raikhelkar J, Lin HM, Neckman D, Afonso A, Scurlock C. Isolated tricuspid valve surgery: predictors of adverse outcome and survival. *Heart Lung Circ* (2013) 22(3):211–20. doi:10.1016/j.hlc.2012.09.006
3. Baumgartner H, Bonhoeffer P, De Groot NMS, de Haan F, Deanfield JE, Galie N, et al. ESC Guidelines for the management of grown-up congenital heart disease (new version 2010). *Eur Heart J* (2010) 31(23):2915–57. doi:10.1093/eurheartj/ehq249
4. Rogers JH, Bolling SF. The tricuspid valve: current perspective and evolving management of tricuspid regurgitation. *Circulation* (2009) 119(20):2718–25. doi:10.1161/CIRCULATIONAHA.108.842773
5. Nath J, Foster E, Heidenreich PA. Impact of tricuspid regurgitation on long-term survival. *J Am Coll Cardiol* (2004) 43(3):405–9. doi:10.1016/j.jacc.2003.09.036
6. Kim Y-J, Kwon D-A, Kim H-K, Park J-S, Hahn S, Kim K-H, et al. Determinants of surgical outcome in patients with isolated tricuspid regurgitation. *Circulation* (2009) 120(17):1672–8. doi:10.1161/CIRCULATIONAHA.109.849448
7. Pfannmüller B, Moz M, Misfeld M, Borger MA, Funkat A-K, Garbade J, et al. Isolated tricuspid valve surgery in patients with previous cardiac surgery. *J Thorac Cardiovasc Surg* (2013) 146:841–7. doi:10.1016/j.jtcvs.2012.07.096
8. Bellomo R, Ronco C, Kellum JA, Mehta RL, Palevsky P; ADQI Workgroup. Acute renal failure – definition, outcome measures, animal models, fluid therapy and information technology needs: the Second International Consensus Conference of the Acute Dialysis Quality Initiative (ADQI) Group. *Crit Care* (2004) 8(4):R204. doi:10.1186/cc2671
9. Myers PO, Bautista-Hernandez V, Baird CW, Emani SM, Marx GR, Del Nido PJ. Tricuspid regurgitation or Ebsteinoid dysplasia of the tricuspid valve in congenitally corrected transposition: is valvuloplasty necessary at anatomic repair? *J Thorac Cardiovasc Surg* (2014) 147(2):576–80. doi:10.1016/j.jtcvs.2013.10.014
10. Zomer AC, Verheugt CL, Vaartjes I, Uiterwaal CSPM, Langemeijer MM, Koolbergen DR, et al. Surgery in adults with congenital heart disease. *Circulation* (2011) 124(20):2195–201. doi:10.1161/CIRCULATIONAHA.111.027763
11. Edmunds LH, Cohn LH, Weisel RD. Guidelines for reporting morbidity and mortality after cardiac valvular operations. *J Thorac Cardiovasc Surg* (1988) 96(3):351–3.
12. Warnes CA. Adult congenital heart disease. Importance of the right ventricle. *J Am Coll Cardiol* (2009) 54(21):1903–10. doi:10.1016/j.jacc.2009.06.048
13. De Bonis M, Taramasso M, Lapenna E, Alfieri O. Management of tricuspid regurgitation. *F1000Prime Rep* (2014) 6:58. doi:10.12703/P6-58
14. da Silva JP, da Silva Lda F. Ebstein's anomaly of the tricuspid valve: the cone repair. *Semin Thorac Cardiovasc Surg Pediatr Card Surg Annu* (2012) 15(1):38–45. doi:10.1053/j.pcsu.2012.01.008
15. McCarthy PM, Bhudia SK, Rajeswaran J, Hoercher KJ, Lytle BW, Cosgrove DM, et al. Tricuspid valve repair: durability and risk factors for failure. *J Thorac Cardiovasc Surg* (2004) 127(3):674–85. doi:10.1016/j.jtcvs.2003.11.019
16. Kobr J, Slavik Z, Uemura H, Saeed I, Furck A, Pizingerová K, et al. Right ventricular pressure overload and pathophysiology of growing porcine biomodel. *Pediatr Cardiol* (2016) 37(8):1498–506. doi:10.1007/s00246-016-1463-y
17. Kim HK, Kim YJ, Kim KI, Jo SH, Kim KB, Ahn H, et al. Impact of the maze operation combined with left-sided valve surgery on the change in tricuspid regurgitation over time. *Circulation* (2005) 112(9 Suppl):I14–9. doi:10.1161/CIRCULATIONAHA.104.524496
18. Lee J-W, Song J-M, Park JP, Lee JW, Kang D-H, Song J-K. Long-term prognosis of isolated significant tricuspid regurgitation. *Circ J* (2010) 74(2):375–80. doi:10.1253/circj.CJ-09-0679
19. Bonello B, Kilner PJ. Review of the role of cardiovascular magnetic resonance in congenital heart disease, with a focus on right ventricle assessment. *Arch Cardiovasc Dis* (2012) 105(11):605–13. doi:10.1016/j.acvd.2012.04.005
20. Beitzke D, Wolf F, Edelhauser G, Lammer J, Loewe C. Right heart dilatation in adult congenital heart disease: imaging appearance on cardiac magnetic resonance. *Br J Radiol* (2011) 84:188–93. doi:10.1259/bjr/13711325
21. Trzebiatowska-Krzynska A, Driessen M, Sieswerda GT, Wallby L, Swahn E, Meijboom F. Knowledge based 3D reconstruction of the right ventricle: comparison with cardiac magnetic resonance in adults with congenital heart disease. *Echo Res Pract* (2015). Available from: http://www.echorespract.com/cgi/doi/10.1530/ERP-15-0029

Conflict of Interest Statement: The authors declare that the research was conducted in the absence of any commercial or financial relationships that could be construed as a potential conflict of interest.

frontiers in Pediatrics

ORIGINAL RESEARCH
published: 06 February 2017
doi: 10.3389/fped.2017.00013

Results of Late Gadolinium Enhancement in Children Affected by Dilated Cardiomyopathy

Giuseppe Muscogiuri[1,2], Paolo Ciliberti[3], Domenico Mastrodicasa[4], Marcello Chinali[3], Gabriele Rinelli[3], Teresa Pia Santangelo[1], Carmela Napolitano[1], Benedetta Leonardi[3] and Aurelio Secinaro[1] for the MD Paedigree Study Investigators*

[1] Department of Imaging, Bambino Gesù – Children's Hospital IRCCS, Rome, Italy, [2] Department of Clinical and Molecular Medicine, University of Rome "Sapienza", Rome, Italy, [3] Department of Pediatric Cardiology and Cardiac Surgery, Bambino Gesù – Children's Hospital IRCCS, Rome, Italy, [4] Department of Neurosciences, Imaging and Clinical Sciences, Diagnostic Imaging and Therapy, University "G. D'Annunzio", Chieti, Italy

Background: Little is known about the clinical value of late gadolinium enhancement (LGE), in children affected by dilated cardiomyopathy (DCM).

Materials and methods: We retrospectively evaluated 15 patients (8 ± 6 years, 6 males) with diagnosis of DCM who underwent cardiac magnetic resonance since 2014. All scans were performed with a 1.5 T system (Aera, Siemens). Study protocol included cine steady-state free precession sequences, followed by administration of 0.2 mmol/kg of gadolinium-based contrast agent. Inversion recovery Turbo Flash sequences, in the same position of cine images, were acquired 10–15 min after the injection of contrast agent, in order to assess the presence of LGE. The latter was considered positive with a signal intensity >6 SD from normal myocardial tissue. Indexed end-diastolic volume (EDVi) and end-systolic volume (ESVi), and left ventricle (LV) ejection fraction (EF) were calculated by using dedicated software on off-line workstation. Global longitudinal strain and diastolic function were evaluated by echocardiography. Clinical follow-up, including death, transplant, and listing for heart transplant [major adverse cardiac events (MACE)], were evaluated. Patients were divided into two different subgroups: negative (Group A) and positive (Group B) for presence of LGE. Statistical analysis was performed by using Mann–Whitney *U* test ($p < 0.05$ considered as statistically significant).

Results: Seven patients (47%) showed LGE. A global diffuse subendocardial pattern was evident in all patients presenting LGE (7/7, 100%). The following main LV indexes were observed in the two subgroups. Group A: EDVi = 96 ± 33 ml, ESVi = 56 ± 29 ml, LV EF = 45 ± 10%, global longitudinal strain = −16 ± 5%, *E/e′* ratio = 10 ± 3, MACE = 1. Group B: EDVi = 130 ± 60 ml, ESVi = 89 ± 43 ml, LV EF = 31 ± 6%, global longitudinal strain = −13 ± 4%, *E/e′* ratio = 9 ± 3, MACE = 3. There was no statistically significant difference between the two groups, in terms of EDVi (p: 0.2), ESVi (p: 0.2), and *E/e′* ratio (0.9), whereas a significant difference of LV EF, presence of significative mitral regurgitation, and global longitudinal strain were observed (respectively, p: 0.03, p: 0.009, and p: 0.03).

Edited by:
Giovanni Biglino, University of Bristol, UK

Reviewed by:
Damiano Caruso, Sapienza University, Italy
Mark Hamilton, University Hospitals Bristol, UK

***Correspondence:**
Giuseppe Muscogiuri
giuseppe.muscogiuri@opbg.net

Specialty section:
This article was submitted to Pediatric Cardiology, a section of the journal Frontiers in Pediatrics

Received: *30 November 2016*
Accepted: *19 January 2017*
Published: *06 February 2017*

Citation:
Muscogiuri G, Ciliberti P, Mastrodicasa D, Chinali M, Rinelli G, Santangelo TP, Napolitano C, Leonardi B and Secinaro A (2017) Results of Late Gadolinium Enhancement in Children Affected by Dilated Cardiomyopathy. Front. Pediatr. 5:13. doi: 10.3389/fped.2017.00013

Conclusion: In our population of children with DCM, LGE shows a global diffuse subendocardial pattern. Presence of LGE seems to play a role in these patients determining a worst global systolic function.

Keywords: dilated cardiomyopathy, late gadolinium enhancement, cardiac magnetic resonance, systolic function, ventricular mechanics

INTRODUCTION

Dilated cardiomyopathy (DCM) is defined as a ventricular dilatation associated with systolic dysfunction not secondary to other cardiac abnormalities such as coronary artery disease, valvular, or congenital heart disease. Incidence of DCM in children is extremely rare (0:58 cases/100,000 children) (1).

Etiology of dilation is known in about three thirds of cases; however, the majority remains without a confirmed diagnosis (1, 2).

Dilated cardiomyopathy development in pediatric patients may be either genetic linked, if genetic pedigree of the family is responsible for it, or non-familiar (1). DCM in children could be expression of neuromuscular disorders, typically characterized by dystrophin mutations. Finally, DCM can be linked to congenital errors of metabolism such as lysosomal storage diseases, carnitine deficiency, and mitochondrial myopathies (3).

Ventricular dilatation may also be due to "non-familiar" conditions. In these cases, DCM is usually the consequence of a previous myocarditis, chemotherapy, or fulminant Kawasaki (1).

Clinical manifestations of DCM can range from asymptomatic patients up to heart failure and development of malignant arrhythmias (4). If medical treatment fails, patients are listed for cardiac transplantation, or must receive mechanical circulatory support.

Cardiac magnetic resonance (CMR) has gained a crucial role in adults with DCM, since CMR provides reliable information about cardiac function and muscle tissue characterization (5). In fact, CMR is able to evaluate with great accuracy regional left ventricle (LV) wall motion, global systolic function, and presence of myocardial fibrosis (6, 7). Late gadolinium enhancement (LGE) imaging enables identification and quantification of areas of myocardial fibrosis. Hence, CMR represents a first etiological non-invasive step, which could be helpful to distinguish between ischemic and non-ischemic DCM.

In adult patients, various studies demonstrated not only a diagnostic but also a prognostic role of LGE especially in non-ischemic disease (5, 8–11).

Cardiac magnetic resonance assessment of myocardial fibrosis has been reported to be useful in patients with congenital heart disease (12–15) and cardiomyopathies; however, data about LGE imaging in children are still limited. Pediatric patients with DCM show a pattern of LGE distribution quite different compared to adults. Furthermore, children usually show a more heterogeneous pattern distribution of LGE compared to adults (15, 16).

Hence, our aim was to investigate the potential role of CMR and LGE in children affected by DCM.

PATIENTS AND METHODS

Patient Selection

We retrospectively evaluated all patients affected by DCM who underwent cardiac MRI, between December 2014 and March 2016, at our institution.

Diagnosis of DCM was based on echocardiographic findings with LV end-diastolic dimension *Z* score >2 and LV EF <50%.

Patients younger than 8 years old underwent cardiac mitral regurgitation (MR) under general anesthesia.

This study was carried out in accordance with the recommendations of the "Ethical Committee of the Ospedale Pediatrico Bambino Gesù" with written informed consent from all subjects. All subjects gave written informed consent in accordance with the Declaration of Helsinki.

CMR Acquisition Protocol

Cardiac magnetic resonance was performed with 1.5 T magnet (Aera, Siemens, Erlangen, Germany). Enrolled patients met the eligibility requirements, according to the guidelines of the American College of Radiology of 2013 (17). Patients with DCM secondary to other cardiac conditions and with glomerular filtration rate <30 ml/min/1.73 m^2, or frequent ventricular arrhythmias, were excluded from the study.

Our protocol included cine steady-state free precession (SSFP) sequences acquired on the long-axis cardiac planes: four chambers, two chambers, and three chambers (FOV 400 × 310 mm^2, slice thickness 6–8 mm, acquisition matrix 256 × 173, voxel size 1.5 mm × 1.5 mm × 7 mm, echo/repetition time (TE/TR) 1.1/40 ms, readout bandwidth 930 Hz/pixel, and flip angle 69°), followed by a "stack" of contiguous SSFP cine images, with the same technical parameters, acquired along cardiac short axis, to cover the whole ventricle—from base to apex.

After 10–15 min of intravenous administration of contrast agent (DOTAREM, Roissy, Guerbet, France), at 0.2 mmol/kg, T1-weighted inversion recovery sequences [FOV 400 × 290 mm^2, slice thickness 6–8 mm, acquisition matrix 256 × 156, voxel size 1.3 × 1.3 × 7, TE/TR 3 ms/747 ms, flip angle 25°, and inversion time (TI) 250–425 ms], were acquired along the same planes of the cine SSFP images, in order to evaluate the presence of LGE.

To determine the correct TI, for nulling normal myocardial signal intensity, a look-locker sequence was acquired in one short-axis plane.

Steady-state free precession cine images and T1 inversion recovery sequence for determining LGE, both were acquired in expiratory apnea.

Left Ventricular Systolic Function

The cine SSFP acquisitions acquired in short axis were transferred to an off-line workstation (CMR42, Circle Cardiovascular Imaging, Calgary, AB, Canada) and analyzed using the Simpson rule. End-diastolic volume (EDV), end-systolic volume (ESV), and ejection fraction (EF) were calculated for each patient. Subsequently, both EDV and ESV have been indexed for body surface area (BSA).

MR and Left Atrial Dilatation

Mitral regurgitation was quantitatively assessed from LV stroke volume and phase contrast velocity mapping flow measurements in the aorta acquired during free-breathing (18). MR regurgitant volume was calculated as LV stroke volume (ml/beat)—aortic forward flow (mL/beat). MR regurgitant fraction (RF) was calculated as: [regurgitant volume (mL/beat) × 100]/LV stroke volume (mL/beat). MR when present was classified as follows: mild (RF < 20%), moderate (20% ≤ RF < 40%), and severe (RF ≥ 40%).

Left atrial dilatation was qualitatively assessed on cine SSFP sequences acquired, respectively, on the three different long axis view (four, two, and three chambers).

Echocardiographic Assessment

All patients underwent a complete transthoracic echocardiographic examination using a Philips iE33 machine (Philips Medical Systems, Andover, MA, USA). Standard Doppler analysis was performed to obtain LV inflow velocities at the mitral valve tips, including peak early diastolic filling (E) and late diastolic peak velocities (A). Tissue Doppler analysis was performed to obtain longitudinal early diastolic (e') myocardial velocity calculated on the septum and lateral wall. Ratio of E/e' was derived to obtain an estimate of LV filling pressure. Speckle tracking imaging was used to obtain longitudinal ($L\varepsilon$) strain of the LV. Longitudinal strain were obtained from the analysis of three consecutive beats from the apical four-chamber window and expressed as percent of systolic deformation.

Clinical Follow-up

The whole population was followed up for major adverse cardiac events (MACE) defined as a composite endpoint of death, transplant, and listing for heart transplant. The median follow-up was 17 months.

Statistical Analysis

Analysis was performed using a commercial software (IBM SPSS Statistics for Macintosh, Version 20.0; IBM Corp., Armonk, NY, USA).

The distribution of indexed end diastolic volume (EDVi), indexed end-systolic volume (ESVi), LV EF, E/e' ratio, and global longitudinal strain was established using the Shapiro–Wilk test. Subsequently Mann–Whitney U test was performed in order to assess a statistical significative difference between patients positive and negative for the presence of myocardial LGE. One-way ANOVA was used to compare severity MR and atrial dilatation in both groups. A cutoff value of $p < 0.05$ was considered statistically significant.

RESULTS

Fifteen patients were enrolled. Mean age was 8 ± 6 years. Main demographic data of the overall population are resumed in **Table 1**.

Within the whole population, the mean LV EF was 38 ± 11%, LV end-diastolic indexed volume was 111 ± 51 ml/m^2. In seven patients (47%), there was significant myocardial LGE. A global diffuse (involving majority of LV segments) subendocardial pattern was evident in all patients presenting LGE (7/7, 100%) (**Figures 1** and **2**). Main CMR findings are summarized in **Table 2**.

The study population was divided into two groups: patients with no evidence of significant LGE (Group A, eight patients) and patients with the presence of diffuse subendocardial LGE (Group B, seven patients). The two subgroups were well matched for age and sex.

In Group A, the main findings were (values expressed as average ± standard deviation): age 7 ± 6 years, indexed EDV 96 ± 33 ml, indexed ESV 56 ± 29 ml, LV EF 45 ± 10%, global longitudinal strain = −16 ± 5%, and E/e' ratio = 10 ± 3. While Group B showed the following data: age 9 ± 4 years, indexed EDV 130 ± 60 ml, indexed ESV 89 ± 43 ml, LV EF 31 ± 6%, global longitudinal strain = −13 ± 4%, and E/e' ratio = 9 ± 3.

Main demographic data, CMR, and echocardiography findings among the two subgroups are shown in **Table 3**.

No significative difference was observed in terms of indexed EDV ($p = 0.2$) and indexed ESV ($p = 0.2$). However, LV EF was significantly lower in Group B patients compared to Group A ($p = 0.03$). Moreover, the presence of MR—at least moderate—was significantly lower in the subgroup of patients with no significant LGE ($p = 0.009$). A significative difference of global longitudinal strain was observed between Groups A and B ($p = 0.03$).

No significative difference in terms of LA dilation ($p = 0.5$), possible indirect sign of diastolic dysfunction, and E/e' ($p = 0.9$) were observed between Groups A and B.

Major adverse cardiac events were more frequent on Group B [3 (38%) vs 1 (14%)], but the small sample size did not allow any survival analysis.

DISCUSSION

This study demonstrates that in children affected by DCM, despite comparable LV volumes, the presence of diffuse subendocardial LGE is associated with a decreased LV global systolic function and worst global longitudinal strain. Interestingly, a global diffuse subendocardial pattern, involving majority of LV segments,

TABLE 1 | Main demographic data of the cohort population.

	Patients (n = 15)
Età	8.4 ± 6.2 anni
Age, years (mean ± SD)	8 ± 6
Male sex, n (%)	6 (40)
Height, cm (mean ± SD)	119 ± 38
Weight, kg (mean ± SD)	29 ± 22
BSA (mean ± SD)	1 ± 0.5

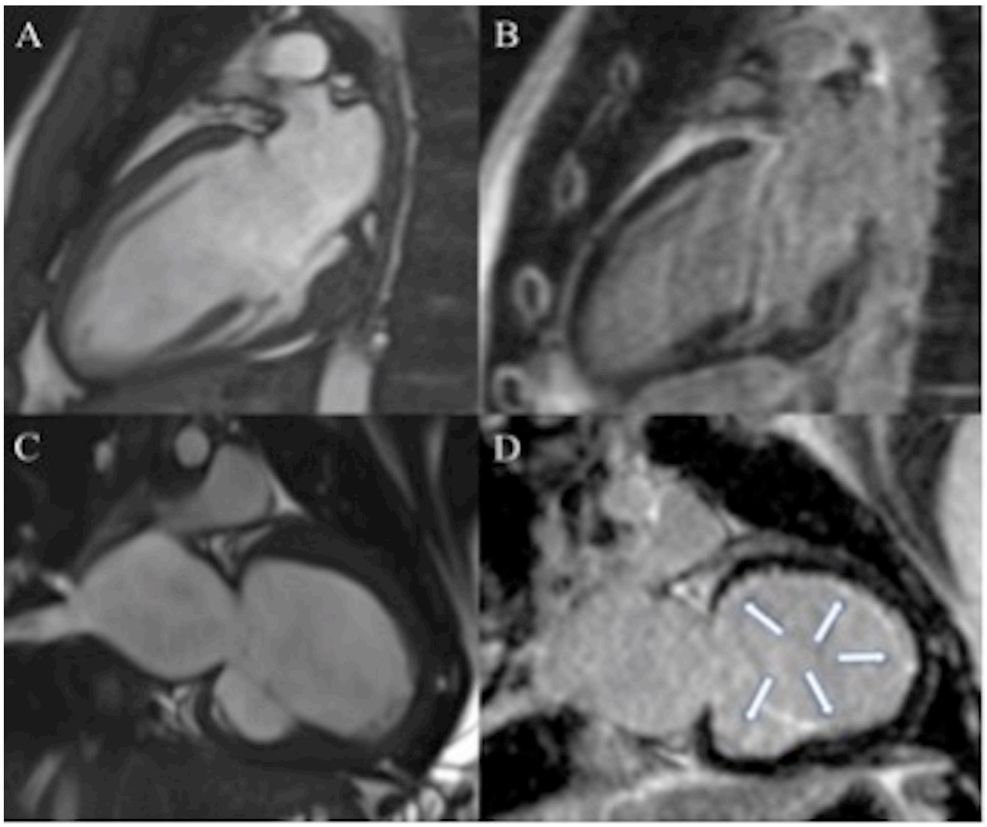

FIGURE 1 | **Seventeen-year-old patient with dilated cardiomyopathy (DCM) (A,B)**. Cine steady-state free precession (SSFP), in two chambers view, shows dilated left ventricle (LV) **(A)** in absence of late gadolinium enhancement (LGE) **(B)**. Three years old patient with DCM **(C,D)**. Dilated LV in two chambers view on cine SSFP **(C)**. Diffuse subendocardial LGE is visible in two chambers view [arrows **(D)**].

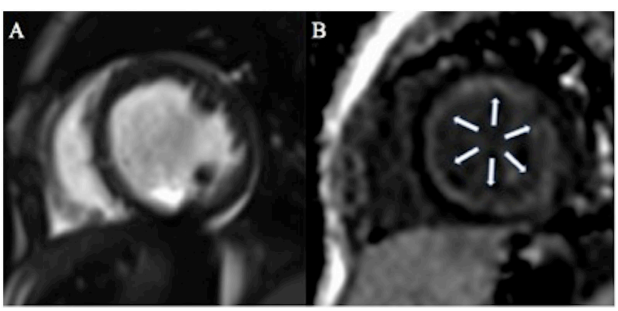

FIGURE 2 | **One-year-old patient with dilated cardiomyopathy**. Cine steady-state free precession on short axis view **(A)** shows dilated left ventricle with associated diffuse global subendocardial late gadolinium enhancement [arrows **(B)**].

TABLE 2 | Left ventricular volumes and function in overall population.

	Patients (*n* = 15)
EDV, ml (mean ± SD)	106 ± 72
EDVi, ml/m^2 (mean ± SD)	111 ± 51
ESV, ml (mean ± SD)	67 ± 48
ESVi, ml/m^2 (mean ± SD)	71 ± 40
EF, % (mean ± SD)	38 ± 11
LA dilation, *n* (%)	5 (33)
Mitral regurgitation, *n* (%)	
Absent	6 (40)
Mild	5 (34)
Moderate	2 (13)
Severe	2 (13)
E/e′ ratio	10 ± 3
Global longitudinal strain, %	−14 ± 4
Major adverse cardiac events (*n*, %)	4 (26)
LGE (*n*, %)	7 (47)

EDV, end-diastolic volume; EDVi, BSA-indexed end-diastolic volume; ESV, end-systolic volume; ESVi, BSA-indexed end-systolic volume; EF, ejection fraction.

papillary muscles, and trabeculae, was evident in all patients presenting LGE.

A typical pediatric cardiomyopathy, quite similar to our finding, had been already described in autopsy since the 1950s, and it was called primary endocardial fibroelastosis (EFE) (19, 20). Such entity was presumed to lead to a DCM (21). Thus, although primary EFE had been previously labeled as a separate form of cardiomyopathy, in 2006 the new classification of the American Heart Association does not consider it anymore as an isolate disease and includes it in the spectrum of DCM (22). Primary

TABLE 3 | Comparison of left ventricular volumes and function between Group A and Group B.

	Group A ($n = 8$)	Group B ($n = 7$)	p Value
Male sex, *n* (%)	3 (38%)	3 (43%)	0.5
Age, years (mean ± SD)	7 ± 6	9 ± 4	0.8
EDVi, ml/m^2 (mean ± SD)	96 ± 33	130 ± 60	0.2
ESVi (ml/m^2; mean ± SD)	56 ± 29	89 ± 43	0.2
EF (*n*, %)	45 ± 10	31 ± 6	0.03
LA dilation (*n*, %)	2 (25)	3 (42)	0.5
MR at least moderate (*n*, %)	0 (0)	4 (60)	0.009
E/e′ ratio	10 ± 3	9 ± 3	0,9
Global longitudinal strain (%)	−16 ± 5	−13 ± 4	0.03

EDVi, end-diastolic volume; ESVi, BSA-indexed end-systolic volume; EF, left ventricle ejection fraction; LA, left atrium; MR, mitral regurgitation.

EFE in the original description is characterized by the presence of ventricular dilatation, diffuse fibrous endocardial thickening, upward displacement of the papillary muscles, and valve leaflets thickening (20, 23, 24). In terms of "outcome," EFE is characterized by a very poor prognosis in pediatric patients (25, 26).

Our findings seem to confirm this report and corroborate the hypothesis that in the presence of EFE the ventricular mechanic is compromised, leading to impaired contraction and expansibility of the cardiac cavity.

Moreover, development of this peculiar LGE pattern does not seem to be related to disease duration, since age of the two subgroups is not significantly different.

Our study also shows that significant MR is more frequent in patients with significant LGE. This finding should not be linked to a functional mechanism, since ventricular dilation is comparable in the two subgroups. Therefore, the increasing leakage seems to be related to a fibrotic involvement of the valve and subvalvar apparatus. This is in keeping with the original description of primary EFE where papillary muscles involvement and valve leaflets thickening were described. Our data hence confirm that the presence of global diffuse EFE in the setting of children affected by DCM identifies a subgroup of patients with a worse disease clinical expression.

The etiology of EFE is still debated in literature. Some articles attribute the development of this condition to an increased response of fetal myocardium in case of viral illnesses including mumps, during pregnancy (27). The other main hypothesis is that a sort of ischemic/vascular problem is the origin of this peculiar finding. This is based on the global hypoperfusion detectable as myocytolysis at the examination of autoptic specimen in these patients. However, this abnormal finding can be commonly found also in patients with DCM (21).

Curiously, between the two subgroups we could not find any difference in terms of LA dilation and *E/e′* ratio. EFE is commonly believed to be a cause of diastolic dysfunction (28, 29). Our finding could be due to the poor sample size. Nevertheless, as it is well known for adult population, diastolic dysfunction might occur later in the natural history of children with DCM.

We must admit that the main limitation of this study is the small number of our cohort, which does not allow any definitive conclusion. Nevertheless, it should be emphasized that indication to CMR for a children affected by DCM is not so straightforward. Since on average general anesthesia is required for patients younger than 8 years old, balancing possible risks and benefits, the number of patients undergoing CMR in this setting is little worldwide, especially in the infancy.

Furthermore, we should admit that the evaluation of MR calculated with free breathing phase contrast may represent a bias if compared with stroke volume deducted by breath-hold cine images. In effect, it has been demonstrated that a trend to have higher stroke volume during free breathing phase contrast sequences if compared to the breath-hold ones (30). This could influence the RF of mitral valve that we calculated with magnetic resonance, although a concordance between data acquired on echocardiography and magnetic resonance in our cohort was observed.

From a clinical point of view, a trend of increased likelihood for developing MACE in population with positive LGE was found. However, the small sample size did not allow any specific survival analysis.

The prognostic role of LGE in children affected by DCM in effect is likely one of the most appealing future perspective, which could arise from our pilot study. Clearly, our initial findings should be confirmed on a wider analysis, performed on a larger cohort of patients.

CONCLUSION

In our population of children affected by DCM, LGE is frequent (47%), and it shows a characteristic global diffuse subendocardial pattern. Despite comparable LV volumes, the presence of fibrosis seems to play a key role in these patients, determining a worst clinical expression of disease. If LGE is present, patients have a significant lower global systolic function and more frequently show a significant MR. More data confirming these findings on a larger population and investigating the prognostic role of LGE in this setting are needed.

ETHICS STATEMENT

The authors declare that this study was performed in accordance with the research ethical guidelines. The study was conducted in retrospective analysis.

AUTHOR CONTRIBUTIONS

GM, PC, and AS wrote the manuscript. DM, CN, and TS collected data and analyzed the images. GR, MC, and BL analyzed data and were involved in manuscript editing.

ACKNOWLEDGMENTS

The MD Paedigree Project is partially funded by the European Union under the Information Communication Technologies Programme (contract number 600932).

REFERENCES

1. Konta L, Franklin RC, Kaski JP. Nomenclature and systems of classification for cardiomyopathy in children. *Cardiol Young* (2015) 25(Suppl 2):31–42. doi:10.1017/S1047951115001201
2. Wilkinson JD, Sleeper LA, Alvarez JA, Bublik N, Lipshultz SE; the Pediatric Cardiomyopathy Study Group. The pediatric cardiomyopathy registry: 1995-2007. *Prog Pediatr Cardiol* (2008) 25(1):31–6. doi:10.1016/j.ppedcard.2007.11.006
3. McNally EM, Golbus JR, Puckelwartz MJ. Genetic mutations and mechanisms in dilated cardiomyopathy. *J Clin Invest* (2013) 123(1):19–26. doi:10.1172/JCI62862
4. Mestroni L, Brun F, Spezzacatene A, Sinagra G, Taylor MR. Genetic causes of dilated cardiomyopathy. *Prog Pediatr Cardiol* (2014) 37(1–2):13–8. doi:10.1016/j.ppedcard.2014.10.003
5. Assomull RG, Prasad SK, Lyne J, Smith G, Burman ED, Khan M, et al. Cardiovascular magnetic resonance, fibrosis, and prognosis in dilated cardiomyopathy. *J Am Coll Cardiol* (2006) 48(10):1977–85. doi:10.1016/j.jacc.2006.07.049
6. Varga-Szemes A, Muscogiuri G, Schoepf UJ, Wichmann JL, Suranyi P, De Cecco CN, et al. Clinical feasibility of a myocardial signal intensity threshold-based semi-automated cardiac magnetic resonance segmentation method. *Eur Radiol* (2016) 26(5):1503–11. doi:10.1007/s00330-015-3952-4
7. Kalisz K, Rajiah P. Impact of cardiac magnetic resonance imaging in non-ischemic cardiomyopathies. *World J Cardiol* (2016) 8(2):132–45. doi:10.4330/wjc.v8.i2.132
8. Wu KC, Weiss RG, Thiemann DR, Kitagawa K, Schmidt A, Dalal D, et al. Late gadolinium enhancement by cardiovascular magnetic resonance heralds an adverse prognosis in nonischemic cardiomyopathy. *J Am Coll Cardiol* (2008) 51(25):2414–21. doi:10.1016/j.jacc.2008.03.018
9. Gulati A, Jabbour A, Ismail TF, Guha K, Khwaja J, Raza S, et al. Association of fibrosis with mortality and sudden cardiac death in patients with nonischemic dilated cardiomyopathy. *JAMA* (2013) 309(9):896–908. doi:10.1001/jama.2013.1363
10. Lehrke S, Lossnitzer D, Schob M, Steen H, Merten C, Kemmling H, et al. Use of cardiovascular magnetic resonance for risk stratification in chronic heart failure: prognostic value of late gadolinium enhancement in patients with non-ischaemic dilated cardiomyopathy. *Heart* (2011) 97(9):727–32. doi:10.1136/hrt.2010.205542
11. Pontone G, Guaricci AI, Andreini D, Solbiati A, Guglielmo M, Mushtaq S, et al. Prognostic benefit of cardiac magnetic resonance over transthoracic echocardiography for the assessment of ischemic and nonischemic dilated cardiomyopathy patients referred for the evaluation of primary prevention implantable cardioverter-defibrillator therapy. *Circ Cardiovasc Imaging* (2016) 9(10):e004956. doi:10.1161/CIRCIMAGING.115.004956
12. Babu-Narayan SV, Goktekin O, Moon JC, Broberg CS, Pantely GA, Pennell DJ, et al. Late gadolinium enhancement cardiovascular magnetic resonance of the systemic right ventricle in adults with previous atrial redirection surgery for transposition of the great arteries. *Circulation* (2005) 111(16):2091–8. doi:10.1161/01.CIR.0000162463.61626.3B
13. Babu-Narayan SV, Kilner PJ, Li W, Moon JC, Goktekin O, Davlouros PA, et al. Ventricular fibrosis suggested by cardiovascular magnetic resonance in adults with repaired tetralogy of fallot and its relationship to adverse markers of clinical outcome. *Circulation* (2006) 113(3):405–13. doi:10.1161/CIRCULATIONAHA.105.548727
14. Smith BM, Dorfman AL, Yu S, Russell MW, Agarwal PP, Mahani MG, et al. Clinical significance of late gadolinium enhancement in patients <20 years of age with hypertrophic cardiomyopathy. *Am J Cardiol* (2014) 113(7):1234–9. doi:10.1016/j.amjcard.2013.12.034
15. Latus H, Gummel K, Klingel K, Moysich A, Khalil M, Mazhari N, et al. Focal myocardial fibrosis assessed by late gadolinium enhancement cardiovascular magnetic resonance in children and adolescents with dilated cardiomyopathy. *J Cardiovasc Magn Reson* (2015) 17:34. doi:10.1186/s12968-015-0142-0
16. Satoh H, Sano M, Suwa K, Saitoh T, Nobuhara M, Saotome M, et al. Distribution of late gadolinium enhancement in various types of cardiomyopathies: significance in differential diagnosis, clinical features and prognosis. *World J Cardiol* (2014) 6(7):585–601. doi:10.4330/wjc.v6.i7.585
17. Expert Panel on MRS, Kanal E, Barkovich AJ, Bell C, Borgstede JP, Bradley WG Jr, et al. ACR guidance document on MR safe practices: 2013. *J Magn Reson Imaging* (2013) 37(3):501–30. doi:10.1002/jmri.24011
18. Taylor AM, Dymarkowski S, Bogaert J. Valvular heart disease. In: Bogaert J, Dymarkowski S, Taylor AM, Muthurangu V, editors. *Clinical Cardiac MRI* Berlin, Heidelberg: Springer (2012). p. 465–509.
19. Linde LM, Adams FH, O'Loughlin BJ. Endocardial fibroelastosis; angiocardiographic studies. *Circulation* (1958) 17(1):40–5. doi:10.1161/01.CIR.17.1.40
20. Moller JH, Lucas RV Jr, Adams P Jr, Anderson RC, Jorgens J, Edwards JE. Endocardial fibroelastosis. A clinical and anatomic study of 47 patients with emphasis on its relationship to mitral insufficiency. *Circulation* (1964) 30:759–82. doi:10.1161/01.CIR.30.5.759
21. Seki A, Patel S, Ashraf S, Perens G, Fishbein MC. Primary endocardial fibroelastosis: an underappreciated cause of cardiomyopathy in children. *Cardiovasc Pathol* (2013) 22(5):345–50. doi:10.1016/j.carpath.2013.02.003
22. Maron BJ, Towbin JA, Thiene G, Antzelevitch C, Corrado D, Arnett D, et al. Contemporary definitions and classification of the cardiomyopathies: an American Heart Association Scientific Statement from the Council on Clinical Cardiology, Heart Failure and Transplantation Committee; Quality of Care and Outcomes Research and Functional Genomics and Translational Biology Interdisciplinary Working Groups; and Council on Epidemiology and Prevention. *Circulation* (2006) 113(14):1807–16. doi:10.1161/CIRCULATIONAHA.106.174287
23. De Letter EA, Piette MH. Endocardial fibroelastosis as a cause of sudden unexpected death. *Am J Forensic Med Pathol* (1999) 20(4):357–63. doi:10.1097/00000433-199912000-00009
24. Akiba T, Nakasato M, Suzuki H, Sato S, Sato T. Contracted form of endocardial fibroelastosis in two siblings. *Pediatr Int* (1999) 41(4):379–81. doi:10.1046/j.1442-200x.1999.01080.x
25. Takahashi S, Kanetake J, Moriya T, Funayama M. Sudden infant death from dilated cardiomyopathy with endocardial fibroelastosis. *Leg Med (Tokyo)* (2008) 10(5):277–80. doi:10.1016/j.legalmed.2008.03.001
26. Steger CM, Antretter H, Moser PL. Endocardial fibroelastosis of the heart. *Lancet* (2012) 379(9819):932. doi:10.1016/S0140-6736(11)61418-9
27. Ni J, Bowles NE, Kim YH, Demmler G, Kearney D, Bricker JT, et al. Viral infection of the myocardium in endocardial fibroelastosis. Molecular evidence for the role of mumps virus as an etiologic agent. *Circulation* (1997) 95(1):133–9. doi:10.1161/01.CIR.95.1.133
28. Emani SM, Marx GR. Operations for improving left ventricular diastolic function. *Curr Opin Cardiol* (2016) 31(1):101–8. doi:10.1097/HCO.0000000000000250
29. Friedman KG, Schidlow D, Freud L, Escobar-Diaz M, Tworetzky W. Left ventricular diastolic function and characteristics in fetal aortic stenosis. *Am J Cardiol* (2014) 114(1):122–7. doi:10.1016/j.amjcard.2014.04.013
30. Bolen MA, Setser RM, Gabriel RS, Renapurkar RD, Tandon Y, Lieber ML, et al. Effect of protocol choice on phase contrast cardiac magnetic resonance flow measurement in the ascending aorta: breath-hold and non-breath-hold. *Int J Cardiovasc Imaging* (2013) 29(1):113–20. doi:10.1007/s10554-012-0047-z

Conflict of Interest Statement: The authors declare that the research was conducted in the absence of any commercial or financial relationships that could be construed as a potential conflict of interest.

frontiers in Pediatrics

ORIGINAL RESEARCH
published: 28 February 2017
doi: 10.3389/fped.2017.00039

Timely Pulmonary Valve Replacement May Allow Preservation of Left Ventricular Circumferential Strain in Patients with Tetralogy of Fallot

Barbara E. U. Burkhardt[1,2], Marí Nieves Velasco Forte[3], Saravanan Durairaj[3], Isma Rafiq[3], Israel Valverde[3], Animesh Tandon[1], John Simpson[3] and Tarique Hussain[1,3]*

[1] Department of Pediatrics, University of Texas Southwestern Medical Center, Dallas, TX, USA, [2] Pediatric Heart Center, University Children's Hospital Zurich, Zurich, Switzerland, [3] Division of Imaging Sciences and Biomedical Engineering, King's College London, London, UK

Introduction: Patients with Tetralogy of Fallot (TOF) and pulmonary insufficiency and a dilated right ventricle (RV) may suffer from a reduction in left ventricular (LV) performance. It is not clear whether timely pulmonary valve replacement (PVR) preserves LV mechanics.

Methods: Ten TOF patients who underwent PVR were identified from hospital records, and pre- and postoperative cardiac magnetic resonance images were post-processed with a semi-automatic tissue tracking software. LV circumferential strain, time to peak strain, and torsion were compared before and after PVR. A control group of 10 age-matched normal volunteers was assessed as a comparison.

Results: LV circumferential strain did not change before vs. after PVR (basal −18.3 ± 3.7 vs. −20.5 ± 3%, $p = 0.082$; mid-ventricular −18.4 ± 3.6 vs. −19.1 ± 2%, $p = 0.571$; apical −22.7 ± 5.2 vs. −22.1 ± 4%; $p = 0.703$). There was also no difference seen between the baseline strain and normal controls (control basal −18.2 ± 3.3%, $p = 0.937$; mid −18 ± 3.2%, $p = 0.798$; apex −24.1 ± 5%, $p = 0.552$). LV torsion remained unchanged from baseline to post PVR [systolic 2.75 (1.23–9.51) °/cm vs. 2.3 ± 1.2°/cm, $p = 0.285$; maximum 5.5 ± 3.5°/cm vs. 2.34 (1.37–8.07) °/cm, $p = 0.083$]. There was no difference in time to measured peak LV circumferential strain before vs. after PVR (basal 0.44 ± 0.1 vs. 0.43 ± 0.05, $p = 0.912$; mid-ventricular 0.42 ± 0.08 vs. 0.38 ± 0.06, $p = 0.186$; apical 0.40 ± 0.08 vs. 0.40 ± 0.06, $p = 0.995$). At the same time, pulmonary regurgitation and RV end-diastolic and end-systolic volume indices decreased and LV end-diastolic volume increased after PVR. RV and LV ejection fractions remained constant.

Conclusion: PVR allows for favorable remodeling of both ventricular volumes for TOF patients with significant pulmonary regurgitation. In this cohort, LV myocardial functional parameters such as circumferential strain, time to peak strain, and LV torsion were normal at baseline and remain unchanged after PVR.

Keywords: Tetralogy of Fallot, congenital heart defects, left ventricle, tissue tracking, strain, magnetic resonance, pulmonary valve replacement, myocardial function

Abbreviations: CMR, cardiac magnetic resonance; LV, left ventricle; PVR, pulmonary valve replacement; RV, right ventricle; TOF, Tetralogy of Fallot.

OPEN ACCESS

Edited by:
Giovanni Biglino, University of Bristol, UK

Reviewed by:
Gianni Pedrizzetti, University of Trieste, Italy
Meena Nathan, Boston Children's Hospital, USA

****Correspondence:***
Barbara E. U. Burkhardt
barbara.burkhardt@kispi.uzh.ch

Specialty section:
This article was submitted to Pediatric Cardiology, a section of the journal Frontiers in Pediatrics

Received: *13 December 2016*
Accepted: *13 February 2017*
Published: *28 February 2017*

Citation:
Burkhardt BEU, Velasco Forte MN, Durairaj S, Rafiq I, Valverde I, Tandon A, Simpson J and Hussain T (2017) Timely Pulmonary Valve Replacement May Allow Preservation of Left Ventricular Circumferential Strain in Patients with Tetralogy of Fallot. Front. Pediatr. 5:39. doi: 10.3389/fped.2017.00039

INTRODUCTION

The right ventricle (RV) in patients with Tetralogy of Fallot (TOF) is at risk for progressive dilation secondary to pulmonary regurgitation. This may lead to an impairment of left ventricular (LV) mechanics, especially to a reduction in LV circumferential and radial strain, even in asymptomatic children and adolescents (1). Reduced RV longitudinal strain was shown to correlate with reduced LV longitudinal strain in adults with TOF (2), and LV circumferential and longitudinal strain have been associated with death or sustained ventricular tachycardia in TOF patients (3).

The indication for treatment by pulmonary valve replacement (PVR) is subject to much discussion currently, as both surgical and transcatheter PVR are being evaluated for their long-term benefit (4). The effects of PVR on myocardial mechanics have been described using echocardiography with tissue Doppler (5) and with speckle tracking or velocity vector analysis (6).

Cardiac magnetic resonance (CMR) is recommended in TOF patients for follow-up of RV volume and function (7). With the advent of tissue tracking, CMR cine images can be post-processed to measure biventricular strain and synchrony (8, 9).

Global circumferential strain has been shown to be the most reproducible measure of strain on CMR feature tracking (9). LV circumferential strain measured in a mid-ventricular slice by CMR feature tracking correlated with functional status and was one of the predictors of poor outcome in a large cohort study of 372 patients with TOF (10).

We hypothesized that LV circumferential strain and time to peak strain as well as LV torsion improve after PVR in TOF patients with dilated RV.

MATERIALS AND METHODS

Patient Selection

The retrospective, anonymized use of data was approved by the St. Thomas' Hospital Research Ethics Committee (London, England) 08/H0810/058. Written informed consent was not required.

Any patient who had undergone surgical PVR for pulmonary regurgitation after repair of TOF was included, if they had undergone pre- and post-procedure cine CMR including a short-axis cine stack of the left ventricle between July 2004 and August 2015, and the MRI study was available in the digital archive. Patients were excluded if other significant hemodynamic lesions were present (e.g., mitral regurgitation or significant branch pulmonary artery stenosis). Sixty-four surgical cases were performed in this time. Of these, only 14 met the inclusion criteria. Of these, four were excluded due to inadequate images.

Patients underwent surgical PVR 19 ± 9 years after initial tetralogy repair due to moderate to severe pulmonary regurgitation with significant RV dilation. The institutional policy at this time was for elective PVR if there was progressive dilation of the RV, significant RV diastolic chamber enlargement (>150 ml/m^2), or any reduction in ventricular ejection fractions.

Imaging

Cardiac magnetic resonance was performed on a 1.5 T scanner (Intera or Achieva, Philips Healthcare, Best, The Netherlands). ECG gated balanced cine steady-state free precession images were obtained in a short-axis stack of 9–13 slices from the atrioventricular valves to the apex, in 20–30 phases per cardiac cycle with a slice thickness of 8–10 mm, gap 0–2 mm, field of view between 272 mm × 272 mm and 390 mm × 390 mm, echo time 1.11–1.68 ms, temporal resolution at a median of 34.5 ms (25.3–50 ms), in breath-holding technique. CMR images of age-matched healthy volunteers were used as a control group.

Off-line post-processing was performed using cmr42 Release 5.3.4 (Circle Cardiovascular Imaging Inc., Calgary, AB, Canada). Ventricular volumes and ejection fractions of both ventricles were obtained from systolic and diastolic tracings as described elsewhere (11), and volumes were indexed to body surface area.

For tissue tracking analysis, basal, mid-ventricular, and apical slices were identified, which displayed myocardium along the entire LV circumference in all phases, avoiding the most basal and the most apical slices. End-diastole and end-systole were manually defined by comparing mid-ventricular slices in all phases. Endocardial and epicardial contours of the left ventricle were drawn manually, starting in end-diastole (**Figure 1**), tracked semi-automatically across all phases, and corrected manually where necessary, in order to accurately mark the endocardial and epicardial borders. Tissue tracking analysis (12) with a local heart coordinate system (13) was used to derive global circumferential strain curves of each slice as well as torsion of the LV. Maximal systolic values were used for analysis, only taking into account measured points, not interpolated graph data. Time to peak strain was measured as the number of phases from end-diastole to peak circumferential strain divided by the total number of phases, thus giving a measure independent of the patient's heart rate.

Statistical Methods

Ventricular volumes were indexed to body surface area. Statistical analyses were performed with IBM SPSS Statistics 24 (IBM Corporation, Armonk, NY, USA). Continuous data are expressed as mean ± SD or as median (range) as appropriate. The one-sample Kolmogorov–Smirnov test was used to test for normal distribution. Pre- and post-PVR conditions were compared by Wilcoxon signed-rank tests for non-normally distributed variables, and paired sample *t*-tests were used for normally distributed variables. Independent sample *t*-tests were used for comparisons between patient groups. Coefficients of variation (SDs of differences between two measurements, divided by the respective means of two measurements) and intraclass correlation coefficients were calculated to describe intra- and interobserver variability of measurements.

RESULTS

Patient Characteristics

Ten patients qualified for pre- and postsurgical CMR analysis (seven males, three females). Patient and control subject ages, weights, and heart rates are summarized in **Table 1**.

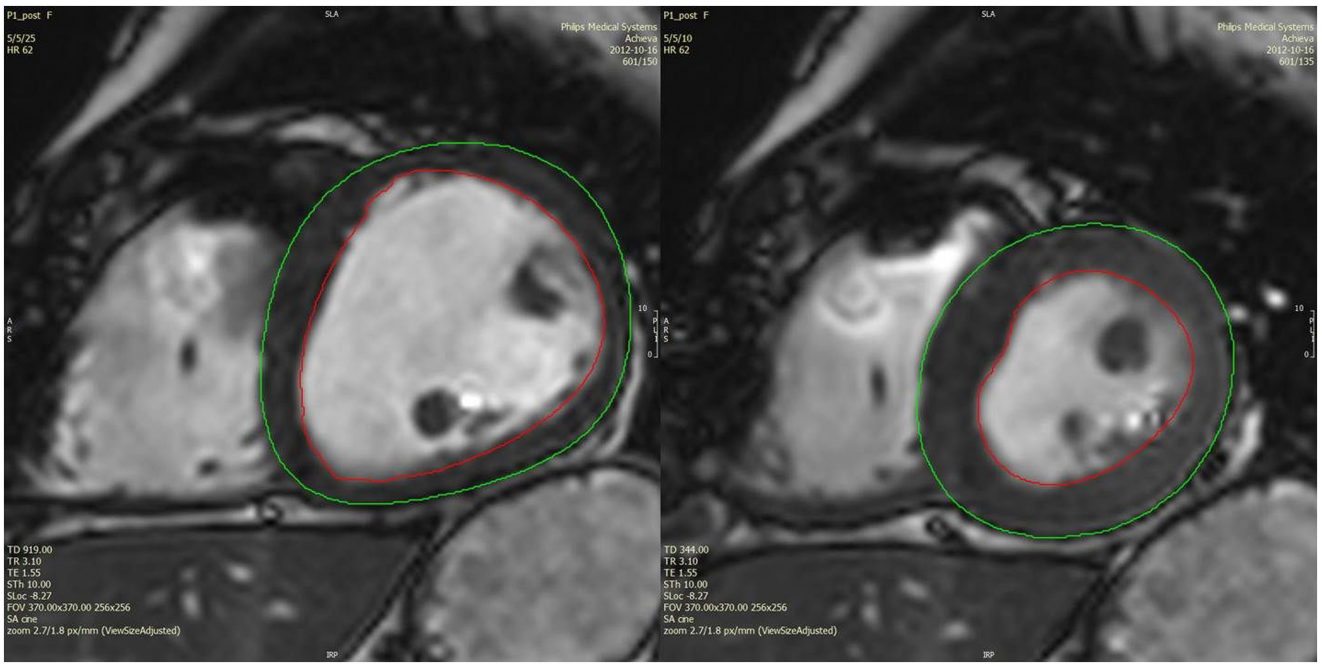

FIGURE 1 | **Example of diastolic and systolic tracings of a mid-ventricular slice in a post-PVR patient**.

TABLE 1 | Patient characteristics.

	Before PVR	After PVR	Controls	*p*-Value before vs. after PVR	*p*-Value before PVR vs. controls
Age (years)	25.1 ± 10.5	29.1 ± 10.8	23.4 ± 3.7	**0.002***	0.634
Weight (kg)	66.4 ± 13.3	68.6 ± 12.9	74.3 ± 19.4	0.565	0.301
Heart rate (bpm)	65.4 ± 10.9	63.8 ± 10.5	72.4 ± 11.8	0.660	0.184

**Statistical significance assumed for p < 0.05.*

PVR, pulmonary valve replacement.

Preoperative cardiac magnetic resonance (CMR) was performed 18 months prior to PVR (median; range 0–49 months). Postoperative CMR was performed 26 months after PVR (median; range 6–117 months).

Ventricular Volumes and Function

Pulmonary regurgitation and RV end-diastolic and end-systolic volumes were significantly reduced after PVR compared to baseline. LV end-diastolic volume showed an increase, although it was not significantly abnormal before PVR. There were no changes in LV end-systolic volume, RV or LV ejection fractions (**Table 2**).

LV Circumferential Strain and Torsion

Left ventricular circumferential strain or torsion did not change at the basal, the mid-ventricular, or the apical level after PVR compared to before PVR (**Table 3**; **Figure 2**). No difference in LV circumferential strain or torsion was seen between TOF patients at baseline and controls (**Figure 2**).

Time to Peak Circumferential Strain

The fraction of phases to peak LV circumferential strain based on the total number of phases per cardiac cycle did not differ before vs. after PVR (**Table 4**).

Reproducibility

(a) Intraobserver variability results of 10 subjects (TOF $n = 5$; control $n = 5$) are presented in **Table 5**.

(b) Interobserver variability results of 10 subjects (TOF $n = 5$; control $n = 5$) are presented in **Table 6**.

DISCUSSION

Pulmonary valve replacement was effective in our patient cohort to reduce pulmonary regurgitation and RV end-diastolic and end-systolic volumes. LV end-diastolic volume increased after PVR, which has been shown by others before (14), and which is most likely due to the interventricular septum making way for LV filling after RV volume overload was relieved. RV and LV ejection fractions were not indicators of the improved physiology.

Interestingly, LV circumferential strain did not show a significant change before vs. after PVR in the basal, mid-ventricular, or apical slices either. Time to peak circumferential strain and LV

TABLE 2 | Ventricular volumes and function before and after PVR.

	Before PVR	After PVR	Controls	*p*-Value before vs. after PVR	*p*-Value before PVR vs. controls
Pulmonary RF (%)	50.3 ± 12.9	12.4 ± 13.3	n/a	**<0.001***	n/a
RVEDVi (ml/m²)	154 ± 22	111 ± 32	91 ± 23	**0.006***	**<0.001***
RVESVi (ml/m²)	79 ± 15	57 ± 19	41 ± 11	**0.021***	**<0.001***
RVEF (%)	49 ± 6	49 ± 6	55 ± 2	0.872	**0.006***
LVEDVi (ml/m²)	78 ± 12 ml/m²	90 ± 20	89 ± 16	**0.038***	0.107
LVESVi (ml/m²)	33 ± 7 ml/m²	37 ± 9	41 ± 8	0.142	0.025
LVEF (%)	57 ± 6	59 ± 6	54 ± 4	0.427	0.172

**Statistical significance assumed for p < 0.05.*
Values are expressed as mean ± SD.
PVR, pulmonary valve replacement; TOF, Tetralogy of Fallot; Pulmonary RF, pulmonary regurgitation fraction; RVEDVi, right ventricular end-diastolic volume indexed to body surface area; RVESVi, right ventricular end-systolic volume indexed to body surface area; RVEF, right ventricular ejection fraction; LVEDVi, left ventricular end-diastolic volume indexed to body surface area; LVESVi, left ventricular end-systolic volume indexed to body surface area; LVEF, left ventricular ejection fraction.

TABLE 3 | Left ventricular circumferential strain and torsion before and after PVR.

	Before PVR	After PVR	Controls	*p*-Value before vs. after PVR	*p*-Value before PVR vs. controls
Basal LV circumferential strain (%)	−18.3 ± 3.7	−20.5 ± 3	−18.2 ± 3.3	0.082	0.937
Mid-ventricular LV circumferential strain (%)	−18.4 ± 3.6	−19.1 ± 2	−18 ± 3.2	0.571	0.798
Apical LV circumferential strain (%)	−22.7 ± 5.2	−22.1 ± 4	−24.1 ± 5	0.703	0.552
Systolic LV torsion (°/cm)	2.75 (1.23–9.51)	2.3 ± 1.2	4 ± 2.5	0.285	0.755

Values are expressed as mean ± SD where appropriate, otherwise as median (range).
PVR, pulmonary valve replacement; TOF, Tetralogy of Fallot; LV, left ventricle.

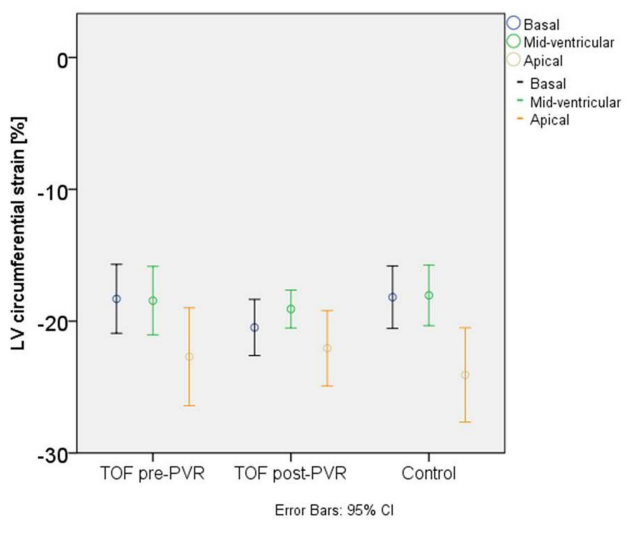

FIGURE 2 | Left ventricular (LV) circumferential strain in patients with Tetralogy of Fallot and in normal controls.

torsion were also unchanged before vs. after PVR. Patients did not have different LV circumferential strain, LV torsion, or time to peak circumferential strain values than controls either before or after PVR.

Like many studies looking at the reproducibility of strain measurements (9, 12), our data also show very good intra- and inter-rater comparisons for LV circumferential strain at the basal, mid-ventricular, and apical levels. Time to peak strain agreement was highest in the apical slice. However, our LV torsion measurements were not as well reproducible using this tissue tracking technique.

The Left Ventricle in Fallot Patients

We did not show any impairment in circumferential strain in our TOF patients compared to controls and no change after PVR. Furthermore, our study confirms the reproducibility of tissue tracking for LV strain analysis. However, the LV in TOF has been shown to suffer together with the RV in the long term. Indeed, adult patients with repaired TOF are presenting with an excess of early onset heart failure (15). This notion is supported by small animal models of chronic RV pressure loading, which show upregulation of LV fibrosis and apoptosis (16, 17). Recent work also suggests that serum biomarkers of heart failure are elevated in this group and track with the degree of right ventricular volume loading (18).

Therefore, it seems reasonable to presume that our findings are incongruent with these facts because our patients underwent early intervention which preserved their LV function. Normal values for LV circumferential strain in young adults by CMR feature tracking have been established in a large cohort by Augustine et al. (19), with LV circumferential strains of −22 ± 4% at the base, −18 ± 3% in mid-ventricular, and −21 ± 38% (*sic*) in apical slices. We found that our TOF patients had strain values largely in this range. Our findings are supported by Kempny et al., whose TOF patients had similar circumferential strain in a single mid-ventricular slice compared to their normal controls (20).

Although Padiyath et al. (21) reported reduced LV mid-ventricular circumferential strain in TOF patients compared to their normal volunteers (21), it should be noted that their TOF patients had strain values that were actually also within the normal

TABLE 4 | Proportion of phases to peak circumferential strain by total number of phases.

	Before PVR	After PVR	Controls	*p*-Value before vs. after PVR	*p*-Value before PVR vs. controls
Basal LV	0.44 ± 0.1	0.43 ± 0.05	0.42 ± 0.08	0.912	0.721
Mid-ventricular LV	0.42 ± 0.08	0.38 ± 0.06	0.44 ± 0.1	0.186	0.729
Apical LV	0.40 ± 0.08	0.40 ± 0.06	0.44 ± 0.06	0.995	0.216

Values are expressed as mean ± SD.
PVR, pulmonary valve replacement; TOF, Tetralogy of Fallot; LV, left ventricle.

TABLE 5 | Intraobserver variability.

Intraobserver variability, $n = 10$

	Mean value	Mean difference	SD of differences	Limits of agreement	CV (%)	ICC
Basal ε circ (%)	−18	1.36	2.61	−0.26; 3.0	14.2	0.790
Mid ε circ (%)	−16.7	0.28	3.00	−1.58; 2.13	13.7	0.681
Apical ε circ (%)	−22	−1.14	2.44	−2.65; 0.37	8.5	0.944
Basal phases to peak strain	0.40	−0.02	0.05	−0.06; 0.01	11.5	0.849
Mid phases to peak strain	0.42	−0.02	0.13	−0.10; 0.06	23.9	0.353
Apical phases to peak strain	0.40	0.01	0.02	−0.01; 0.02	5.5	0.961
Systolic LV torsion (°/cm)	3.43	1.42	2.96	−0.42; 3.25	66.8	0.250

Basal ε circ, basal left ventricular circumferential strain; mid ε circ, mid left ventricular circumferential strain; apical ε circ, apical left ventricular circumferential strain; basal phases to peak strain, proportion of phases to peak basal left ventricular circumferential strain by total number of phases; mid phases to peak strain, proportion of phases to peak mid left ventricular circumferential strain by total number of phases; apical phases to peak strain, proportion of phases to peak apical left ventricular circumferential strain by total number of phases; LV, left ventricle; CV, coefficient of variation = SD of differences between two measurements, divided by mean of two measurements; ICC, intraclass correlation coefficient (average measures).
Limits of agreement encompass the 95% confidence interval of the difference between measurements.

TABLE 6 | Interobserver variability.

	Mean value	Mean difference	SD of differences	Limits of agreement	CV (%)	ICC
Basal ε circ (%)	−17.8	0.77	1.28	−0.02; 1.57	5.6	0.942
Mid ε circ (%)	−16.3	−0.7	2.21	−2.07; 0.67	10.1	0.815
Apical ε circ (%)	−22.4	−0.44	2.83	−2.19; 1.32	6.1	0.922
Basal phases to peak strain	0.41	−0.05	0.08	−0.10; 0.00	17.9	0.263
Mid phases to peak strain	0.39	0.04	0.07	−0.01; 0.08	15.2	0.584
Apical phases to peak strain	0.40	0.01	0.04	−0.01; 0.03	7.7	0.902
Systolic LV torsion (°/cm)	3.67	0.92	2.48	−0.62; 2.46	41.8	0.621

Basal ε circ, basal left ventricular circumferential strain; mid ε circ, mid left ventricular circumferential strain; apical ε circ, apical left ventricular circumferential strain; basal phases to peak strain, proportion of phases to peak basal left ventricular circumferential strain by total number of phases; mid phases to peak strain, proportion of phases to peak mid left ventricular circumferential strain by total number of phases; apical phases to peak strain, proportion of phases to peak apical left ventricular circumferential strain by total number of phases; LV, left ventricle; CV, coefficient of variation = SD of differences between two measurements, divided by mean of two measurements; ICC, intraclass correlation coefficient (average measures).
Limits of agreement encompass the 95% confidence interval of the difference between measurements.

range of the large healthy volunteer study (19). In keeping with this, in the largest analysis of strain in TOF patients performed to date (10), LV circumferential strain was also in the normal range [−21.6; 95% CI (18.9, 24.5)]. This finding is mirrored by findings from Moon et al. (3), again showing normal strain values in TOF patients (circumferential strain 23%) but reduced strain in a very small cohort that had adverse outcomes (17%, $p = 0.003$). A reduction in circumferential strain may therefore be a late sign of adverse LV myocardial condition.

LV Torsion

Young adults with repaired TOF with and without PVR both show decreased LV twist on 3D echocardiography (22). There is very little available literature on LV torsion measured by CMR tissue tracking in patients with TOF. However, our data showed that reproducibility for LV torsion was poor, and others have shown considerable coefficients of variation in healthy volunteers before (12). The higher variability of torsion compared to circumferential strain is not surprising, because torsion is calculated from two separate LV slices instead of one. Further work is necessary before this analysis is applicable to these patients.

Time to Peak Strain

Time to peak strain is easy to measure from strain curves and was prolonged for longitudinal strain in the RV of TOF

patients in an echocardiographic speckle tracking analysis by Mueller et al. (23) but not in the LV [see also Ref. (24)]. However, as the LV primarily consists of circumferential fibers, the circumferential direction of deformation could be more indicative of dysfunctional LV mechanics, even more so in the context of a flattened interventricular septum in TOF patients with RV volume overload prior to PVR. The fact that our study did not find any difference in time to peak LV circumferential strain before and after PVR could be due to the relatively low number of phases per cardiac cycle, so that differences in short time intervals may have been missed.

Pulmonary Valve Replacement

All patients in this study had PVR surgery. In a similarly small cohort of 13 patients with pulmonary regurgitation undergoing transcatheter PVR, most of them with an underlying diagnosis of TOF, Harrild et al. (25) found an increase in the amount of LV circumferential strain by CMR tissue tracking, even though mean values were higher than published normal (19) even prior to PVR.

In our cohort of patients with repaired TOF, LV myocardial deformation parameters were in normal ranges both before and after PVR. Again, this may be due to an institutional bias to replace a dysfunctional pulmonary valve early, before RV and LV function might suffer.

Limitations

Patient recruitment for this analysis was retrospective. It is possible that statistical significance for some parameters was not reached because of the number of patients being too small. However, *post hoc* analysis showed that at a significance level of 0.05 and 80% power, the study was empowered to show a 3% difference in circumferential strain at the mid-ventricular level.

CONCLUSION

Pulmonary valve replacement improves the interventricular interaction of TOF patients to volume unloading, but intrinsic LV myocardial function parameters such as LV circumferential strain and LV torsion, as measured by CMR tissue tracking, are normal in the majority of TOF patients and remain unchanged after PVR. The literature suggests that there is a small subgroup of patients that have reduced circumferential strain and have adverse outcomes, whereas torsion requires further study in this context.

ETHICS STATEMENT

This study was carried out in accordance with the recommendations of the St. Thomas' Hospital Research Ethics Committee (London, England) with a waiver of written informed consent from all subjects in accordance with the Declaration of Helsinki, for the retrospective use of anonymized data. The protocol was approved by the St. Thomas' Hospital Research Ethics Committee (London, England) under 08/H0810/058.

AUTHOR CONTRIBUTIONS

BB contributed to research question, measured and analyzed data, interpreted data, and wrote the manuscript. MF contributed to research question, acquired data, and revised manuscript for intellectual content. SD and IR acquired data and revised manuscript for intellectual content. AT performed measurements and revised manuscript for intellectual content. JS revised manuscript for intellectual content. TH conceived research question, identified cases, analyzed data, interpreted data, and revised manuscript for intellectual content.

REFERENCES

1. Fernandes FP, Manlhiot C, Roche SL, Grosse-Wortmann L, Slorach C, McCrindle BW, et al. Impaired left ventricular myocardial mechanics and their relation to pulmonary regurgitation, right ventricular enlargement and exercise capacity in asymptomatic children after repair of Tetralogy of Fallot. *J Am Soc Echocardiogr* (2012) 25(5):494–503. doi:10.1016/j.echo.2012.01.014
2. Kempny A, Diller GP, Orwat S, Kaleschke G, Kerckhoff G, Bunck A, et al. Right ventricular-left ventricular interaction in adults with Tetralogy of Fallot: a combined cardiac magnetic resonance and echocardiographic speckle tracking study. *Int J Cardiol* (2012) 154(3):259–64. doi:10.1016/j.ijcard.2010.09.031
3. Moon TJ, Choueiter N, Geva T, Valente AM, Gauvreau K, Harrild DM. Relation of biventricular strain and dyssynchrony in repaired Tetralogy of Fallot measured by cardiac magnetic resonance to death and sustained ventricular tachycardia. *Am J Cardiol* (2015) 115(5):676–80. doi:10.1016/j.amjcard.2014.12.024
4. Tretter JT, Friedberg MK, Wald RM, McElhinney DB. Defining and refining indications for transcatheter pulmonary valve replacement in patients with repaired Tetralogy of Fallot: contributions from anatomical and functional imaging. *Int J Cardiol* (2016) 221:916–25. doi:10.1016/j.ijcard.2016.07.120
5. Knirsch W, Dodge-Khatami A, Kadner A, Kretschmar O, Steiner J, Bottler P, et al. Assessment of myocardial function in pediatric patients with operated Tetralogy of Fallot: preliminary results with 2D strain echocardiography. *Pediatr Cardiol* (2008) 29(4):718–25. doi:10.1007/s00246-008-9227-y
6. Sabate Rotes A, Bonnichsen CR, Reece CL, Connolly HM, Burkhart HM, Dearani JA, et al. Long-term follow-up in repaired Tetralogy of Fallot: can deformation imaging help identify optimal timing of pulmonary valve replacement? *J Am Soc Echocardiogr* (2014) 27(12):1305–10. doi:10.1016/j.echo.2014.09.012
7. Baumgartner H, Bonhoeffer P, De Groot NM, de Haan F, Deanfield JE, Galie N, et al. ESC guidelines for the management of grown-up congenital heart disease (new version 2010). *Eur Heart J* (2010) 31(23):2915–57. doi:10.1093/eurheartj/ehq249
8. Maret E, Todt T, Brudin L, Nylander E, Swahn E, Ohlsson JL, et al. Functional measurements based on feature tracking of cine magnetic resonance images identify left ventricular segments with myocardial scar. *Cardiovasc Ultrasound* (2009) 7:53. doi:10.1186/1476-7120-7-53
9. Morton G, Schuster A, Jogiya R, Kutty S, Beerbaum P, Nagel E. Inter-study reproducibility of cardiovascular magnetic resonance myocardial feature tracking. *J Cardiovasc Magn Reson* (2012) 14:43. doi:10.1186/1532-429X-14-43
10. Orwat S, Diller GP, Kempny A, Radke R, Peters B, Kuhne T, et al. Myocardial deformation parameters predict outcome in patients with repaired Tetralogy of Fallot. *Heart* (2016) 102(3):209–15. doi:10.1136/heartjnl-2015-308569
11. Buechel EV, Kaiser T, Jackson C, Schmitz A, Kellenberger CJ. Normal right- and left ventricular volumes and myocardial mass in children measured by steady state free precession cardiovascular magnetic resonance. *J Cardiovasc Magn Reson* (2009) 11:19. doi:10.1186/1532-429X-11-19
12. Schuster A, Stahnke VC, Unterberg-Buchwald C, Kowallick JT, Lamata P, Steinmetz M, et al. Cardiovascular magnetic resonance feature-tracking assessment of myocardial mechanics: intervendor agreement and considerations

regarding reproducibility. *Clin Radiol* (2015) 70(9):989–98. doi:10.1016/j.crad.2015.05.006
13. D'Hooge J, Heimdal A, Jamal F, Kukulski T, Bijnens B, Rademakers F, et al. Regional strain and strain rate measurements by cardiac ultrasound: principles, implementation and limitations. *Eur J Echocardiogr* (2000) 1(3):154–70. doi:10.1053/euje.2000.0031
14. Frigiola A, Tsang V, Bull C, Coats L, Khambadkone S, Derrick G, et al. Biventricular response after pulmonary valve replacement for right ventricular outflow tract dysfunction: is age a predictor of outcome? *Circulation* (2008) 118(14 Suppl):S182–90. doi:10.1161/CIRCULATIONAHA.107.756825
15. Bradley E, Parker J, Novak E, Ludbrook P, Billadello J, Cedars A. Cardiovascular disease in late survivors of Tetralogy of Fallot: a tertiary care center experience. *Tex Heart Inst J* (2013) 40(4):418–23.
16. Nielsen EA, Sun M, Honjo O, Hjortdal VE, Redington AN, Friedberg MK. Dual endothelin receptor blockade abrogates right ventricular remodeling and biventricular fibrosis in isolated elevated right ventricular afterload. *PLoS One* (2016) 11(1):e0146767. doi:10.1371/journal.pone.0146767
17. Apitz C, Honjo O, Humpl T, Li J, Assad RS, Cho MY, et al. Biventricular structural and functional responses to aortic constriction in a rabbit model of chronic right ventricular pressure overload. *J Thorac Cardiovasc Surg* (2012) 144(6):1494–501. doi:10.1016/j.jtcvs.2012.06.027
18. Paolino A, Hussain T, Pavon A, Velasco MN, Uribe S, Ordonez A, et al. NT-proBNP as marker of ventricular dilatation and pulmonary regurgitation after surgical correction of Tetralogy of Fallot: a MRI validation study. *Pediatr Cardiol* (2016). doi:10.1007/s00246-016-1516-2
19. Augustine D, Lewandowski AJ, Lazdam M, Rai A, Francis J, Myerson S, et al. Global and regional left ventricular myocardial deformation measures by magnetic resonance feature tracking in healthy volunteers: comparison with tagging and relevance of gender. *J Cardiovasc Magn Reson* (2013) 15:8. doi:10.1186/1532-429X-15-8
20. Kempny A, Fernandez-Jimenez R, Orwat S, Schuler P, Bunck AC, Maintz D, et al. Quantification of biventricular myocardial function using cardiac magnetic resonance feature tracking, endocardial border delineation and echocardiographic speckle tracking in patients with repaired Tetralogy of Fallot and healthy controls. *J Cardiovasc Magn Reson* (2012) 14:32. doi:10.1186/1532-429X-14-32
21. Padiyath A, Gribben P, Abraham JR, Li L, Rangamani S, Schuster A, et al. Echocardiography and cardiac magnetic resonance-based feature tracking in the assessment of myocardial mechanics in Tetralogy of Fallot: an intermodality comparison. *Echocardiography* (2013) 30(2):203–10. doi:10.1111/echo.12016
22. Li SN, Yu W, Lai CT, Wong SJ, Cheung YF. Left ventricular mechanics in repaired Tetralogy of Fallot with and without pulmonary valve replacement: analysis by three-dimensional speckle tracking echocardiography. *PLoS One* (2013) 8(11):e78826. doi:10.1371/journal.pone.0078826
23. Mueller M, Rentzsch A, Hoetzer K, Raedle-Hurst T, Boettler P, Stiller B, et al. Assessment of interventricular and right-intraventricular dyssynchrony in patients with surgically repaired Tetralogy of Fallot by two-dimensional speckle tracking. *Eur J Echocardiogr* (2010) 11(9):786–92. doi:10.1093/ejechocard/jeq067
24. Abd El Rahman MY, Hui W, Yigitbasi M, Dsebissowa F, Schubert S, Hetzer R, et al. Detection of left ventricular asynchrony in patients with right bundle branch block after repair of Tetralogy of Fallot using tissue-Doppler imaging-derived strain. *J Am Coll Cardiol* (2005) 45(6):915–21. doi:10.1016/j.jacc.2004.11.049
25. Harrild DM, Marcus E, Hasan B, Alexander ME, Powell AJ, Geva T, et al. Impact of transcatheter pulmonary valve replacement on biventricular strain and synchrony assessed by cardiac magnetic resonance feature tracking. *Circ Cardiovasc Interv* (2013) 6(6):680–7. doi:10.1161/CIRCINTERVENTIONS.113.000690

Conflict of Interest Statement: The authors declare that the research was conducted in the absence of any commercial or financial relationships that could be construed as a potential conflict of interest.

frontiers in Pediatrics

ORIGINAL RESEARCH
published: 03 April 2017
doi: 10.3389/fped.2017.00065

Utility of Cardiovascular Magnetic Resonance-Derived Wave Intensity Analysis As a Marker of Ventricular Function in Children with Heart Failure and Normal Ejection Fraction

Hopewell N. Ntsinjana[1,2,3], Robin Chung[1,2], Paolo Ciliberti[2,4], Vivek Muthurangu[1,2], Silvia Schievano[1,2], Jan Marek[2], Kim H. Parker[5], Andrew M. Taylor[1,2] and Giovanni Biglino[2,6]*

[1] Centre for Cardiovascular Imaging, Institute of Cardiovascular Science, University College London, London, UK, [2] Cardiorespiratory Division, Great Ormond Street Hospital for Children, NHS Foundation Trust, London, UK, [3] Department of Paediatrics, Paediatric Cardiology Division, CH Baragwanath Academic Hospital, University of the Witwatersrand, Johannesburg, South Africa, [4] Department of Pediatric Cardiology and Cardiac Surgery, Pediatric Hospital "Bambino Gesù", Rome, Italy, [5] Department of Bioengineering, Imperial College, London, UK, [6] School of Clinical Sciences, Bristol Heart Institute, University of Bristol, Bristol, UK

OPEN ACCESS

Edited by:
Cecile Tissot,
The University Children's Hospital, Switzerland

Reviewed by:
Madhusudan Ganigara,
Mt Slnai Medical Centre, USA
Joan Sanchez-de-Toledo,
Hospital Sant Joan de Déu Barcelona, Spain

***Correspondence:**
Andrew M. Taylor
a.taylor76@ucl.ac.uk

Specialty section:
This article was submitted to Pediatric Cardiology, a section of the journal Frontiers in Pediatrics

Received: 01 December 2016
Accepted: 17 March 2017
Published: 03 April 2017

Citation:
Ntsinjana HN, Chung R, Ciliberti P, Muthurangu V, Schievano S, Marek J, Parker KH, Taylor AM and Biglino G (2017) Utility of Cardiovascular Magnetic Resonance-Derived Wave Intensity Analysis As a Marker of Ventricular Function in Children with Heart Failure and Normal Ejection Fraction.
Front. Pediatr. 5:65.
doi: 10.3389/fped.2017.00065

Objective: This study sought to explore the diagnostic insight of cardiovascular magnetic resonance (CMR)-derived wave intensity analysis to better study systolic dysfunction in young patients with chronic diastolic dysfunction and preserved ejection fraction (EF), comparing it against other echocardiographic and CMR parameters.

Background: Evaluating systolic and diastolic dysfunctions in children is challenging, and a gold standard method is currently lacking.

Methods: Patients with presumed diastolic dysfunction [n = 18; nine aortic stenosis (AS), five hypertrophic, and four restrictive cardiomyopathies] were compared with age-matched control subjects (n = 18). All patients had no mitral or aortic incompetence, significant AS, or reduced systolic EF. E/A ratio, E/E' ratio, deceleration time, and isovolumetric contraction time were assessed on echocardiography, and indexed left atrial volume (LAVi), acceleration time (AT), ejection time (ET), and wave intensity analyses were calculated from CMR. The latter was performed on CMR phase-contrast flow sequences, defining a ratio of the peaks of the early systolic forward compression wave (FCW) and the end-systolic forward expansion wave (FEW).

Results: Significant differences between patients and controls were seen in the E/E' ratio (8.7 ± 4.0 vs. 5.1 ± 1.3, p = 0.001) and FCW/FEW ratio (2.5 ± 1.6 vs. 7.2 ± 4.2 × 10^{-5} m/s, $p < 0.001$), as well as—as expected—LAVi (80.7 ± 22.5 vs. 51.0 ± 10.9 mL/m^2, $p < 0.001$). In particular, patients exhibited a lower FCW (2.5 ± 1.6 vs. 7.2 ± 4.2 × 10^{-5} m/s, $p < 0.001$) in the face of preserved EF (67 ± 11 vs. 69 ± 5%, p = 0.392), as well as longer isovolumetric contraction time (49 ± 7 vs. 34 ± 7 ms, $p < 0.001$) and ET/AT (0.35 ± 0.04 vs. 0.27 ± 0.04, $p < 0.001$).

Conclusion: This study shows that the wave intensity-derived ratio summarizing systolic and diastolic function could provide insight into ventricular function in children, on top of CMR and echocardiography, and it was here able to identify an element of ventricular dysfunction with preserved EF in a small group of young patients.

Keywords: systolic function, diastolic function, wave intensity analysis, ventricular mechanics, cardiovascular magnetic resonance

INTRODUCTION

Assessment of systolic and diastolic dysfunctions in pediatric patients poses difficulties due to the lack of a "gold standard" diagnostic biomarker. Currently, ventricular function, in particular diastolic dysfunction, is best assessed using catheter-based techniques, though these are invasive in nature and present technical limitations (1). Echocardiography offers a non-invasive alternative, including detection of early myocardial dysfunction before any detectable change in ejection fraction (EF) (2), but it also presents limitations, partly due to the fact that existing normal echocardiographic values have too broad a range in the pediatric population (3).

In the adult population, up to 50% of elderly patients with heart failure have a normal ejection fraction (HFNEF) (4). This entity has also been observed in the pediatric literature, with several pediatric cardiac diseases that can present with diastolic dysfunction in the face of a normal EF. These include congenital aortic stenosis (AS) (5), hypertrophic cardiomyopathy (HCM) (6), and restrictive cardiomyopathy (RCM) (6), where young patients had findings consistent with diastolic dysfunction and normal EF. With the current diagnostic tests having potential limitations in children (and also in adults), we sought to assess a novel index obtained from wave intensity analysis [derived non-invasively from cardiovascular magnetic resonance (CMR) data] in children with a high likelihood of diastolic dysfunction but normal EF, in order to gather better insight into their ventricular function.

Wave intensity represents energy flux per unit area carried by waves traveling in the cardiovascular network (7). This hemodynamic quantity carries information on interactions between the heart and the vasculature, i.e., ventriculoarterial coupling (8–10). Early work in this context suggested the potential of this method to provide insight into ventricular filling mechanics and speculated that it could help in the detection and characterization of diastolic dysfunction (11). This article aims to explore the diagnostic insight of CMR-derived wave intensity analysis in a group of children with preserved EF and chronic diastolic dysfunction, as a way to better study systolic dysfunction in patients with diastolic dysfunction.

MATERIALS AND METHODS

Patient Population

We retrospectively identified a total of 31 patients who had undergone both CMR and detailed echocardiogram and were labeled to have presumed diastolic dysfunction. The datasets from these patients were then subjected to strict inclusion criteria for further analysis with wave intensity, namely:

(a) Dilated left atrium (LA) on CMR and echocardiogram (Z-score $\geq +2.0$)
(b) Normal EF $\geq 55\%$ on CMR
(c) No mitral valve stenosis or regurgitation
(d) No significant AS (V_{max} gradient < 30 mmHg) or aortic regurgitation.

Eighteen subjects fitted the criteria, whereby no study patient had mitral or aortic incompetence, significant AS or reduced systolic EF:

- Nine patients had congenital AS—four patients had neonatal balloon aortic valvuloplasty followed by Ross procedure (pulmonary autograft aortic valve replacement and pulmonary homograft procedure) to treat residual AS and five patients had neonatal surgical valvotomy, followed by Ross procedure.
- Five patients had HCM with the evidence of dilated LA on CMR or echocardiography, normal EF on CMR (>55%), no left ventricular outflow tract obstruction, and no history of myomectomy or alcohol ablation.
- Four patients had idiopathic RCM based on high end-diastolic pressures (EDP) on previous catheterization, echocardiographic features reported as restrictive physiology (dilated LA and Doppler evidence of restriction), and normal EF (>55%).

Eighteen healthy age-matched controls with no current or past evidence of phenotypic cardiovascular disorders served as our control subjects.

Echocardiographic Data

All patients had an echocardiographic examination as a part of their assessment. Diastolic function assessment included pulsed Doppler of the mitral inflow and tissue Doppler imaging (TDI). All measurements of diastolic variables were retrospectively re-measured by a single echocardiographer. Conventional pulsed Doppler indices of diastolic function, peak early (E) and late (A) diastolic trans-mitral velocities, E/A ratio, and E-wave deceleration time (DT) were measured from the spectral Doppler signal of the mitral valve inflow, together with the isovolumetric contraction time (IVCT). Pulsed-wave TDI velocities were obtained from the septal mitral annulus (apical four-chamber view). TDI measurements for each myocardial segment included peak early diastolic velocity (E') and peak late diastolic velocity (A'). Only tracings that demonstrated a clear E' were used. Each TDI velocity was measured on three consecutive cardiac cycles and averaged for the analysis. The ratio of peak early diastolic mitral inflow velocity and early septal TDI velocity (E/E') was calculated. Examples of echocardiographic data are provided in **Figure 1.**

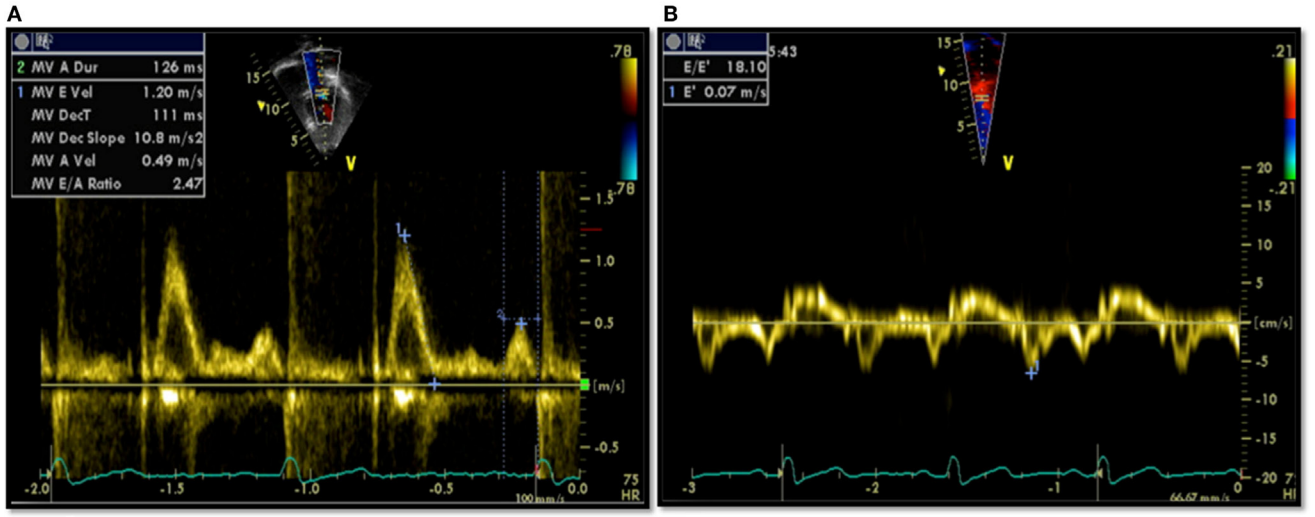

FIGURE 1 | **Echocardiographic data from a patient showing diastolic dysfunction: (A) trans-mitral Doppler *E/A* = 2.4, deceleration time = 111 ms; (B) tissue Doppler imaging *E′* = 0.07, a high *E/E′* ratio of 18.1 signifying diastolic dysfunction**.

CMR Data

Cardiovascular magnetic resonance data were acquired with a 1.5-T scanner (Avanto; Siemens Medical Solutions, Erlangen, Germany). Flow quantification was performed using phase-contrast sequences, with through-plane flow data acquired with the use of retrospective cardiac gating. Appropriate velocity-encoding values were set ~250 cm/s for through-plane flow quantification. Indicative parameters for the flow phase-contrast sequences were TR/TE = 27/3 ms, flip angle = 30°, and pixel size = 1.25 × 1.25, with a field of view = 240 × 320 or smaller. Acquisition parameters were adapted if necessary to optimize the quality of the scan for each case. Retrospectively gated, balanced, steady-state free precession cine images were acquired in the vertical long-axis (two-chamber), four-chamber, and the short-axis covering the entirety of both ventricles (9–12 slices). Myocardial late gadolinium enhancement for tissue characterization was performed in the long- and short-axis planes, using inversion recovery prepared gradient recalled echo sequence 10–15 min after injection of gadolinium (Dotarem®, gadoterate meglumine, Gd-DOTA, 0.1 mmol/kg; Guerbet, Paris, France). Inversion time was adjusted (250–350 ms) in order to null the normal viable myocardium. All postprocessing was carried out using in-house written plug-ins (OsiriX; Pixmeo, Geneva, Switzerland).

Left ventricular end-diastolic and end-systolic volumes were measured and indexed for BSA (i). The stroke volume, EF, and cardiac output were derived from these measurements. On top of the functional data, LA area and length were also measured from the two-chamber and four-chamber views, respectively, at the end of ventricular systole. The LA area was obtained by tracing its endocardial border excluding the pulmonary veins, LA appendage, and mitral valve recess. These parameters were used to calculate LA volume (LAV) using the formula (12, 13):

$$\mathrm{LAV} = \frac{8(\mathrm{A2ch})(\mathrm{A4ch})}{3\pi \mathrm{L}}$$

where A2ch is the area of the two-chamber view, A4ch is the area of the four-chamber view, and *L* is the shorter of the two LA length measurements (L2Ch and L4Ch) from these views (**Figure 2**).

The aortic velocity waveforms were used to compute peak velocity, acceleration time (AT), and ejection time (ET).

Wave Intensity Analysis

Wave intensity carries important information on ventriculoarterial interactions as well as time-domain information on wave reflections (7). By formulating wave intensity in terms of area (A) and velocity (U) differentials, i.e. $dI = dUd\ln A$, as opposed to the traditional pressure-based formulation, i.e., $dI = dPdU$, the analysis can be performed non-invasively based on CMR phase-contrast acquisitions. Wave intensity information was derived from CMR data using a previously proposed methodology (14). The image processing was carried out using an in-house written plug-in (OsiriX), whereby images are semiautomatically segmented to extract the A and U signals from the ascending aortic flow sequence and these are then combined to compute dI.

The following two dominant waves are identified in a typical dI pattern: a forward compression wave (FCW) at systolic ejection and a forward expansion wave (FEW) at end systole (**Figure 3**). Previous work has linked FCW with ventricular dP/dt and FEW with diastolic time relaxation constant (τ), suggesting dI as a clinically useful parameter for concurrently assessing LV systolic and early diastolic performance (15). Not only systolic and diastolic dysfunctions are unlikely to occur in isolation, but furthermore a desirable test for patients with heart failure has been suggested to be a non-invasive assessment of systolic and diastolic left ventricular functions together, not to uncouple systolic from diastolic function (16). For this reason, a single, non-dimensional parameter is proposed here and calculated as the ratio of dI peaks, i.e., =FCW/FEW, as an indicator of ventricular function. The rationale for choosing this parameter was based on the observation that systolic and diastolic dysfunctions often coexist, and

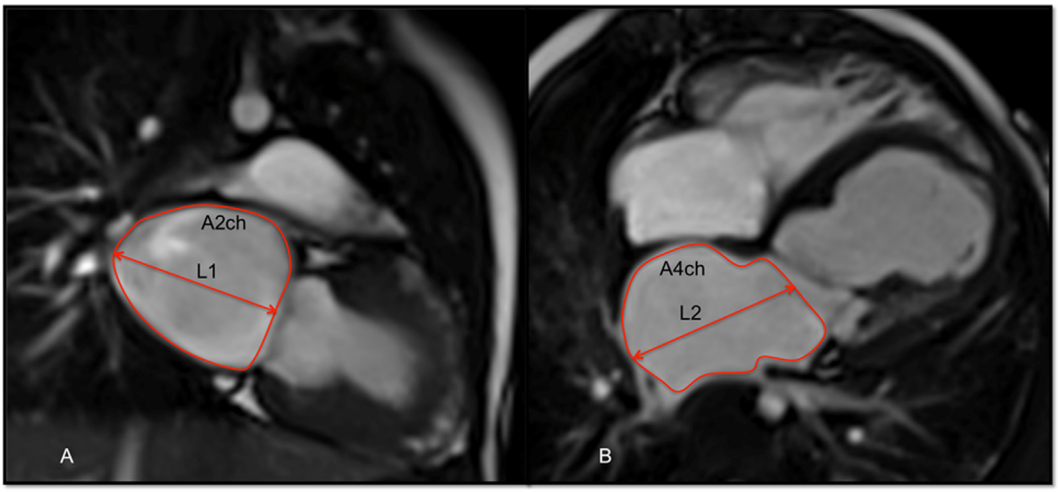

FIGURE 2 | Balanced-SSFP cine images of: (A) two-chamber (2ch) view and (B) four-chamber (4ch) at end systole showing measurement of the left atrial volume (LAV) by the biplane area–length method. The atrial endocardial border was traced to delineate left atrium (LA) area excluding the pulmonary veins, LA appendage, and mitral valve recess. LA volume was measured as reported in the Section "Materials and Methods."

the combined ratio would likely be more informative of cardiac dysfunction than systolic/diastolic measures alone (17, 18).

Data Analysis

All data processing was carried out in Matlab (MathWorks, Natick, MA, USA). Healthy controls and patients were compared for the following parameters: E/A, E/E', DT, and IVCT from echocardiography; EF, indexed left atrial volume (LAVi) and AT/ET from CMR; and FCW/FEW. Aortic distensibility (D) was inferred from wave speed (c) according to the Bramwell–Hill formula, $c^2 = 1/\rho D$, with ρ = density of blood and c estimated as a part of the CMR-based wave intensity analysis.

Statistical Analysis

Statistical analysis was carried out with commercial software (SPSS v.22; SPSS Inc., Chicago, IL, USA). Data are presented as mean ± SD. Comparisons of continuous variables of unpaired samples between groups (controls vs. patients) were performed using unpaired two-tailed Student's t-test, or Mann–Whitney U test for non-parametric data. Linear correlation among different variables was assessed using the Pearson r coefficient. A value of $p < 0.05$ was regarded as statistically significant.

RESULTS

Baseline characteristics, CMR, echocardiography, and wave intensity data between patients and healthy control subjects are presented in **Table 1**. Baseline characteristics showed that patients were age-matched with healthy controls (13.6 ± 4.5 vs. 14.9 ± 2.2 years, $p = 0.259$). There were no blood pressure differences between the two groups.

Echocardiographic Evaluation

Indices of conventional pulsed-wave Doppler across the mitral valve and TDI are listed in **Table 1**. There was no significant difference of E/A ratio and DT between patients and healthy controls. E/E' showed a statistically significant difference between patients and controls (8.7 ± 4.0 vs. 5.1 ± 1.3 $p = 0.001$). IVCT was significantly longer in patients compared to controls (49 ± 7 vs. 34 ± 7 ms, $p < 0.001$).

CMR Evaluation

Left ventricular functional assessment showed no significant differences of the indexed volumes (LV ESVi and LV EDVi) and EF (67 ± 11 vs. 69 ± 5%, $p = 0.392$) between patients and controls. The LAVi, as expected, was significantly larger in patients with presumed diastolic dysfunction compared to healthy controls (80.7 ± 22.5 vs. 51.0 ± 10.9 mL/m^2, $p < 0.001$, **Table 1**). On tissue characterization imaging, four AS patients and one patient with idiopathic RCM displayed endomyocardial fibroelastosis (EFE). Furthermore, patients exhibited lower peak aortic velocity, as well as significantly longer AT and similar ET, resulting in AT/ET = 0.35 ± 0.04 in patients and AT/ET = 0.27 ± 0.04 in controls ($p < 0.001$).

Wave Intensity Analysis

Peak FCW was significantly lower in patients compared with normal healthy controls (2.5 ± 1.6 vs. 7.2 ± 4.2 × 10^{-5} m/s, $p < 0.001$), while peak FEW was not significantly different (7.8 ± 4.2 vs. 6.9 ± 3.9 × 10^{-6} m/s, $p = 0.551$). The ratio FCW/FEW was thus significantly lower in patients (3.7 ± 2.7 vs. 12.7 ± 7.9, $p < 0.001$). Pearson correlation of the FCW/FEW with well-known echocardiographic and CMR biomarkers of diastolic dysfunction is shown in **Table 2**. The FCW/FEW ratio had a significant moderate negative correlation with E/E' ($r = -0.325$, $p = 0.027$) and a significant negative correlation with presence of EFE ($r = -0.343$, $p = 0.020$), while the correlation with LAVi was just above the significance threshold ($r = -0.264$, $p = 0.060$). Furthermore, a significant negative correlation was found between FCW and IVCT measured from echocardiography ($r = -0.459$, $p = 0.012$)

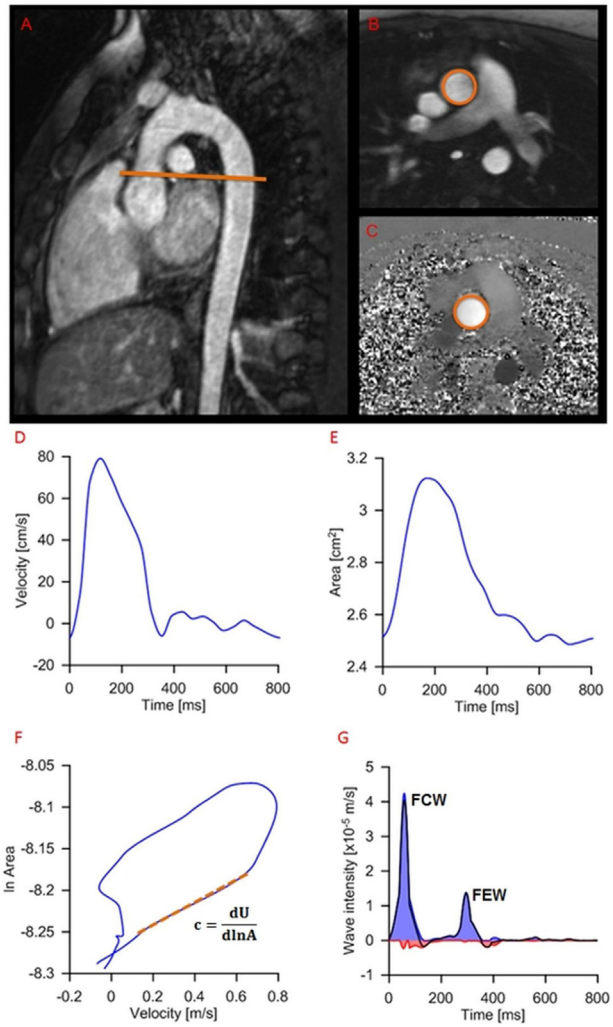

FIGURE 3 | Example of wave intensity analysis methodology from a patient, showing positioning of the slice for flow assessment (A) and modulus (B) and phase (C) images of the phase-contrast acquisition. Aortic velocity **(D)** and area **(E)** are semiautomatically extracted and combined for wave speed calculation **(F)** and wave intensity analysis **(G)**: *c*, wave speed; *A*, area; *U*, aortic velocity; FCW, forward compression wave (early systole); FEW, forward expansion wave (end systole).

TABLE 1 | Summary of demographic, echocardiography, CMR, and wave intensity data for patients and healthy controls groups.

Variables	Patients ($n = 18$)	Controls ($n = 18$)	*p*-Value
Demographic data			
Age (years)	13.6 ± 4.5	14.9 ± 2.2	0.259
BSA (m^2)	1.4 ± 0.4	1.7 ± 0.4	0.005*
Sex (F/M)	7/11	4/14	0.04*
HR (bpm)	78 ± 12	72 ± 12	0.157
DBP (mmHg)	62 ± 11	62 ± 10	0.940
SBP (mmHg)	104 ± 14	106 ± 10	0.520
Echocardiography data			
E/A	2.3 ± 1.1	2.5 ± 1.2	0.625
Deceleration time (ms)	137.0 ± 53.1	154.3 ± 48.5	0.307
E/E′	8.7 ± 4.0	5.1 ± 1.3	0.001*
IVCT (ms)	49 ± 7	34 ± 7	<0.001*
CMR data			
LV ESVi (mL/m^2)	23.0 ± 9.5	23.6 ± 6.7	0.817
LV EDVi (mL/m^2)	68.4 ± 11.9	75.2 ± 12.6	0.099
iSV (mL/m^2)	43 ± 10	52 ± 8	0.010*
LV ejection fraction (%)	67 ± 11	69 ± 5.0	0.392
Indexed left atrial volume (mL/m^2)	80.7 ± 22.5	51.0 ± 10.9	<0.001*
Peak U (cm/s)	62 ± 16	90 ± 14	<0.001*
Acceleration time (AT) (ms)	117 ± 21	92 ± 15	<0.001*
Ejection time (ET) (ms)	332 ± 36	341 ± 21	0.334
AT/ET	0.35 ± 0.04	0.27 ± 0.04	<0.001*
WIA data			
Distensibility ($\times 10^{-3}$ 1/mmHg)	4.3 ± 3.7	6.5 ± 4.3	0.116
Wave speed (m/s)	8.2 ± 7.2	5.3 ± 2.7	0.115
Peak forward compression wave (FCW) ($\times 10^{-5}$ m/s)	2.5 ± 1.6	7.2 ± 4.2	<0.001*
Peak forward expansion wave (FEW) ($\times 10^{-6}$ m/s)	7.8 ± 4.2	6.9 ± 3.9	0.551
FCW/FEW	3.7 ± 2.9	12.7 ± 7.9	<0.001*

*$p < 0.05$.

TABLE 2 | Values of Pearson's coefficient (*r*) and *p* values for correlations between forward compression wave/forward expansion wave ratio and other parameters.

Variables	Pearson's (*r*)	*p*-Value
Age	0.005	0.487
SBP	0.047	0.393
DBP	0.156	0.181
E/A	0.163	0.171
E/E′	−0.325	0.027*
Deceleration time	0.028	0.473
LV ejection fraction	0.226	0.093
Endomyocardial fibroelastosis	−0.343	0.02*
Indexed left atrial volume	−0.264	0.060
Distensibility	0.618	<0.001*

*$p < 0.05$.

and between FCW and AT/ET derived from CMR aortic velocity data ($r = -0.386$, $p = 0.018$).

DISCUSSION

In this study, we demonstrate the diagnostic potential of a novel, wave intensity analysis biomarker, derived from CMR flow data. Importantly, the wave intensity data (i.e., reduced FCW) provided insight into an element of load-independent systolic dysfunction in children with normal EF and chronic diastolic dysfunction. This observation was corroborated by prolonged IVCT on the face of normal diastolic blood pressure; however, IVCT on its own is limited by the fact that invasive pressure data is needed in order to comment on systolic function. The systolic impairment was further confirmed by observing aortic velocity waveforms, whereby peak velocity is significantly lower in patients who concurrently exhibit a longer AT. This indicates that peak aortic acceleration was lower, i.e., lower inotropy (19). Overall, FCW could then be a non-invasive marker for load-independent systolic dysfunction in the face of normal EF.

We have shown that the FCW/FEW ratio provided insight in the physiology of patients with chronic diastolic dysfunction despite normal EF when compared with more conventional

non-invasive parameters. Such a non-invasive measurement may prove particularly useful in the pediatric population, as diagnostic tools that are adequate for use in adult populations for the diagnosis of diastolic dysfunction fail to do so in pediatric patients, including echocardiographic parameters routinely used in the clinic (3).

Potential confounders for abnormal diagnostic tests were purposefully eliminated in this study. All patients with mitral valve disease, aortic incompetence, or residual stenosis and those with reduced LV EF were excluded in an attempt to make the study group more homogenous. Our primary objective was to test the potential of the wave intensity data for assessment of sub-clinical ventricular dysfunction. There was no difference in EF between patients and control subjects but significantly increased LAVi in the patient group. This is important as there is a significant relationship between increased LAVi and elevated LV EDP as well as echocardiographic indices of diastolic dysfunction, as shown in adult patients (20, 21). We presume therefore that the abnormally increased LAVi in the diseased subjects in our study is due to chronic diastolic dysfunction, an entity previously shown in pediatric echocardiographic studies (13). The combination of these abnormal and normal measured parameters then gave us this study cohort with normal EF in the presence of diastolic dysfunction.

Our results agree with the literature with regard to echocardiographic parameters in children in that only the E/E' was significantly different between patients and healthy control subjects (3, 22, 23). As a proof of principle, the new biomarker was then correlated with the established diagnostic tests for diastolic dysfunction, correlating with the two reliable indicators of diastolic dysfunction, namely E/E' and LAVi. An even stronger correlation was found between FCW/FEW and EFE. EFE was detected in 28% of the patients with presumed diastolic dysfunction, 80% of whom had congenital AS as a primary cardiac diagnosis. Physiologically, EFE renders the LV less distensible, thus potentially causing further impairment of diastolic filling (24, 25). Though the majority of our patient group did not have overt heart failure, many of HFNEF has been attributed to LV remodeling associated with concentric hypertrophy and increased end-diastolic volume, hence increased LV stiffness (26, 27). LV systolic and diastolic dysfunctions have long been known to induce impaired relaxation; this has been proven to be true by a myocardial performance index previously proposed by Tei et al. (18), showing a positive correlation between myocardial performance index and τ. The Tei index is, however, limited by pseudonormalization in the face of HFNEF and largely susceptible to activation delay (28, 29). Instead, the wave intensity biomarker could be used to complement and/or augment already existing parameters in those patients with HFNEF. From a methodological perspective, this postprocessing methodology does not impinge on scan time (i.e., does not require additional sequences acquisition) and has been semi-automated to facilitate the analysis.

Limitations and Future Directions

The first limitation is the small number of patients studied, partly due to strict inclusion criteria adopted to avoid clinical confounders. Second, this study was performed on patients with presumed rather than definitive diastolic dysfunction due to no pressure–volume loop data being available as a reference standard; however, we used acceptable non-invasive surrogates of diastolic dysfunction. Third, out-of-plane motion in CMR flow sequences may represent a problem for aortic area measurements. However, this movement has been quantified in the range of <1 cm (30, 31), and assuming no significant tapering in the region of the ascending aorta and constant regional wall properties, area measurements should not be substantially affected. Finally, the diagnostic potential of the proposed wave intensity ratio should be tested in a larger cohort of prospective patients and we intend to carry this out in the near future.

CONCLUSION

This study suggests a novel, non-invasive biomarker for assessing sub-clinical ventricular dysfunction in pediatric patients, based on CMR-derived wave intensity analysis, with diagnostic capabilities that appeared to perform better that the standard available parameters. This parameter could be easily implemented in routine CMR examinations (in both children and adults), providing additional and complementary information on combined systolic and diastolic performances.

ETHICS STATEMENT

Informed consent for the use of imaging data was obtained from all parents of patients who were imaged as a part of the patient clinical follow-up. The study was carried out in accordance with the ethical guidelines of the 1975 Declaration of Helsinki, as reflected in prior approval by the institutional and research ethics committee.

AUTHOR CONTRIBUTIONS

HN, RC, PC, VM, SS, JM, KP, AT, and GB designed the study, contributed to the data acquisition, analysis, and data interpretation; drafted the article; contributed to the data acquisition, analysis, and interpretation of results and revised critically the article. All authors read and approved the final article.

FUNDING

The authors gratefully acknowledge the support of the following funding bodies: Commonwealth Scholarships, Discovery foundation, Fondation Leducq, UK National Institute of Health Research (NIHR), British Heart Foundation, Royal Academy of Engineering/EPSRC and Heart Research UK. This report is independent research by the National Institute for Health Research Biomedical Research Centre Funding Scheme. The views expressed in this publication are those of the author(s) and not necessarily those of the NHS, the National Institute for Health Research or the Department of Health.

REFERENCES

1. Kass DA. Assessment of diastolic dysfunction. Invasive modalities. *Cardiol Clin* (2000) 18:571–86. doi:10.1016/S0733-8651(05)70162-4
2. Oz F, Cizgici AY, Ucar A, Karaayvaz EB, Kocaaga M, Bugra Z, et al. Doppler-derived strain imaging detects left ventricular systolic dysfunction in children with turner syndrome. *Echocardiography* (2013) 31(8):1017–22. doi:10.1111/echo.12500
3. Dragulescu A, Mertens L, Friedberg MK. Interpretation of left ventricular diastolic dysfunction in children with cardiomyopathy by echocardiography: problems and limitations. *Circ Cardiovasc Imaging* (2013) 6:254–61. doi:10.1161/CIRCIMAGING.112.000175
4. Owan TE, Hodge DO, Herges RM, Jacobsen SJ, Roger VL, Redfield MM. Trends in prevalence and outcome of heart failure with preserved ejection fraction. *N Engl J Med* (2006) 355:251–9. doi:10.1056/NEJMoa052256
5. Friedman KG, McElhinney DB, Rhodes J, Powell AJ, Colan SD, Lock JE, et al. Left ventricular diastolic function in children and young adults with congenital aortic valve disease. *Am J Cardiol* (2013) 111:243–9. doi:10.1016/j.amjcard.2012.09.026
6. McMahon CJ, Nagueh SF, Pignatelli RH, Denfield SW, Dreyer WJ, Price JF, et al. Characterization of left ventricular diastolic function by tissue Doppler imaging and clinical status in children with hypertrophic cardiomyopathy. *Circulation* (2004) 109:1756–62. doi:10.1161/01.CIR.0000124723.16433.31
7. Parker KH. An introduction to wave intensity analysis. *Med Biol Eng Comput* (2009) 47:175–88. doi:10.1007/s11517-009-0439-y
8. Biglino G, Schievano S, Steeden JA, Ntsinjana H, Baker C, Khambadkone S, et al. Reduced ascending aorta distensibility relates to adverse ventricular mechanics in patients with hypoplastic left heart syndrome: noninvasive study using wave intensity analysis. *J Thorac Cardiovasc Surg* (2012) 144:1307–13. doi:10.1016/j.jtcvs.2012.08.028
9. Ramsey MW, Sugawara M. Arterial wave intensity and ventriculoarterial interaction. *Heart Vessels* (1997) Suppl 12:128–34.
10. Smolich JJ, Mynard JP, Penny DJ. Simultaneous pulmonary trunk and pulmonary arterial wave intensity analysis in fetal lambs: evidence for cyclical, midsystolic pulmonary vasoconstriction. *Am J Physiol Regul Integr Comp Physiol* (2008) 294:R1554–62. doi:10.1152/ajpregu.00743.2007
11. MacRae JM, Sun YH, Isaac DL, Dobson GM, Cheng CP, Little WC, et al. Wave-intensity analysis: a new approach to left ventricular filling dynamics. *Heart Vessels* (1997) 12:53–9. doi:10.1007/BF02820867
12. Gulati A, Ismail TF, Jabbour A, Ismail NA, Morarji K, Ali A, et al. Clinical utility and prognostic value of left atrial volume assessment by cardiovascular magnetic resonance in non-ischaemic dilated cardiomyopathy. *Eur J Heart Fail* (2013) 15:660–70. doi:10.1093/eurjhf/hft019
13. Taggart NW, Cetta F, O'Leary PW, Seward JB, Eidem BW. Left atrial volume in children without heart disease and in those with ventricular septal defect or patent ductus arteriosus or hypertrophic cardiomyopathy. *Am J Cardiol* (2010) 106:1500–4. doi:10.1016/j.amjcard.2010.07.015
14. Biglino G, Steeden JA, Baker C, Schievano S, Taylor AM, Parker KH, et al. A non-invasive clinical application of wave intensity analysis based on ultra-high temporal resolution phase-contrast cardiovascular magnetic resonance. *J Cardiovasc Magn Reson* (2012) 14:57. doi:10.1186/1532-429X-14-57
15. Ohte N, Narita H, Sugawara M, Niki K, Okada T, Harada A, et al. Clinical usefulness of carotid arterial wave intensity in assessing left ventricular systolic and early diastolic performance. *Heart Vessels* (2003) 18:107–11. doi:10.1007/s00380-003-0700-5
16. St. John Sutton M, Wiegers SE. The Tei Index – a role in the diagnosis of heart failure? *Eur Heart J* (2000) 21:1822–4. doi:10.1053/euhj.2000.2391
17. Tei C, Ling LH, Hodge DO, Bailey KR, Oh JK, Rodeheffer RJ, et al. New index of combined systolic and diastolic myocardial performance: a simple and reproducible measure of cardiac function – a study in normals and dilated cardiomyopathy. *J Cardiol* (1995) 26:357–66.
18. Tei C, Nishimura RA, Seward JB, Tajik AJ. Noninvasive Doppler-derived myocardial performance index: correlation with simultaneous measurements of cardiac catheterization measurements. *J Am Soc Echocardiogr* (1997) 10:169–78. doi:10.1016/S0894-7317(97)70090-7
19. Duncan AM, Lim E, Gibson DG, Henein MY. Effect of dobutamine stress on left ventricular filling in ischemic dilated cardiomyopathy: pathophysiology and prognostic implications. *J Am Coll Cardiol* (2005) 46:488–96. doi:10.1016/j.jacc.2005.04.048
20. Posina K, McLaughlin J, Rhee P, Li L, Cheng J, Schapiro W, et al. Relationship of phasic left atrial volume and emptying function to left ventricular filling pressure: a cardiovascular magnetic resonance study. *J Cardiovasc Magn Reson* (2013) 15:99. doi:10.1186/1532-429X-15-99
21. Tsang TSM, Barnes ME, Gersh BJ, Bailey KR, Seward JB. Left atrial volume as a morphophysiologic expression of left ventricular diastolic dysfunction and relation to cardiovascular risk burden. *Am J Cardiol* (2002) 90:1284–9. doi:10.1016/S0002-9149(02)02864-3
22. Westenberg JJ. CMR for assessment of diastolic function. *Curr Cardiovasc Imaging Rep* (2011) 4:149–58. doi:10.1007/s12410-011-9070-z
23. Rathi VK, Doyle M, Yamrozik J, Williams RB, Caruppannan K, Truman C, et al. Routine evaluation of left ventricular diastolic function by cardiovascular magnetic resonance: a practical approach. *J Cardiovasc Magn Reson* (2008) 10:36. doi:10.1186/1532-429X-10-36
24. McElhinney DB, Vogel M, Benson CB, Marshall AC, Wilkins-Haug LE, Silva V, et al. Assessment of left ventricular endocardial fibroelastosis in fetuses with aortic stenosis and evolving hypoplastic left heart syndrome. *Am J Cardiol* (2010) 106:1792–7. doi:10.1016/j.amjcard.2010.08.022
25. Stranzinger E, Ensing GJ, Hernandez RJ. MR findings of endocardial fibroelastosis in children. *Pediatr Radiol* (2008) 38:292–6. doi:10.1007/s00247-007-0707-7
26. Westermann D, Kasner M, Steendijk P, Spillmann F, Riad A, Weitmann K, et al. Role of left ventricular stiffness in heart failure with normal ejection fraction. *Circulation* (2008) 117:2051–60. doi:10.1161/CIRCULATIONAHA.107.716886
27. Friedman KG, McElhinney DB, Colan SD, Porras D, Powell AJ, Lock JE, et al. Left ventricular remodeling and improvement in diastolic function after balloon aortic valvuloplasty for congenital aortic stenosis. *Circ Cardiovasc Interv* (2012) 5:549–54. doi:10.1161/CIRCINTERVENTIONS.112.968958
28. Gibson DG, Francis DP. Clinical assessment of left ventricular diastolic function. *Heart* (2003) 89:231–8. doi:10.1136/heart.89.2.231
29. Duncan AM, Francis DP, Henein MY, Gibson DG. Importance of left ventricular activation in determining myocardial performance (Tei) index: comparison with total isovolumic time. *Int J Cardiol* (2004) 95:211–7. doi:10.1016/j.ijcard.2003.07.007
30. Kilner PJ, Gatehouse PD, Firmin DN. Flow measurement by magnetic resonance: a unique asset worth optimising. *J Cardiovasc Magn Reson* (2007) 9:723–8. doi:10.1080/10976640701465090
31. Kozerke S, Scheidegger MB, Pedersen EM, Boesiger P. Heart motion adapted cine phase-contrast flow measurements through the aortic valve. *Magn Reson Med* (1999) 42:970–8. doi:10.1002/(SICI)1522-2594(199911)42:5<970::AID-MRM18>3.3.CO;2-9

Conflict of Interest Statement: The authors declare that the research was conducted in the absence of any commercial or financial relationships that could be construed as a potential conflict of interest.

frontiers in Pediatrics

ORIGINAL RESEARCH
published: 08 March 2017
doi: 10.3389/fped.2017.00034

Investigating Cardiac Motion Patterns Using Synthetic High-Resolution 3D Cardiovascular Magnetic Resonance Images and Statistical Shape Analysis

Benedetta Biffi[1,2], Jan L. Bruse[1], Maria A. Zuluaga[3], Hopewell N. Ntsinjana[1], Andrew M. Taylor[1] and Silvia Schievano[1]*

[1] Centre for Cardiovascular Imaging, UCL Institute of Cardiovascular Science & Great Ormond Street Hospital for Children, London, UK, [2] Department of Medical Physics and Biomedical Engineering, University College London, London, UK, [3] Translational Imaging Group, Centre for Medical Image Computing, University College London, London, UK

OPEN ACCESS

Edited by:
Adelaide De Vecchi, King's College London, UK

Reviewed by:
Meena Nathan, Boston Children's Hospital, USA
Gianluca Trocchio, Istituto Giannina Gaslini, Italy

***Correspondence:**
Benedetta Biffi
b.biffi@ucl.ac.uk

Specialty section:
This article was submitted to Pediatric Cardiology, a section of the journal Frontiers in Pediatrics

Received: *01 December 2016*
Accepted: *06 February 2017*
Published: *08 March 2017*

Citation:
Biffi B, Bruse JL, Zuluaga MA, Ntsinjana HN, Taylor AM and Schievano S (2017) Investigating Cardiac Motion Patterns Using Synthetic High-Resolution 3D Cardiovascular Magnetic Resonance Images and Statistical Shape Analysis. Front. Pediatr. 5:34. doi: 10.3389/fped.2017.00034

Diagnosis of ventricular dysfunction in congenital heart disease is more and more based on medical imaging, which allows investigation of abnormal cardiac morphology and correlated abnormal function. Although analysis of 2D images represents the clinical standard, novel tools performing automatic processing of 3D images are becoming available, providing more detailed and comprehensive information than simple 2D morphometry. Among these, statistical shape analysis (SSA) allows a consistent and quantitative description of a population of complex shapes, as a way to detect novel biomarkers, ultimately improving diagnosis and pathology understanding. The aim of this study is to describe the implementation of a SSA method for the investigation of 3D left ventricular shape and motion patterns and to test it on a small sample of 4 congenital repaired aortic stenosis patients and 4 age-matched healthy volunteers to demonstrate its potential. The advantage of this method is the capability of analyzing subject-specific motion patterns separately from the individual morphology, visually and quantitatively, as a way to identify functional abnormalities related to both dynamics and shape. Specifically, we combined 3D, high-resolution whole heart data with 2D, temporal information provided by cine cardiovascular magnetic resonance images, and we used an SSA approach to analyze 3D motion *per se*. Preliminary results of this pilot study showed that using this method, some differences in end-diastolic and end-systolic ventricular shapes could be captured, but it was not possible to clearly separate the two cohorts based on shape information alone. However, further analyses on ventricular motion allowed to qualitatively identify differences between the two populations. Moreover, by describing shape and motion with a small number of principal components, this method offers a fully automated process to obtain visually intuitive and numerical information on cardiac shape and motion, which could be, once validated on a larger sample size, easily integrated into the clinical workflow. To conclude, in this preliminary work, we have

implemented state-of-the-art automatic segmentation and SSA methods, and we have shown how they could improve our understanding of ventricular kinetics by visually and potentially quantitatively highlighting aspects that are usually not picked up by traditional approaches.

Keywords: ventricular mechanics, congenital heart disease, cardiac magnetic resonance, automatic segmentation, statistical shape analysis

1. INTRODUCTION

Imaging plays a crucial role in the diagnosis of congenital heart disease (CHD), allowing investigation of complex morphology and correlated pathophysiology (1). In particular, echocardiography and cardiovascular magnetic resonance (CMR) are used to directly or indirectly derive parameters (e.g., ejection fraction, valve inflow profile, strain, and strain rate) used to describe myocardial shape and kinetics, aiding in the diagnosis of ventricular dysfunction (2–5). While advanced image modalities can provide detailed 3D anatomical data, their analysis in clinical practice is often limited to simple 2D morphometry, which does not take into consideration the contribution of the third dimension. Moreover, the estimation of useful parameters from medical images is mostly performed using manual methods, which are time consuming and strongly rely on the specific expertise of the operator, therefore prone to human error. This does not allow for image-processing standardization and prevents the adoption of more complex analyses in routine clinical practice.

Recently, sophisticated engineering techniques for automatic medical image processing have been developed, which provide faster and more accurate ways of extracting the large amount of 3D shape and temporal information carried by medical images. This large amount of data is naturally suited for computer-based analyses, such as statistical shape analysis (SSA) (6), a tool that provides a consistent and quantitative technique of describing complex shapes, ultimately leading to the discovery of novel shape biomarkers or unexpected trends, clusters, or outliers (7). By correlating cardiac shape with clinical or functional parameters by means of regression or classification techniques, SSA can also be used in a predictive way (8–12). To date, most SSA studies have focused on 2D cine images to explore motion features for diagnostic or prognostic purposes (13–16), hence potentially losing crucial 3D information that can only be provided by high-resolution volumetric images, such as whole heart (WH) datasets.

Here, we present a novel method that (i) combines 3D, high-resolution WH data with 2D, temporal information provided by cine images, to extract the most complete information out of the data clinically acquired by CMR and (ii) uses a SSA approach to consistently analyze 3D motion *per se*, allowing to gain insight into ventricular kinetics by visually and quantitatively highlighting aspects of ventricular motion that are usually not picked up by traditional approaches. The wide anatomical and functional variations encountered in CHD are ideal to test the capability of this new tool for independent assessment of shape and motion. In this study, we first present the implementation of an automatic pipeline for the processing of volumetric WH and dynamic cine CMR images, where the motion information provided by the cine is propagated onto the WH images. By exploiting an automatic, atlas-based segmentation method and a shape analysis tool, our pipeline can generate a computational surface mesh of the left ventricle (LV) and parametrize the movement of each subject LV during the cardiac cycle. The principal contributors of ventricular shape and motion, generated from the obtained surface meshes and shape deformations via principal component analysis (PCA), are finally presented with powerful visualization tools. We show the potential of the developed methodology to qualitatively and quantitatively evaluate the difference in both LV 3D shape and motion patterns between healthy subjects and congenital repaired aortic stenosis (AS) patients characterized by LV dysfunction. Results from such analysis may provide novel shape and motion biomarker information, which could ultimately improve the understanding of complex cardiac disease.

2. MATERIALS AND METHODS

2.1. Population and Images

Clinically acquired data of 4 congenital repaired aortic stenosis (AS) patients (14 $\pm$ 2 years) and 4 age-matched (17 $\pm$ 3 years) healthy volunteers (control group) were retrospectively used for this study. Ethical approval was obtained by the Institute of Child Health/Great Ormond Street Hospital for Children Research Ethics Committee, and all patients or legal parent or guardian gave informed consent for research use of the data. The patients were diagnosed with chronic ventricular dysfunction as a sequel of congenital aortic stenosis (2 neonatal surgical valvotomy followed by Ross procedure, 1 neonatal balloon aortic valvuloplasty followed by Ross procedure, 1 neonatal surgical valvotomy followed by balloon aortic valvuloplasty). Age, LV end-diastolic volume (EDV), and ejection fraction (EF) of the sample population are shown in **Table 1**. CMR data were acquired at Great Ormond Street Hospital for Children (Great Ormond Street, London, UK) with a 1.5-T scanner (Avanto, Siemens Medical Solutions, Erlangen, Germany), in the patients as part of the clinical follow-up. For each subject, the following two sets of images were used in this study: (i) balanced steady-state free precession (bSSFP) 3D WH (isotropic voxel size of 1.4 mm), acquired during the mid-diastolic rest period in free breathing and with ECG- and respiratory-gating and (ii) retrospectively gated bSSFP cine

images, acquired in breath-hold (~20 frames per cardiac cycle) in the short-axis (SAX) from the valves plane to the apex (slice spacing ~8 mm, in plane isotropic voxel size of 1.4 mm).

2.2. Workflow

The workflow developed in this study is illustrated in **Figures 1** and **2**. The first step involved processing of the subject image data (**Figure 1**, central panel). Highly detailed shape features from the WH sequence were combined with the motion from cine images, in order to provide synthetic high-resolution 3D images throughout the full cardiac cycle (i.e., Motion propagation step in **Figure 1**). An automatic segmentation method previously developed was used to label the main cardiac structures of interest (i.e., Automatic segmentation step in **Figure 1**), and triangulated meshes were obtained from the segmented LV masks (see 2.3.1). Each subject LV j was represented in terms of an anatomical model, i.e., a template mesh $LV_{j,Template}$ and a set of deformations ϕ_{jt} warping the template to each temporal occurrence t of the cardiac cycle (i.e., Anatomical model step in **Figure 1** and paragraph 2.3.2).

In the second step, LV anatomical models generated for each subject were processed to perform shape and motion analysis separately (**Figure 2**). $LV_{j,Template}$ from each subject j was scaled, rigidly aligned (**Figure 2**, 1), and inputted into our SSA framework. For shape analysis alone (**Figure 2**, 2a), ED and ES meshes were analyzed across subjects (see 2.3.3). For motion analysis (**Figure 2**, 2b), each estimated subject-specific motion was used to deform a newly calculated general template shape ($LV_{SuperTemplate}$) from the full population geometrical inputs, allowing study of subject-specific motion without the influence of the subject-specific shape. The resulting temporal datasets were analyzed with an SSA approach similar to that used for pure shape (see 2.3.4).

TABLE 1 | Age, LV EDV, and EF of the 4 AS patients and the 4 healthy volunteers analyzed in this study.

	Age (years)	EDV (mL)	EF (%)
$Control_1$	19	151	63
$Control_2$	13	130	73
$Control_3$	20	119	62
$Control_4$	16	96	66
AS_1	14	113	80
AS_2	14	147	51
AS_3	17	132	68
AS_4	11	64	68

2.3. Computational Framework

2.3.1. Subject Data Processing: Motion Propagation and Automatic Segmentation

An automatic image-processing pipeline able to exploit and combine both 3D WH and temporal information provided by cine CMR images was developed and applied to each subject set of images. First, initial 3D images of the heart ($CINE_{jt}$) were obtained from the cine SAX stack via combination of all the images acquired in the same phase of the cardiac cycle, t, based on the trigger time. DICOM tags referring to slice spacing and orientation were used to guarantee correct slice alignment. Despite their low resolution in the long axis plane, $CINE_{jt}$ images retain the temporal information of the LV motion throughout the full cardiac cycle. To integrate the motion information with the detailed 3D spatial resolution provided by the WH dataset WH_j, synthetic WH images ($WH_{Syn,jt}$) were obtained for each of the 20 acquisition frames via non-rigid image registration (17), i.e., a transformation in which WH_j is deformed and morphed to replicate the LV configuration represented in each $CINE_{jt}$. More specifically (18), all the $CINE_{jt}$ were scored depending on the resemblance with WH_j, the latter quantified by the sum of squared difference between voxel intensities similarity measure (SSD). A threshold was set as $SSD_{Th} = 0.5 * SSD_{Max}$, where SSD_{Max} was the maximum value found for each subject, and $CINE_{jt}$ with $SSD_{jt} < SSD_{Th}$ were classified as "highly similar," while the others as "poorly similar." In case of highly similar $CINE_{jt}$ (usually in the diastolic phase), $WH_{Syn,jt}$ was generated by directly registering

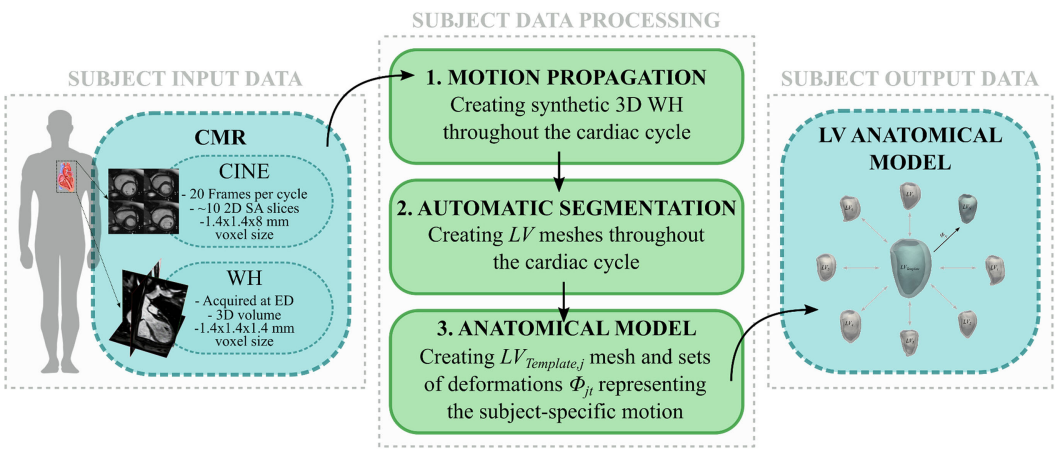

FIGURE 1 | Image-processing pipeline to generate each subject LV anatomical model starting from cine and WH CMR images: (1) Synthetic WH images were created by combining WH with the cine images (2) and segmented with our automatic segmentation method; (3) LV meshes were exported and used to create the subject LV anatomical model.

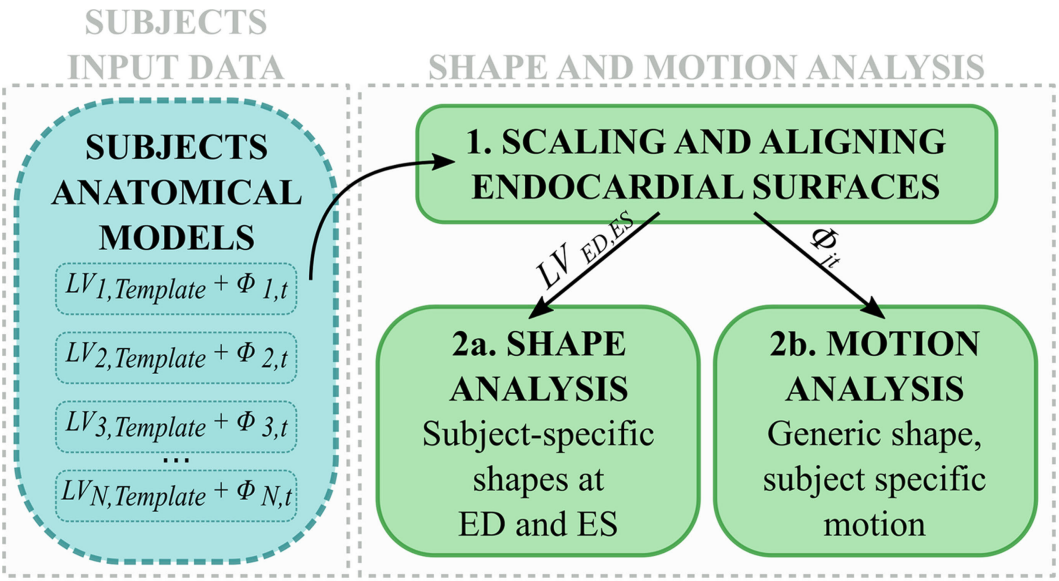

FIGURE 2 | After scaling and alignment (1), subject anatomical models were used to perform (2a) shape analysis on end-diastolic and end-systolic shapes, and (2b) motion analysis after subject-specific shape was removed.

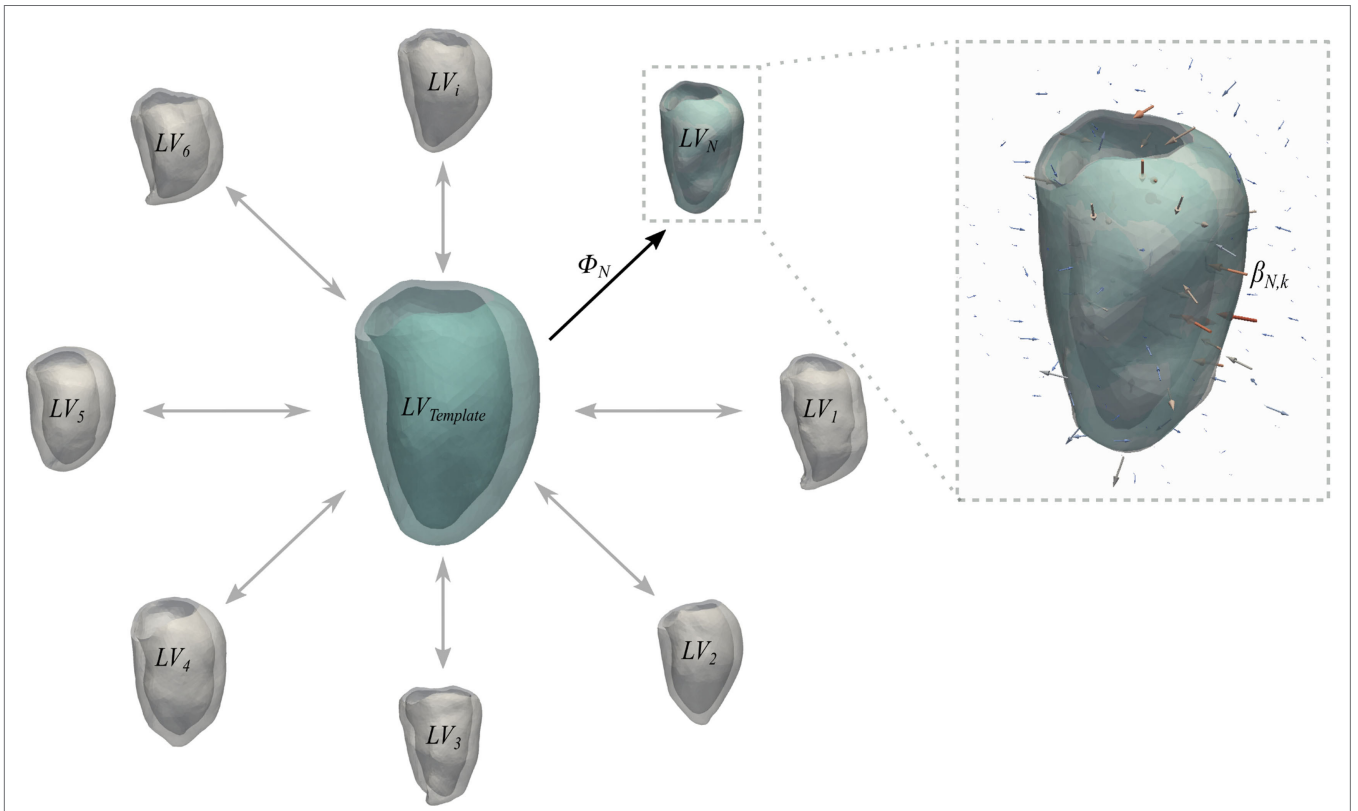

FIGURE 3 | Schematic representation of the concept of anatomical model. Template and deformations ϕ_i toward each shape are estimated with an alternate registration algorithm. The template is initialized as the mean shape and the deformations ϕ_i are estimated using a Large Deformation Diffeomorphic Mappings framework (23, 24). Each deformation ϕ_i is defined by a set of momenta vectors β_{ik} (arrows in the magnified panel) located at the control points grid.

WH_j to $CINE_{jt}$. In case of poorly similar $CINE_{jt}$ (usually in the systolic phase) $WH_{Syn,jt}$ was generated by registering the previously obtained $WH_{Syn,j(t-1)}$ to $CINE_{jt}$. Image registration and transformation were performed exploiting the open-source library `niftyreg` (19). Each $WH_{Syn,jt}$ was segmented using an in-house atlas-based segmentation method previously validated (20, 21), able to automatically label the main cardiac structures of interest.

2.3.2. Subject Data Processing: Creating LV Subject-Specific Anatomical Models

For each subject, LV myocardium masks obtained from segmentation were converted in surface meshes (LV_{jt}) and used to build the subject anatomical model using the code Deformetrica (22).

Briefly, a generic anatomical model is the ensemble of a *Template* mesh, which represents the 3D average of the input shapes, and a set of deformations ϕ_i of the 3D space warping the template to each one of the input shapes (**Figure 3**). Specifically, deformations are represented by a set of vectors—namely, momenta β_{ik}—attached in the 3D space to a control point grid. For the latter, the amount of control points k is chosen by the user, while their position is automatically optimized to densely sample the most variable regions of the template shape (22). Parameters to be set by the user are the resolution λ_w of the shape representation (i.e., how fine are the details we want to capture) and the stiffness of the deformation λ_v, both in millimeters (9).

In this case, the template mesh ($LV_{j,Template}$) represented the time-averaged subject-specific ventricle shape, and the momenta warped the template to each temporal occurrence within the subject-specific cardiac cycle. As suggested by Bruse et al. (7), the parameters (i.e., resolution λ_w and transformation stiffness λ_v) required to run the computation of each subjects anatomical model were iteratively tuned to maximize the matching of the template with the original shapes. This was quantified by computing the average euclidean surface distance between computed (i.e., template-matched) and original shapes. These values were further averaged between the 20 frames to give a unique value for each subject. Surface distances were computed as the pointwise minimum distance of the input surface from a reference surface by exploiting `The Vascular Modeling Toolkit` (25) (VMTK, Orobix, Bergamo, Italy; www.vmtk.org) function `vmtksurfacedistance`. In order to minimize the effect of size and orientation on the next steps of the analysis, all anatomical models were first scaled with respect to each $LV_{j,Template}$ endocardial volume, and then rigidly aligned (26) throughout a generalized procrustes analysis (27) iterative process on the $LV_{j,Template}$ endocardial surfaces, implemented with the functions available in the open-source library `niftyreg` (19).

2.3.3. Shape Analysis

In order to quantitatively describe anatomical shape and motion variations within a population, we herein extensively adopted an SSA approach (7, 11). As the variation of the data within an anatomical model is described by a large number of momenta vectors, output data are not trivial to analyze and interpret. Therefore, the

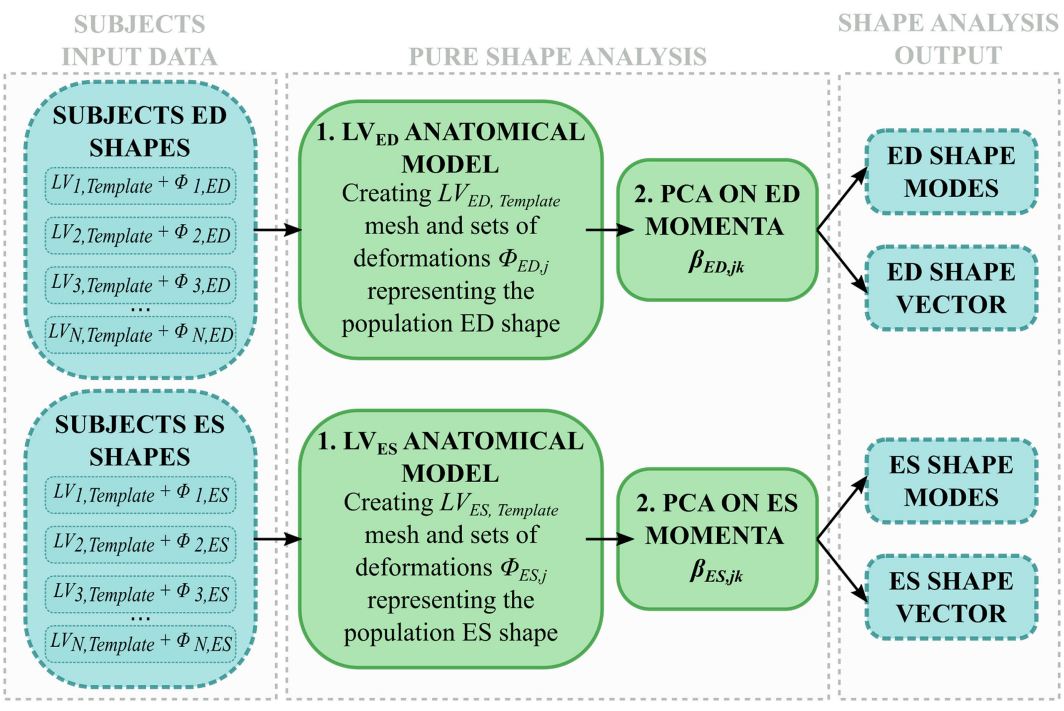

FIGURE 4 | Shape analysis pipeline: for each subject, only ED and ES shapes are used to (1) build an anatomical model representing the LV_{ED}, LV_{ES} shape variability within the population; (2) the momenta vectors are decomposed with a PCA and the resulting shape modes and shape vector are analyzed.

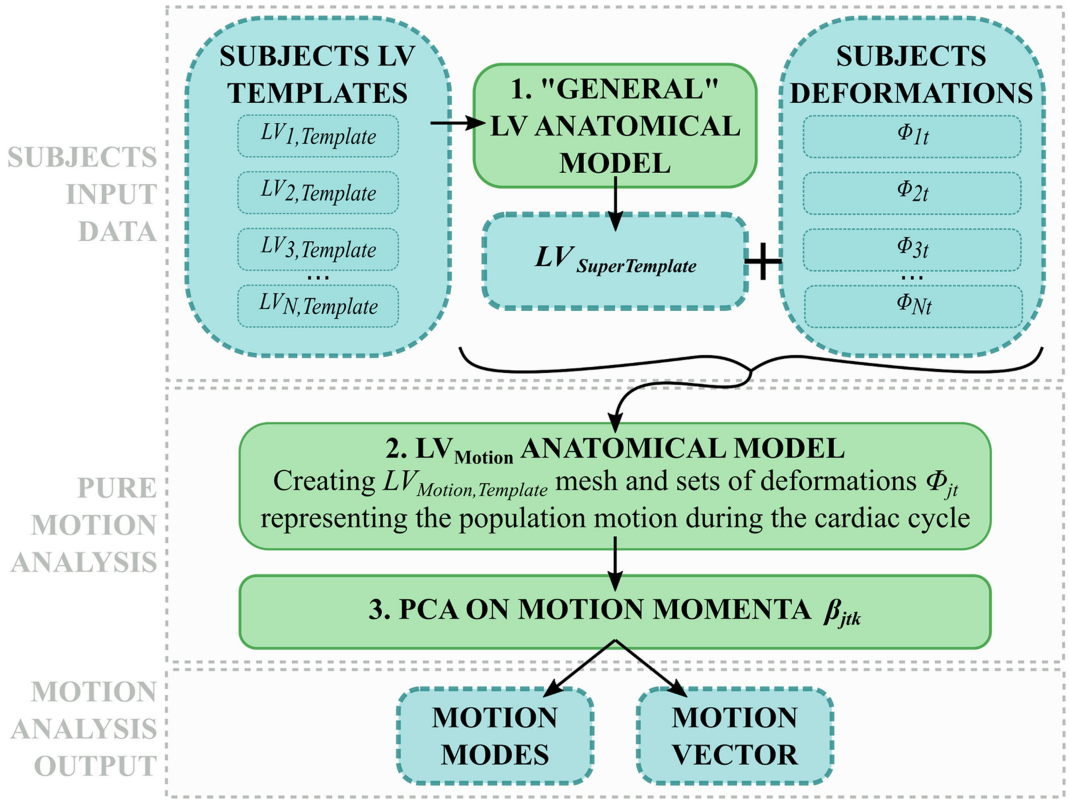

FIGURE 5 | Motion analysis pipeline: (1) each subject $LV_{i,Template}$ is used to compute a general LV shape called $LV_{SuperTemplate}$. (2) The latter is deformed with each subject-specific deformation, and all the obtained shapes are used to build a motion anatomical model (2). The resulting momenta vectors are decomposed with PCA (3), generating motion modes and motion vector describing each subject motion within the cardiac cycle.

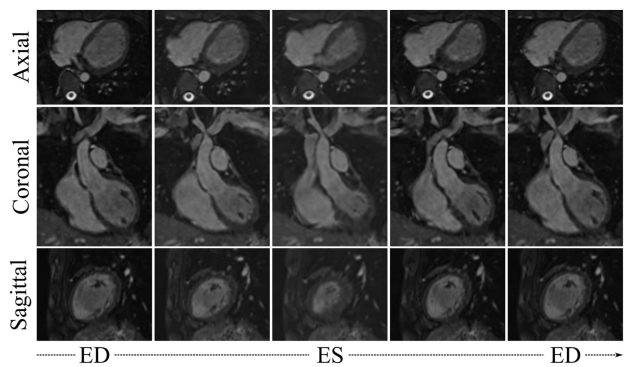

FIGURE 6 | $WH_{Syn,jt}$ from 5 evenly spaced frames of the cardiac cycle of the subject $j = Control_2$, obtained by propagating the subject's motion from the cine dataset onto the high-resolution WH image.

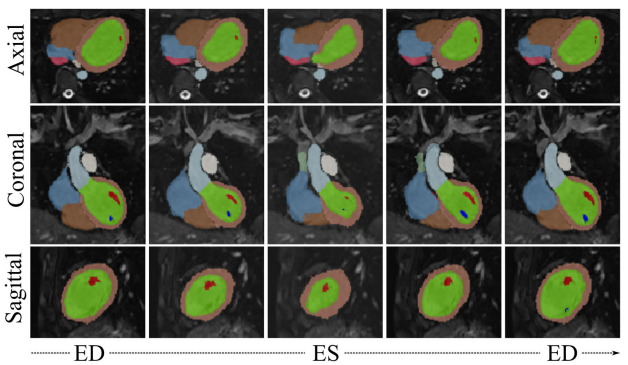

FIGURE 7 | $WH_{Syn,jt}$ with overlaid automatic segmentation from 5 evenly spaced frames of the cardiac cycle of the subject $j = Control_2$. Color code for main segmented structures: lemon-green, LV blood pool; orange, LV myocardium; red and dark blue, papillary muscles; light blue, aorta; brown, right ventricle; azure, right atrium; green, superior vena cava; pink, inferior vena cava; white, pulmonary trunk.

second step required to analyze variability is to apply dimensionality reduction [i.e., PCA (28)] to the momenta vectors, a common mathematical technique that discards any redundant information while keeping principal contributors to variability. Specifically, momenta vectors are projected onto the space that maximizes their covariance, and only the components—also called modes—that contain most of the information are retained as descriptors.

By deforming the template shape along the derived modes toward negative and positive extremes of each mode ($\pm 2\sigma$), it is possible to visualize and thus qualitatively assess the dominant global and local shape variations characterizing the examined population. The amount of information carried for each subject by each mode

is summarized in the shape vector, i.e., a vector where each entry represents how much the template has to be deformed along the corresponding mode in order to match each specific input shape (7, 10). Analysis of the shape vectors allows quantification of the differences in shape within the population.

Shape analysis was applied separately to the end-diastolic (ED) meshes (LV_{ED}) and the end-systolic (ES) meshes (LV_{ES}) (**Figure 4**). The two groups (i.e., 8 shapes each) were separately processed using the abovementioned SSA framework, i.e., two anatomical models were obtained from only ED and ES shapes, respectively, generating $LV_{ED,Template}$, $LV_{ES,Template}$, and associated deformations ($\phi_{ED,j}$, $\phi_{ES,j}$). Both the anatomical models modes and shape vector were then computed and analyzed.

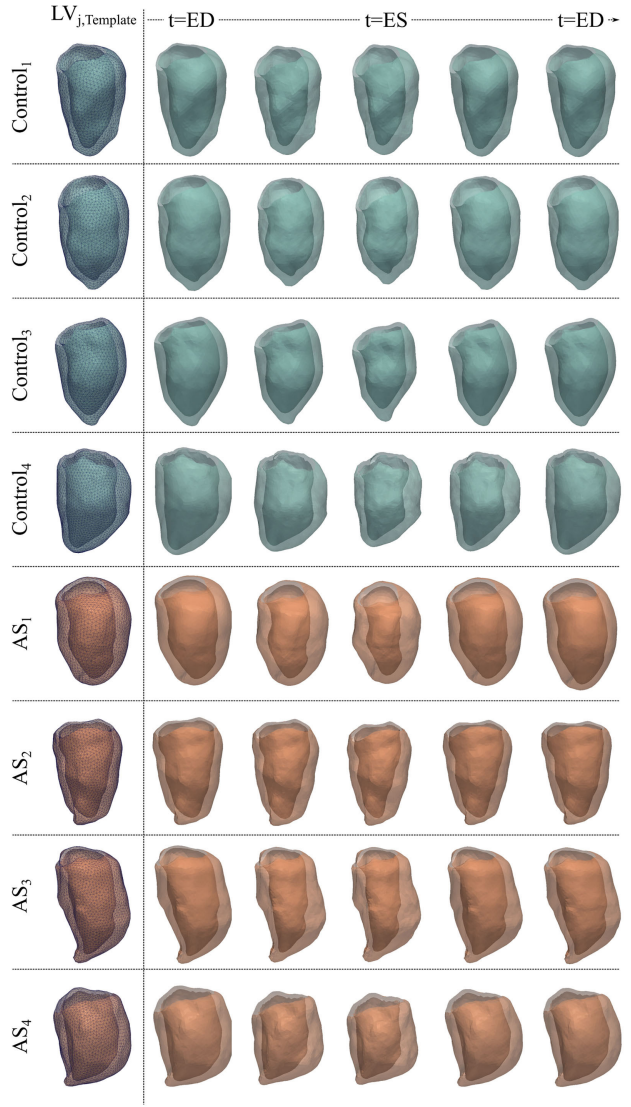

FIGURE 8 | LV_{jt} meshes for the 4 control and 4 AS subjects obtained by deforming subject-specific $LV_{j,Template}$ (first column) with the deformations estimated during the anatomical model computation, to reproduce 5 evenly spaced frames of the cardiac cycle illustrated in Figures 6 and 7 for each subject.

The shape variability expressed by each mode ($LV_{ED,Template} \pm 2\sigma_{modeED,x}$, $LV_{ES,Template} \pm 2\sigma_{modeES,x}$) was first qualitatively observed. This visual description, in conjunction with the respective shape vector coefficients, was then used to numerically characterize each subject LV 3D shape at ED or ES, eventually highlighting shape similarities and differences within the joint population of patients and control group.

2.3.4. Motion Analysis

To extend the SSA framework to the analysis of subject-specific cardiac contraction, motion was interpreted as an ensemble of relatively small, periodical variations of the same shape during the cardiac cycle. In order to describe motion *per se* without geometrical confounding factors, the effect of the subject-specific shape had to be removed from each anatomical model, hence retaining only the subject-specific motion information. Therefore, we exploited the momenta vectors and control point grids computed within each subject anatomical model (see 2.3.2), and we used them to deform a generic template ventricle (namely, $LV_{SuperTemplate}$), obtained as the average shape of all the 8 subjects $LV_{j,Template}$ (**Figure 5**, 1). As a result, $LV_{SuperTemplate}$ deformed throughout the cardiac cycle following each subject-specific contraction pattern. The same SSA framework described above (see 2.3.3) was then applied to this set of 160 shapes (20 frames for each of the 8 subjects, **Figure 5**).

The motion patterns characterized by each mode were first qualitatively assessed by visual observation. By exploiting the quantitative information given by the motion vector, each subject's LV contraction pathway was then numerically described in terms of the identified motion modes. This allowed us to consistently characterize each subject LV dynamics independent from its shape within the same mathematical framework, ideally providing insight into ventricular function and dysfunction.

3. RESULTS

3.1. Subject Data Processing

Visual results from the image processing pipeline are shown in **Figures 6** and **7** for a healthy subject ($Control_2$), where we can observe realistic systolic contraction and myocardial wall thickening on synthetic images (**Figure 6**), as well as an accurate identification of the main cardiac structures performed by our automatic segmentation method (**Figure 7**). Considering our main focus on shape and shape variations more than on cardiac volume quantification, our method allows fast and consistent processing and segmentation of a large amount of WH data, which would be otherwise challenging to process manually.

The parameters required to run the computation of each subject anatomical model were set to $\lambda_w = 13$ mm and $\lambda_v = 23$ mm, leading to an intersubject averaged surface distance between computed (i.e., template-matched) and original shapes of 1.0 mm (*max surface distance* = 2.5 mm in AS_1, *min surface distance* = 0.4 mm in AS_2, *standard deviation* = 0.8 mm). The results of anatomical model computation are shown in **Figure 8** for each subject. In

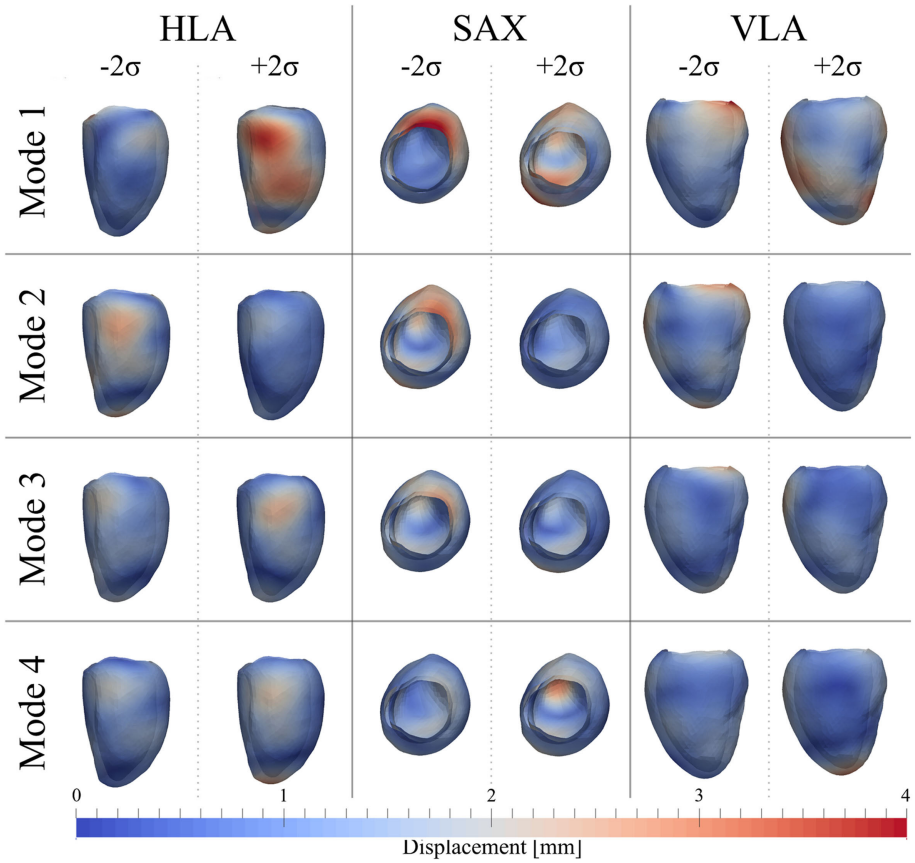

FIGURE 9 | Extreme features ($\pm 2\sigma$) of each of the first 4 modes of the shape analysis on LV shapes at ED are shown in the canonical cardiac views (horizontal long axis (HLA), SAX, and vertical long axis (VLA)). Each depicted shape was obtained by morphing the template shape with the extreme deformation represented by each mode. Colormap represents the distribution of regional deformations within each mode, obtained by deforming the ED template shape along the mode (red, high deformation; blue, low deformation).

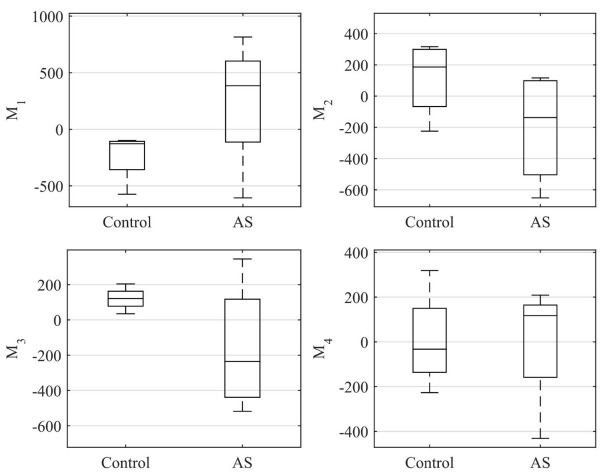

FIGURE 10 | Boxplot showing the variability of the coefficients of the shape vector of LV_{ED} shape analysis for the first 4 modes. Single values are reported in **Table 2**. On each box, the central mark is the median, the edges of the box are the 25th and 75th percentiles, the whiskers extend to the most extreme data points not considered outliers.

particular, we show the $LV_{j,Template}$ shape and examples of meshes resulting from morphing the template with 5 of the estimated deformations, evenly spaced across the cardiac cycle.

3.2. Shape Analysis

3.2.1. ED Shape Analysis

After PCA, the first four modes were considered the most relevant for ED shape analysis, accounting for 76% (28%$Mode_1$, 19%$Mode_2$, 16%$Mode_3$, 13%$Mode_4$) of the total shape information present in the population. **Figure 9** illustrates the extreme features ($\pm 2\sigma$) represented by each mode, in the standard cardiac views. Each depicted shape was obtained by morphing the template shape with the extreme deformation represented by each mode, and the colormap identifies the regions where the highest deformation (in red) occurs. Upon visual inspection, all modes showed a general rounding and circumferential expansion of the basal-mid walls, while the apical region was thinning in $Mode_{1-2\sigma}$ and $Mode_{4-2\sigma}$, and rounding in all the other modes, causing a shortening of the ventricle. $Mode_1$, which reflects the most dominant shape variation in the cohort of patients/controls, was locally characterized by a bulging of the basal inferior and inferolateral walls and the

TABLE 2 | Coefficients of the shape vector of LV_{ED} shape analysis for the first 4 modes.

Subject	$Mode_1$	$Mode_2$	$Mode_3$	$Mode_4$	Subject	$Mode_1$	$Mode_2$	$Mode_3$	$Mode_4$
$Control_1$	−140	316	121	−20	AS_1	816	117	−359	209
$Control_2$	−98	282	204	319	AS_2	−607	−356	−518	120
$Control_3$	−574	91	121	−46	AS_3	390	81	−111	−432
$Control_4$	−116	−224	34	−227	AS_4	380	−652	346	114
Median	−128	186	121	−33	Median	385	−137	−235	117
IQR	137	279	43	156	IQR	363	520	402	164

Control subjects (left) and AS (right). Within each mode, data are summarized in median ± IQR.

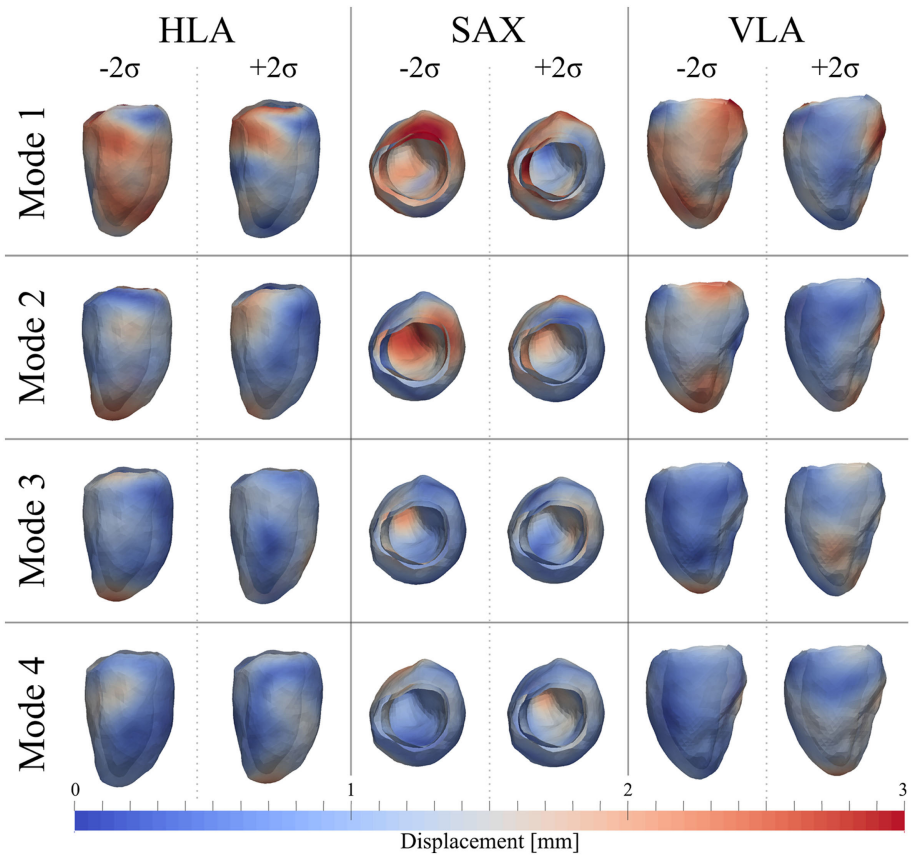

FIGURE 11 | Extreme features (±2σ) of each of the first 4 modes of the shape analysis on LV shapes at ES are shown in the canonical cardiac views (HLA, SAX, and VLA). Each depicted shape was obtained by morphing the template shape with the extreme deformation represented by each mode. Colormap represents the distribution of regional deformations within each mode, obtained by deforming the ES template shape along the mode (red, high deformation; blue, low deformation).

dilation of the mitral valve annulus in $Mode_{1-2\sigma}$, and by a local outward expansion of the mid anteroseptum and anterior wall in $Mode_{1+2\sigma}$. $Mode_{2-2\sigma}$ had an outward dilation and bulging of the mid anteroseptum, the basal inferior and inferolateral walls, while $Mode_{2+2\sigma}$ did not show substantial local deformations. In $Mode_{3-2\sigma}$, there was a bulging of the basal inferior wall, while in $Mode_{3+2\sigma}$, we observed a mild expansion of the mid anterior wall. Finally, the region of the anteroseptum was predominantly bulging in $Mode_{4-2\sigma}$, while the mid anterior wall was expanding outward in $Mode_{4+2\sigma}$.

Figure 10 shows a boxplot representing the variability of the shape vector entries (**Table 2**) for control group and AS patients, allowing to describe each subject LV shape numerically according to the modes previously illustrated. In this example population, overall the control group had an ED shape characterized by the negative extreme of $Mode_1$, the positive extreme of $Mode_2$ and $Mode_3$, and a predominantly negative extreme of $Mode_4$. As expected, the AS patients showed more variability within each mode, with some subjects sitting within the control range of variability, but single subjects being clearly outside the control

range. Given the small sample size (n = 4 for each population), no significant difference ($p > 0.05$ from Mann–Whitney U test) could be found between the two groups medians, for each of the mode. Following the visual results, ED shape of the AS patients was therefore characterized by a local outward expansion of the mid anteroseptum and anterior wall ($Mode_{1+2\sigma}$), outward dilation and bulging of the mid anteroseptum, the basal inferior and inferolateral walls ($Mode_{2-2\sigma}$ and $Mode_{3-2\sigma}$) and mid anterior wall ($Mode_{4+2\sigma}$), according to the descriptions above.

3.2.2. ES Shape Analysis

As for the ED shape analysis, the first four modes were considered the most relevant for ES shape analysis, capturing 75% (28%$Mode_1$, 17%$Mode_2$, 16%$Mode_3$, 14%$Mode_4$) of the shape variability in our population. The deformations represented by each mode are shown in **Figure 11**, as for the ED case. In ES, shape of $Mode_{1-2\sigma}$ was characterized by an overall smaller size, especially locally at the basal inferior and inferolateral walls. In $Mode_{1+2\sigma}$, the base was shortening and the mid walls bulging outward, while the mitral valve annulus was circumferentially smaller, and the basal infero- and anteroseptum and mid inferolateral walls were reduced. In $Mode_{2-2\sigma}$, the apex and the apical walls were bent more anteriorly and toward the right, the basal lateral wall was positioned more posteriorly, and the mitral valve annulus was more dilated, while in $Mode_{2+2\sigma}$, the septum was positioned more posteriorly. Shape in $Mode_{3-2\sigma}$ was generally shorter, the apex rounder and slightly bent anteriorly and toward the right, while in $Mode_{3+2\sigma}$, the mid walls were circumferentially shrunk, especially in the apical lateral wall. Finally, in $Mode_{4-2\sigma}$, the septal wall was slightly reduced, especially in the mid inferoseptum, and in $Mode_{4+2\sigma}$, the apex was rounder and bent more posteriorly.

The ES shape vector entries variability for control group and AS patients are represented in the boxplot in **Figure 12** and **Table 3**. As for the ED case, variance of the control group coefficients was overall less than that for the AS patients. In particular, coefficients of the control group were all in the negative extreme for $Mode_1$, predominantly positive in $Mode_2$ and predominantly negative in $Mode_3$ and $Mode_4$. Even though shape vector entries for single AS patients showed differences from the control group, not all the shape modes could clearly distinguish the two groups, similar to the ED shape analysis. Also in this case, the small sample size (n = 4 for each population) did not allow to show significant difference (p > 0.05 from Mann–Whitney U test) between the two groups medians, for each of the mode.

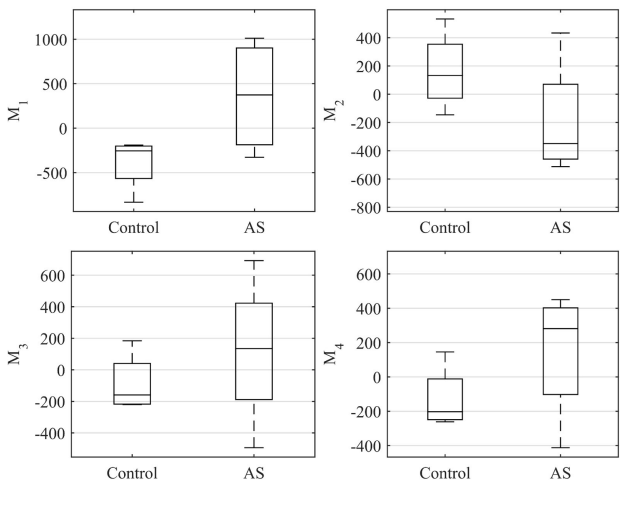

FIGURE 12 | Boxplot showing the variability of the coefficients of the shape vector of LV_{ES} shape analysis for the first 4 modes. Single values are reported in **Table 3**. On each box, the central mark is the median, the edges of the box are the 25th and 75th percentiles, the whiskers extend to the most extreme data points not considered outliers.

3.3. Motion Analysis

After PCA, the first four modes were considered the most relevant for motion analysis alone, accounting for 70% (52%$Mode_1$, 7%$Mode_2$, 6%$Mode_3$, 5%$Mode_4$) of the population total variability in motion information. **Figure 13** illustrates the extreme motion patterns represented by each mode, in standard cardiac views. Similar to the shape example, here each figure was obtained by morphing $LV_{SuperTemplate}$ with the extreme deformations represented by each mode ($\pm 2\sigma$), with the arrows identifying local motion direction and magnitude (red color highlights the regions of highest motion). After qualitative visual assessment, $Mode_1$ represented the overall ventricular contraction ($Mode_{1-2\sigma}$) and expansion ($Mode_{1+2\sigma}$), which characterize the systole–diastole alternation typical of the cardiac cycle. On top of this general trend, contraction in $Mode_{1-2\sigma}$ prevailed in regions such as the basal and mid anterior wall, but also mid lateral and mid inferior walls, while the basal anteroseptum was the most affected by expansion in $Mode_{1+2\sigma}$. Toward the negative extreme, in $Mode_{2-2\sigma}$ the apex and apical portion of the lateral wall moved rightward, and the basal anterolateral wall moved up, anteriorly and rightward. Toward the positive extreme ($Mode_{2+2\sigma}$), the basal anteroseptum

TABLE 3 | Coefficients of the shape vector of LV_{ES} shape analysis for the first 4 modes.

Subject	$Mode_1$	$Mode_2$	$Mode_3$	$Mode_4$	Subject	$Mode_1$	$Mode_2$	$Mode_3$	$Mode_4$
$Control_1$	−190	175	−220	−170	AS_1	1,012	434	117	208
$Control_2$	−299	533	−104	146	AS_2	−328	−292	693	355
$Control_3$	−834	90	184	−262	AS_3	792	−406	153	−413
$Control_4$	−212	−145	−214	−237	AS_4	−45	−512	−494	450
Median	−256	133	−159	−203	Median	374	−349	135	281
IQR	226	234	184	152	IQR	963	322	323	326

Control subjects (left) and AS (right). Within each mode, data are summarized in median ± IQR.

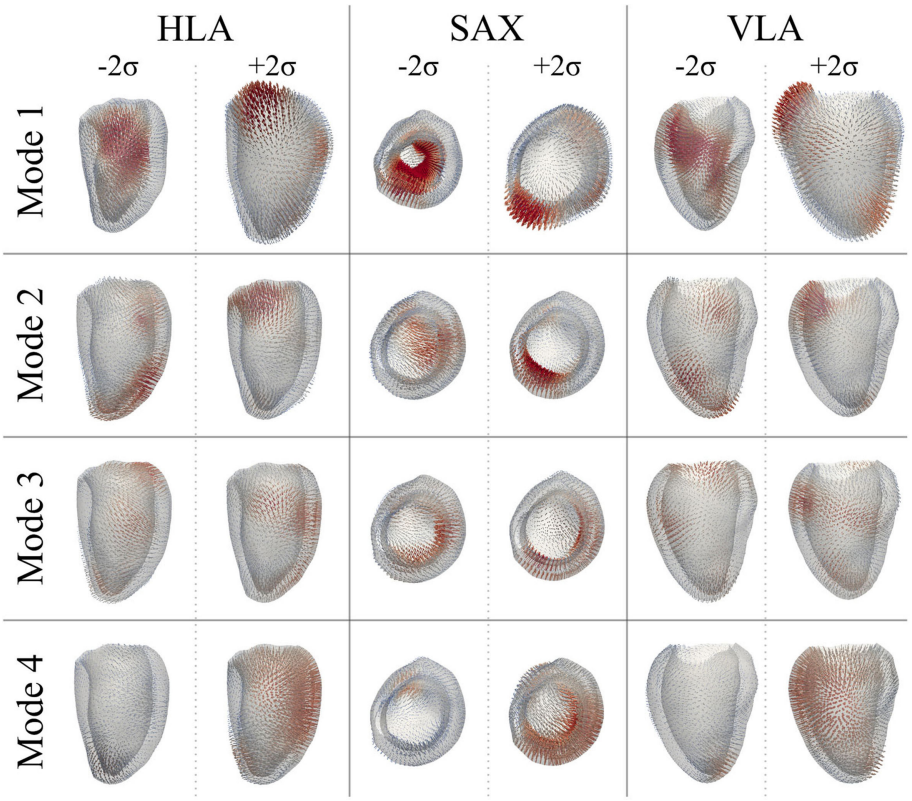

FIGURE 13 | Extreme motion patterns ($\pm 2\sigma$) represented by each mode of the motion analysis on LV shapes are shown in the canonical cardiac views (HLA, SAX, and VLA). Each depicted shape was obtained by morphing the $LV_{SuperTemplate}$ shape with the extreme deformation represented by each mode. Arrows represents the direction and magnitude of the movement from the template (red color highlights the regions of highest motion).

and anterior wall moved downward, while the apical septum moved posteriorly. $Mode_{3-2\sigma}$ was characterized by the basal portion of the lateral wall moving upward and anteriorly, the mid anterior and anterolateral walls moving upward and rightward, and the whole apical region moving anteriorly. $Mode_{3+2\sigma}$ was described by a downward movement of both the mid anterior wall and the basal lateral wall, and by an upward-rightward movement of the apical lateral wall. Finally, in $Mode_{4-2\sigma}$, the apical septum and lateral walls were moving upward and posteriorly, while in $Mode_{4+2\sigma}$, the basal and mid anterior and lateral walls were contracting, with the apical septum moving anteriorly and rightward. Looking at the valves plane, this moved upward in $Mode_{1+2\sigma}$, $Mode_{2-2\sigma}$, and $Mode_{4-2\sigma}$, while it moved downward in all the other mode occurrences.

In **Figure 14**, we plotted the values of the motion vectors over two cardiac cycles to understand which motion pattern was predominant in every subject, and in which part of the cardiac cycle. As a proof of concept, we show the potentiality of this method in quantifying local 3D variations in motion patterns, by showing extreme results obtained with the examined population. The trend of the shape vector coefficients relating to $Mode_1$ showed to be consistent between all subjects, suggesting that the normal overall pattern of contraction and expansion between systole and diastole is maintained in both patients and control group. $Mode_2$, mostly accounting for basal and apical motion, resulted to be expressed in a completely opposite way for $Control_4$ (purple line) and AS_3 (red dashed line), during the whole cardiac cycle. This can be seen in Videos S1–S3 in Supplementary Material, where during the systolic phase the apex of AS_3 strongly moves to the right, and the basal septum of $Control_4$ moves downward. Extreme behaviors in $Mode_3$ were expressed by $Control_3$ (yellow line) and AS_2 (azure dashed line), and in $Mode_4$ by AS_2, AS_3 and AS_1, AS_4. However, considering the less importance of these modes compared to the first two, the visual effect on the overall motion was more difficult to identify, which is why a quantitative analysis like that shown in **Figure 14** could help highlight small issues in LV motion, not easily detectable at visual observation.

4. DISCUSSION

In this study, we presented an automated medical image processing pipeline for qualitative and quantitative analysis of LV 3D shape and motion patterns from clinically acquired CMR data, and apply it to a sample population of AS patients and aged-matched healthy volunteers. The main novelty of this work is the development of an image analysis framework that allows combination of temporal (cine) and high resolution spatial information (WH) for 3D subject-specific shape and motion analyses, which are

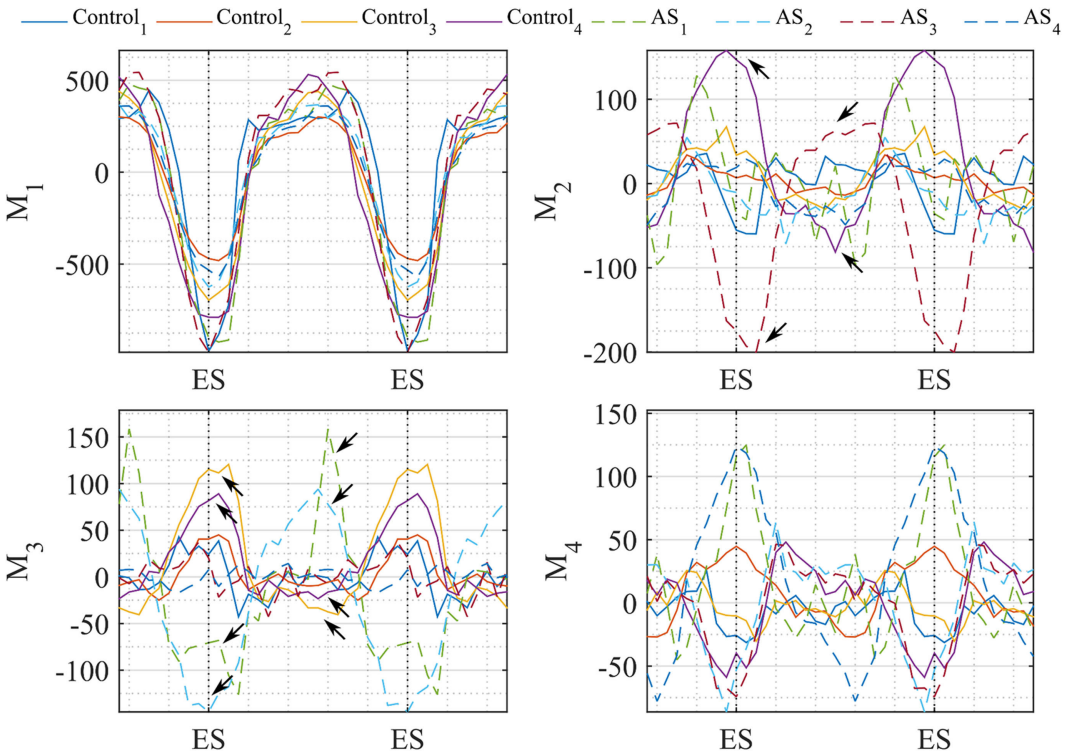

FIGURE 14 | Coefficients of the motion vector plotted against time (2 cardiac cycles are herein represented). Each line represents one subject, i.e., Control subjects are plotted in continuous line and AS in dashed line. Temporal variation of the coefficients resulting from our motion analysis is plotted for the first 4 modes. Arrows highlight the values where coefficients differ mostly between control-AS subjects comparison.

usually considered separately due to the lack of comprehensive and high-resolution 4D CMR image sequences. Dominant shape and motion patterns in both diseased and healthy cohorts were visualized in 3D and could be quantified for in-depth assessment of cardiac function. Results showed that in congenital repaired aortic stenosis, pure analysis of cardiac morphology can be complemented by detailed motion analysis, highlighting regional differences in ventricular contraction patterns.

Since our approach is based on image sequences currently acquired in clinical practice, it does not require further acquisition protocols or increased scanning time. Our pipeline allows using the full image data provided by clinical CMR acquisition, and thus provides more insight than each image set by itself. Shape analysis has been shown in the literature to be a promising technique for differentiating healthy from pathological subjects, and for quantitatively classifying and describing anatomical shapes (9–12, 29, 30). When applied to ED and ES ventricles in our example population, shape analysis allowed us to observe and quantify differences between AS and controls for single cases. However, due to the small sample size, we were not able to claim any statistically significant difference between the two populations. Specifically, due to the fact that the overall anatomical shape of this set of AS was not excessively abnormal, we do not expect any significant shape difference between the two populations, even in larger cohorts. Generalizing from this result we can hypothesize that, depending on the examined population, shape analysis alone may be not sufficient to robustly classify and describe pathological states based only on anatomy differences, especially in those subjects where the cardiac pathology mostly arises due to contraction/functional deficiency and not as a consequence of abnormal morphology. In this sense, our proposed motion analysis method may represent a new tool to summarize, complement, and enrich the information provided by separate CMR imaging sequences. By removing the subject-specific shape information, retaining only the 3D details related to the subject-specific dynamics applied to a generic representative shape of the population ($LV_{SuperTemplate}$), our motion analysis method could become useful for the visualization of differences in motion between healthy and pathological subjects, which may otherwise be hidden behind individual shape features. This tool could hence be used for intuitive, easily comprehensible visualization of motion differences and dominant patterns, even in clinical practice. Moreover, if used in comparison with a quantitative analysis of the motion vector, this technique could numerically highlight cardiac motion differences that may be difficult to catch by eye, hence facilitating objective patient diagnosis.

The main limitation of this work is the small sample size used to test the computational framework. With a larger number of healthy subjects, it would be possible to build a comprehensive healthy population atlas, which would allow further, more elaborate statistical analysis. We are currently working on increasing the number of subjects to be included in the tested

population, and also on performing further validation. It is to be noted that our analysis pipeline is independent from a specific anatomical region of the heart, i.e., it can be used for shape and motion analysis on structures different from the LV, provided that these are imaged in both WH and cine CMR sequences. Other than for better understanding the pathology, results (i.e., in particular motion propagation plus PCA) could also be used as input for structural or computational fluid dynamics computer simulations with moving boundaries, in particular to provide subject-specific geometries and boundary conditions for realistic analysis of ventricular mechanics or interaction with cardiac devices.

In conclusion, this preliminary work demonstrates the feasibility of using statistical shape analysis in combination with motion analysis based on CMR image data and its potential to detect new shape and motion biomarkers, for a detailed visual and quantitative analysis of cardiac function. Our processing pipeline is fully automatic and requires only basic user input, which makes it an attractive alternative to tedious manual segmentation, measurements, and motion mapping as currently done in clinical practice. Applying state-of-the-art automatic segmentation algorithms in conjunction with statistical shape modeling tools to cardiac image data allows detailed analysis of cardiac shape and motion patterns, which may ultimately facilitate and improve diagnosis and understanding of complex cardiac disease.

AUTHOR CONTRIBUTIONS

BB designed the study, implemented and tested the computational framework, and drafted the manuscript. JLB supported the implementation of the statistical shape analysis and revised the manuscript. MAZ supported the implementation of the image processing pipeline and revised the manuscript. HNN enrolled the patients and acquired the images used for this study. AMT and SS conceived the study, participated in its design and coordination, and helped to draft the manuscript. All the authors read and approved the final manuscript.

FUNDING

This research was supported by EPSRC-funded UCL Centre for Doctoral Training in Medical Imaging, the Department of Health's NIHR-funded Biomedical Research Centre at Great Ormond Street Hospital, Fondation Leducq, Innovative Engineering for Health award by the Wellcome Trust, Engineering and Physical Sciences Research Council (EPSRC) and FP7 integrated project MD-Paedigree (partially funded by the European Commission). This report is independent research from the National Institute for Health Research Biomedical Research Centre Funding Scheme. The views expressed in this publication are those of the author(s) and not necessarily those of the National Health Service, the National Institute for Health Research or the Department of Health.

SUPPLEMENTARY MATERIAL

The Supplementary Material for this article can be found online at http://journal.frontiersin.org/article/10.3389/fped.2017.00034/full#supplementary-material.

VIDEO S1 | Arrow representation of $Mode_2$ throughout the cardiac cycle for $Control_4$ (light blue) and AS_3 (orange) in the HLA view. One can notice that during the systolic phase the apex of AS_3 moves to the right, while the basal septum of $Control_4$ moves downwards.

VIDEO S2 | Arrow representation of $Mode_2$ throughout the cardiac cycle for $Control_4$ (light blue) and AS_3 (orange) in the VLA view.

VIDEO S3 | Arrow representation of $Mode_2$ throughout the cardiac cycle for $Control_4$ (light blue) and AS_3 (orange) in the SA view.

REFERENCES

1. Vieira MS, Hussain T, Figueroa CA. Patient-specific image-based computational modeling in congenital heart disease: a clinician perspective. *J Cardiol Ther* (2015) 2(6):436–48. doi:10.17554/j.issn.2309-6861.2015.02.96
2. Dragulescu A, Mertens L, Friedberg MK. Interpretation of left ventricular diastolic dysfunction in children with cardiomyopathy by echocardiography problems and limitations. *Circulation* (2013) 6(2):254–61. doi:10.1161/CIRCIMAGING.112.000175
3. Singh GK, Holland MR. Diastolic dysfunction in pediatric cardiac patients: evaluation and management. *Curr Treat Options Cardiovasc Med* (2010) 12(5):503–17. doi:10.1007/s11936-010-0086-5
4. Zile MR, Brutsaert DL. New concepts in diastolic dysfunction and diastolic heart failure: part I diagnosis, prognosis, and measurements of diastolic function. *Circulation* (2002) 105(11):1387–93. doi:10.1161/hc1102.105289
5. Kass DA. Assessment of diastolic dysfunction: invasive modalities. *Cardiol Clin* (2000) 18(3):571–86. doi:10.1016/s0733-8651(05)70162-4
6. Young AA, Frangi AF. Computational cardiac atlases: from patient to population and back. *Exp Physiol* (2009) 94(5):578–96. doi:10.1113/expphysiol.2008.044081
7. Bruse JL, McLeod K, Biglino G, Ntsinjana HN, Capelli C, Hsia T-Y, et al. A statistical shape modelling framework to extract 3D shape biomarkers from medical imaging data: assessing arch morphology of repaired coarctation of the aorta. *BMC Med Imaging* (2016) 16(1):1. doi:10.1186/s12880-016-0142-z
8. Biglino G, Capelli C, Bruse J, Bosi GM, Taylor AM, Schievano S. Computational modelling for congenital heart disease: how far are we from clinical translation? *Heart* (2016) 103(2):98–103. doi:10.1136/heartjnl-2016-310423
9. Bruse JL, Cervi E, McLeod K, Biglino G, Sermesant M, Pennec X, et al. Looks do matter! Aortic arch shape after hypoplastic left heart syndrome palliation correlates with cavopulmonary outcomes. *Ann Thorac Surg* (2017) 103(2):645–54. doi:10.1016/j.athoracsur.2016.06.041
10. Mansi T, Durrleman S, Bernhardt B, Sermesant M, Delingette H, Voigt I, et al. A statistical model of right ventricle in tetralogy of fallot for prediction of remodelling and therapy planning. *International Conference on Medical Image Computing and Computer-Assisted Intervention*. Springer (2009). p. 214–21.
11. Mansi T, Voigt I, Leonardi B, Pennec X, Durrleman S, Sermesant M, et al. A statistical model for quantification and prediction of cardiac remodelling: application to tetralogy of fallot. *IEEE Trans Med Imaging* (2011) 30(9):1605–16. doi:10.1109/TMI.2011.2135375
12. McLeod K, Wall S, Leren IS, Saberniak J, Haugaa KH. Ventricular structure in ARVC: going beyond volumes as a measure of risk. *J Cardiovasc Magn Reson* (2016) 18(1):73. doi:10.1186/s12968-016-0291-9
13. Ardekani S, Jain S, Sanzi A, Corona-Villalobos CP, Abraham TP, Abraham MR, et al. Shape analysis of hypertrophic and hypertensive heart disease using MRI-based 3D surface models of left ventricular geometry. *Med Image Anal* (2016) 29:12–23. doi:10.1016/j.media.2015.11.004
14. Chandrashekara R, Rao A, Sanchez-Ortiz GI, Mohiaddin RH, Rueckert D. Construction of a statistical model for cardiac motion analysis using nonrigid image registration. *Biennial International Conference on*

Information Processing in Medical Imaging. Springer (2003). p. 599–610. doi:10.1007/978-3-540-45087-0_50
15. Farrar G, Suinesiaputra A, Gilbert K, Perry JC, Hegde S, Marsden A, et al. Atlas-based ventricular shape analysis for understanding congenital heart disease. *Prog Pediatr Cardiol* (2016) 43:61–9. doi:10.1016/j.ppedcard.2016.07.010
16. Wu J, Wang Y, Simon MA, Brigham JC. A new approach to kinematic feature extraction from the human right ventricle for classification of hypertension: a feasibility study. *Phys Med Biol* (2012) 57(23):7905. doi:10.1088/0031-9155/57/23/7905
17. Rueckert D, Sonoda LI, Hayes C, Hill DL, Leach MO, Hawkes DJ. Nonrigid registration using free-form deformations: application to breast MR images. *IEEE Trans Med Imaging* (1999) 18(8):712–21.
18. Biffi B, Giusti G, Zuluaga MA, Bruse JL, Taylor AM, Schievano S. Automatic processing of cardiac MR images: towards clinical translation of patient-specific modelling. *VPH2016, Book of Abstracts*. University of Amsterdam (2016). p. 505–8.
19. Modat M, Ridgway GR, Taylor ZA, Lehmann M, Barnes J, Hawkes DJ, et al. Fast free-form deformation using graphics processing units. *Comput Methods Programs Biomed* (2010) 98(3):278–84. doi:10.1016/j.cmpb.2009.09.002
20. Zuluaga MA, Cardoso MJ, Modat M, Ourselin S. Multi-atlas propagation whole heart segmentation from MRI and CTA using a local normalised correlation coefficient criterion. *International Conference on Functional Imaging and Modeling of the Heart*. Springer (2013). p. 174–81. doi:10.1007/978-3-642-38899-6_21
21. Biffi B, Zuluaga MA, Ourselin S, Taylor AM, Schievano S. Papillary muscle segmentation from a multi-atlas database: a feasibility study. *International Workshop on Statistical Atlases and Computational Models of the Heart*. Springer (2015). p. 80–9. doi:10.1007/978-3-319-28712-6_9
22. Durrleman S, Prastawa M, Charon N, Korenberg JR, Joshi S, Gerig G, et al. Morphometry of anatomical shape complexes with dense deformations and sparse parameters. *Neuroimage* (2014) 101:35–49. doi:10.1016/j.neuroimage.2014.06.043
23. Durrleman S, Pennec X, Trouvé A, Ayache N. Statistical models of sets of curves and surfaces based on currents. *Med Image Anal* (2009) 13(5):793–808. doi:10.1016/j.media.2009.07.007
24. Vaillant M, Glaunès J. Surface matching via currents. *Biennial International Conference on Information Processing in Medical Imaging*. Springer (2005). p. 381–92. doi:10.1007/11505730_32
25. Antiga L, Piccinelli M, Botti L, Ene-Iordache B, Remuzzi A, Steinman DA. An image-based modeling framework for patient-specific computational hemodynamics. *Med Biol Eng Comput* (2008) 46(11):1097–112. doi:10.1007/s11517-008-0420-1
26. Ourselin S, Roche A, Subsol G, Pennec X, Ayache N. Reconstructing a 3D structure from serial histological sections. *Image Vis Comput* (2001) 19(1):25–31. doi:10.1016/s0262-8856(00)00052-4
27. Gower JC. Generalized procrustes analysis. *Psychometrika* (1975) 40(1): 33–51.
28. Jolliffe I. *Principal Component Analysis*. Wiley Online Library (2002). doi:10.1007/b98835
29. Lewandowski AJ, Augustine D, Lamata P, Davis EF, Lazdam M, Francis J, et al. The preterm heart in adult life: cardiovascular magnetic resonance reveals distinct differences in left ventricular mass, geometry and function. *Circulation* (2012) 127(2):197–206. doi:10.1161/CIRCULATIONAHA
30. Bruse JL, Mcleod K, Biglino G, Ntsinjana HN, Capelli C, Hsia T-Y, et al. A non-parametric statistical shape model for assessment of the surgically repaired aortic arch in coarctation of the aorta: how normal is abnormal? *International Workshop on Statistical Atlases and Computational Models of the Heart*. Springer (2015). p. 21–9. doi:10.1007/978-3-319-28712-6_3

Conflict of Interest Statement: The authors declare that the research was conducted in the absence of any commercial or financial relationships that could be construed as a potential conflict of interest.

frontiers in Pediatrics

ORIGINAL RESEARCH
published: 22 February 2017
doi: 10.3389/fped.2017.00025

Model of Human Fetal Growth in Hypoplastic Left Heart Syndrome: Reduced Ventricular Growth Due to Decreased Ventricular Filling and Altered Shape

Sukriti Dewan[1], Adarsh Krishnamurthy[1,2], Devleena Kole[1], Giulia Conca[1], Roy Kerckhoffs[1], Michael D. Puchalski[3], Jeffrey H. Omens[1,4], Heather Sun[5], Vishal Nigam[5] and Andrew D. McCulloch[1,4]**

[1] Department of Bioengineering, University of California at San Diego, La Jolla, CA, USA, [2] Department of Mechanical Engineering, Iowa State University, Ames, IA, USA, [3] Pediatric Cardiology, Primary Children's Hospital, University of Utah, Salt Lake City, UT, USA, [4] Department of Medicine, University of California at San Diego, La Jolla, CA, USA, [5] Pediatric Cardiology, Rady Children's Hospital, University of California at San Diego, San Diego, CA, USA

OPEN ACCESS

Edited by:
Giovanni Biglino,
University of Bristol, UK

Reviewed by:
Silvia Schievano,
University College London, UK
Richard Figliola,
Clemson University, USA

***Correspondence:**
Vishal Nigam
vnigam@ucsd.edu;
Andrew D. McCulloch
amcculloch@ucsd.edu

Specialty section:
This article was submitted to Pediatric Cardiology, a section of the journal Frontiers in Pediatrics

Received: 02 December 2016
Accepted: 01 February 2017
Published: 22 February 2017

Citation:
Dewan S, Krishnamurthy A, Kole D, Conca G, Kerckhoffs R, Puchalski MD, Omens JH, Sun H, Nigam V and McCulloch AD (2017) Model of Human Fetal Growth in Hypoplastic Left Heart Syndrome: Reduced Ventricular Growth Due to Decreased Ventricular Filling and Altered Shape. Front. Pediatr. 5:25. doi: 10.3389/fped.2017.00025

Introduction: Hypoplastic left heart syndrome (HLHS) is a congenital condition with an underdeveloped left ventricle (LV) that provides inadequate systemic blood flow postnatally. The development of HLHS is postulated to be due to altered biomechanical stimuli during gestation. Predicting LV size at birth using mid-gestation fetal echocardiography is a clinical challenge critical to prognostic counseling.

Hypothesis: We hypothesized that decreased ventricular filling *in utero* due to mitral stenosis may reduce LV growth in the fetal heart via mechanical growth signaling.

Methods: We developed a novel finite element model of the human fetal heart in which cardiac myocyte growth rates are a function of fiber and cross-fiber strains, which is affected by altered ventricular filling, to simulate alterations in LV growth and remodeling. Model results were tested with echocardiogram measurements from normal and HLHS fetal hearts.

Results: A strain-based fetal growth model with a normal 22-week ventricular filling (1.04 mL) was able to replicate published measurements of changes between mid-gestation to birth of mean LV end-diastolic volume (EDV) (1.1–8.3 mL) and dimensions (long-axis, 18–35 mm; short-axis, 9–18 mm) within 15% root mean squared deviation error. By decreasing volumetric load (–25%) at mid-gestation in the model, which emulates mitral stenosis *in utero*, a 65% reduction in LV EDV and a 46% reduction in LV wall volume were predicted at birth, similar to observations in HLHS patients. In retrospective blinded case studies for HLHS, using mid-gestation echocardiographic data, the model predicted a borderline and severe hypoplastic LV, consistent with the patients' late-gestation data in both cases. Notably, the model prediction was validated by testing for changes in LV shape in the model against clinical data for each HLHS case study.

Conclusion: Reduced ventricular filling and altered shape may lead to reduced LV growth and a hypoplastic phenotype by reducing myocardial strains that serve as a myocyte growth stimulus. The human fetal growth model presented here may lead to a clinical tool that can help predict LV size and shape at birth based on mid-gestation LV echocardiographic measurements.

Keywords: HLHS, growth hormone, biomechanics, sarcomeres, computational model, patient-specific modeling, mechanobiology

INTRODUCTION

Hypoplastic left heart syndrome (HLHS), one of the most severe congenital heart defects, occurs when the left ventricle (LV) is not adequate to provide sufficient blood flow to the systemic circulation (1). Despite recent improvements in clinical management, HLHS patients face substantial morbidity and mortality, with a 1-year transplant-free survival of 64–74% (2–4). The role of biomechanics in normal and pathologic cardiac development *in utero* is an understudied topic. Experimental studies suggest that perturbations in biomechanical stimuli during development can result in HLHS (5–7). The treatment of HLHS can be one of the most expensive neonatal diagnoses, so there is a need for improved quantitative approaches.

Fetal growth occurs *via* hyperplasia (cell proliferation by cell division) and hypertrophy (enlargement of cell size by addition of sarcomeres) and is regulated by developmental stage, growth factors, and hemodynamic load (8–11). During early stages of gestation, when the cardiac structures are still developing, growth is highly regulated by growth factors when hemodynamic load is significantly low. However, after 10–14 weeks of gestation, when the process of cardiac looping is complete and cardiac chambers are fully formed structurally, hemodynamic load is gradually increasing and accelerates hypertrophic cardiac growth significantly (5, 8).

Several studies have shown that cardiac morphogenesis and remodeling adapts in response to changes in biomechanical stress or strain (11–16). Experimental studies in isolated cardiomyocytes have reported sarcomere addition in series or parallel leading to cellular hypertrophy in response to mechanical stretch (13, 17, 18). Altered loading conditions significantly affect gene expression changes at the cellular level via proliferation, mechanotransduction, and hypertrophy signaling pathways resulting in increased mRNA and changes in cardiomyocyte size and shape (8, 19–23). Embryonic sheep, chicken, and zebrafish models with decreased ventricular filling also develop ventricular hypoplasia (6, 7, 14, 24, 25). Partial LV inflow obstruction in the fetal sheep model at mid-gestation resulted in an early form of HLHS within 7 days of the surgical procedure as a 30% decrease in cardiac output and a 70% decrease in LV/right ventricle ratio was reported (6, 13, 16, 26, 27). Additionally, studies have shown that restoring blood flow to the LV can "hemodynamically rescue" the chick model of HLHS (26, 28–34). Importantly, fetuses with narrowing or obstruction of the foramen ovale, mitral valve, or aortic valve frequently develop HLHS (35–37).

Based on these observations, it is likely that decreased biomechanical load associated with impaired ventricular filling can lead to ventricular hypoplasia. Obstruction at the level of the mitral valve (stenosis/atresia) or foramen ovale result in decreased diastolic filling of the LV. This perturbed filling could result in decreased passive stretching of ventricular cardiomyocytes, which would alter the biomechanical-mediated signaling response, thereby affecting cellular and organ level growth (13, 17, 18, 23). Given the limited understanding of the molecular pathogenesis of HLHS and the poor outcomes of current treatments, there is an urgent need to characterize the effects of abnormal ventricular filling and cardiac stretch on embryonic cardiomyocyte growth in the ventricle.

Multiscale computational models of LV growth and remodeling have been used to provide insight into the morphogenetic process of cardiac looping in the embryonic chick heart, cardiac growth in the postnatal rat, and the mechanical mechanisms regulating cardiac remodeling in the adult heart (26, 28, 30–33, 38–41). However, there has been limited use of *in silico* models to study ventricular mechanics and growth in human congenital heart disease. While there have been a limited number of simulations examining the blood flow patterns in congenital heart disease patients (42, 43), there have been no reports of computational models of alterations in LV growth and morphogenesis in human HLHS.

Computational growth modeling of healthy and diseased human fetal hearts requires structural and functional measurements that can accurately elucidate physiological behavior of the heart (28, 31, 44). These data can provide unique information in the fetal heart including the 3D geometry, mechanical parameters, and clinical measures of function. To build an accurate computational model, reliable clinical and experimental measurements are necessary at various fetal developmental stages. To contextualize the findings of disease models and to identify the functional differences from a normally developing heart, it is critical to first understand and characterize the growth behavior and mechanical properties of a normal human fetal heart under varying physiological conditions. Therefore, we developed a single ventricle model of an average-sized human fetal heart to calibrate a normal strain-dependent growth law to serve as a reference model. We sought to understand and quantify the effect of mechanical loads on human fetal ventricular growth using patient-specific computational models of HLHS patients derived from fetal echocardiograms. Specifically, based on the experimental observation that cardiac myocytes hypertrophy in response to stretch as a stimulus (13, 45, 46), we test the hypothesis that reduced ventricular filling observed at end-diastole can predict reduced ventricular growth in HLHS patients with an etiology of inadequate mitral valve patency. Computer-aided

diagnostics employing predictive patient-specific models of fetal ventricular growth in HLHS could allow for improved prenatal counseling and potential early selection of candidates for *in utero* interventions.

MATERIALS AND METHODS

Model Development Framework

We developed a computational model of human fetal LV growth using the framework of a previously established strain-based growth law (26, 32) (**Figure 1**). The human LV fetal growth model uses a finite element (FE) model of LV geometry with empirical myocardial material properties adjusted to match the human fetal ventricular measurements at mid-gestation in normal hearts. Experimentally measured LV dimensions were used to generate a FE mesh in a prolate spheroidal coordinate system for describing the ellipsoidal nature of the heart: a thick-walled truncated ellipsoidal shell bounded by inner and outer surfaces. Twenty-four different FE models of idealized LV fetal geometry at 22 weeks of gestation were constructed to optimize the normal fetal LV growth model (Data Sheet S1 in Supplementary Material). The idealized LV geometry was selected based on retrospective error analysis and computation of the least cumulative error for all constraining model parameters and LV shape during growth. The best-fit FE model was used as the reference model for growth simulations.

Unloaded Fetal LV Geometry

In order to develop the human fetal growth model, we created a FE mesh of the unloaded LV that matches fetal LV dimensions obtained from median dimensions of 14 formalin-fixed human fetal hearts at 22 weeks of gestation (47). Based on the median dimensions, we constructed 24 idealized LV geometries in prolate spheroidal coordinates with 4 radial (endocardium to epicardium) and 5 longitudinal (apex to base) elements. The axisymmetric LV FE mesh used for the simulations consisted of 30 nodes, 20 FEs (5 longitudinal, 4 transmural, and 1 circumferential) with cubic

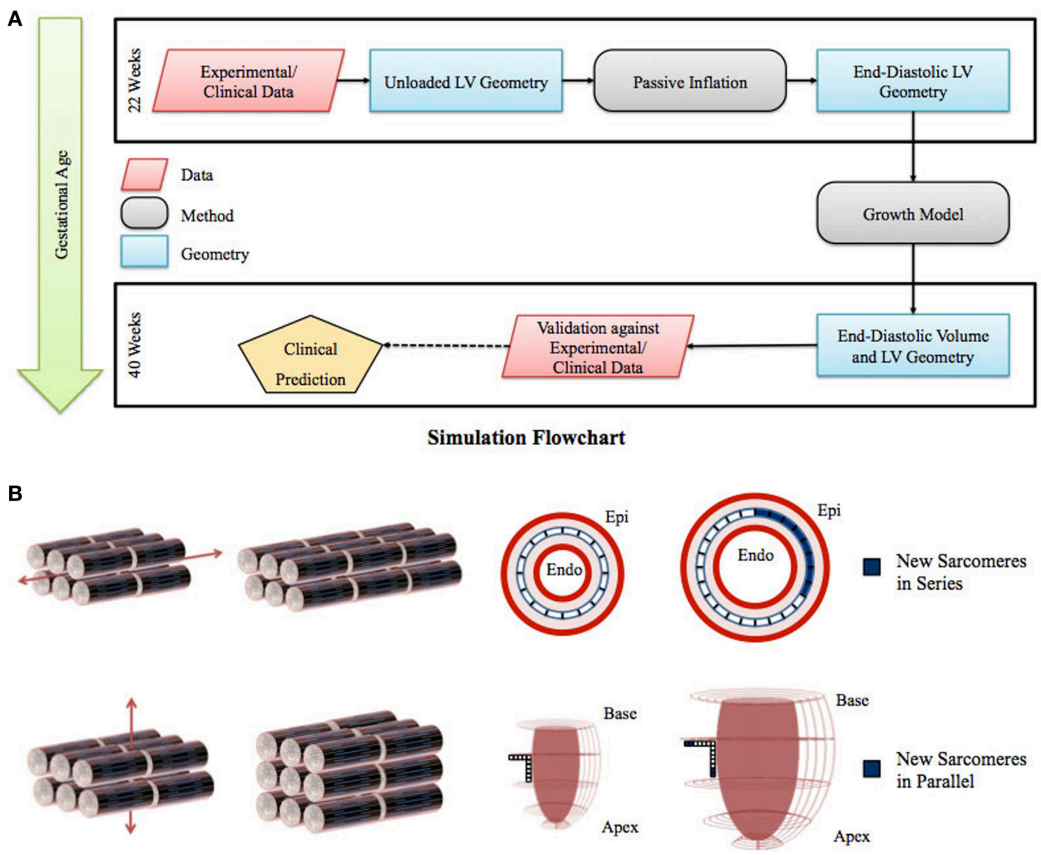

FIGURE 1 | **(A)** Flowchart of left ventricle (LV) fetal growth model. Normative data from fixed fetal hearts were used to construct the unloaded LV geometry at 22 weeks. This geometry was inflated to LV end-diastolic pressure; the passive material properties were adjusted to match the LV dimensions and cavity volume. Growth simulations were then performed to obtain the new LV end-diastolic geometry at each time step. The growth constants were then adjusted to match the LV volumetric growth. The growth in the geometry was validated by comparing the resulting LV end-diastolic dimensions with the dimensions obtained from normal fetuses using echocardiography. **(B)** Graphical representation of the sarcomere addition in series and parallel. Axial strain leads to sarcomere addition in series, which translates to circumferential growth in the LV model. Transverse strain leads to sarcomere addition in parallel, which translates to longitudinal and wall thickness growth in the LV model.

Hermite basis functions for all prolate spheroidal coordinates in the transmural (λ) and longitudinal (μ) directions and linear basis functions for all coordinates in circumferential direction (φ). Cardiomyocyte fiber angles were then incorporated into the model by assigning an inplane angle of −37° (relative to circumferential) at the epicardium, and 83° at the endocardium, with a linear variation across the ventricular wall (48, 49).

End-Diastolic Fetal LV Geometry

We obtained the end-diastolic fetal LV geometry by passively inflating the unloaded LV mesh. In order to model the resting properties of the myocardium, we make use of the transversely isotropic form of the constitutive model developed by Guccione et al. (50) (Methods S1 in Supplementary Material). The passive material properties of the myocardium were adjusted such that the end-diastolic fetal LV geometry was constrained by clinically measured median values of end-diastolic volume (EDV) (51), EDP (52), and LV dimensions (inner length and diameter) (47, 53) corresponding to 22 weeks of gestation (Table S1 in Supplementary Material).

Growth Model

The inflated mesh was then set to grow from mid-gestation to birth at a constant EDP with the parameters listed (Methods S2 and Table S2 in Supplementary Material). Briefly, our group previously developed a strain-based volumetric growth model that deforms the stress-free tissue configuration B_0 to a grown configuration *Bg*, which will generally not be stress free (Methods S2 in Supplementary Material) (32). The biomechanical stimuli for growth in these models are derived from maximal strains. The growth deformation gradient tensors are defined with respect to the local fiber orientation (with component F_{ff} in the fiber direction, component F_{cc} in cross-fiber direction parallel to the wall, and F_{rr} the radial component, perpendicular to the two former), which allows for the definition of a transversely isotropic growth tensor (54).

Geometric Model Optimization

Twenty-four unique FE model geometries were constructed. All 24 FE model geometries have been listed with their parameter values and explicitly shown in Data Sheet S1 in Supplementary Material. These geometries were constrained by the median values of (a) *ex vivo* unloaded fetal LV dimensions of LV length or long-axis (LA), LV diameter or short-axis (SA), and LV wall thickness (WT), as measured by morphometric analysis of 14 fixed hearts (47); (b) end-diastolic LV geometry (LA and SA) as measured by echocardiography (53); and (c) clinical measures of end-diastolic function (EDP and EDV) as measured by *in utero* catheterization (52) and echocardiography, respectively (51), at 22 weeks of gestation (Data Sheet S1 in Supplementary Material). The 24 LV geometries were constructed such that each FE model was unique with various combinations of values of the seven constraining parameters (unloaded LV LA, LV SA, and LV WT dimensions, EDP, EDV, LV LA, and LV SA dimensions at end-diastole, at 22 weeks). Each FE model had to satisfy the condition that every constraining parameter is within the reported measurement/clinical range for that parameter. The idealized LV geometry was selected based on retrospective error analysis of each model (Methods S3 in Supplementary Material). Error analysis was done by computing cumulative *z*-scores for each model, such that each model was fitted to the mean of aforementioned seven constraining model parameters and mean of LV shape growth at incremental time points from mid-gestation to birth. The larger the deviation of the model values from the mean values, the higher the error value for the model. For every model, individual *z*-scores were calculated for all model parameters, i.e., clinical measures of unloaded shape, loaded shape, EDV, and EDP at 22 weeks of gestation, and for LV shape from mid-gestation to term. Individual *z*-scores of all parameters and LV shape growth were summed up for each model to compute the cumulative *z*-score corresponding to the model (see **Tables 1** and **2**). The model with the lowest cumulative *z*-score was selected as the optimum fetal model.

Model Simulations

The FE model developed in this study was numerically solved using *Continuity 6.4*, a problem-solving environment for multiscale modeling of cardiac biomechanics and electrophysiology. It is distributed free for academic research by the National Biomedical Computation Resource and can be downloaded at http://www.continuity.ucsd.edu/Continuity.

The different steps in performing the growth simulations are shown in **Figure 1**. The unloaded fetal LV geometry was inflated to the end-diastolic pressure to obtain the starting LV end-diastolic geometry at 22 weeks of gestation. The growth simulations were then performed by repeatedly applying the growth laws to this end-diastolic geometry to directly compute the grown end-diastolic geometry at each time step. Once the growth simulations were performed, the growth time step that accounts for rate of growth was adjusted to match the normative EDV growth. These growth constants were then kept the same for all subsequent simulations for the different cases.

The non-linear FE models were solved with a modified Newton-Raphson iteration scheme. Integration was performed with 3 × 3 × 3 Gaussian quadrature points. Convergence was reached when both the sum of incremental displacements and the sum of the residuals were lower than 10^{-3} mm and 10^{-5} N, respectively. The Jacobian was calculated and factorized in the first iteration of a new time step and when the solution was diverging. The system of linear equations was solved using SuperLU (55). Boundary conditions in the models were such that the apex was only allowed to move along the LV LA, the base was constrained in longitudinal direction, and the epicardium of the base was constrained in circumferential direction.

Model fits to experimental data were evaluated based on standard error from the data mean or root mean squared deviation (RMSD) from the regression line of the experimental data. The RMSD is calculated using the following formula,

$$\mathrm{RMSD}=\frac{\sqrt{\sum\left(V_{\mathrm{model}}-V_{\mathrm{regression}}\right)^2}}{n_{\mathrm{data}}}$$

where V_{model} is the model-predicted EDV, $V_{\mathrm{regression}}$ is the EDV calculated using the exponential regression fit to the data, and n_{data} is the number of data points.

TABLE 1 | *z*-Scores for geometry and function model parameters at the unloaded and loaded state prior to growth, and cumulative *z*-scores for each dimension during growth from 22 to 40 weeks of gestational stage.

Model	Pregrowth (22 weeks)							Postgrowth (22–40 weeks)	
	Unloaded dimensions			Loaded dimensions		End diastolic volume	EDP	Dimensions	
	Short-axis (SA)	Long-axis (LA)	Wall thickness	SA	LA			SA	LA
1	0.26	0.24	4.08	1.15	1.13	1.62	1.09	5.55	5.88
2	1.77	1.35	3.55	2.46	0.16	0.75	1.09	24.35	10.72
3	0.28	1.30	1.40	1.28	0.04	1.95	1.09	20.24	18.52
4	0.28	1.26	5.05	1.33	0.08	1.94	1.09	8.90	21.87
5	3.28	0.74	1.27	3.77	0.85	1.25	1.09	44.51	12.29
6	4.83	0.64	2.91	5.02	0.99	2.25	1.09	67.86	5.60
7	2.53	0.74	2.04	3.16	0.70	0.40	1.09	32.38	6.80
8	3.24	0.19	1.43	3.71	1.38	1.66	1.09	43.98	9.39
9	1.74	0.19	1.84	2.44	1.22	0.20	1.09	22.56	8.51
10	1.78	0.74	0.10	2.52	0.63	0.46	1.09	21.76	9.81
11	1.46	0.43	2.03	2.21	0.95	0.63	1.09	18.48	5.32
12	2.67	0.37	0.81	3.25	0.63	0.55	1.09	34.72	9.71
13	2.21	0.38	0.21	2.88	1.01	0.11	1.09	27.73	9.56
14	1.93	0.74	0.06	2.65	0.64	0.32	1.09	23.87	9.31
15	2.22	0.74	1.94	2.90	0.68	0.09	1.09	28.16	8.57
16	1.74	0.24	3.76	2.41	1.33	0.02	1.09	23.92	5.24
17	1.18	0.99	0.28	0.53	0.39	0.72	0.74	14.99	9.73
18	0.59	0.79	0.30	1.83	0.67	0.71	0.74	7.11	8.19
19	0.29	0.88	0.39	1.57	0.57	0.80	0.74	12.37	4.21
20	0.29	1.02	0.33	1.58	0.44	1.05	0.74	6.95	8.69
21	0.29	0.96	0.38	1.56	0.49	1.06	0.74	8.41	6.68
22	0.06	0.88	0.36	1.55	0.57	1.03	0.74	9.40	5.11
23	0.00	0.96	0.38	1.32	0.49	0.97	0.74	5.44	6.71
24	0.00	0.84	0.42	1.30	0.62	0.95	0.74	5.29	5.25

Clinical Cases Explored by Model

Once the baseline parameters of the growth model were determined, various growth cases were simulated to determine the effect of volumetric filling, preload, material properties, and shape, on the LV growth. To determine the effect of ventricular filling on growth, the same unloaded geometry was inflated to different preloads by changing the end-diastolic pressure while keeping the material properties constant, and then the growth simulations were performed during which pressures were maintained.

To quantify the effect of ventricular shape and WT on fetal growth, the reference FE model shape was modified by either changing SA to LA ratio or average WT of the LV, prior to inflation. To achieve this, four unloaded geometries were constructed with the same initial volume as the normal unloaded geometry. Two geometries were developed by changing the location of the epicardium nodes uniformly along the LV to yield a thick-walled LV (thick; WT: +30%) and a thin-walled LV (thin; WT: −30%) relative to normal. The other two were developed by manipulating the overall shape of the LV to yield "TallNarrow" (LA:SA: +20%) and "ShortWide" (LA:SA: −20%) geometries. The four geometries were then inflated at a (a) constant preload of 0.75 kPa and (b) constant end-diastolic filling volume relative to unloaded (EDV-V_0) of 383 μL.

Patient-Specific Simulations

The fetal echocardiograms were conducted in the Pediatric Cardiology Division of Rady Children's Hospital, San Diego, and Primary Children's Hospital, Utah, following standard guidelines set by the American Society of Echocardiography. All patient data were retrospectively collected and de-identified. Measurements of the hypoplastic LV were made retrospectively from the recorded echocardiogram clips. Measurements were made in the four-chamber view of the LV internal and external diameters (width) at the base and mid-level, as well as the inner and outer length of the cavity only when the image quality allowed clear definition of the endocardium and epicardium.

Two case studies of HLHS patients were evaluated. The patient-specific FE models were constructed using end-diastolic LV dimensions measured at first clinical time point of study (23.1 and 31 weeks of gestation, respectively). The unloaded geometry was computed using the same material parameter values as the normal fetal heart using the methods described by Krishnamurthy et al. (49). Growth simulations were then performed using the reference growth model parameter values and the LV EDV at second clinical time point of study (30 and 39.1 weeks, respectively) was computed. The predictions from the growth simulations were then independently tested by comparing the simulated LV end-diastolic dimensions at the second

TABLE 2 | Cumulative *z*-scores for the model geometries pre- and postgrowth with the minimum cumulative *z*-score highlighted in blue, representing the selected model geometry for reference normal human fetal growth model.

Model	Cumulative *z*-score		
	Pregrowth	Postgrowth	Total
1	9.57	11.43	21.01
2	11.12	35.07	46.19
3	7.33	38.76	46.09
4	11.03	30.77	41.80
5	12.24	56.81	69.05
6	17.72	73.46	91.18
7	10.65	39.18	49.83
8	12.70	53.37	66.07
9	8.71	31.07	39.78
10	7.32	31.57	38.89
11	8.80	23.80	32.59
12	9.37	44.42	53.79
13	7.88	37.29	45.17
14	7.42	33.17	40.60
15	9.67	36.73	46.40
16	11.47	29.16	40.63
17	4.84	24.72	29.56
18	5.63	15.29	20.93
19	5.24	16.58	21.82
20	5.46	15.63	21.09
21	5.47	15.09	20.56
22	5.19	14.51	19.71
23	4.87	12.16	17.03
24	4.87	10.55	15.41

clinical time point of study with echocardiographic measurements for the same.

RESULTS

Human Fetal LV Reference Model

Upon *z*-score analysis of all geometric models constructed (Data Sheet S1 in Supplementary Material), Model 24 resulted with the lowest cumulative *z*-score and was chosen as the working reference human fetal LV model for normal growth (**Tables 1** and **2**). The geometry of the unloaded FE mesh for the optimum model at mid-gestation (**Figure 2A**) was within the experimentally reported values of fixed LV hearts at 22 weeks of age (**Figure 2B**). At end-diastole, the working reference fetal LV model geometry fit at the high-end of the normal clinical range of reported values for LV length and LV diameter (**Figure 2C**), albeit at the median of clinical values of EDP (5.63 mmHg) and EDV (1.02 mL) (**Figures 2D,E**).

Human Fetal LV Growth Model from Mid-Gestation to Birth

Normal fetal LV growth is quantified from mid-gestation to term and quantified as volumetric and shape growth of the LV cavity and wall. Simulating fetal growth from mid-gestation to birth in the reference human fetal LV model replicated the measured end-diastolic LV cavity volume (**Figures 3A,C**) and LV geometric dimensions (**Figure 3B**), and LV wall volume (**Figure 3D**) to within 15% RMSD error based on echocardiographic measurements (53, 56–61), in both forward and reverse directions, during the third trimester of pregnancy. Specifically, the RMSD between the model-predicted EDV and the exponential regression fit to the EDV data is 0.89 mL. The maximum deviation occurred at 40 weeks, where the percentage of RMSD with respect to the range of data is 13.4%. The RMSD between the model-predicted SA diameter and the linear regression to SA data is 0.606 mm, and the RMSD between the model-predicted LA lengths to the linear regression to the LA data is 1.126 mm. The maximum deviations from data occurred at 22 weeks in both cases and were within 0.55 and 0.61 SDs, respectively. The model was able to accurately predict the physiological unloaded state of the LV at around 12–14 weeks (**Figure 3C**). However, greater deviation from clinical values is observed for LV wall mass during forward and reverse growth for early-fetal (0–14 weeks) growth (**Figure 3D**). The RMSD between the model-predicted LV wall mass and the exponential regression to the four different data sets were computed to be 0.99 mL (60), 1.11 mL (57), 1.14 mL (59), and 1.25 mL (58), respectively.

Human Fetal LV Growth Model Sensitivity to EDV

In fetal echocardiograms, patients with narrowing or obstruction of the foramen ovale, mitral valve, and/or aortic valve frequently develop HLHS. Fetal sheep, chicken, and zebrafish models with decreased ventricular filling also develop ventricular hypoplasia (6, 14, 46). Decreasing the ventricular filling volume in the reference normal growth FE model at 22 weeks, while keeping the material properties of LV constant (**Figure 4A**), resulted in drastic decreases in LV cavity volume (**Figure 4B**) and LV wall volume (**Figure 4C**) during fetal LV growth from mid-gestation to birth. Simulated growth of a hypoplastic LV (reduced ventricular filling) (−25%) resulted in significant reduction in LV EDV (−65%) and LV wall volume (−46%) at birth (**Figures 4B,C**). A linear correlation was determined between LV filling volume and LV cavity growth/LV wall growth (**Figure 4D**). Every 10% decrease in LV filling volume at mid-gestation resulted in a 25% decrease in LV cavity volume and 17% decrease in LV wall volume at birth in the reference model.

Human Fetal LV Growth Model Sensitivity to LV Shape

Patient-specific changes in LV shape, as observed routinely during clinical investigations, can result in deviations from the idealized LV growth and might be prognostic of HLHS phenotype (62). Modifying the reference FE model while maintaining constant initial volume, preload, LV filling volume (EDV-V_0), and material properties (**Figure 5A**) showed that that thin-walled ventricles grew larger in size and volume than the equivalent thick-walled models (**Figure 5B**). The effects of changing ventricular length-to-width ratio (**Figure 5A**) while holding other properties constant were comparatively small. However, the ShortWide LV did grow more than the TallNarrow model (**Figure 5B**). A steep inverse linear correlation was determined between LV WT and LV cavity growth (**Figure 5C**). Every 10% increase in LV WT at mid-gestation resulted in a 6.8% decrease in LV cavity volume at

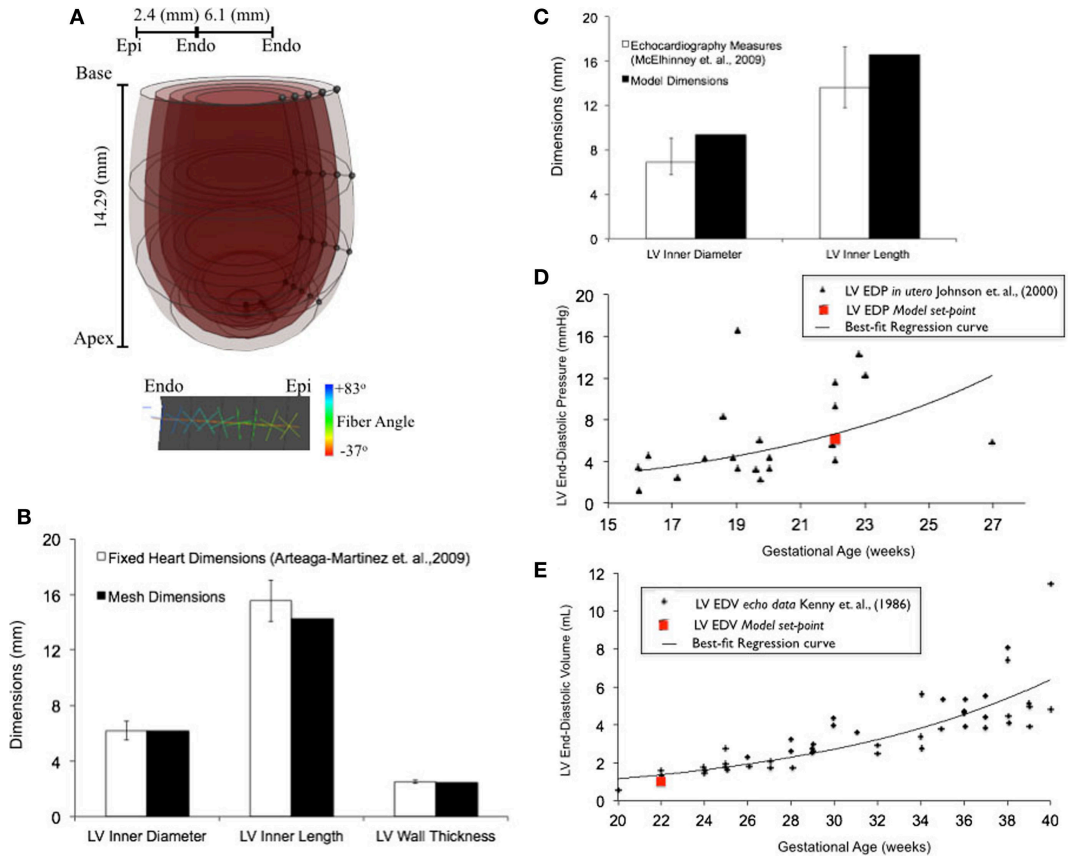

FIGURE 2 | **(A)** Rendered finite element (FE) mesh of unloaded human fetal left ventricle (LV) at 22 weeks of gestational age depicting the four transmural LV wall elements (epicardium to endocardium shade gradations), the five longitudinal elements from apex to base (cross-sectional discs), transmural helical fiber angles from +83° to −37° (endocardium to epicardium; color-mapped sprites) w.r.t. circumferential direction and mesh dimensions for LV inner length, LV inner diameter, and LV wall thickness. **(B)** Bar graph showing comparisons for unloaded LV dimensions between morphometric measurements (white bars) from fixed fetal hearts (47) and FE mesh (black bars) at 22 weeks of gestational age. **(C)** Fitting of simulated LV end-diastolic model geometry (black bars) against echocardiographic measures of LV dimensions (white bars) (53) at 22 weeks of gestational age. Simulation set points (solid red dot) of EDP **(D)** and end-diastolic volume (EDV) **(E)** from human patient data as measured by fetal cardiac catheterization (52) and echocardiography (51), respectively, at 22 weeks of gestational age.

birth. Also, a shallow inverse linear correlation was determined between LV LA:SA ratio and LV cavity growth (**Figure 5C**), wherein, a 10% increase in LA:SA ratio at mid-gestation resulted in a 2% decrease in LV growth at birth.

Patient-Specific Human Fetal LV Growth Model Case Study 1

In a blinded case study, using echocardiographic data (for LV geometry) from a severely hypoplastic fetus at 23.1 weeks as the input, we constructed a patient-specific FE model (**Figure 6A**). The patient-specific FE model was in good agreement with the echocardiography data with highest variability in WT dimension from apex to base (**Figure 6A**). At end-diastole, the current patient-specific model presented with a significantly lower ventricular filling volume at 0.187 mL, decreased LA:SA ratio at 1.2, and decreased WT relative to a normal healthy LV (**Figure 6B**). Based on our previous analysis of the reference model, the patient-specific case was predisposed to faster growth as a function of altered geometry (thinner wall and lower LA:SA). In contrast, the patient-specific case was predisposed to much slower growth as a function of lower ventricular filling. The simulated growth of the patient-specific model predicted a severely hypoplastic LV at birth, consistent with the patient diagnosis (**Figure 6C**). The patient-specific growth model predicted a consistent match in the observed reduction in the measured LV cavity volume (**Figure 6C**) and end-diastolic LV geometric dimensions (**Figure 6D**) at 30.1 weeks, to within 15% clinical error based on echocardiographic measurements.

Patient-Specific Human Fetal LV Growth Model Case Study 2

In a blinded case study, using echocardiographic data (LV geometry) from a borderline hypoplastic fetus at 31 weeks as the input, we constructed a well-matched patient-specific FE model (**Figure 7A**). At end-diastole at 31 weeks, the patient-specific model had a significantly lower ventricular filling volume, increased LA:SA ratio, and increased WT relative to a normal healthy LV (**Figure 7B**). Based on our previous analysis

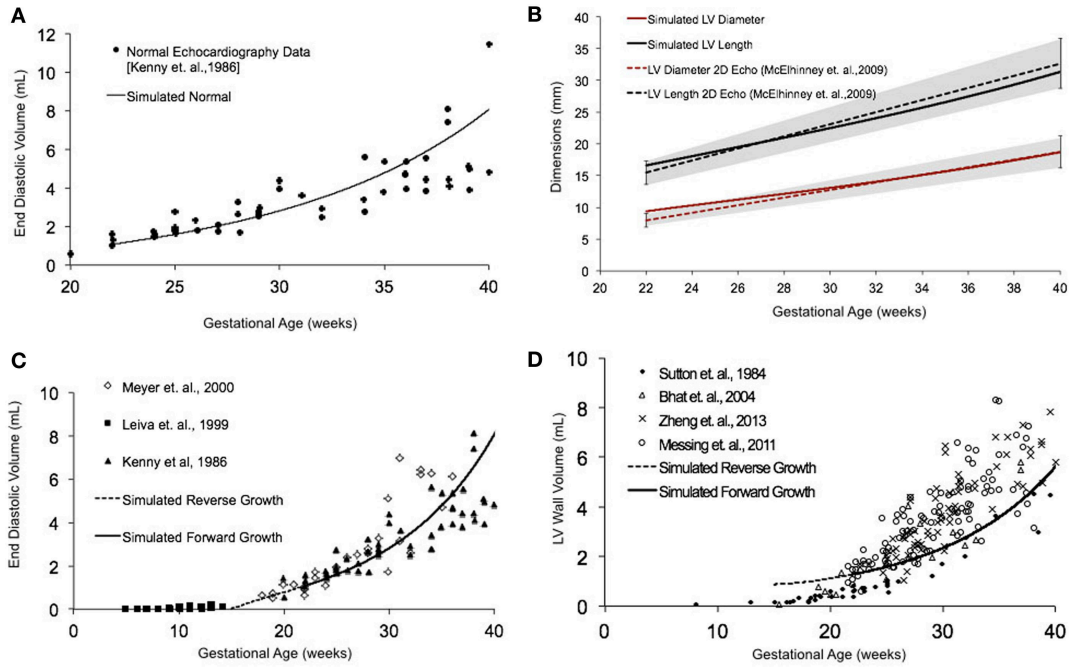

FIGURE 3 | **(A)** Simulated normal human fetal left ventricle (LV) volumetric growth (solid black trace) fitted to normal fetal echocardiographic measures of end-diastolic volume (EDV) (solid black circles) (51) from onset of third trimester of pregnancy (22 weeks of gestational age) to birth (40 weeks of gestational age). **(B)** Validation of simulated LV length (solid black trace) and LV diameter (solid red trace) against clinical echocardiographic measures (dotted lines) (53). Validation of simulated LV EDV **(C)** and LV wall volume **(D)** in forward (solid black line) and reverse (black dotted line) against multiple clinical data sets.

of the reference model, the patient-specific case was predisposed to slower growth as a function of both altered geometry (thicker wall and higher LA:SA) and lower ventricular filling. The simulated growth of the patient-specific model predicted a borderline hypoplastic LV at birth, consistent with the patient diagnosis (**Figure 7C**). The patient-specific growth model predicted a consistent match between the measured LV cavity volume (**Figure 7C**) and end-diastolic LV geometric dimensions (**Figure 7D**) at 39 weeks, to within 15% clinical error based on echocardiographic measurements.

DISCUSSION

In this study, we quantitatively investigated, *in silico*, the effect of reduced ventricular filling at end-diastole, in patient-specific models of HLHS, on LV fetal growth. A novel FE growth model of the healthy human fetal LV, using a previously described strain-based growth law, with idealized average geometry at mid-gestation using clinical data, has been presented as a reference human fetal LV growth model from mid-gestation to birth. Model prediction results from the two blinded case studies of HLHS patients are in good agreement with the clinically observed values for LV cavity volume growth and shape changes. To our knowledge, this is the first study to attempt to investigate the biomechanical relationship between LV filling at end-diastole and LV ventricular growth in human fetal hearts with HLHS. The human fetal growth model presented here is a significant step toward the development of a clinical tool that may be used to predict LV size and shape at birth based on mid-gestation LV filling.

Computational Models of Fetal Growth and HLHS

The specific biomechanical stimuli that trigger cardiac growth are not completely understood. There is general agreement in the field that an increase in stress or strain at organ level and/or cellular level leads to a growth response in the heart (13, 16, 26–28, 30–34). Most cardiac growth models have been formulated, wherein growth is regulated by changes in mechanical stress and/or strain (13, 16, 26, 27). These computational models are based on the experimental observation that at the organ level, volume overload or pressure overload triggers eccentric or concentric hypertrophy, respectively, via changes in regional wall stresses and strains (13, 16, 26–28). Peña et al. constructed simplified ellipsoidal meshes of the human fetal heart from *in vivo* echocardiographic measurements at different gestational ages, which were then used to optimize for the material properties using FE analysis (28). However, they did not directly apply a growth law. They found that while the active tension of the models increased with gestational age, there was not a significant change in the passive material properties. Ohayon et al. used a global stress-based growth law applied directly to the unloaded geometry to simulate global human fetal LV growth (26, 28, 32). Though able to predict the growth of the fetal LV, this model is not based on sarcomere addition along the fiber and cross-fiber direction that happens

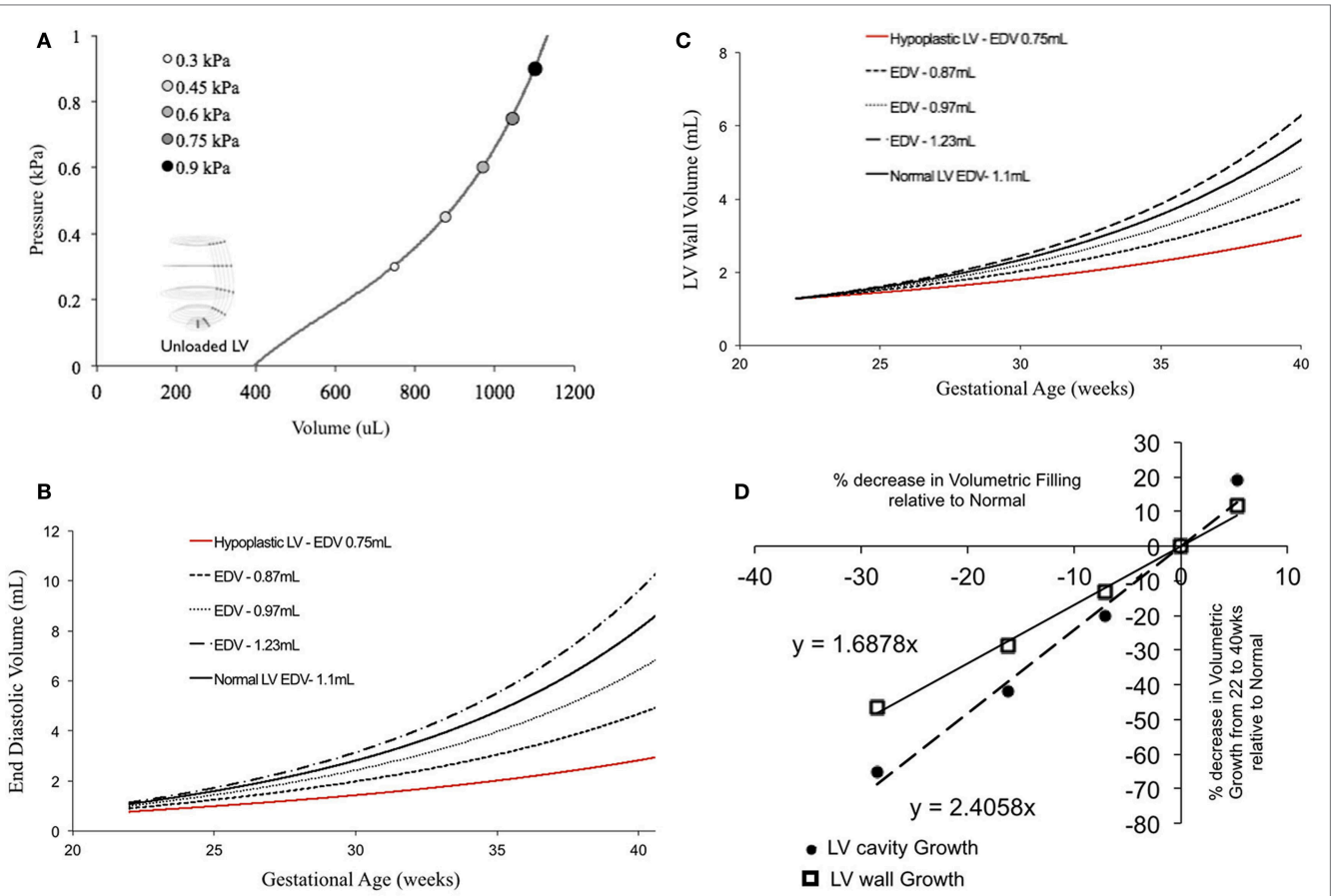

FIGURE 4 | **(A)** Passive inflation of unloaded left ventricle (LV) reference finite element model to varying ventricular filling volumes by varying ventricular loading. Simulated LV cavity volume **(B)** and LV wall volume **(C)** growth under varying ventricular filling conditions. **(D)** Relationship between ventricular filling and LV cavity volume and LV wall volume growth in the reference model.

in cardiac growth. In this model of fetal growth, interpreting the direct effects of stresses and strains along the local fiber directions on LV growth are difficult as global growth has be transformed to the local fiber directions.

The changes in LV WT are mediated by cellular remodeling of cardiomyocytes via sarcomere addition in series or parallel. We applied a previously described strain-dependent growth law acting locally at each gauss point based on the fiber and cross-fiber strains, which has been used to describe both eccentric and concentric remodeling in dogs and neonatal rat growth, in our fetal heart model (31, 51, 52, 56, 61). Earlier studies have reported a monoexponential increase in fetal LV EDV and a linear increase in fetal systolic and diastolic pressures during the course of human gestation (26, 32, 63). Thus, it would suggest that fetal heart growth is largely driven by volume overload as the biomechanical stimuli. Accordingly, growth in our model is driven via maximal fiber and cross-fiber strains at each gauss point. In addition, decrease in ventricular flow is routinely documented in the experimental models and clinical studies of HLHS.

The single ventricle model for normal fetal growth is a significant step toward building subject-specific models based on fetal echocardiography data. To the best of our knowledge, this is the first computational model that describes LV growth behavior in the human fetus by integrating information on LV geometry and function from multiple clinical measurements and predicts patient diagnoses based on mid-gestation echocardiographic geometry. Our fetal human growth model is based on idealized LV geometry at mid-gestation and is able to replicate the later-gestation fetal LV volumetric and geometric growth (size and shape) observed clinically with less than 15% error. Fetal LV dimensions obtained from retrospective echocardiographic images are valuable measurements as they provide routine clinical information about ventricular structure in HLHS patients (49, 51, 52, 56, 61). Fetal ventricles are of smaller scale relative to adult ventricles, which compounds the difficulty of taking accurate measurements from echocardiography, especially for LV WT measurements. This was reflected in the significant variation within the four experimental data sets of fetal LV wall mass (57–60). All four data sets employed different experimental techniques to acquire data that would have led to technical variability within these data. Of the four data sets for WT, our model was able to match the results of only one data set within acceptable

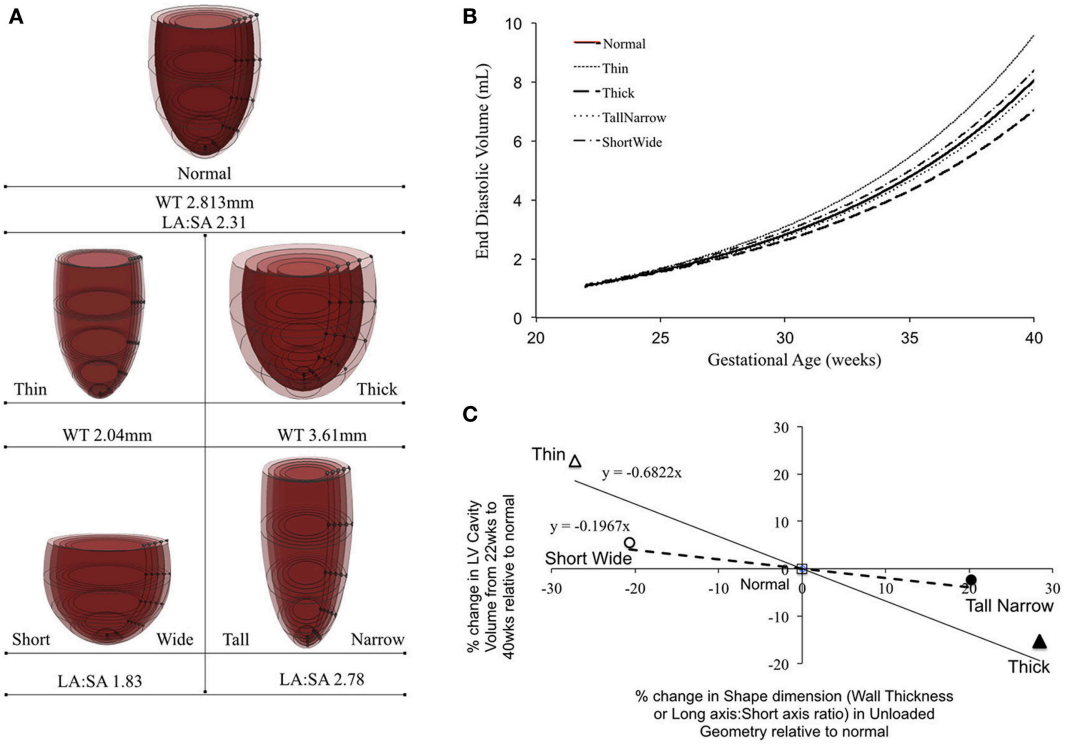

FIGURE 5 | **(A)** Representations of the shape modifications of the reference finite element model by either changing short-axis (SA) to long-axis (LA) ratio or average wall thickness (WT) of the left ventricle (LV), prior to inflation. **(B)** Simulated LV cavity volume growth under varying LV shapes. **(C)** Relationship between LV shape changes and LV cavity volume growth in the reference model.

values (60). Notably, St John Sutton et al. was the only group to compare their *in vivo* measurements to explanted LV mass measurements (60). More validation with serial data consisting of paired measurements for LV dimensions (LA, SA, and WT) will be required to improve model results given the scatter in data. This becomes pertinent as LV growth is strongly influenced by WT in our model.

Patient-Specific Human Fetal LV Growth Model Case Studies

In case of subject-specific data obtained from echocardiograms of fetuses diagnosed with HLHS, measurements were only made when the structures were visibly clear and delineated. Nonetheless, there is the possibility of introducing error due to intraobserver variability. Additionally, error can be greater in hypoplastic LV measurements due to their smaller LV size relative to normally developing LV. In order to assess LV geometry accurately for these case studies, six geometric measurements of LV dimensions were provided at different LV planes from apex to base from the 2D echocardiogram four-chamber view. For both patient-specific cases, model predictions matched the clinical data for LV EDV and shape reasonably well. Specifically, the model predicted the shape better for the borderline HLHS case than the severe HLHS case. Interestingly, the biggest discrepancy in shape results for the borderline HLHS case was observed in the LV WT growth. Additionally, the prediction for EDV was much better for the severe HLHS case than for the borderline HLHS case. Nonetheless, in both cases, the model was able to predict the clinical diagnosis of the fetal subject. Ideally, using MRI data and LV inflow, data would allow for more constraints on the developed mesh and, therefore, a more faithful patient-specific geometry. However, early-fetal MRI is a developing field and not a routine clinical procedure as yet. Additionally, LV inflow data were not available for the current case studies. Also, measurements at more than two time points would be valuable in validating the patient-specific model and its predictive capability. In future studies, protocols need to be developed to ensure consistent methods between patients and, if possible, reduce manual error by having multiple experts obtain measurements.

It is noteworthy that the ventricular geometry was imaged at end-diastole when the heart experiences a significant amount of load. An unloading algorithm developed by Krishnamurthy et al. was used to predict the unloaded configuration of the 3D FE model under normal preload and passive material properties, which may not hold true for the patient-specific case (49). This unloaded LV configuration is important computationally and biomechanically, as it serves as the reference unstressed state for calculation of the developed strains in the model. However, the predicted unloaded geometry is able to successfully deform to the measured end-diastolic geometry, demonstrating promising results. Repeating this with a larger set of patients would serve to

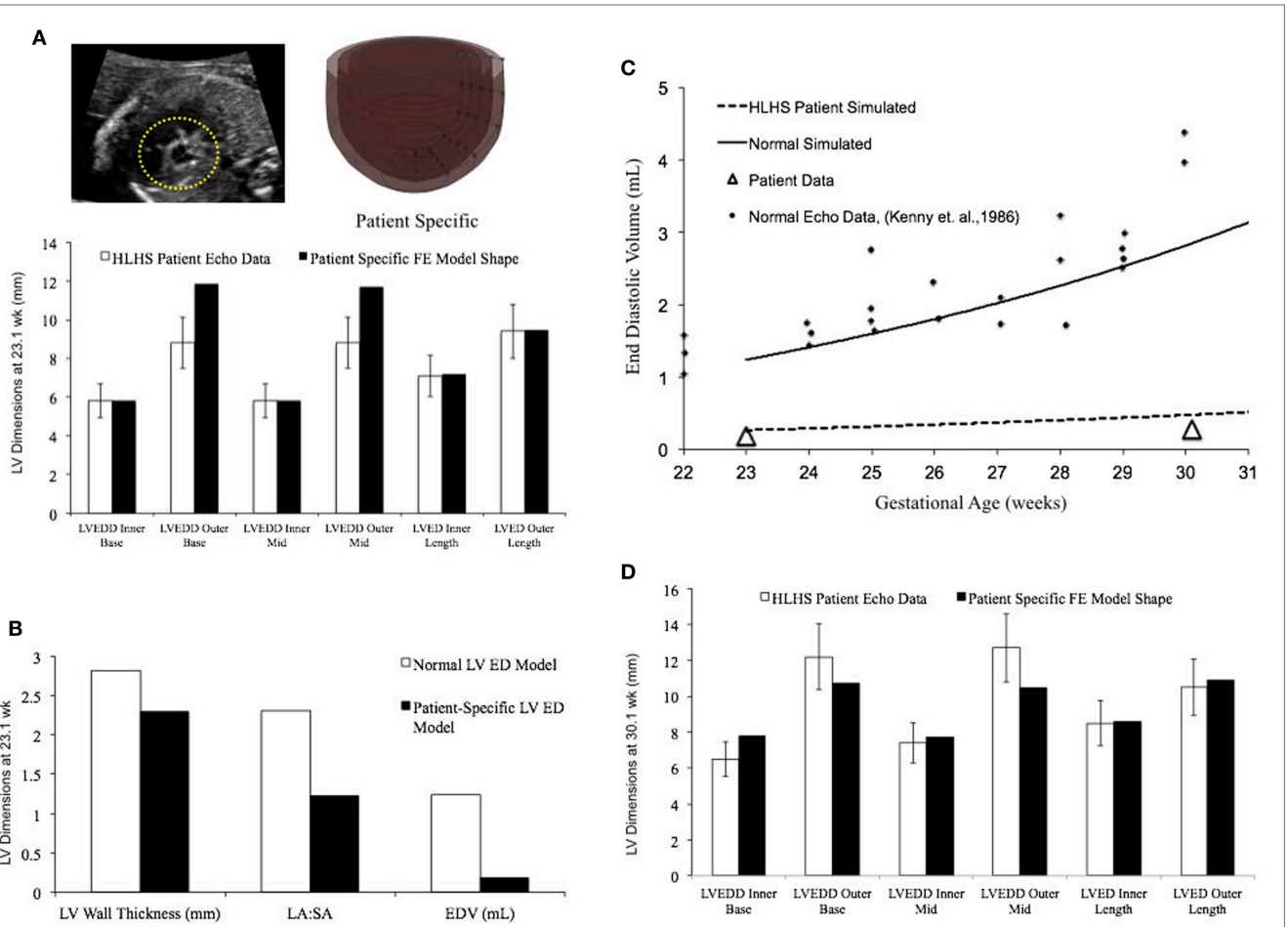

FIGURE 6 | **(A)** Rendering of the patient-specific mesh at end-diastole, generated based on echocardiographic data obtained at 23.1 weeks. Bar graph showing the morphometric match between echocardiographic data (white bars) and patient-specific finite element (FE) model (black bars) at 23.1 weeks. **(B)** Comparison of model shape and ventricular filling between reference FE model of healthy fetal left ventricle (LV) model (white bars) and patient-specific LV model (black bars). **(C)** Simulation of LV cavity growth in patient-specific model (black dotted line) and its comparison to clinically observed growth for the patient (open triangles) and normal LV growth (solid circles and solid line). **(D)** Bar graph showing the morphometric match between echocardiographic data (white bars) and patient-specific FE model (black bars) at 30.1 weeks.

validate the algorithm as well as the ability of the growth model to predict dimensions at a future time point.

In addition to ventricular filling at EDV, altered shape plays a significant role in altering local strain distribution contributing to LV growth in our model. A greater understanding of the strain distribution experimentally may shed insight into the mechanism underlying the significant wall thickening observed in hypoplastic hearts. Earlier studies report variable systolic strain distribution in hemodynamic chick model of HLHS (28, 49). Further investigation into the role of LV shape and diastolic strain distributions along with myocardial passive material properties is merited to fully comprehend mechanisms underlying HLHS. We quantified the effect of both shape and ventricular filling on LV growth in our model. Once the patient shape is accounted for by using echocardiography data, then based on volumetric filling and shape changes, one can attempt to predict normal and hypoplastic LV growth by using our model. In the future, it would be invaluable to generate a biventricular mesh of the fetal heart with fetal circulation in order to improve the physiological relevance of the model as well as understand the interactive effects between the ventricles in a normal and diseased state. This would be specifically useful in a clinical case such as HLHS where the right ventricle often compensates for the compromised structure and function of the LV.

Model assumptions and limitations:

(a) The simplified ellipsoid shape of the LV used for the reference normal model of fetal growth represents an idealized geometry of the LV. Even in "patient-specific" cases, the FE model is a simplified axis-symmetric representation of the actual LV geometry derived from six-planar measurements of 2-D echocardiography in the four-chamber view. However, the volume calculations and shape calculations based on this LV geometric approximation match the clinical data reasonably well.

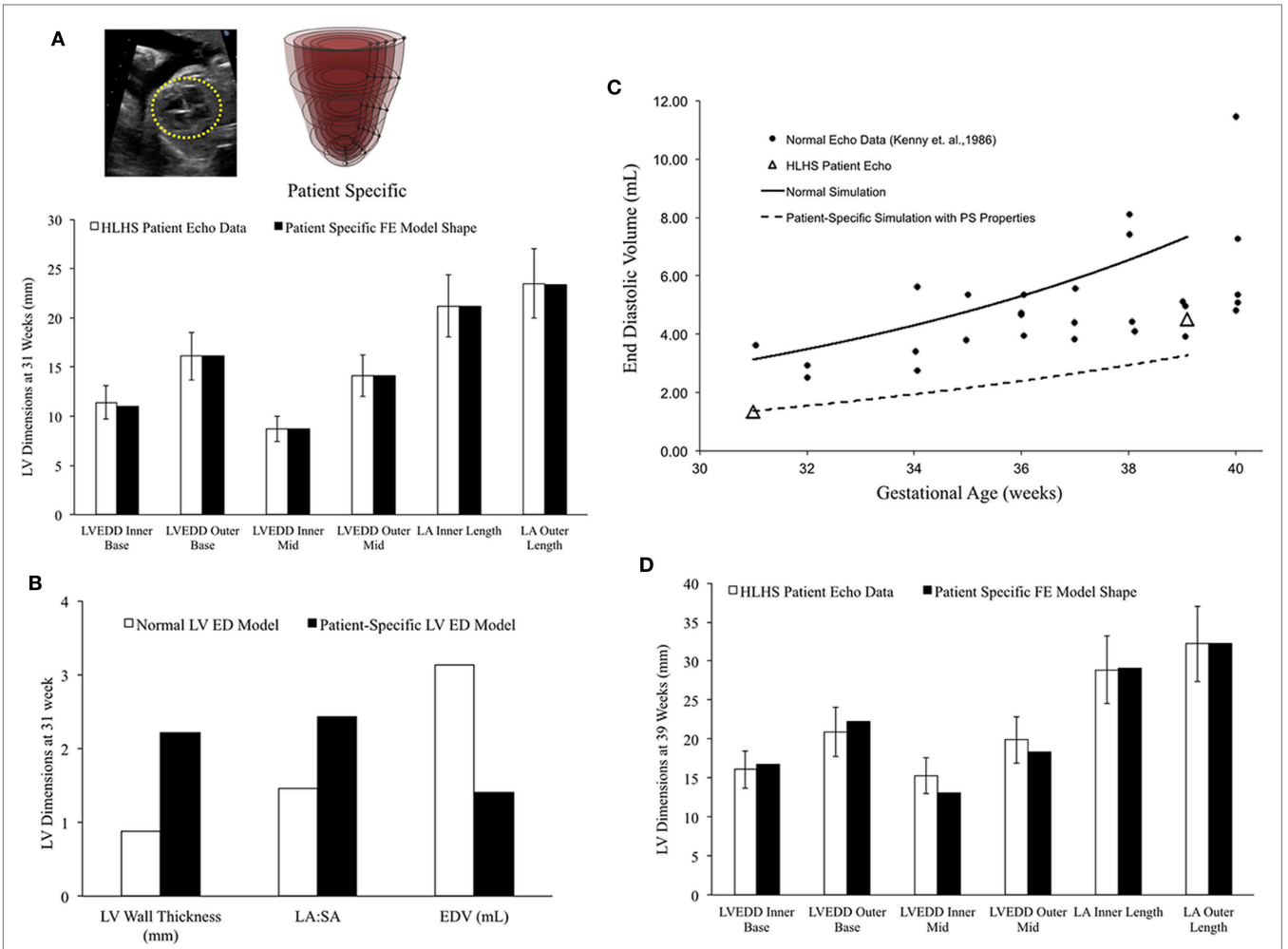

FIGURE 7 | **(A)** Rendering of the patient-specific mesh at end-diastole, generated based on echocardiographic data obtained at 31 weeks. Bar graph showing the morphometric match between echocardiographic data (white bars) and patient-specific finite element (FE) model (black bars) at 31 weeks. **(B)** Comparison of model shape and ventricular filling between reference FE model of healthy fetal left ventricle (LV) model (white bars) and patient-specific LV model (black bars). **(C)** Simulation of LV cavity growth in patient-specific model (black dotted line) and its comparison to clinically observed growth for the patient (open triangles) and normal LV growth (solid circles and solid line). **(D)** Bar graph showing the morphometric match between echocardiographic data (white bars) and patient-specific FE model (black bars) at 39 weeks.

(b) The FE model assumes an initial stress-free state of the myocardium and residual stresses are not factored in. More human fetal data are needed to substantiate these assumptions.

(c) In fetal heart growth, cell proliferation substantially contributes to cardiac growth (24, 44, 64). Studies in animal models of sheep have attempted to quantify the contribution of hyperplasia to cardiac growth and shown that this decreases significantly during the third trimester of pregnancy. However, these data and the kinematics of this process, specifically in human fetal hearts, still remain to be elucidated.

(d) We assume that there is no change in passive material properties during growth. An earlier study by Peña et al. supports this (28).

(e) The kinematics of LV growth allows the radial displacement of the base while the apex is free to move.

(f) Growth of the heart is mediated by loading and biomechanical tissue strain, without other stimuli such as growth hormones.

Clinical Perspective

Hypoplastic left heart syndrome can be diagnosed by fetal echocardiography between 18 and 22 weeks of gestation (44, 64, 65). However, borderline cases of HLHS can go undetected in many early to mid-gestation fetal exams. Studies have reported that neonates with prenatal diagnosis of HLHS show improved hemodynamic stability in addition to providing the opportunity to plan management and counseling for the family (64, 65). Patient-specific computational modeling of developing fetuses with HLHS could serve to improve prenatal diagnosis by providing insight into the biomechanics and growth behavior of the affected ventricle. The methods developed in this study aim to

facilitate understanding of fetal growth behavior undergoing normal development and provide a benchmark model for normal growth in the human fetal LV, enabling comparison with patient-specific fetal LV models. Ultimately, with further testing and refinement, the model has potential to aid a clinician in counseling, surgical planning, and management of HLHS with consideration of rescue options for borderline cases of HLHS.

CONCLUSION

The human fetal growth model is a novel tool that may be used to understand biomechanical mechanisms underlying HLHS and ultimately quantitatively predict the degree of LV hypoplasia to potentially guide timing of clinical intervention aimed at rescuing the hypoplastic LV in HLHS patients.

AUTHOR CONTRIBUTIONS

SD is the lead author who conceptualized the idea, researched the study topic, designed the study, ran the simulations, and wrote the paper. AK, DK, and GC significantly contributed by assisting in study design, running simulations, writing the manuscript, and completing the study. RK formulated the growth law. MP and HS provided the clinical data and assisted in editing the manuscript. JO, VN, and AM supervised the study and provided with all resources to do so.

FUNDING

We would like to thank members of Cardiac Mechanics Research Group for useful discussions. This work was supported by National Institutes of Health grants including the Cardiac Atlas Project (1R01HL121754) to AM and JO, (1R01 HL128630) to VN, the National Biomedical Computation Resource (P41 GM103426) to AM and R. Amaro, a systems biology center grant (P50 GM094503) to AM and D. Beard, U01 grant HL122199 (to AM and J. Bassingthwaighte), HL105242 (to AM), and HL111197.

SUPPLEMENTARY MATERIAL

The Supplementary Material for this article can be found online at http://journal.frontiersin.org/article/10.3389/fped.2017.00025/full#supplementary-material.

REFERENCES

1. Greenleaf CE, Urencio JM, Salazar JD, Dodge-Khatami A. Hypoplastic left heart syndrome: current perspectives. *Transl Pediatr* (2016) 5:142–7. doi:10.21037/tp.2016.05.04
2. Parker SE, Mai CT, Canfield MA, Rickard R, Wang Y, Meyer RE, et al. Updated national birth prevalence estimates for selected birth defects in the United States, 2004-2006. *Birth Defects Res A Clin Mol Teratol* (2010) 88:1008–16. doi:10.1002/bdra.20735
3. Lara DA, Ethen MK, Canfield MA, Nembhard WN, Morris SA. A population-based analysis of mortality in patients with Turner syndrome and hypoplastic left heart syndrome using the Texas Birth Defects Registry. *Congenit Heart Dis* (2017) 12:105–12. doi:10.1111/chd.12413
4. Yabrodi M, Mastropietro CW. Hypoplastic left heart syndrome: from comfort care to long-term survival. *Pediatr Res* (2017) 81:142–9. doi:10.1038/pr.2016.194
5. Kowalski WJ, Pekkan K, Tinney JP, Keller BB. Investigating developmental cardiovascular biomechanics and the origins of congenital heart defects. *Front Physiol* (2014) 5:408. doi:10.3389/fphys.2014.00408
6. Fishman NH, Hof RB, Rudolph AM, Heymann MA. Models of congenital heart disease in fetal lambs. *Circulation* (1978) 58:354–64.
7. Sedmera D, Hu N, Weiss KM, Keller BB, Denslow S, Thompson RP. Cellular changes in experimental left heart hypoplasia. *Anat Rec* (2002) 267:137–45. doi:10.1002/ar.10098
8. Jonker SS, Zhang L, Louey S, Giraud GD, Thornburg KL, Faber JJ. Myocyte enlargement, differentiation, and proliferation kinetics in the fetal sheep heart. *J Appl Physiol* (2007) 102(3):1130–42. doi:10.1152/japplphysiol.00937.2006
9. Reckova M, Rosengarten C, deAlmeida A, Stanley CP, Wessels A, Gourdie RG, et al. Hemodynamics is a key epigenetic factor in development of the cardiac conduction system. *Circ Res* (2003) 93:77–85. doi:10.1161/01.RES.0000079488.91342.B7
10. Grossfeld P, Ye M, Harvey R. Hypoplastic left heart syndrome: new genetic insights. *J Am Coll Cardiol* (2009) 53(12):1072–4. doi:10.1016/j.jacc.2008.12.024
11. Goenezen S, Rennie MY, Rugonyi S. Biomechanics of early cardiac development. *Biomech Model Mechanobiol* (2012) 11:1187–204. doi:10.1007/s10237-012-0414-7
12. Lin IE, Taber LA. Mechanical effects of looping in the embryonic chick heart. *J Biomech* (1994) 27:311–21.
13. Russell B, Curtis MW, Koshman YE, Samarel AM. Mechanical stress-induced sarcomere assembly for cardiac muscle growth in length and width. *J Mol Cell Cardiol* (2010) 48(5):817–23. doi:10.1016/j.yjmcc.2010.02.016
14. Sedmera D, Pexieder T, Rychterova V, Hu N, Clark EB. Remodeling of chick embryonic ventricular myoarchitecture under experimentally changed loading conditions. *Anat Rec* (1999) 254:238–52.
15. Thornburg K, Jonker S, O'Tierney P, Chattergoon N, Louey S, Faber J, et al. Regulation of the cardiomyocyte population in the developing heart. *Prog Biophys Mol Biol* (2011) 106(1):289–99. doi:10.1016/j.pbiomolbio.2010.11.010
16. Omens JH. Stress and strain as regulators of myocardial growth. *Prog Biophys Mol Biol* (1998) 69:559–72.
17. Mansour H, de Tombe PP, Samarel AM, Russell B. Restoration of resting sarcomere length after uniaxial static strain is regulated by protein kinase Cepsilon and focal adhesion kinase. *Circ Res* (2004) 94:642–9. doi:10.1161/01.RES.0000121101.32286.C8
18. Simpson DG, Majeski M, Borg TK, Terracio L. Regulation of cardiac myocyte protein turnover and myofibrillar structure in vitro by specific directions of stretch. *Circ Res* (1999) 85:e59–69.
19. deAlmeida A, Sedmera D. Fibroblast growth factor-2 regulates proliferation of cardiac myocytes in normal and hypoplastic left ventricles in the developing chick. *Cardiol Young* (2009) 19:159–69. doi:10.1017/S1047951109003552
20. Sedmera D, Cook AC, Shirali G, McQuinn TC. Current issues and perspectives in hypoplasia of the left heart. *Cardiol Young* (2005) 15:56–72. doi:10.1017/S1047951105000132
21. Gopalan SM, Flaim C, Bhatia SN, Hoshijima M, Knoell R, Chien KR, et al. Anisotropic stretch-induced hypertrophy in neonatal ventricular myocytes micropatterned on deformable elastomers. *Biotechnol Bioeng* (2003) 81:578–87. doi:10.1002/bit.10506
22. Zhang Y, Sekar RB, McCulloch AD, Tung L. Cell cultures as models of cardiac mechanoelectric feedback. *Prog Biophys Mol Biol* (2008) 97:367–82. doi:10.1016/j.pbiomolbio.2008.02.017
23. Raskin AM, Hoshijima M, Swanson E, McCulloch AD, Omens JH. Hypertrophic gene expression induced by chronic stretch of excised mouse heart muscle. *Mol Cell Biomech* (2009) 6:145–59.
24. Tobita K, Keller BB. Right and left ventricular wall deformation patterns in normal and left heart hypoplasia chick embryos. *Am J Physiol Heart Circ Physiol* (2000) 279:H959–69.
25. Berdougo E, Coleman H, Lee DH, Stainier DY, Yelon D. Mutation of weak atrium/atrial myosin heavy chain disrupts atrial function and influences

ventricular morphogenesis in zebrafish. *Development* (2003) 130:6121–9. doi:10.1242/dev.00838
26. Kerckhoffs RC, Omens J, McCulloch AD. A single strain-based growth law predicts concentric and eccentric cardiac growth during pressure and volume overload. *Mech Res Commun* (2012) 42:40–50. doi:10.1016/j.mechrescom.2011.11.004
27. Omens JH, McCulloch AD, Criscione JC. Complex distributions of residual stress and strain in the mouse left ventricle: experimental and theoretical models. *Biomech Model Mechanobiol* (2003) 1:267–77. doi:10.1007/s10237-002-0021-0
28. Peña E, Tracqui P, Azancot A, Doblare M, Ohayon J. Unraveling changes in myocardial contractility during human fetal growth: a finite element analysis based on in vivo ultrasound measurements. *Ann Biomed Eng* (2010) 38:2702–15. doi:10.1007/s10439-010-0010-x
29. deAlmeida A, McQuinn T, Sedmera D. Increased ventricular preload is compensated by myocyte proliferation in normal and hypoplastic fetal chick left ventricle. *Circ Res* (2007) 100:1363–70. doi:10.1161/01.RES.0000266606.88463.cb
30. Lin IE, Taber LA. A model for stress-induced growth in the developing heart. *J Biomech Eng* (1995) 117:343–9.
31. Ohayon J, Cai H, Jouk PS, Usson Y, Azancot A. A model of the structural and functional development of the normal human fetal left ventricle based on a global growth law. *Comput Methods Biomech Biomed Engin* (2002) 5:113–26. doi:10.1080/10255840290032135
32. Kerckhoffs RC. Computational modeling of cardiac growth in the post-natal rat with a strain-based growth law. *J Biomech* (2012) 45:865–71. doi:10.1016/j.jbiomech.2011.11.028
33. Göktepe S, Abilez OJ, Parker KK, Kuhl E. A multiscale model for eccentric and concentric cardiac growth through sarcomerogenesis. *J Theor Biol* (2010) 265:433–42. doi:10.1016/j.jtbi.2010.04.023
34. Lee LC, Genet M, Acevedo-Bolton G, Ordovas K, Guccione JM, Kuhl E. A computational model that predicts reverse growth in response to mechanical unloading. *Biomech Model Mechanobiol* (2015) 14:217–29. doi:10.1007/s10237-014-0598-0
35. Trines J, Hornberger LK. Evolution of heart disease in utero. *Pediatr Cardiol* (2004) 25:287–98. doi:10.1007/s00246-003-0592-2
36. Hornberger LK, Sanders SP, Rein AJ, Spevak PJ, Parness IA, Colan SD. Left heart obstructive lesions and left ventricular growth in the midtrimester fetus. A longitudinal study. *Circulation* (1995) 92:1531–8.
37. Simpson JM, Sharland GK. Natural history and outcome of aortic stenosis diagnosed prenatally. *Heart* (1997) 77:205–10.
38. Kuhl E. Growing matter: a review of growth in living systems. *J Mech Behav Biomed Mater* (2014) 29:529–43. doi:10.1016/j.jmbbm.2013.10.009
39. Garcia-Canadilla P, Rudenick PA, Crispi F, Cruz-Lemini M, Palau G, Camara O, et al. A computational model of the fetal circulation to quantify blood redistribution in intrauterine growth restriction. *PLoS Comput Biol* (2014) 10:e1003667. doi:10.1371/journal.pcbi.1003667
40. Zeigler AC, Richardson WJ, Holmes JW, Saucerman JJ. A computational model of cardiac fibroblast signaling predicts context-dependent drivers of myofibroblast differentiation. *J Mol Cell Cardiol* (2016) 94:72–81. doi:10.1016/j.yjmcc.2016.03.008
41. Ma X, Gao L, Karamanlidis G, Gao P, Lee CF, Garcia-Menendez L, et al. Revealing pathway dynamics in heart diseases by analyzing multiple differential networks. *PLoS Comput Biol* (2015) 11:e1004332. doi:10.1371/journal.pcbi.1004332
42. Kowalski WJ, Teslovich NC, Menon PG, Tinney JP, Keller BB, Pekkan K. Left atrial ligation alters intracardiac flow patterns and the biomechanical landscape in the chick embryo. *Dev Dyn* (2014) 243:652–62.
43. Hove JR, Köster RW, Forouhar AS, Acevedo-Bolton G, Fraser SE, Gharib M. Intracardiac fluid forces are an essential epigenetic factor for embryonic cardiogenesis. *Nature* (2003) 421:172–7. doi:10.1038/nature01282
44. Mohammed NB, Chinnaiya A. Evolution of foetal echocardiography as a screening tool for prenatal diagnosis of congenital heart disease. *J Pak Med Assoc* (2011) 61:904–9.
45. Curtis MW, Russell B. Micromechanical regulation in cardiac myocytes and fibroblasts: implications for tissue remodeling. *Pflugers Arch* (2011) 462(1):105–17. doi:10.1007/s00424-011-0931-8
46. Lin YF, Swinburne I, Yelon D. Multiple influences of blood flow on cardiomyocyte hypertrophy in the embryonic zebrafish heart. *Dev Biol* (2012) 362(2):242–53. doi:10.1016/j.ydbio.2011.12.005
47. Arteaga-Martínez M, Halley-Castillo E, García-Peláez I, Villasis-Keever MA, Aguirre OM, Vizcaino-Alarcón A. Morphometric study of the ventricular segment of the human fetal heart between 13 and 20 weeks' gestation. *Fetal Pediatr Pathol* (2009) 28:78–94. doi:10.1080/15513810802679449
48. Vetter FJ, McCulloch AD. Three-dimensional analysis of regional cardiac function: a model of rabbit ventricular anatomy. *Prog Biophys Mol Biol* (1998) 69(2–3):157–83.
49. Krishnamurthy A, Villongco CT, Chuang J, Frank LR, Nigam V, Belezzuoli E, et al. Patient-specific models of cardiac biomechanics. *J Comput Phys* (2013) 244:4–21. doi:10.1016/j.jcp.2012.09.015
50. Guccione JM, McCulloch AD, Waldman LK. Passive material properties of intact ventricular myocardium determined from a cylindrical model. *J Biomech Eng* (1991) 113:42–55.
51. Kenny JF, Plappert T, Doubilet P, Saltzman DH, Cartier M, Zollars L, et al. Changes in intracardiac blood flow velocities and right and left ventricular stroke volumes with gestational age in the normal human fetus: a prospective Doppler echocardiographic study. *Circulation* (1986) 74:1208–16.
52. Johnson P, Maxwell DJ, Tynan MJ, Allan LD. Intracardiac pressures in the human fetus. *Heart* (2000) 84:59–63.
53. McElhinney DB, Marshall AC, Wilkins-Haug LE, Brown DW, Benson CB, Silva V, et al. Predictors of technical success and postnatal biventricular outcome after in utero aortic valvuloplasty for aortic stenosis with evolving hypoplastic left heart syndrome. *Circulation* (2009) 120:1482–90. doi:10.1161/CIRCULATIONAHA.109.848994
54. Banerjee I, Carrion K, Serrano R, Dyo J, Sasik R, Lund S, et al. Cyclic stretch of embryonic cardiomyocytes increases proliferation, growth, and expression while repressing Tgf-β signaling. *J Mol Cell Cardiol* (2015) 79:133–44. doi:10.1016/j.yjmcc.2014.11.003
55. Li XS, Demmel JW. SuperLU_DIST: a scalable distributed-memory sparse direct solver for unsymmetric linear systems. *ACM Trans Math Software (TOMS)* (2003) 29(2):110–40. doi:10.1145/779359.779361
56. Leiva MC, Tolosa JE, Binotto CN, Weiner S, Huppert L, Denis AL, et al. Fetal cardiac development and hemodynamics in the first trimester. *Ultrasound Obstet Gynecol* (1999) 14:169–74. doi:10.1046/j.1469-0705.1999.14030169.x
57. Bhat AH, Corbett V, Carpenter N, Liu N, Liu R, Wu A, et al. Fetal ventricular mass determination on three-dimensional echocardiography: studies in normal fetuses and validation experiments. *Circulation* (2004) 110:1054–60. doi:10.1161/01.CIR.0000139848.33468.22
58. Zheng M, Schaal M, Chen Y, Li X, Shentu W, Zhang P, et al. Real-time 3-dimensional echocardiographic assessment of ventricular volume, mass, and function in human fetuses. *PLoS One* (2013) 8:e58494. doi:10.1371/journal.pone.0058494
59. Messing B, Cohen SM, Valsky DV, Shen O, Rosenak D, Lipschuetz M, et al. Fetal heart ventricular mass obtained by STIC acquisition combined with inversion mode and VOCAL. *Ultrasound Obstet Gynecol* (2011) 38:191–7. doi:10.1002/uog.8980
60. St John Sutton MG, Gewitz MH, Shah B, Cohen A, Reichek N, Gabbe S, et al. Quantitative assessment of growth and function of the cardiac chambers in the normal human fetus: a prospective longitudinal echocardiographic study. *Circulation* (1984) 69:645–54.
61. Meyer-Wittkopf M, Rappe N, Sierra F, Barth H, Schmidt S. Three-dimensional (3-D) ultrasonography for obtaining the four and five-chamber view: comparison with cross-sectional (2-D) fetal sonographic screening. *Ultrasound Obstet Gynecol* (2000) 15:397–402. doi:10.1046/j.1469-0705.2000.00108.x
62. Zhou J, Zhou Q, Zhang M, Zeng S, Peng Q, Tian L. Echocardiographic follow-up and pregnancy outcome of fetuses with cardiac asymmetry at 18-22 weeks of gestation. *Prenat Diagn* (2014) 34:900–7. doi:10.1002/pd.4391
63. Kovalchin JP, Silverman NH. The impact of fetal echocardiography. *Pediatr Cardiol* (2004) 25:299–306. doi:10.1007/s00246-003-0593-1
64. Kluckow MR, Cooper S, Sholler GF. Prenatal diagnosis of hypoplastic left heart syndrome. *Aust N Z J Obstet Gynaecol* (1993) 33:135–9.
65. Thakur V, Munk N, Mertens L, Nield LE. Does prenatal diagnosis of hypoplastic left heart syndrome make a difference? A systematic review. *Prenat Diagn* (2016) 36:854–63. doi:10.1002/pd.4873

Conflict of Interest Statement: AM and JO are co-founders of and have an equity interest in Insilicomed, Inc., a licensee of UCSD software used in this research, and they serve as scientific advisors to Insilicomed, Inc. Some research grants to AM and JO, including those acknowledged here, have been identified for conflict of interest management based on the overall scope of the project and its potential benefit to Insilicomed, Inc. They are required to disclose this relationship in publications acknowledging the grant support; however, the research subject and findings reported here did not involve the company in any way and have no known relationship to the business activities or scientific interests of the company. The terms of this arrangement have been reviewed and approved by the University of California San Diego in accordance with its conflict of interest policies. The other authors have no competing interests to declare.

frontiers in Pediatrics

ORIGINAL RESEARCH
published: 12 December 2016
doi: 10.3389/fped.2016.00133

Regional Differences in End-Diastolic Volumes between 3D Echo and CMR in HLHS Patients

Alberto Gomez[1], Ozan Oktay[2], Daniel Rueckert[2], Graeme P. Penney[1], Julia A. Schnabel[1], John M. Simpson[1,3] and Kuberan Pushparajah[3]*

[1] *Department of Biomedical Engineering, King's College London, London, UK,* [2] *Biomedical Image Analysis Group, Imperial College London, London, UK,* [3] *Department of Congenital Heart Disease, Evelina London Children's Hospital, London, UK*

Ultrasound is commonly thought to underestimate ventricular volumes compared to magnetic resonance imaging (MRI), although the reason for this and the spatial distribution of the volume difference is not well understood. In this paper, we use landmark-based image registration to spatially align MRI and ultrasound images from patients with hypoplastic left heart syndrome and carry out a qualitative and quantitative spatial comparison of manual segmentations of the ventricular volume obtained from the respective modalities. In our experiments, we have found a trend showing volumes estimated from ultrasound to be smaller than those obtained from MRI (by approximately up to 20 ml), and that important contributors to this difference are the presence of artifacts such as shadows in the echo images and the different criteria to include or exclude image features as part of the ventricular volume.

Keywords: volume estimation, ventricular function, ultrasound imaging, cardiac magnetic resonance, image registration

OPEN ACCESS

Edited by:
Giovanni Biglino, University of Bristol, UK

Reviewed by:
Gianni Pedrizzetti, University of Trieste, Italy
Ethan Kung, Clemson University, USA

****Correspondence:***
Alberto Gomez
alberto.gomez@kcl.ac.uk

Specialty section:
This article was submitted to Pediatric Cardiology, a section of the journal Frontiers in Pediatrics

Received: *28 October 2016*
Accepted: *24 November 2016*
Published: *12 December 2016*

Citation:
Gomez A, Oktay O, Rueckert D, Penney GP, Schnabel JA, Simpson JM and Pushparajah K (2016) Regional Differences in End-Diastolic Volumes between 3D Echo and CMR in HLHS Patients. Front. Pediatr. 4:133. doi: 10.3389/fped.2016.00133

1. INTRODUCTION

Accurate estimation of ventricular volumes is critical for a number of clinical applications, particularly in patients with congenital heart disease (CHD). In hypoplastic left heart syndrome (HLHS), the left heart structures are underdeveloped to the extent that they are unable to support the systemic circulation. The right ventricle (RV) is dilated and hypertrophied as a consequence, supporting the systemic circulation on its own. This results in abnormal RV geometry.

Ultrasound (US) is the most widespread cardiac imaging modality. However, image quality can be poor compared to other non-invasive techniques such as cardiac magnetic resonance (CMR) imaging. CMR is considered to provide reference images of the heart (1) and hence CMR images are frequently used to estimate reference values for cardiac shape, size, and function, as discussed by Kjaergaard et al. and Greupner et al. (2, 3). Previous studies, for example Bell et al. (4) have compared ventricular volumes obtained from CMR and echo. Moreover, numerous studies, summarized in Ref. (5), showed that echo-derived end-diastolic volumes (EDV) systematically underestimate EDV values derived from CMR images by up to 20 ml in average and up to 34% in relative terms. These differences are more significant in CHD patients than in healthy subjects or in other patient groups.

The objective of this study is to investigate the spatial distribution of the difference in reported EDV between MR-derived segmentations and echo-derived segmentations in HLHS patients. In particular, we analyze what features of the image lead to differences in contour delineation, and where these differences occur. The contribution of this paper is to describe the spatial distribution

of differences between volume estimates obtained from paired CMR and echocardiographic (echo) images.

2. MATERIALS AND METHODS

2.1. Patient Selection and Data Acquisition

We study multimodal images acquired from 5 patients with hypoplastic left heart syndrome (HLHS), 3 post-Norwood 1, and 2 post-Hemifontan, with an age range of 0.18–3.40 years, and weight in the range of 4.93–15.4 kg. These patients underwent a research ultrasound examination immediately after the clinical MR examination, both under general anesthesia (GA). Transthoracic ultrasound volumes were acquired using a Philips iE33 system and a cardiac X5-1 3D transducer, from subcostal windows.

Cardiac magnetic resonance (CMR) imaging was performed using a 1.5 T MRI scanner (Philips Intera Achieva, Philips Healthcare, Best, Netherlands). RV volumes and function were obtained as part of a comprehensive functional evaluation. In accordance with our unit protocol for CMR evaluation of HLHS, a single stack of contiguous 6–8 mm balanced SSFP slices (TR 1.8 ms, TE 3.5 ms, FOV 180–320, 40 phases per cardiac cycle, 6–12 lines per segment depending on heart rate, acquired resolution 1.2 mm × 1.2 mm to 1.8 mm × 1.8 mm) oriented in a plane equivalent to the short axis of the tricuspid valve were obtained in an end-expiratory breath-hold of 4–7 s per slice.

This study was carried out in accordance with the principles of the Declaration of Helsinki. Ethical approval was granted by the local ethics committee "Advanced Echocardiography in Pediatric Patients" at Guy's and St. Thomas's and King's College London (09/H0802/116) after informed consent was obtained from the patients parents.

2.2. Ventricle Segmentation

Segmentations on both MR and ultrasound images were done manually. Semiautomatic methods based on processing of the image data, such as model based segmentation, level sets, region growing, and other methods can introduce a bias in the comparison because MR and ultrasound images perform very differently on them. Consequently, we have used the manual segmentation tool provided by the MITK software (6) to segment both modalities. The segmentation was carried out by contouring the endocardium on a stack of short-axis planes and then interpolating the contours to form a volume.

2.3. Ultrasound to MR Image Alignment

Echo to CMR alignment (registration) is a challenging problem. Image features are normally not consistent between the two modalities because not all structures that are visible in the ultrasound image (e.g., trabeculae, valves) are also visible in the CMR image. Moreover, view-dependent artifacts characteristic to ultrasound imaging (e.g., shadows, reverberations) lead to erroneous image features that obviously are not present in the CMR image. Last, structures that are visible in both modalities are captured in a very different way: for example, ultrasound image formation can cause thickening or narrowing of these structures depending on the angle of incidence of the ultrasound wave, while no such view dependency takes place in CMR image acquisition. As a result, most automated and semi-automated, image- or feature-based registration algorithms fail to align CMR and echo images accurately.

For this study, we have carried out image alignment by manually selecting corresponding ventricular landmarks in both modalities and calculating the rigid transform (rotation and translation) between the two landmark sets. An independent operator carried out registrations for all patients to ensure that the same alignment was used when comparing segmentations carried out by different experts.

Landmark selection is done as follows: first, the base-to-apex axis was found (**Figures 1A,B**). Along this axis, a point at mid-height of the ventricle (represented in the figure by a white dot) is selected to produce a short-axis slice (**Figure 1C**). On this short view, the in-plane axes are rotated and translated so that one plane is parallel to the diaphragm, and the other passes by the closest papillary muscle (**Figure 1D**) while maintaining the slicing planes orthogonal to each other.

Without changing the orientations of the slicing planes, the crosshair is translated following the through short-axis direction to the atrioventricular valve plane (**Figures 1E,F**). At that location, six landmarks are selected: the center of the atrioventricular valve (1), the inferior (2), anterior (3), left (4) and right (5) sides of the valve annulus, and the ventricular apex (6). Following the same process, corresponding landmarks are selected in the CMR image (**Figures 1G,H**). The rigid transformation between the two point sets was found using the least squares method described by Arun et al. (7).

Figure 2 shows the image registration results for 5 patients. A superimposition of the medial short-axis slice from both CMR and echo images, for each patient, is shown. A selection of movies showing the achieved alignment and its consistency over time are included in Supplementary Material.

2.4. Regional Division of the RV

In order to carry out a regional analysis of the difference in estimated volume, we need to divide the ventricular volume into sectors. There is little literature on regional analysis of the right ventricle (RV) in Fontan patients like those with hypoplastic left heart syndrome (HLHS). For repaired Tetralogy of Fallot (ToF) patients, Zhong et al. (8) proposed a 15-segment subdivision.

This subdivision is, however, not well suited for single ventricle circulation because of the essential differences in RV morphology between the two cases. In repaired ToF, the RV morphology is not very different from a normal RV. In Fontan circulation, there is no functional left ventricle (LV), hence the RV supports the systemic circulation and has adapted its morphology becoming more globular, toward the shape of a normal LV.

For this reason, other means of describing the RV anatomy in a standardized way have been proposed. Menon et al. (9) carried out regional analysis from 2D echocardiography by dividing the myocardium in a parasternal long-axis view into four sections and in a four chamber view into 6 segments. Wong et al. (10) carried out a 3D analysis on RV morphology and function in HLHS using a population-based atlas, which defined ventricular

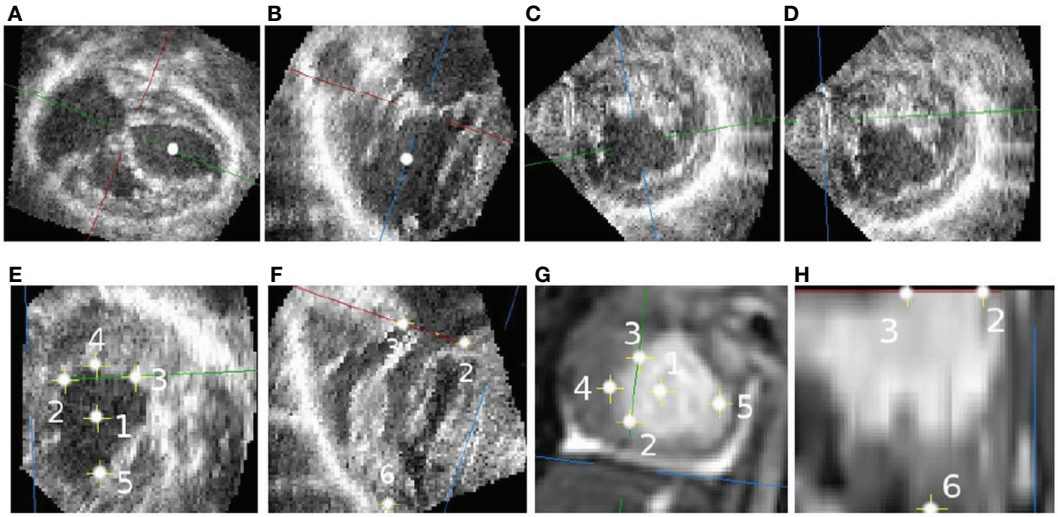

FIGURE 1 | **Selecting corresponding landmarks in echo and CMR images**. **(A)** Long axis slice. **(B)** RVOT view. **(C)** Short-axis view with arbitrary rotation. **(D)** Short-axis view parallel to the diaphragm. **(E)** Valve-plane landmarks. **(F)** Valve and apex landmarks. **(G)** CMR landmarks. **(H)** CMR landmarks.

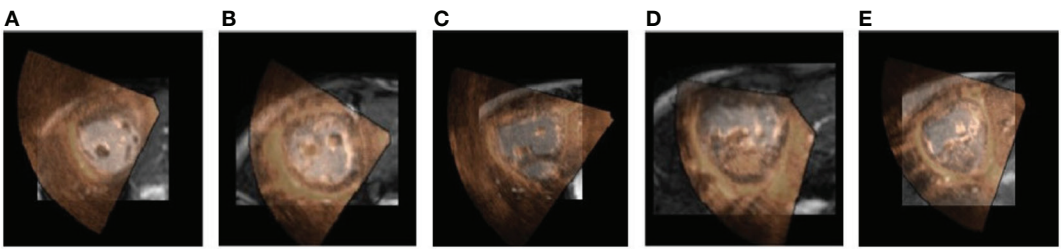

FIGURE 2 | **Alignment results**. The figure shows a 2D short-axis slice of the aligned volumes for 5 patients. The CMR image is shown in the background in grayscale and the echo image is overlaid on top using a red-to-yellow colormap. A selection of movies showing the achieved alignment and its consistency over time are included in Supplementary Material. **(A)** Pat 1. **(B)** Pat 2. **(C)** Pat 3. **(D)** Pat 4. **(E)** Pat 5.

anatomy with respect to the position of the LV remnant. This representation allowed the estimation of regional strain dividing the RV into basal, medial, and apical layers.

Inspired by the divisions carried out by Menon et al., Zhong et al., and Wong et al. (8–10), and taking into account the standard AHA 17 segment division for the LV proposed in Ref. (11), in this paper, we propose to divide the 3D RV shape into 14 segments as indicated in **Figure 3**. Along the RV axis, four layers are defined: apical, medial, basal, and valvular. The apical layer consists of a single sector. The medial layer and the basal layer are divided into 4 and 6 sectors, respectively (similar to the LV AHA division). The valvular layer is divided into 3 sectors that cover half of the circle reflecting the asymmetric shape of the RV, and cover the "shoulder" area underneath the inflow valve. This layer covers the upper anterior wall (1), the upper lateral free wall (2), and upper inferior free wall (3). The basal layer, situated below the valvular layer, starts at the intersection point with the anterior (4), lateral (5), and inferior (6) parts of the free wall and the inferoseptal (7), lateral-septal (8), and anteroseptal (9) sectors. The medial layer includes four sectors covering the anterior (10), the lateral free wall (11), the inferior (12), and the septal (13) sectors. The apical layer includes a single sector (14). **Figure 3A** shows a representation of a RV for reference. **Figure 3** shows a 3D representation of the segment division for one patient from the echo-derived segmentation and from the CMR-derived segmentation. Colors are matched by the bulls-eye plot diagram in **Figure 3D**, which is used as model for the results in the remainder of this paper. The orientation of the bulls-eye plot and the denominations "anterior" (A) and "inferior" (I) are consistent with that in Ref. (11). We have replaced the septal and lateral names in (11) by right (R) and left (L), because we believe this is a more straightforward and intuitive notation in systemic RV patients.

An advantage of the landmark selection process described in Sec 2.3 is that it allows to define the segment division automatically since the RV axis is defined by points 1 (center of tricuspid valve) and 6 (RV apex), and the superior-to-inferior direction is defined by the points 2 and 3.

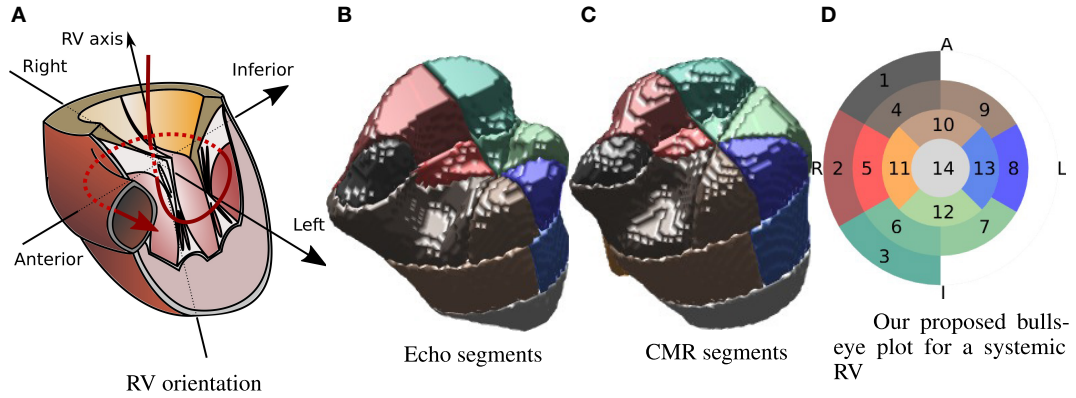

FIGURE 3 | Segment division on the RV. Representation of the RV and its main axes **(A)**. Example of segment division for patient 2 from echo **(B)** and CMR **(C)**. Bulls-eye plot representation of the proposed 14-segment systemic RV division **(D)**. Annotations indicate left (L), right (R), inferior (I), and anterior (A).

2.5. Experiments and Data Analysis

Three experts carried out EDV segmentations on 5 pairs of pre-aligned MR and ultrasound images, as described in Sec. 2.2. These images were spatially aligned as indicated in Sec. 2.3. The resulting aligned segmentations were divided into 14 segments as described in Sec. 2.4.

The resulting end diastolic volumes (EDVs) are compared globally ($\Delta EDV = EDV_{echo} - EDV_{CMR}$) in absolute terms, and also regionally. For the regional analysis, the difference between echo-derived and CMR derived regional volumes is expressed as a fraction of the total EDV volume estimated from CMR:

$$\Delta EDV_r = \frac{EDV_{r,echo} - EDV_{r,CMR}}{EDV_{CMR}}, \text{ for every region } r \qquad (1)$$

This allows us to compare the obtained values across patients. In order to compute statistics on segmentations from multiple experts, the average segmentation was computed by averaging the binary masks representing the EDV segmentations followed by a thresholding operation where voxels with an intensity greater than 0.5 were kept.

In addition to the numerical analysis, we have carried out a qualitative analysis by comparing the average segmentation contours at four different short-axis planes uniformly spaced along the RV axis for each patient.

3. RESULTS

3.1. Numerical Results

Global EDV differences are shown in **Table 1**. The numbers reflect the average ± SD over all experts, for each patient and each modality, in milliliters. The numbers reported are within the normal range and variability to other studies in the literature as reported by Simpson et al. (5).

Large variability in the CMR derived volumes in patient 1 are associated to low echo image quality (as shown in **Figure 6**, top left), which led to large differences on how experts decided to include some structures like the papillary muscles.

TABLE 1 | Ventricular volumes at end diastole in milliliters, including segmentations from all experts.

Patient	Echo	CMR	$EDV_{echo}-EDV_{cmr}$
1	29.69 ± 2.67	57.73 ± 16.98	−28.05 ± 14.75
2	18.27 ± 1.27	27.70 ± 5.58	−9.44 ± 4.37
3	31.17 ± 2.54	51.17 ± 8.59	−20.00 ± 9.61
4	26.23 ± 5.90	24.95 ± 10.12	1.29 ± 7.74
5	21.17 ± 3.28	26.97 ± 9.87	−5.79 ± 6.96

The results of the regional analysis of EDV differences are shown in **Figures 4** and **5**. **Figure 4** shows the average relative difference in regional EDV bulls-eye plot for each patient, in percentage. There is a common pattern across all datasets where the highest disagreement is near the apex, decreasing gradually near the valve plane.

Figure 5 shows the integrated results from all patients as a bar chart. This representation has been chosen instead of the bulls-eye plot in order to accurately show the average values as well as the SD as error bars. The sector number corresponding to each bar is indicated next to the bar. Note that, in the basal layer, the order of the bars has been modified so that sectors that are approximately aligned vertically are represented as bars that are aligned horizontally.

The results shown in **Figure 5** are consistent with the results shown in **Figure 4E**. The highest average disagreement takes place at the apex, with a −14.2% relative difference between echo-derived volume and CMR-derived volume. The spatial distribution of the error in the medial layer is uniformly distributed and close to −5% in average. In the basal and the valvular layers, the difference between the two modalities is significantly smaller. Interestingly, in sectors near the outflow tracts (1, 2, 4, and 5), there is a high variance across patients and operators. The qualitative results in the next section expand on the potential reasons for this.

3.2. Qualitative Results

Figure 6 shows a selection of short-axis, end-diastole views of both CMR and echo including the outline of both echo and

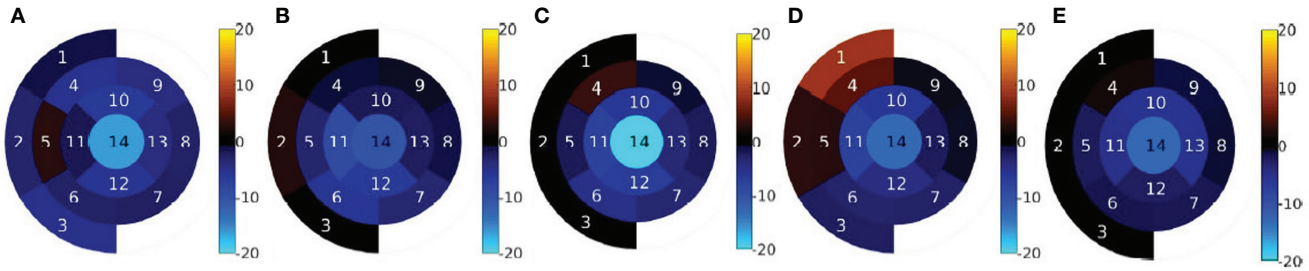

FIGURE 4 | **Regional volume difference relative to the global CMR-derived volume, in percentage**. **(A)** Pat 1. **(B)** Pat 2. **(C)** Pat 3. **(D)** Pat 4. **(E)** Pat 5.

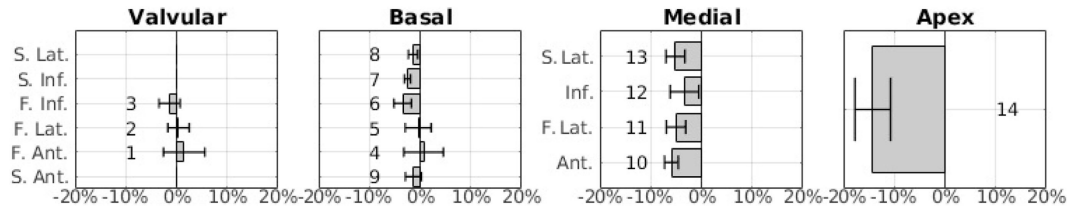

FIGURE 5 | **Average regional volume difference relative to the global (CMR)-derived volume between the regional CMR derived volume and the echo-derived volume, in percentage**. The error bars indicate ± SD.

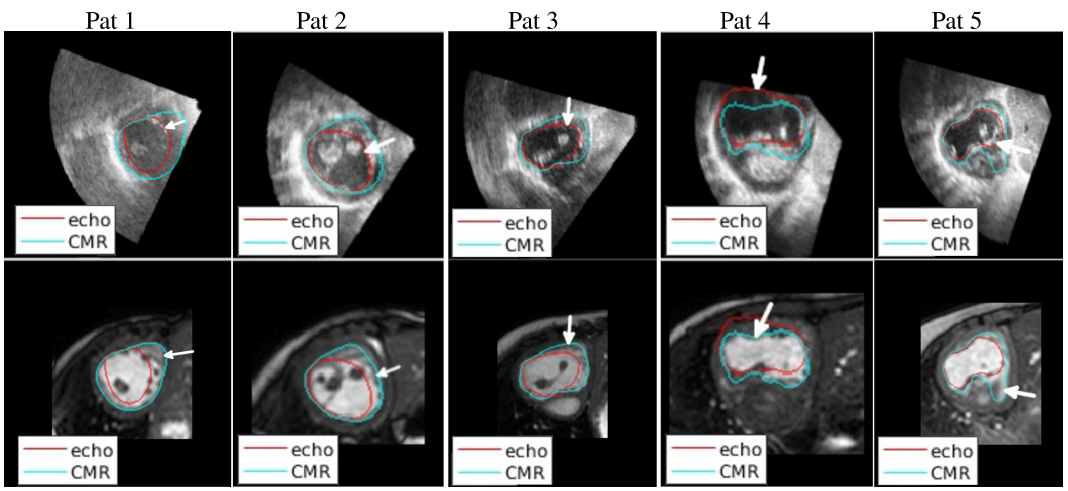

FIGURE 6 | **Qualitative results**. Visual comparison of the echo-derived segmentation and the CMR-derived segmentation superimposed on the aligned echo image (top row) and on the aligned CMR image (bottom row).

CMR-derived segmentations (after alignment), to illustrate the most significant findings of this study. The ventricular segmentation from echo is represented as a red contour and the CMR-derived segmentation as a green contour. A comprehensive collection of short-axis views for all patients at different planes is included in Supplementary Material.

The 2D slices in **Figure 6** illustrate sources of systematic differences between EDV segmentations carried out using CMR images and echo images. On the first column on the left, a very significant difference between the two contours can be observed. Echo-derived segmentation was particularly challenging in this patient due to the low-image quality (compared to images from other patients). Additionally, the echo-derived contour was drawn excluding trabeculae from the segmentation. In the CMR image, where the visibility of the endocardium is poor, the segmentation appears to run closer to the myocardium.

On the second column from the left, it can be seen that image quality is relatively high in both modalities, but the difference comes from the contours delineating different structures. The

echo-derived contour (in red) correctly follows an image edge (top row), and the CMR-derived contour (in blue) also follows an edge in the CMR image (bottom row). The edge in the echo image represents the trabeculations, which are not visible in the CMR image, where the contour follows the myocardium. A similar effect can be observed in the third column (patient 3).

The fourth column shows the effect of lack of boundary definition in the ultrasound image on the resulting segmentation. In this case, overall image quality is high, but the anterior wall is not visible due to shadowing from the air in the lung. As a result, the delineated contour does not match the real structure, which is visible in the CMR image. This finding is reflected in our proposed bulls-eye plot in **Figure 4D**.

The fifth column illustrates disagreement due to lack of boundary definition. An unclear boundary was delineated as a true boundary on the echo image, while it was considered part of the ventricular cavity in the CMR.

4. DISCUSSION

In this paper, we have investigated the spatial distribution of RV volume differences by comparing ventricular segmentations from CMR and from echo after aligning the two modalities on patients with HLHS. We have found a similar level of overall volume difference (up to a 20 ml) between echo and CMR as in related literature, summarized in (5). We have found that there are two major causes for this volume difference. First, the lack of boundary definition in some echo images as a consequence of shadowing artifacts produces large errors in the segmentation. These kind of artifacts occur more commonly near the anterior-free ventricular wall because of the proximity to the lungs.

The second finding, perhaps more interesting, is that the trabeculations in the right ventricular surface are captured in a very different way in the CMR images and in the echo images. Mostly, CMR images show the inner RV surface as flat and free from the characteristic foldings and complex structures that are visible in the echo images. In these cases, the CMR segmentation lies closer to the epicardium. This partly explains the consistent bias for echocardiography to produce lower volumes than MRI.

A third, less significant cause of volume disagreement appears to be the lack of agreement between experts on where to finish the ventricular segmentation near the inlet and outlet of the RV.

In the case where echo image quality is significantly low, for example in patient 1 (**Figure 6**, top left), the segmentation process can be very challenging and the difference with CMR-derived volumes can be extremely large. A larger study is required to ascertain whether patient 1 is representative, in terms of image quality, of this patient group.

A limitation of the manual registration is that it can introduce a bias due to operator dependency inherent to a manual process. This would not affect overall segmentations (since segmentations are carried out before registration). We believe the impact of this potential error is relatively small since manually picked landmarks are commonly used as reference (12, 13) when a ground truth registration is not available. An interesting consideration of the proposed landmark-based registration method is that although excellent image alignment can be achieved, the landmark set alignment can yield a relatively large residual error (up to 4 mm). The reason for this residual error is that landmarks do not necessarily provide a very good pairwise correspondence, but still provide an accurate groupwise correspondence. For example, points (2–5) are picked at the intersection of specific axes with the visible valve annulus contour, but this contour can be captured differently in CMR and echo, which is consistent with the endocardial segmentations done on CMRI and echo images that we have shown.

The limited number of patients and the lack of a ground truth volume measurement prevents us from making a strong statement on which volume estimate is more accurate; however, our data suggest that, when high-quality echo data are available, RV estimates can be as good as those from CMR. This can be of particular clinical significance if not only ED volumes are required but also time-resolved volume estimations are sought, because echocardiography is uniquely placed to provide high temporal and spatial resolution images of the heart.

AUTHOR CONTRIBUTIONS

All the co-authors have had substantial scientific input and have agreed upon the current content.

ACKNOWLEDGMENTS

The authors would like to acknowledge Dr. Hannah Bellsham-Revell and Dr. Aaron Bell for their help with data acquisition.

FUNDING

This work was supported by the Wellcome Trust IEH Award (102431). The authors acknowledge financial support from the Department of Health via the National Institute for Health Research (NIHR) comprehensive Biomedical Research Centre award to Guy's and St. Thomas' NHS Foundation Trust in partnership with King's College London and King's College Hospital NHS Foundation Trust.

SUPPLEMENTARY MATERIAL

The Supplementary Material for this article can be found online at http://journal.frontiersin.org/article/10.3389/fped.2016.00133/full#supplementary-material.

VIDEO S1 | Fused visualization of 3D echo and stack-cine CMR from patient 1.

VIDEO S2 | Fused visualization of 3D echo and stack-cine CMR from patient 2.

VIDEO S3 | Fused visualization of 3D echo and stack-cine CMR from patient 3.

VIDEO S4 | Fused visualization of 3D echo and stack-cine CMR from patient 4.

REFERENCES

1. Grothues F, Smith GC, Moon JC, Bellenger NG, Collins P, Klein HU, et al. Comparison of interstudy reproducibility of cardiovascular magnetic resonance with two-dimensional echocardiography in normal subjects and in patients with heart failure or left ventricular hypertrophy. *Am J Cardiol* (2002) 90(1):29–34. doi:10.1016/S0002-9149(02)02381-0
2. Kjaergaard J, Petersen CL, Kjaer A, Schaadt BK, Oh JK, Hassager C. Evaluation of right ventricular volume and function by 2D and 3D echocardiography compared to MRI. *Eur J Echocardiogr* (2006) 7(6):430–8. doi:10.1016/j.euje.2005.10.009
3. Greupner J, Zimmermann E, Grohmann A, Dübel H-P, Althoff T, Borges AC, et al. Head-to-head comparison of left ventricular function assessment with 64-row computed tomography. *J Am Coll Cardiol* (2012) 59(21):1897–907. doi:10.1016/j.jacc.2012.01.046
4. Bell A, Rawlins D, Bellsham-Revell H, Miller O, Razavi R, Simpson J. Assessment of right ventricular volumes in hypoplastic left heart syndrome by real-time three-dimensional echocardiography: comparison with cardiac magnetic resonance imaging. *Eur Heart J Cardiovasc Imaging* (2014) 15(3):257–66. doi:10.1093/ehjci/jet145
5. Simpson J, Lopez L, Acar P, Friedberg M, Khoo N, Ko H, et al. Three-dimensional echocardiography in congenital heart disease: an expert consensus document from the European Association of Cardiovascular Imaging and the American Society of Echocardiography. *J Am Soc Echocardiogr* (2016) 17(10):S0894–7317.
6. Wolf I, Vetter M, Wegner I, Böttger T, Nolden M, Schöbinger M, et al. The medical imaging interaction toolkit. *Med Image Anal* (2005) 9(6):594–604. doi:10.1016/j.media.2005.04.005
7. Arun KS, Huang TS, Blostein SD. Least-squares fitting of two 3-D point sets. *IEEE Trans Pattern Anal Mach Intell* (1987) 9(5):698–700. doi:10.1109/TPAMI.1987.4767965
8. Zhong L, Gobeawan L, Su Y, Tan J-L, Ghista D, Chua T, et al. Right ventricular regional wall curvedness and area strain in patients with repaired tetralogy of Fallot. *Am J Physiol Heart Circ Physiol* (2012) 302(6):H1306–16. doi:10.1152/ajpheart.00679.2011
9. Menon SC, Minich LL, Casper TC, Puchalski MD, Hawkins JA, Tani LY. Regional myocardial dysfunction following Norwood with right ventricle to pulmonary artery conduit in patients with hypoplastic left heart syndrome. *J Am Soc Echocardiogr* (2011) 24(8):826–33. doi:10.1016/j.echo.2011.05.008
10. Wong J, Lamata P, Rathod RH, Bertaud S, Dedieu N, Bellsham-Revell H, et al. Right ventricular morphology and function following stage I palliation with a modified Blalock-Taussig shunt versus a right ventricle-to-pulmonary artery conduit. *Eur J Cardiothorac Surg* (2016). doi:10.1093/ejcts/ezw227
11. Cerqueira MD, Weissman NJ, Dilsizian V, Jacobs AK, Laskey WK, Pennell DJ, et al. Standardized myocardial segmentation and nomenclature for tomographic imaging of the heart. *Circulation* (2002) 105(4):539–42. doi:10.1161/hc0402.102975
12. Fitzpatrick J, West J, Maurer C. Predicting error in rigid-body point-based registration. *IEEE Trans Med Imaging* (1998) 17(5):694–702. doi:10.1109/42.736021
13. Pantazis D, Joshi A, Jiang J, Shattuck DW, Bernstein LE, Damasio H, et al. Comparison of landmark-based and automatic methods for cortical surface registration. *Neuroimage* (2010) 49(3):2479–93. doi:10.1016/j.neuroimage.2009.09.027

Conflict of Interest Statement: The authors declare that the research was conducted in the absence of any commercial or financial relationships that could be construed as a potential conflict of interest.

frontiers in Pediatrics

ORIGINAL RESEARCH
published: 26 April 2017
doi: 10.3389/fped.2017.00078

Reproducing Patient-Specific Hemodynamics in the Blalock–Taussig Circulation Using a Flexible Multi-Domain Simulation Framework: Applications for Optimal Shunt Design

Christopher J. Arthurs[1†], Pradyumn Agarwal[2†], Anna V. John[2], Adam L. Dorfman[3], Ronald G. Grifka[3] and C. Alberto Figueroa[2,4]*

[1] Division of Imaging Sciences and Biomedical Engineering, King's College London, King's Health Partners, St. Thomas' Hospital, London, UK, [2] Department of Biomedical Engineering, University of Michigan, Ann Arbor, MI, USA, [3] Department of Pediatric Cardiology, University of Michigan Health System, Ann Arbor, MI, USA, [4] Department of Surgery, University of Michigan, Ann Arbor, MI, USA

OPEN ACCESS

Edited by:
Giovanni Biglino, University of Bristol, UK

Reviewed by:
Neil W. Bressloff, University of Southampton, UK
Yasuhiro Fujii, Okayama University, Japan

***Correspondence:**
Christopher J. Arthurs
christopher.arthurs@kcl.ac.uk

[†]*Joint first authors.*

Specialty section:
This article was submitted to Pediatric Cardiology, a section of the journal Frontiers in Pediatrics

Received: *11 January 2017*
Accepted: *31 March 2017*
Published: *26 April 2017*

Citation:
Arthurs CJ, Agarwal P, John AV, Dorfman AL, Grifka RG and Figueroa CA (2017) Reproducing Patient-Specific Hemodynamics in the Blalock–Taussig Circulation Using a Flexible Multi-Domain Simulation Framework: Applications for Optimal Shunt Design. Front. Pediatr. 5:78. doi: 10.3389/fped.2017.00078

For babies born with hypoplastic left heart syndrome, several open-heart surgeries are required. During Stage I, a Norwood procedure is performed to construct an appropriate circulation to both the systemic and the pulmonary arteries. The pulmonary arteries receive flow from the systemic circulation, often using a Blalock–Taussig (BT) shunt between the innominate artery and the right pulmonary artery. This procedure causes significantly disturbed flow in the pulmonary arteries. In this study, we use computational hemodynamic simulations to demonstrate its capacity for examining the properties of the flow through and near the BT shunt. Initially, we construct a computational model which produces blood flow and pressure measurements matching the clinical magnetic resonance imaging (MRI) and catheterization data. Achieving this required us to determine the level of BT shunt occlusion; because the occlusion is below the MRI resolution, this information is difficult to recover without the aid of computational simulations. We determined that the shunt had undergone an effective diameter reduction of 22% since the time of surgery. Using the resulting geometric model, we show that we can computationally reproduce the clinical data. We, then, replace the BT shunt with a hypothetical alternative shunt design with a flare at the distal end. Investigation of the impact of the shunt design reveals that the flare can increase pulmonary pressure by as much as 7% and flow by as much as 9% in the main pulmonary branches, which may be beneficial to the pulmonary circulation.

Keywords: hypoplastic left heart syndrome, Blalock–Taussig shunt, computational hemodynamics, simulation, multi-domain, CRIMSON

1. INTRODUCTION

Each year in the United States, 1 out of every 4,344 babies are born with hypoplastic left heart syndrome (HLHS) (1). Soon after birth, they develop respiratory distress, elevated heart rate, and hypoxemia. A multi-stage surgical program is required to construct pathways for blood flow

to both the systemic and pulmonary circulations using only the single (right) ventricle. The Norwood procedure is the first stage of the surgical repair and is performed within the first week of life. The main pulmonary artery is detached from the branches, then connected to the hypoplastic aorta, creating a single arterial vessel. Then, a cylindrical 3.5- or 4.0-mm diameter tube, known as the Blalock–Taussig (BT) shunt, is placed between the innominate artery and the main pulmonary artery (MPA), allowing blood to supply the pulmonary circulation. This BT shunt operation is followed by two additional procedures, the Glenn procedure (performed at 4–6 months of age), and the Fontan procedure (performed at 18–36 months of age). During the Glenn procedure, the BT shunt is disconnected from the MPA and replaced with flow from the superior vena cava. Even in the best cases, the Norwood procedure can have several complications, including low cardiac output, arrhythmias, respiratory insufficiency, and stenosis of the pulmonary arteries or aorta (2). These complications can be affected by the function of the shunt. The first stage (Norwood) is crucial, as any complication can be magnified at subsequent operations, leading to increased morbidity and mortality. Currently, the mortality rate of the Norwood procedure is 15–25% (2). Over the years, the Norwood procedure has been refined. However, in spite of the refinements, there remain several shortcomings, such as the inability to adapt to the growing child, a high incidence of stenosis developing at the site of the pulmonary artery anastomosis, and even complete shunt occlusion. If stenosis develops at the pulmonary artery anastomosis, this markedly alters the amount and velocity of blood flow delivered to the pulmonary circulation, leading to adverse hemodynamics and propensity for developing progressive stenosis, all of which can add to morbidity and mortality. Therefore, there is interest in applying the

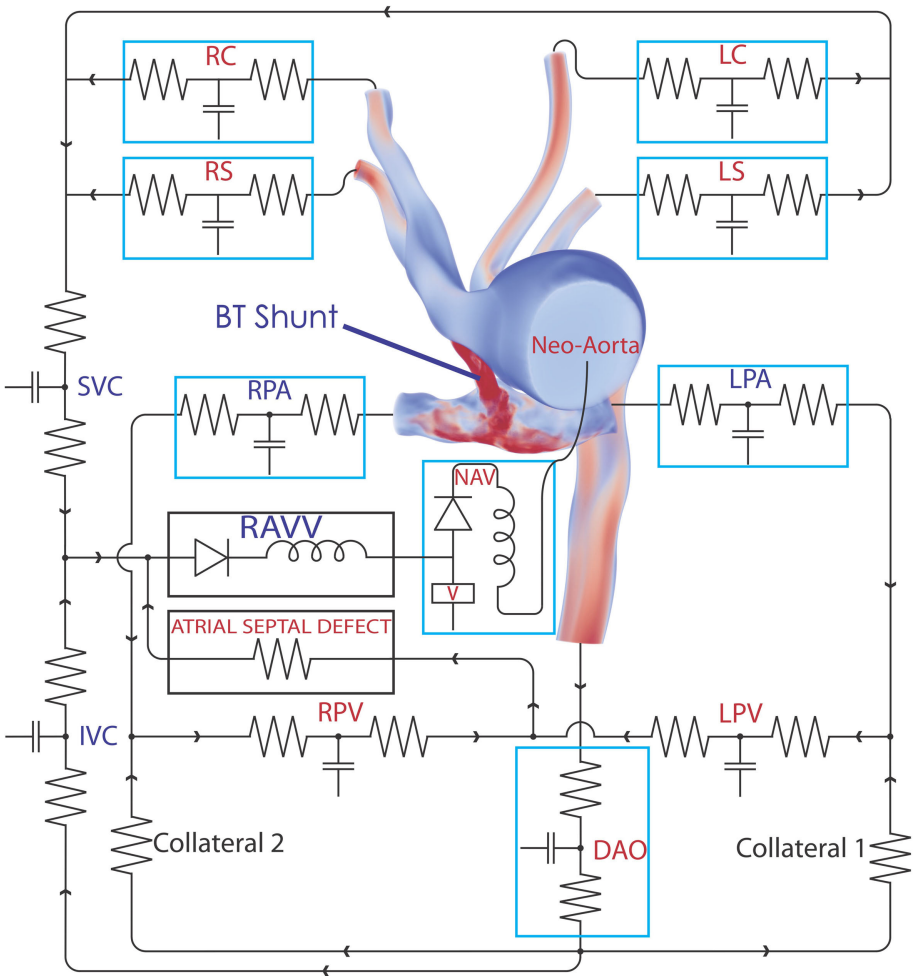

FIGURE 1 | The complete 3D–0D multi-domain model, including the closed-loop LPN circuit representing the physiological circulation of this patient. The single functioning ventricle, atrial septal defect, and collateralization are all modeled. A representative volume rendering of the velocity field is shown at one instant in time; red indicates high velocity and blue low velocity. Abbreviations: RC, right common carotid; RS, right subclavian; LC, left common carotid; LS, left subclavian; SVC, superior vena cava; IVC, inferior vena cava; RPV, right pulmonary vein; LPV, left pulmonary vein; DAO, descending aorta; LPA, left pulmonary artery; RPA, right pulmonary artery; RAVV, right atrio-ventricular valve; V, ventricle; NAV, neo-aortic valve. See **Tables 1**–**3** for all component parameter values.

tools of computational hemodynamics to this problem (3, 4). In this study, we investigate the computational reproduction of the hemodynamics, following BT shunt placement, and the impact of an alternative shunt design. To do this, we create a complex, patient-specific circulatory model, designed to reproduce the hemodynamic data recorded in a 4-month-old HLHS patient. We utilized our in-house geometric modeling, closed-loop circulatory design, and Navier–Stokes computational hemodynamics simulation package (5–7). These tools allow us to develop highly customizable lumped parameter model circuits that can capture complex facets of the patient's presentation, including aortic atresia and mitral stenosis, as well as a large atrial septal defect and evidence of bilateral aortopulmonary collateralization with discrete collaterals to the right lung. Then, we use the model to consider an alternative, flared design for the BT shunt.

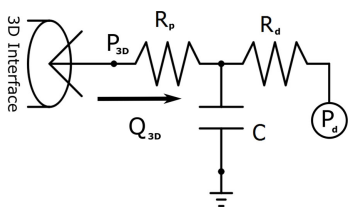

FIGURE 2 | The three-element Windkessel model, which is used to create boundary conditions at the vascular outflows of the three-dimensional domain. Note that P_d is given a fixed value in initial simulations, but once the full closed-loop circulation is created, it becomes a solution variable determined by the downstream venous system model to which it is connected.

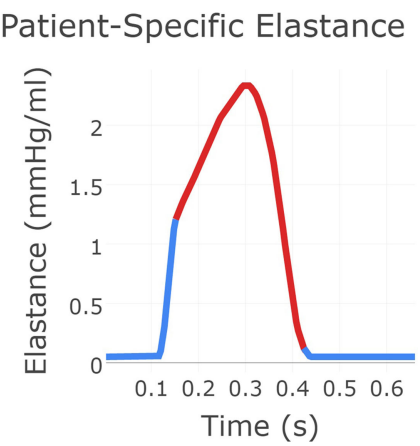

FIGURE 3 | The patient-specific time-varying elastance function created using a combination of data and exponential decay fitting. The red region was derived from patient recordings of flow through the neo-aortic valve and continuous pressure recording in the ventricle. The blue region for which no data were available was produced using Gaussian extrapolation. This gives the time-varying relationship between pressure and flow in the patient's ventricle.

2. MATERIALS AND METHODS

2.1. Patient Data

Clinical data were acquired for a 4-month-old child who was born with hypoplastic left heart syndrome. The patient had undergone a Stage 1 Norwood procedure at 5 days of age, in which the innominate artery was connected to the MPA via a 3.5 mm diameter modified BT shunt. At 4 months of age, during pre-hemi-Fontan cardiac catheterization, the pulmonary arterial pressures were measured using left and right pulmonary venous wedge pressure measurements. During the same procedure, pressures were measured in the ascending and descending aorta. In an additional pre-hemi-Fontan research procedure, cardiac MRI and MRA were performed, providing data on ventricular end-systolic and end-diastolic volumes and flows through the superior and inferior vena cava, the ascending and descending

TABLE 1 | Parameter values for the three-element Windkessel models attached directly to the three-dimensional domain.

	Rp	Rd	C
RC	0.50931	2.68885	0.71603
LC	0.50004	2.43319	0.74383
RS	0.50878	2.6307	0.74512
LS	0.45264	2.10615	0.84197
DAo	5.919×10^{-2}	0.28437	5.01933
RPA	3.277×10^{-2}	0.1361	1.76235
LPA	3.108×10^{-2}	0.31950	1.00099

Rp, proximal (closer to the aorta) resistance (Pa s mm^{-3}); Rd, distal resistance (Pa s mm^{-3}); C, compliance (mm^3 Pa^{-1}).
*See **Figure 1** and its caption for the names and abbreviations of the vascular regions.*

TABLE 2 | Parameter values for the three-element Windkessel-like sections of the loop-closing circuit.

	Rp	Rd	C
SVC	0.15500	1.807×10^{-2}	284.73779
IVC	0.22075	2.261×10^{-2}	135.95630
RPV	2.693×10^{-2}	2.040×10^{-2}	72.05470
LPV	1.027×10^{-2}	8.970×10^{-3}	132.96730

Rp, proximal (closer to the aorta) resistance (Pa s mm^{-3}); Rd, distal resistance (Pa s mm^{-3}); C, compliance (mm^3 Pa^{-1}).
*See **Figure 1** and its caption for the names and abbreviations of the vascular regions.*

TABLE 3 | Parameter values for the remaining (i.e., not covered by Table 1 or Table 2) sections of the loop-closing circuit.

Component	Value
RA valve open resistance	3.3×10^{-3}
RA valve inertance	6.667×10^{-5}
Neo-aortic valve (NAV) open resistance	1.0×10^{-3}
Neo-aortic valve (NAV) inertance	1.0×10^{-5}
Collateral 1 resistance	9.69600×10^{-2}
Collateral 2 resistance	0.05
Atrial septal defect resistance	3.0×10^{-4}

*Resistances have units Pa s mm^{-3}, inductances have units Pa s^2 mm^{-3}. See **Figure 1** and its caption for the names and abbreviations of the vascular regions.*

aorta, the left and right pulmonary arteries (LPA; RPA), and veins (LPV; RPV).

2.2. Geometric Modeling and Discretization

A patient-specific computer-aided design (CAD) model of the arteries of the chest region was segmented from MRI image data of the patient using the geometric modeling tools within CRIMSON. This model contains the following vessels: ascending and descending aorta, left and right subclavian arteries, left and right common carotid arteries, left and right pulmonary artery, and surgically placed BT shunt. The model consists of one inlet (i.e., the ascending aorta) and seven outlets (i.e., all other vessels described above). The extent of the model is sufficient to capture complex blood flow in the BT shunt and the pulmonary artery anastomosis. The hemodynamic description of this circulation is displayed in **Figure 1**. In preparation for finite element simulation, a linear tetrahedral finite element mesh was generated, consisting of 231,484 nodes and 1,215,138 elements. A preliminary simulation was performed using this mesh, and an adaptive field-based mesh refinement strategy, striving to ensure the mesh was sufficiently refined for our studies was subsequently employed (8). This approach produced additional meshes consisting of 659,851 nodes and 3,722,358 elements, and finally 872,046 nodes and 4,993,559 elements; the final reported results use this finest mesh. All simulations were performed using a time-step of 0.1 ms, and the time integration scheme utilized, the generalized α-method, provided second-order accuracy and unconditional stability (9).

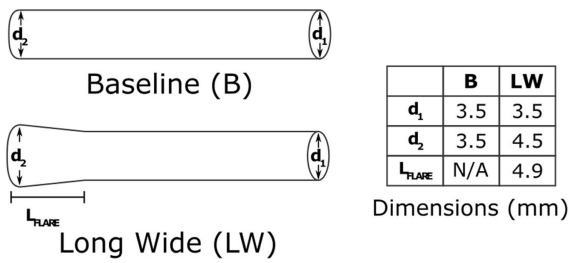

	B	LW
d_1	3.5	3.5
d_2	3.5	4.5
L_{FLARE}	N/A	4.9

Dimensions (mm)

FIGURE 4 | The two shunt designs which we will consider in this paper. The baseline shunt is the design that was used in the patient. The Long Wide flared shunt is a hypothetical alternative, which we evaluate numerically. The diameters are as they would be at the time of manufacture, without any occlusion. The shunts are both 14 mm in length.

2.3. Model Boundary Condition Design

A multi-domain modeling approach (10) was used to characterize the hemodynamics, whereby the full 3D non-linear incompressible three-dimensional Navier–Stokes equations are used in the image-based CAD portion of the model, and a series of customizable 0D lumped parameter networks (LPN) are used to model the distal pulmonary and systemic circulations, as well as the patient's collateral circulations and ventricular function, in a closed-loop manner. This 3D–0D multi-domain, closed-loop modeling approach has been previously used successfully to represent complex hemodynamics involving dynamic autoregulation (11, 12) and single-ventricle physiology (13). The CRIMSON Netlist Editor Boundary Condition Toolbox (NEBCT) enables the definition of complex cardiovascular LPN circuits and to easily account for atrial and ventricular septal defects, valve abnormalities, as well as abnormal collateral branches. All simulations were run under the assumption of rigid walls.

2.4. Model Boundary Condition Design and Parameterization

Design and parameterization of the 0D LPN in order to achieve the full multi-domain closed-loop (10) model shown in **Figure 1** proceeded in several stages. First, three-element Windkessel boundary conditions were applied at all outlet faces of the model

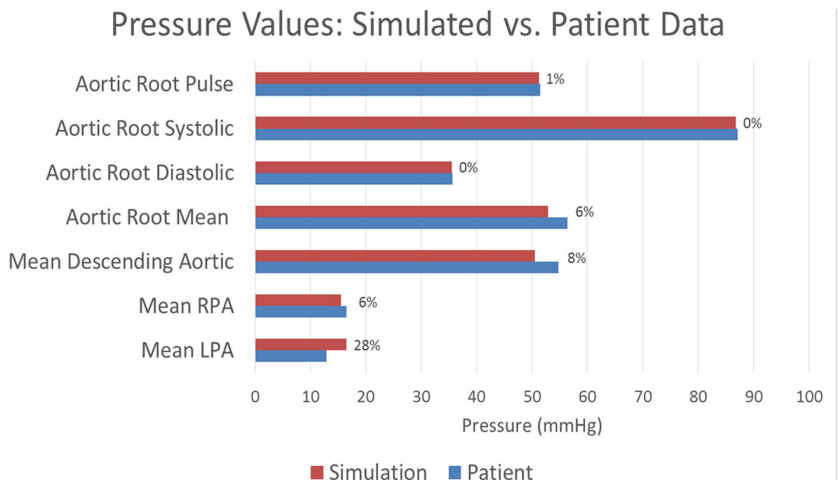

FIGURE 5 | A comparison between the pressures achieved in the baseline simulation and the pressures recorded in the patient at various locations throughout the model. Each bar is marked with the percentage error in the simulated value relative to the patient recording. All assessed locations are visible in **Figure 1**.

(14), and the inflow at the neo-aortic valve was imposed according to PC-MRI flow recordings from the patient. The Windkessel model is shown in **Figure 2**; the equation for this model, relating pressure, P_{3D}, and flow, Q_{3D} at the three-dimensional interface, and with C the compliance of the vascular bed, R_P the proximal resistance, R_d the distal resistance, and P_d the distal pressure, is given by

$$\frac{dP_{3D}}{dt}CR_d + P_{3D} - P_d + Q_{3D}(R_d - R_p) - \frac{dQ_{3D}}{dt}R_pR_dC = 0, \quad (1)$$

with suitable physiological initial values for Q_{3D} and P_{3D}, and with P_{3D} fixed to zero in the initial simulations. Note that in the final complete closed loop, P_d shown in **Figure 2** becomes a solution variable determined by the state of the downstream vasculature model, as opposed to the fixed value that it was given during initial parameterization.

Iterative simulations were performed using the CRIMSON stabilized incompressible Navier–Stokes flow solver on 80 cores of the University of Michigan's Flux High Performance Computing (HPC) cluster ConFlux, or 256 cores of a SGI UV 1000 HPC system at King's College London. The resistances of the three-element Windkessel models were adjusted until the correct mean blood flow was observed at each outlet (targeting within 10% of the PC-MRI data), and the mean aortic root pressure matched the patient data. The Windkessel compliances were further tuned to approximately achieve the correct pulse pressure in the aortic root (targeting within 10% of the cardiac catheterization data).

Next, the flow through the neo-aortic valve was extracted from PC-MRI data, integrated in time and subtracted from the patient's end-diastolic volume as given in the clinical report. This produced a systolic ventricular volume curve. This curve was aligned with the continuous pressure recording data taken inside the ventricle, and the pressure curve was point-wise divided by the volume curve. The result produced the patient-specific time-varying ventricular elastance during the period when the aortic valve is open. In order to complete the elastance function for the entire cycle, a single Gaussian curve was used to extrapolate the patient-specific systolic elastance on both sides. A Fourier smoothing was applied, ensuring that the interpolated function was C^1-continuous throughout. Finally, the curve was scaled to ensure the peak elastance was not changed by the smoothing step. The resulting time-varying elastance function is shown in **Figure 3**. The red segment of the curve shows the patient-specific systolic portion of the elastance function, the blue corresponds to the Gaussian extrapolation of the remaining diastolic portion. A single-ventricle model with an atrial septal defect, informed by the clinical reports, was drawn using the CRIMSON Netlist Editor Boundary Condition Toolbox (NEBCT) (5–7) (see **Figure 1**), and the constructed elastance function was imposed on the ventricle using the CRIMSON Dynamic LPN Framework. Further LPN circuitry was drawn in the NEBCT, representing the inferior and superior vena cava, left and right pulmonary veins, and the aorto-pulmonary collateralization (Collaterals 1 and 2, **Figure 1**). The drag-and-drop circuit design tools of CRIMSON NEBCT permitted the creation of a physiological circulation, which

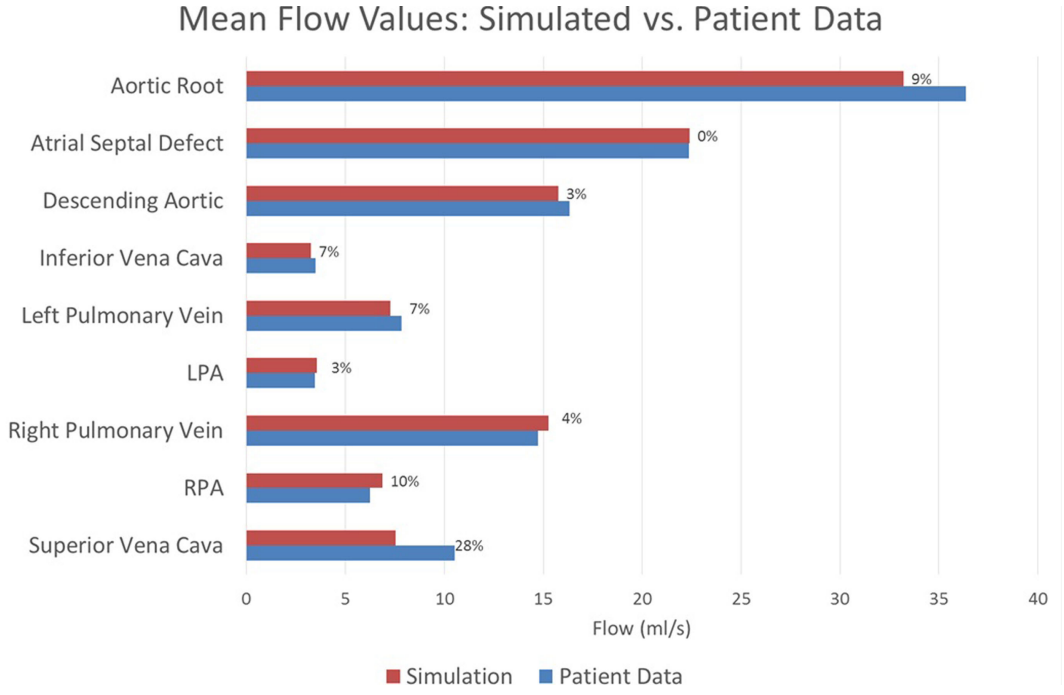

FIGURE 6 | A comparison between the flows achieved in the baseline simulation and the heart rate-adjusted flows from the patient at various locations throughout the model. Each bar is marked with the percentage error in the simulated value relative to the patient recording. All assessed locations are visible in **Figure 1**. Note that the patient data for the atrial septal defect flow were computed by subtracting the patient data vena cava flow from the patient data cardiac output; all remaining patient data values were direct measurements.

would have otherwise been a difficult and arduous task. NEBCT also made straightforward any iterative redesign required during model development. The resulting closed-loop, single-ventricle circulation is shown in **Figure 1**.

The heart model was divided into a series of 0D components representing the right atrial, left atrial, and right ventricular compartments, including only the valves connecting directly to the single functioning ventricle. The atrial septal defect was modeled so that blood from the systemic venous and pulmonary venous circulation drains into the right ventricle through the tricuspid valve. The pulsatile contraction and relaxation of the right ventricle was modeled using the patient-specific elastance function described above, giving the time-varying ratio of the ventricular pressure to the difference between the ventricular volume and the unstressed ventricular volume (11). The valves were modeled via diodes that permit flow only in the forward direction. This heart model was connected to the neo-aortic valve surface of the ascending aorta. Due to the closed-loop approach, regional flows in the different systemic and pulmonary beds drain into a model of the venous system, thus enforcing the proper continuity of flow within the circulatory system. The final step of the parameterization was to fine-tune the closed-loop LPN component parameters to recover the hemodynamics (e.g., flow splits and pressures) observed in the individual. This required multiple iterative simulations, which were performed manually. While further tuning of the model parameters could have been performed, we were willing to tolerate some percentage of error, especially in cases where the absolute errors were small, since local small absolute errors have minimal global impact. The numerical values for parameters of all the LPN given in **Figure 1** are summarized in **Tables 1–3**.

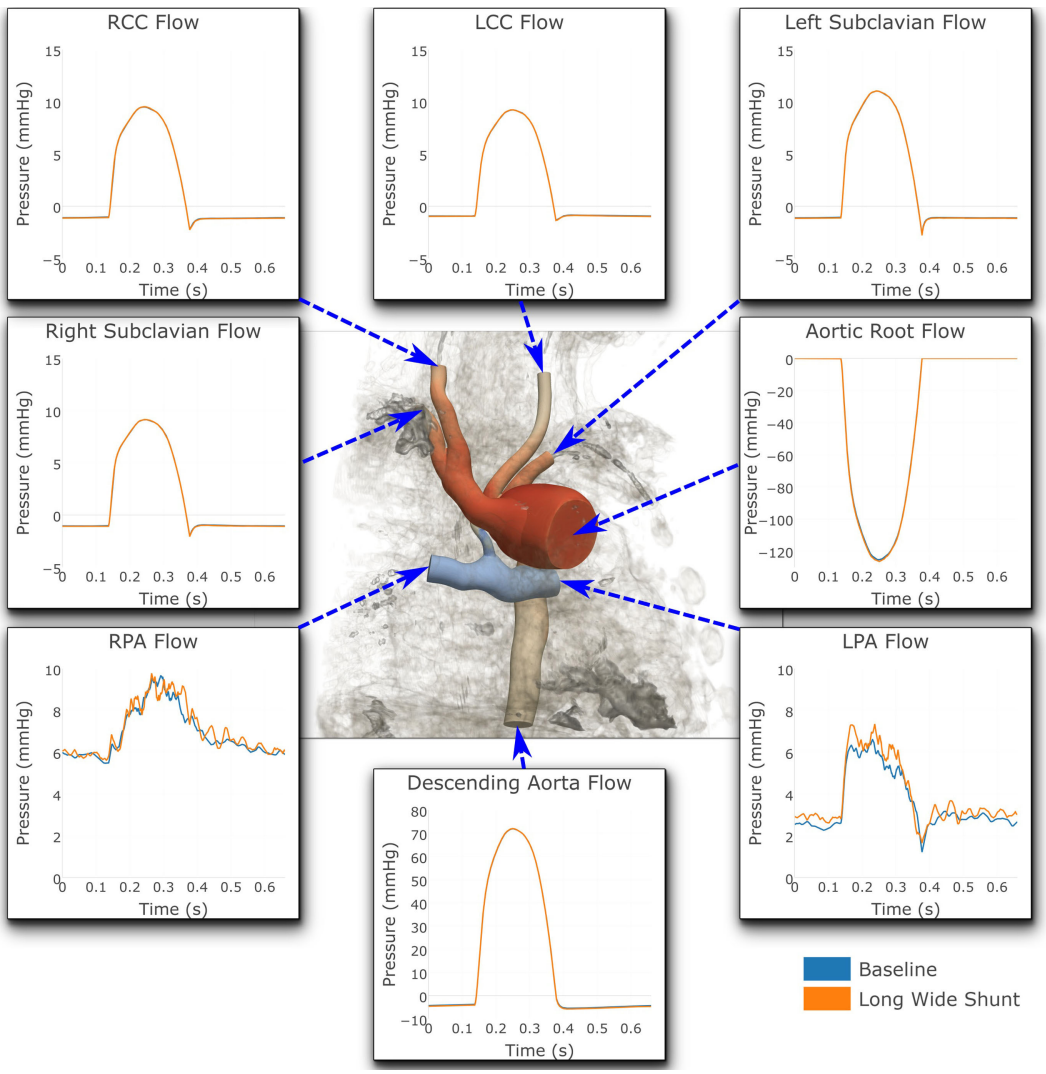

FIGURE 7 | Flows at all the boundaries of the three-dimensional domain. At most locations, the flows are indistinguishable from one another. Note that three different *y*-axis scales have been used: one for the LPA and RPA, another for the aortic root and descending aorta, and a third for all the remaining outlets. For illustrative purposes, the geometric model has been embedded in a volume-rendering of the MRA image data, and a non-dimensionalized pressure coloring has been used on the surface of the geometry.

2.5. Computational Derivation of the Percentage of Shunt Occlusion

During parameterization of the model, it was determined that it was impossible to achieve the patient data pressures recorded in the aorta and pulmonary arteries, while simultaneously achieving the patient-recorded flow through the BT shunt. This gave a fundamental indication that the resistance to flow of the BT shunt was no longer consistent with a BT shunt tube having the originally specified 3.5-mm diameter corresponding to the post-operative conditions. We determined that a suitable resistance could be achieved by reducing the shunt diameter by 22%; this corresponds to a 40% area occlusion in the shunt after 4 months. BT shunt stenosis or occlusion is a well-documented complication (15–17). Due to limitations in the resolution of the available MRI data, it was not possible to directly observe this degree of occlusion in the original dimensions of the shunt. Thus, this

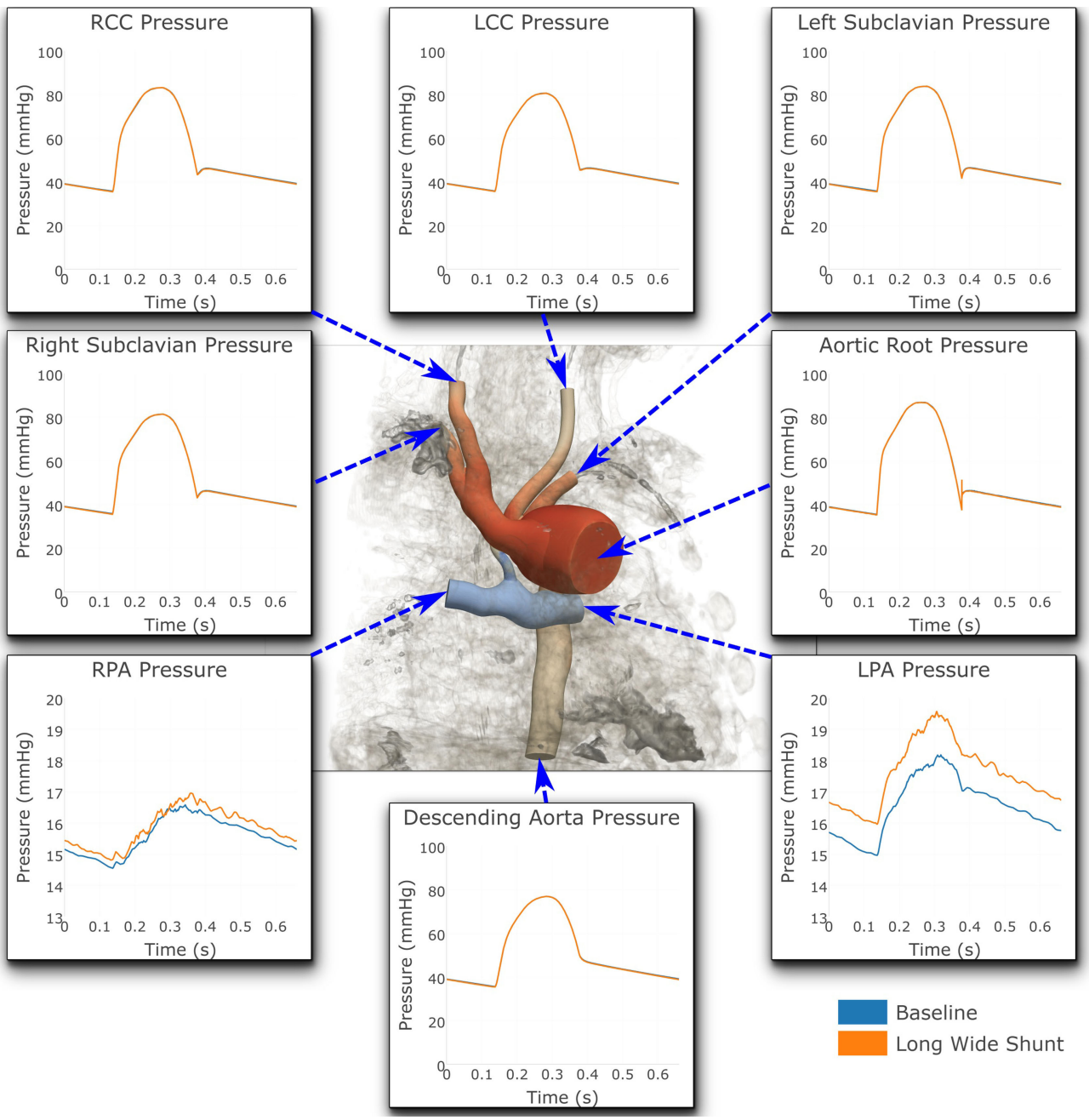

FIGURE 8 | Pressures at all the boundaries of the three-dimensional domain. At most locations, the pressures are indistinguishable from one another. Note that two different *y*-axis scales have been used: One for the LPA and RPA, and another for all the remaining outlets. For illustrative purposes, the geometric model has been embedded in a volume-rendering of the MRI image data, and a non-dimensionalized pressure coloring has been used on the surface of the geometry.

illustrates how computational simulations can enhance the available data on the individual without the need for further invasive assessments.

2.6. Examining the Hemodynamic Impact of an Alternative BT Shunt Design

Upon completion of a baseline model reproducing the patient's clinical data, we used the model to investigate the impact of an alternative BT shunt on the hemodynamics in the pulmonary arteries. To achieve that, we adjusted the three-dimensional geometric model by replacing the original (cylindrical) shunt with a flared design, having nominal dimensions as shown in **Figure 4**. In light of the reduction in baseline shunt diameter described above, for the flared shunt, we also reduced all nominal diameters by 22%. After anisotropic mesh refinement, a finite element mesh of the geometric model of the Long Wide alternative shunt was created, consisting of 860,884 nodes and 4,707,343 elements. We then simulated the use of this shunt, without changing the parameters of the LPN circuit from those determined for the baseline case.

The impact of the different shunt designs on the hemodynamics in the PAs was evaluated by examining the resulting differences in mean pressure and mean flow in the left and right pulmonary arteries.

TABLE 4 | Breakdown of the change in hemodynamic parameters in the LPA and RPA, caused by the shunt flaring.

	LPA pressure	RPA pressure	LPA flow	RPA flow
Baseline	16.5	15.6	3.6	6.9
Long wide	17.6	15.9	3.9	7.1
Change (%)	7	2	9	3

Pressures are given in millimeters of mercury and flows in milliliters per second.

TABLE 5 | The impact of shunt flaring on pressure in, and flow to, the pulmonary arteries.

	Baseline shunt	Long wide flared shunt
Mean aortic pressure (mmHg)	52.9	52.9
Mean pulmonary pressure (mmHg)	16.0	16.7
Shunt pressure gradient (mmHg)	36.9	36.2
Mean shunt flow (ml s^{-1})	10.4	11.0
Shunt resistance (mmHg ml^{-1} s)	3.5	3.3

TABLE 6 | The disagreement between the patient data and the hemodynamic parameters of the baseline shunt when using implant-time dimensions and the agreement that was obtained by reducing the shunt diameter by 22% in our simulations.

	Patient data	Shunt conforming to implant-time dimensions	Shunt with 22% diameter occlusion
Mean aortic pressure (mmHg)	56.4	58.5	52.9
Mean pulmonary pressure (mmHg)	14.7	38.6	16.0
Shunt pressure gradient (mmHg)	41.7	19.9	36.9
Mean shunt flow (ml s^{-1})	9.7	9.6	10.4
Shunt resistance (mmHg ml^{-1} s)	4.3	2.1	3.5

3. RESULTS

3.1. Flow and Pressure Indices in the Baseline Shunt

The baseline shunt model successfully reproduced the patient's hemodynamic data, given by the clinical report, the PC-MRI, and the cardiac catheterization data. **Figures 5** and **6** show a comparison between computed and measured flow and pressure indices at different locations of the aorto–pulmonary circulation. Aortic root mean, pulse, systolic and diastolic pressures, and mean flow are recovered through the carefully adjusted patient-specific elastance function given in **Figure 3**. Fourteen of the 16 reported indices lie within 10% of the data. The biggest discrepancies are observed in the mean LPA pressure (28% error) and in the superior vena cava flow (27.8% error, which corresponds to a small absolute discrepancy of 2.92 ml/s). We note that despite the relatively large error in mean LPA pressure, both LPA and RPA pressures lie between the LPA and RPA mean pressure values recorded in the patient. Therefore, we claim that our model performs well in reproducing the hemodynamics for the baseline BT shunt case (with the noted 22% diameter reduction), indicating that we have created an accurate model and a solid foundation on which to perform further investigations into the impact of creating a flare on the distal end of the BT shunt. We remark that our baseline simulations indicate that the flow through Collateral 1 was 4 ml/s and the flow through Collateral 2 was 8.6 ml/s; comparable information was not available among the clinical recordings.

3.2. Comparative Impact of Shunt Flaring on Pulmonary Artery Hemodynamics

Figures 7 and **8** show a comparison of the hemodynamics between the two studied shunt geometries, given in terms of

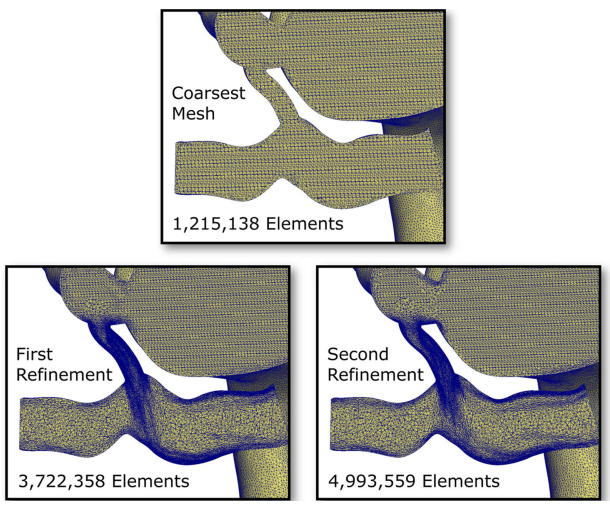

FIGURE 9 | Cut-through views of the finite element meshes within the pulmonary arteries and shunt in the baseline shunt design case. Three levels of mesh refinement are shown; the refinements were generated algorithmically, based on a local velocity gradient error indicator (8). Notice the high level of refinement occurring in the shunt and the LPA.

time-resolved flow and pressure waveforms at each of the inlets and outlets of the three-dimensional model. The geometry is shown embedded within a three-dimensional volume-rendering of the original MRA data, providing anatomical context. We observe that suitable pressure and flow patterns are reproduced at all locations. In general, the pressure and flow traces at each outlet were not strongly affected by the shunt geometry, with the exception being the left and right pulmonary arteries. In the pulmonary arteries, we see that the waveforms for the two cases display different patterns of high-frequency oscillation within the data. This is likely indicative of the disturbed flow patterns within the pulmonary arteries being highly sensitive to the model geometry, due to the large Reynolds number flow through the BT shunt (in the baseline shunt, peak systolic Re = 1,830; shunt diameter 2.71 mm, peak systolic volumetric flow = 14,800 $mm^3\ s^{-1}$, viscosity = 0.004 Pa s, density = 0.00106 g mm^3). The maximum difference in LPA and RPA mean flows between the two models is 9%, and occurs in the LPA.

Figure 8 shows that the baseline shunt model presents lower mean pressure values in the LPA and RPA, of 16.51 and 15.55 mmHg, respectively. Conversely, the Long Wide flared shunt presents larger mean pressure values in LPA and RPA, 17.59 and 15.85 mmHg, respectively. This illustrates the impact of the smaller resistance to flow offered by the longer and wider flare compared to the baseline model.

A full numerical comparison of the impact of flaring on pressure and flow in the LPA and RPA is given in **Table 4**. We observe that flaring leads to an increase in mean pressure and flow in both the left and right pulmonary arteries, but there is considerable asymmetry in the effect; the LPA receives three times as much additional flow as the RPA with the flare present.

3.3. Comparison of Shunt Properties

In **Table 5**, we see the impact of shunt flaring on pressure in and flow to the pulmonary arteries. Total flow to the pulmonary arteries increases by 6%, and mean pulmonary pressure increases by 4%. These results indicate that flaring may be beneficial if additional flow to the pulmonary arteries is required.

4. DISCUSSION

4.1. Determining Shunt Occlusion from the Computations

In the initial simulations using the originally specified dimensions of the BT shunt, we were unable to find a set of parameters which allowed reproduction of the clinical data. The best-case results obtained had mean aortic root pressure of 58.5 mmHg, mean pulmonary pressure of 38.6 mmHg, giving an approximate pressure gradient across the BT shunt of 19.9 mmHg, and mean BT shunt flow of 9.6 ml/s. This compared to the patient data indicating that the mean aortic root pressure should be 56.4 mmHg, the mean pulmonary pressure 14.7 mmHg, and the approximate pressure gradient across the BT shunt 41.7 mmHg, with a mean BT shunt flow of 9.7 ml/s. Thus, considering only the BT shunt, the simulation produced a 52% error in the pressure gradient

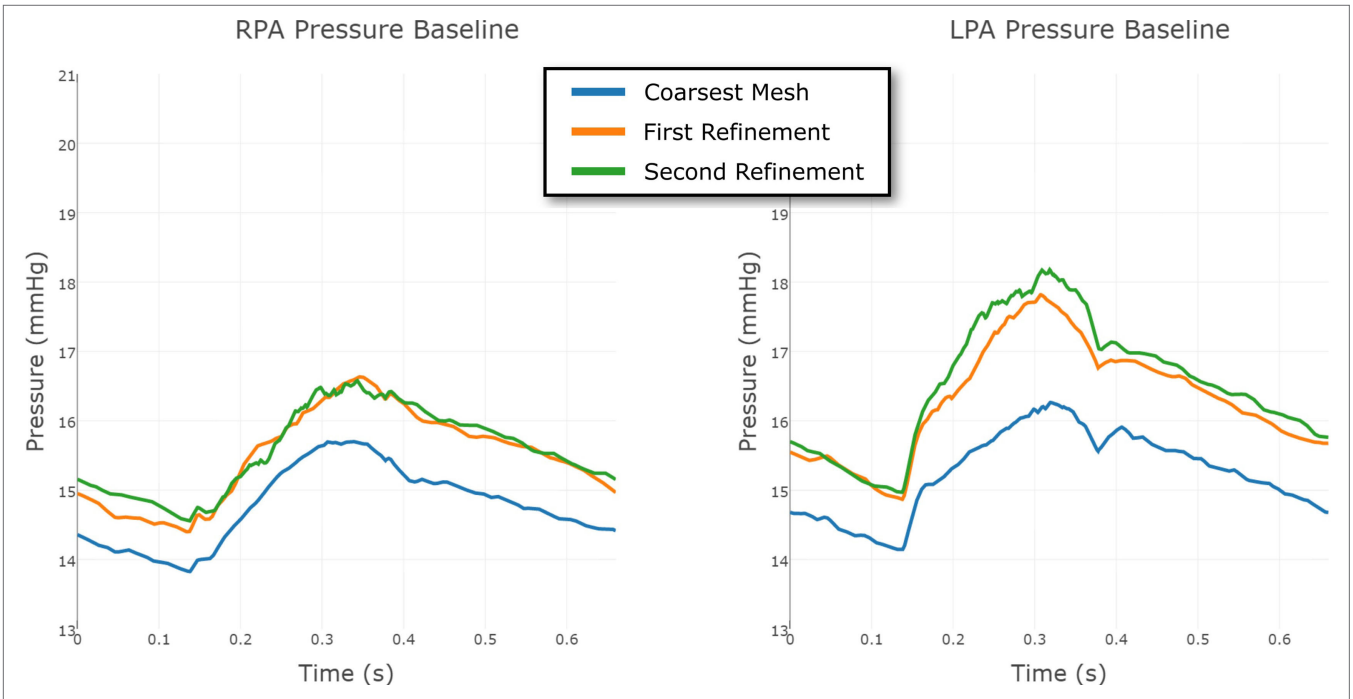

FIGURE 10 | Comparison between the pressure at the RPA and LPA outflows in the baseline shunt model, using three different levels of finite element mesh refinement. The results are shown over a full cardiac cycle. The *coarsest mesh* consisted of 231,484 nodes and 1,215,138 elements; the *First Refinement* mesh consisted of 659,851 nodes and 3,722,358 elements; and the *Second Refinement* mesh consisted of 872,046 nodes and 4,993,559 elements. The mesh refinement is local, informed by an error indicator.

estimate, while the error in the BT shunt flow was only 1%. This indicated that the resistance, and thus the assumed geometry of the BT shunt was incorrect. Using the Hagen–Poiseuille equation, we estimated that the diameter of the shunt should be reduced by 22% to achieve the correct resistance. Subsequent numerical simulations proved this estimate to be accurate, allowing us to recover the mean pressure in and flow to the pulmonary arteries with an error tolerance of 10%, compared to the previous 52% error. Specifically, with this geometry we achieved mean aortic root pressure of 52.9 mmHg, mean pulmonary pressure of 16.0 mmHg, giving an approximate BT shunt pressure gradient of 36.9 mmHg and a mean BT shunt flow of 10.4 ml/s. These values are summarized in **Table 6**, and correspond to errors relative to the patient data of 11 and 7%, respectively.

We have not directly confirmed that the diameter of the shunt has uniformly reduced by 22% along its length. Rather, we state that this or an equivalent change must have taken place in the patient in order to account for the observed results. An alternative scenario would be a greater level of narrowing at one end of the shunt, resulting in the same through shunt-equivalent resistance. Due to the resolution of the MRI images, we were not able to assess how the BT shunt geometry has truly changed in the patient.

4.2. Determination of Model Parameters

Significant effort was required during manual parameter tuning of our closed-loop LPN model. While the present work demonstrates the feasibility of such an approach, an important future development will be to begin using data assimilation techniques to determine these parameters algorithmically, and to a large extent, automatically (18, 19). This will be an important development, allowing us to examine and compare multiple such clinical cases.

4.3. Impact of Shunt Flaring on Pulmonary Artery Hemodynamics

The results show that there is potential for achieving increased pulmonary pressure and blood flow by using flared BT shunts, including changes in flow of up to 9% in the LPA. While it is clear that more pressure or flow is not automatically beneficial, such increases may have clinical value; given that a common complication after BT shunt placement is shunt stenosis, a shunt capable of delivering more flow may reduce the impact of the narrowing on PA hemodynamics (15–17). We believe that investigation of further alternative shunt designs is warranted. The flare we have used is relatively short, but we have demonstrated the feasibility and power of this modeling technique, laying a solid foundation for further investigation of alternative flared designs.

There may be limitations in terms of the widest possible flare, given the size of neonatal pulmonary arteries, but given that the largest diameter considered was 4.5 mm, and that the healthy 40-week gestation diameters for the main, left, and right pulmonary arteries has been reported to be 9.23, 5.65, and 5.49 mm, respectively (20), it is not inconceivable that the use of such flares may be clinically possible.

FIGURE 11 | Comparison between the pressure at the RPA and LPA outflows in the Long Wide shunt model, using three different levels of finite element mesh refinement. The results are shown over a full cardiac cycle. The *coarsest mesh* consisted of 231,740 nodes and 1,216,259 elements; the *First Refinement* mesh consisted of 549,040 nodes and 2,919,044 elements; and the *Second Refinement* mesh consisted of 860,884 nodes and 4,707,343 elements. The mesh refinement is local, informed by an error indicator.

4.4. Pulmonary Artery Mean Pressure Discrepancy with Data

The clinical report indicated a pressure difference between the left and right pulmonary arteries of 3.6 mmHg. The largest such difference we could achieve computationally was 1.7 mmHg, which represents a significant discrepancy with the data. Most likely this indicates that some unknown factor, probably geometric, is not included in our model, although it may also be an error in the clinical measurement. For this reason, during parameterization, we chose to accept pulmonary artery pressures anywhere within the 3.6 mmHg range reported in the data (i.e., any values in the range 12.9–16.5 mmHg). Thus, the errors in the mean LPA and RPA pressures shown in **Figure 5** should be understood within this context. Indeed, if we instead considered any simulated LPA and RPA pressure lying in this range to be of low error, then together with the 10% error tolerance used for all other values, the accuracy of our baseline simulation is even greater: fifteen of the sixteen reported indices considered in **Figures 5** and **6** achieve or exceed our accuracy target.

4.5. Disturbed Flow in the Pulmonary Arteries and Numerical Accuracy

Flow within the pulmonary arteries was observed to be highly disturbed. This is apparent from the high-frequency oscillations which are present in the LPA and RPA pressure and flow waveforms, shown in **Figures 7** and **8**. By these measures, the degree of flow disturbance does not appear to be strongly dependent on the shunt geometry in the cases examined.

To eliminate the possibility of this oscillatory behavior being a numerical artifact, we attempted to eliminate numerical error by increasing the resolution of the finite element mesh. Mesh refinement was performed using an offline anisotropic adaptive meshing strategy, whereby a coarse mesh was generated, the simulation run, then a local error indicator based upon the hessian of the velocity field was used to perform mesh refinement (8). This strategy was repeated twice, resulting in three successively finer meshes, with the additional nodes and elements concentrated in regions of higher error. This can be seen in **Figure 9**, where we see that the shunt and LPA receives most of the refinement, whereas the mesh of the aorta and systemic vessels remains relatively unchanged. The pressure over one cycle in the LPA and RPA in the baseline shunt case with these levels of mesh refinement is shown in **Figure 10**. The *coarsest mesh* consisted of 231,484 nodes and 1,215,138 elements; the *First Refinement* mesh consisted of 659,851 nodes and 3,722,358 elements; and the *Second Refinement* mesh consisted of 872,046 nodes and 4,993,559 elements. The final results reported in this work were obtained using the *Second Refinement* mesh, and we see from **Figure 10** that the level of convergence of the pressure waveform is sufficient (i.e., there is a reasonably small difference between results obtained with the second and first refinements), and that the oscillations do not reduce with mesh refinement.

The same strategy was employed for the Long Wide shunt model. The three meshes, from coarsest to finest, had 231,740

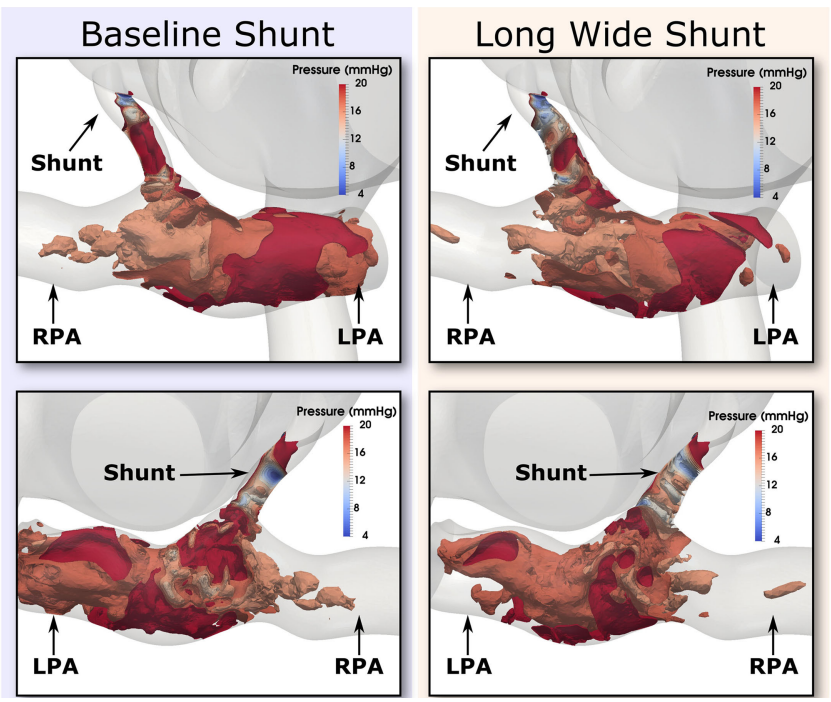

FIGURE 12 | Pressure isosurfaces at peak systole in the shunt and pulmonary arteries, with one isosurface every 2 mmHg in the inclusive range 4 and 20 mmHg. Comparison is presented between baseline (left column) and the Long Wide alternative (right column) shunt. The views provided are approximately anterior (top row) and posterior (bottom row). Flow is highly complex in both cases.

nodes and 1,216,259 elements; 549,040 nodes and 2,919,044 elements; and 860,884 nodes and 4,707,343 elements, respectively. The convergence of the LPA and RPA pressure in this case is shown in **Figure 11**. The finest mesh was used for the results reported here, and this figure shows that the mesh is sufficiently refined for us to have confidence in the results.

Further evidence in support of the level of flow disturbance in the PAs is provided in **Figure 12**, where highly complex pressure isosurfaces at peak systole are shown for both the baseline and Long Wide shunt cases, using the most refined mesh for each. It is thus likely that the complexity of these flow patterns explains the high-frequency oscillations in the reported flow and pressure LPA and RPA waveforms. In a pulsatile flow such as this, it is possible that the maximum Reynolds number attained in the shunt (1,830) is associated with turbulence. Direct numerical simulations (DNS) would be required to further resolve the small scales of the flow and to properly quantify turbulence (21). Currently, there are no suitable mathematical turbulence models for pulsatile cardiovascular flows (22). However, this is beyond the scope of the present work.

To conclude, these results suggest that the oscillations are a genuine physical phenomenon, not uncharacteristic of the moderately high Reynolds numbers of the flow through the BT shunt (max. Re = 1,830). Further evidence for this being a physical phenomenon is given by the fact that the clinical pressure recordings taken in the PAs was observed to be qualitatively noisier than that taken in the aorta.

5. CONCLUSION

In the present work, we have demonstrated that we can reproduce the hemodynamics in a highly complex physiological case of a 4-month-old child who has a BT shunt, as measured by a rich patient dataset with sixteen points of comparison. The achieved fidelity to data was very good; as discussed above, fifteen of the sixteen indices examined can be considered to agree well with the patient data. The demonstration of the capability of this modeling approach to accurately and simultaneously reproduce many pressure and flow values is striking and will create a valuable starting point for further studies.

We were able to use simulations to enhance the information available in the MRI data and the pressure recordings. Specifically, we discovered that the resistance between the systemic circulation and the pulmonary arteries through the BT shunt was not what would be expected for a tube cleanly attached to each vessel and retaining its original effective internal diameter without any stenosis developing within it or near its points of anastomosis, and computing that the effective diameter of the BT shunt has reduced by 22% since the time of the initial surgery. This value corresponds to a 40% area reduction.

Examining the impact of flaring the shunt on the hemodynamics within the pulmonary arteries indicates that increases in PA pressures and flows are possible with the use of flared shunts. Further work should examine the impact of the shunt design on the wall shear stress and oscillatory shear index within the pulmonary arteries, as well as examining other hemodynamic indices of interest, such as platelet activation potential (PLAP), which may be relevant given the disturbed hemodynamics caused by the shunt (23–25). It should also be determined whether other alternate shunt designs can have further hemodynamic benefits. The work should be extended to investigate whether the same conclusions drawn here regarding the effective decrease in luminal diameter of the BT shunt also hold for other patients.

The creation of the highly complex simulation model (**Figure 1**), together with the modified versions with the different BT shunt designs, was enabled by the flexibility of our computational hemodynamics modeling and simulation package (5–7).

ETHICS STATEMENT

This study has been performed with institutional review board (IRB) approval of the University of Michigan Health System. The title and ID of the protocol are "Assessment of Patient-Specific Hemodynamics Through Retrospective Clinical Data" (HUM00112350). Global IRB consent has been obtained to retrospectively analyze data for investigational studies using MRI images that have been anonymized.

AUTHOR CONTRIBUTIONS

CA wrote the paper, created the figures, developed the simulation tools, assisted in building the models, ran the simulations, and analyzed the results. PA built the geometric models, processed the data, wrote part of the paper, created figures, and ran simulations. AJ performed preliminary simulations and assisted in the preparation of the manuscript. AD and RG acquired the clinical data. RG and AF developed the concepts and assisted manuscript preparation. AF provided analysis of the simulation results.

FUNDING

The authors gratefully acknowledge support from the Edward B. Diethrich M.D. professorship, the University of Michigan CHAMPS/GHW award #322874, the Helen Kay Trust Charitable Trust, the European Research Council under the European Union's Seventh Framework Programme (FP/2007-2013)/ERC Grant Agreement no. 307532, and the United Kingdom Department of Health via the National Institute for Health Research (NIHR) comprehensive Biomedical Research Centre award to Guy's and St Thomas' NHS Foundation Trust in partnership with King's College London and King's College Hospital NHS Foundation Trust. Additional computing resources were provided by the NSF via grant 1531752 MRI: Acquisition of Conflux, A Novel Platform for Data-Driven Computational Physics (Tech. Monitor: EdWalker).

REFERENCES

1. Parker SE, Mai CT, Canfield MA, Rickard R, Wang Y, Meyer RE, et al. Updated national birth prevalence estimates for selected birth defects in the united states, 2004-2006. *Birth Defects Res A Clin Mol Teratol* (2010) 88:1008–16. doi:10.1002/bdra.20735
2. Hornik CP, He X, Jacobs JP, Li JS, Jaquiss RDB, Jacobs ML, et al. Complications after the Norwood operation: an analysis of the STS congenital heart surgery database. *Ann Thorac Surg* (2011) 92:1734–40. doi:10.1016/j.athoracsur.2011.05.100
3. Quarteroni A, Veneziani A. Analysis of a geometrical multiscale model based on the coupling of ODE and PDE for blood flow simulations. *Multiscale Model Simul* (2003) 1:173–95. doi:10.1137/S1540345902408482
4. Corsini C, Biglino G, Schievano S, Hsia T-Y, Migliavacca F, Pennati G, et al. The effect of modified Blalock-Taussig shunt size and coarctation severity on coronary perfusion after the Norwood operation. *Ann Thorac Surg* (2014) 98:648–54. doi:10.1016/j.athoracsur.2014.04.047
5. CRIMSON. *Software Website: CRIMSON (CardiovasculaR Integrated Modelling and SimulatiON)*. (2017). Available from: http://www.crimson.software
6. Khlebnikov R, Figueroa CA. Crimson: towards a software environment for patient-specific blood flow simulation for diagnosis and treatment. *Clinical Image-Based Procedures. Translational Research in Medical Imaging. CLIP 2015. Lecture Notes in Computer Science*. (Vol. 9401), Munich: Springer (2016). p. 10–8.
7. Arthurs CJ, Figueroa CA. Integration of an electrophysiologically driven heart model into three-dimensional haemodynamics simulation using the crimson control systems framework. *Computational Biomechanics for Medicine*. Munich: Springer (2016). p. 155–66.
8. Sahni O, Müller J, Jansen KE, Shephard MS, Taylor CA. Efficient anisotropic adaptive discretization of the cardiovascular system. *Comput Method Appl Mech Eng* (2006) 195:5634–55. doi:10.1016/j.cma.2005.10.018
9. Jansen KE, Whiting CH, Hulbert GM. A generalized-α method for integrating the filtered Navier-Stokes equations with a stabilized finite element method. *Comput Methods Appl Mech Eng* (2000) 190(3):305–19. doi:10.1016/S0045-7825(00)00203-6
10. Vignon-Clementel IE, Figueroa CA, Jansen KE, Taylor CA. Outflow boundary conditions for 3d simulations of non-periodic blood flow and pressure fields in deformable arteries. *Comput Methods Biomech Biomed Engin* (2010) 13:625–40. doi:10.1080/10255840903413565
11. Lau K, Figueroa CA. Simulation of short-term pressure regulation during the tilt test in a coupled 3d-0d closed-loop model of the circulation. *Biomech Model Mechanobiol* (2015) 14:915–29. doi:10.1007/s10237-014-0645-x
12. Arthurs CJ, Lau KD, Asrress KN, Redwood SR, Figueroa CA. A mathematical model of coronary blood flow control: simulation of patient-specific three-dimensional hemodynamics during exercise. *Am J Physiol Heart Circ Physiol* (2016) 310:H1242–58. doi:10.1152/ajpheart.00517.2015
13. Baretta A, Corsini C, Marsden AL, Vignon-Clementel IE, Hsia T, Dubini G, et al. Respiratory effects on hemodynamics in patient-specific CFD models of the Fontan circulation under exercise conditions. *Eur J Mech B Fluids* (2012) 35:61–9. doi:10.1016/j.euromechflu.2012.01.012
14. Westerhof N, Lankhaar J-W, Westerhof BE. The arterial Windkessel. *Med Biol Eng Comput* (2009) 47:131–41. doi:10.1007/s11517-008-0359-2
15. Moszura T, Zubrzycka M, Michalak KW, Rewers B, Dryzek P, Moll JJ, et al. Acute and late obstruction of a modified Blalock-Taussig shunt: a two-center experience in different catheter-based methods of treatment. *Interact Cardiovasc Thorac Surg* (2010) 10:727–31. doi:10.1510/icvts.2009.219741
16. Sachweh J, Däbritz S, Didilis V, Vazquez-Jimeneza JF, v Bernuthb G, Messmera BJ. Pulmonary artery stenosis after systemic-to-pulmonary shunt operations. *Eur J Cardiothorac Surg* (1998) 14:229–34. doi:10.1016/S1010-7940(98)00185-7
17. Godart F, Qureshi SA, Simha A, Deverall PB, Anderson DR, Baker EJ, et al. Effects of modified and classic Blalock-Taussig shunts on the pulmonary arterial tree. *Ann Thorac Surg* (1998) 66:512–7. doi:10.1016/S0003-4975(98)00461-5
18. Julier SJ, Uhlmann JK, Durrant-Whyte HF. A new approach for filtering nonlinear systems. *American Control Conference, Proceedings of the 1995*. (Vol. 3), Seattle: IEEE (1995). p. 1628–32.
19. Moireau P, Bertoglio C, Xiao N, Figueroa CA, Taylor C, Chapelle D, et al. Sequential identification of boundary support parameters in a fluid-structure vascular model using patient image data. *Biomech Model Mechanobiol* (2013) 12:475–96. doi:10.1007/s10237-012-0418-3
20. Ruano R, de Fatima YMM, Niigaki JI, Zugaib M. Pulmonary artery diameters in healthy fetuses from 19 to 40 weeks' gestation. *J Ultrasound Med* (2007) 26:309–16. doi:10.7863/jum.2007.26.3.309
21. Les AS, Shadden SC, Figueroa CA, Park JM, Tedesco MM, Herfkens RJ, et al. Quantification of hemodynamics in abdominal aortic aneurysms during rest and exercise using magnetic resonance imaging and computational fluid dynamics. *Ann Biomed Eng* (2010) 30:1288–313. doi:10.1007/s10439-010-9949-x
22. Banks J, Bressloff NW. Turbulence modeling in three-dimensional stenosed arterial bifurcations. *J Biomech Eng* (2007) 129:40–50. doi:10.1115/1.2401182
23. Nauta FJH, Lau KD, Arthurs CJ, Eagle KA, Williams DM, Trimarchi S, et al. Computational fluid dynamics and aortic thrombus formation following thoracic endovascular aortic repair. *Ann Thorac Surg* (2016). doi:10.1016/j.athoracsur.2016.09.067
24. Achille PD, Tellides G, Figueroa CA, Humphrey JD. A haemodynamic predictor of intraluminal thrombus formation in abdominal aortic aneurysms. *Proc R Soc A Math Phys Eng Sci* (2014) 470:2172. doi:10.1098/rspa.2014.0163
25. Shadden SC, Hendabadi S. Potential fluid mechanic pathways of platelet activation. *Biomech Model Mechanobiol* (2013) 12:467–74. doi:10.1007/s10237-012-0417-4

Conflict of Interest Statement: The authors declare that the research was conducted in the absence of any commercial or financial relationships that could be construed as a potential conflict of interest.

Advantages of publishing in Frontiers

OPEN ACCESS
Articles are free to read, for greatest visibility

COLLABORATIVE PEER-REVIEW
Designed to be rigorous – yet also collaborative, fair and constructive

FAST PUBLICATION
Average 85 days from submission to publication (across all journals)

COPYRIGHT TO AUTHORS
No limit to article distribution and re-use

TRANSPARENT
Editors and reviewers acknowledged by name on published articles

SUPPORT
By our Swiss-based editorial team

IMPACT METRICS
Advanced metrics track your article's impact

GLOBAL SPREAD
5'100'000+ monthly article views and downloads

LOOP RESEARCH NETWORK
Our network increases readership for your article

Frontiers
EPFL Innovation Park, Building I • 1015 Lausanne • Switzerland
Tel +41 21 510 17 00 • Fax +41 21 510 17 01 • info@frontiersin.org
www.frontiersin.org

Find us on